BEILSTEIN JOURNAL OF NANOTECHNOLOGY

Properties and applications of magnetic nanoparticles

Edited by Ulf Wiedwald and Paul Ziemann

Generated on 08 November 2026, 02:44

Imprint

Beilstein Journal of Nanotechnology
www.bjnano.org
ISSN 2190-4286
Email: journals-support@beilstein-institut.de

The *Beilstein Journal of Nanotechnology* is published by the Beilstein-Institut zur Förderung der Chemischen Wissenschaften.

Beilstein-Institut zur Förderung der Chemischen Wissenschaften
Trakehner Straße 7–9
60487 Frankfurt am Main
Germany
www.beilstein-institut.de

The copyright to this document as a whole, which is published in the *Beilstein Journal of Nanotechnology*, is held by the Beilstein-Institut zur Förderung der Chemischen Wissenschaften. The copyright to the individual articles in this document is held by the respective authors, subject to a Creative Commons Attribution license.

Beilstein Journal of Nanotechnology

Preparation, properties and applications of magnetic nanoparticles

Ulf Wiedwald* and Paul Ziemann*

Editorial

Open Access

Address:
Institut für Festkörperphysik, Universität Ulm, 89069 Ulm, Germany

Email:
Ulf Wiedwald* - ulf.wiedwald@uni-ulm.de; Paul Ziemann* - paul.ziemann@uni-ulm.de

* Corresponding author

Beilstein J. Nanotechnol. **2010,** *1,* 21–23.
doi:10.3762/bjnano.1.4

Received: 12 November 2010
Accepted: 19 November 2010
Published: 22 November 2010

Guest Editors: U. Wiedwald and P. Ziemann

© 2010 Wiedwald and Ziemann; licensee Beilstein-Institut.
License and terms: see end of document.

Though studies on small particles of various materials go way back before Nanoscience was emerging, this new interdisciplinary branch of science not only re-termed them into nanoparticles (NPs), but also lead to a dramatically enhanced interest in this type of nanoscaled material with an often given though arbitrary upper diameter limit of 100 nm [1]. As a natural consequence of this worldwide growing interest, the toolbox for preparing NPs has been amazingly broadened including now both, physics and chemistry related approaches. Furthermore, the meanwhile widely accepted distinction between top down and bottom up preparational methods can be applied to the fabrication of NPs as well. Examples for top down approaches are sculpting NPs out of a previously deposited thin film by e.g. Focused Ion Beam techniques [2] or evaporating/sputtering/laser ablating the desired material through nanomasks as e.g. provided by close packed or etched colloidal particles [3,4]. These methods can be applied even if one aims at spherical NPs by subsequent heating resulting in a surface minimizing dewetting process on top of an appropriately chosen substrate [5].

Bottom up approaches mainly can be divided into gas phase condensation [2] or various wet chemical routes [1]. Besides scientific curiosity, the motivation behind all these preparational efforts is certainly to obtain NPs optimized for specific applications. However, as often when surprising new properties are observed for materials, theoretical description and understanding demand for a high reproducibility of the experimental results and, thus, for an optimized sample quality allowing to address specific theoretical questions by corresponding experiments. Such a development can clearly be observed for all types of NPs as well. Indeed, the mere preparation of NPs with broad distributions of size, shape and composition is no longer sufficient. This trend will be briefly demonstrated for a well defined subclass of NPs, the *magnetic* NPs, which are in the focus of the present Thematic Series entitled *"Preparation, properties and applications of magnetic nanoparticles"*.

While the most notable feature of magnetic NPs, their superparamagnetic behavior, has already been reported by Neel as early as 1949 [6], this phenomenon remained rather unnoticed by the broader physics community. Due to the rapid development of information technology, however, with its ever growing demand for higher storage densities, miniaturization of magnetic bits became an important issue. Thus, roughly since the mid nineties, when the corresponding road map of storage density opened the horizon towards the magic Tbits/inch^2 goal,

the idea of using densely packed magnetic NPs for that purpose immediately brought back and spread the awareness of their related superparamagnetic behavior. Trivially, data storage at ambient temperature over a time scale of typically a decade is not at all compatible with superparamagnetism.

A natural way out of this problem is to look for materials exhibiting an as high as possible magnetocrystalline anisotropy which suppresses fluctuations of the effective magnetic moment of the NPs [7]. For binary alloys like FePt or CoPt, which are well known for their high anisotropies, this approach should allow enhancing the related blocking temperatures significantly above ambient even for corresponding NPs with diameters of 3 nm if the particle anisotropy keeps its bulk value. In practice, however, that is exactly the problem: For NPs significantly smaller anisotropies or, closely related to that, smaller coercive fields are generally found shifting their tolerable size for data storage up to approximately 7 nm. Though coupling of NPs to an antiferromagnetic support layer via exchange bias may offer an alternative remedy of the problem [8], a thorough understanding of the reduced magnetocrystalline anisotropy in nanoparticles is still missing. The route to such an understanding is, however, tedious and requires highest possible particle quality. It turns out that the application of magnetic NPs for data storage indeed implies the most stringent conditions like narrow distributions of particle size and, in case of alloys, of chemical composition as well as stability. Furthermore, in order to write and read the information into and from a NP, its position has to be accurately defined. This demands highly ordered arrays of the NPs, in the ideal case two-dimensionally periodic arrangements. To this end, highly reliable and reproducible self-organizing processes are sought allowing a high throughput at a tolerable price.

Preparation, however, has to be accompanied by a strict quality control including the particles' arrangement, their shape and structure as well as their magnetic properties. While corresponding characterization tools are available to extract averaged information on a particle array supported on top of a suitable substrate, direct measurements on single particles are either often hampered by a relative small statistical significance like in case of High Resolution Transmission Electron Microscopy (HR-TEM) and Spin Polarized Scanning Tunneling Microscopy (SP-STM) or the necessary lateral resolution is only on the verge of being approached as in case of synchrotron-based microscopy methods like Photoemission Electron Microscopy with element-specific magnetic contrast (X-PEEM) [9]. Thus, at the moment one mostly has to rely on ensemble averages and, consequently, this again poses strong requirements on preparation with respect to narrow distributions whenever size dependent properties play a role. This close interrelation between preparation, properties and control is certainly emphasized in the present thematic series reflecting also the fact that the field of magnetic NPs is maturing.

Finally, this series addresses applications of magnetic NPs. Besides the obvious and most demanding one related to magnetic data storage, the use of such particles in the much broader field of sensor technology is described including especially medical diagnostics.

We hope that the selection of review articles as well as full research papers we have chosen is found consistent and useful by the readers interested in that topic and we would like to thank all colleagues for their valuable contributions.

Ulf Wiedwald and Paul Ziemann

Ulm, November 2010

References

1. Goesmann, H.; Feldmann, C. *Angew. Chem., Int. Ed.* **2010,** *49,* 1362–1395. doi:10.1002/anie.200903053
2. Blackman, J. A. *Metallic Nanoparticles*; Misra, P., Ed.; Handbook of Metal Physics, Vol. 5; Elsevier: Amsterdam, The Netherlands, 2009.
3. Fischer, U. C.; Zingsheim, H. P. *J. Vac. Sci. Technol. (N. Y., NY, U. S.)* **1981,** *19,* 881–885. doi:10.1116/1.571227
4. Plettl, A.; Enderle, F.; Saitner, M.; Manzke, A.; Pfahler, C.; Wiedemann, S.; Ziemann, P. *Adv. Funct. Mater.* **2009,** *19,* 3279–3284. doi:10.1002/adfm.200900907
5. Ziemann, P.; Landfester, K.; Leiderer, P.; Schimmel, T. In *Nanotechnology – Physics, Chemistry, and Biology of Functional Nanostructures;* Schimmel, T.; v. Löhneysen, H.; Barczewski, M.; Obermair, C., Eds.; Schriftenreihe der LANDESSTIFTUNG Baden-Württemberg, Vol. 32; LANDESSTIFTUNG Baden-Württemberg: Stuttgart, Germany, 2008.
6. Neel, L. *Ann. Geophys. (C. N. R. S.)* **1949,** *5,* 99.
7. Coey, J. M. D. *Magnetism and Magnetic Materials;* Cambridge University Press: Cambridge, 2010.
8. Eisenmenger, J.; Schuller, I. K. *Nat. Mater.* **2003,** *2,* 437–438. doi:10.1038/nmat934
9. Dürr, H. A.; Eimüller, T.; Elmers, H.-J.; Eisebitt, S.; Farle, M.; Kuch, W.; Matthes, F.; Martins, M.; Mertins, H.-C.; Oppeneer, P. M.; Plucinski, L.; Schneider, C. M.; Wende, H.; Wurth, W.; Zabel, H. *IEEE Trans. Magn.* **2009,** *45,* 15–57. doi:10.1109/TMAG.2008.2006667

License and Terms

This is an Open Access article under the terms of the Creative Commons Attribution License (http://creativecommons.org/licenses/by/2.0), which permits unrestricted use, distribution, and reproduction in any medium, provided the original work is properly cited.

The license is subject to the *Beilstein Journal of Nanotechnology* terms and conditions: (http://www.beilstein-journals.org/bjnano)

The definitive version of this article is the electronic one which can be found at: doi:10.3762/bjnano.1.4

Beilstein Journal of Nanotechnology

Preparation and characterization of supported magnetic nanoparticles prepared by reverse micelles

Ulf Wiedwald*[1], Luyang Han[1], Johannes Biskupek[2], Ute Kaiser[2] and Paul Ziemann[1]

Full Research Paper

Open Access

Address:
[1]Institut für Festkörperphysik, Universität Ulm, 89069 Ulm, Germany and [2]Materialwissenschaftliche Elektronenmikroskopie, Universität Ulm, 89069 Ulm, Germany

Email:
Ulf Wiedwald* - ulf.wiedwald@uni-ulm.de; Luyang Han - luyang.han@uni-ulm.de; Johannes Biskupek - johannes.biskupek@uni-ulm.de; Ute Kaiser - ute.kaiser@uni-ulm.de; Paul Ziemann - paul.ziemann@uni-ulm.de

* Corresponding author

Keywords:
Co; CoPt; core–shell particles; FePt; magnetic anisotropy; magnetic particles; plasma etching; reverse micelles; self-assembly

Beilstein J. Nanotechnol. **2010,** *1,* 24–47.
doi:10.3762/bjnano.1.5

Received: 12 September 2010
Accepted: 06 November 2010
Published: 22 November 2010

Guest Editors: U. Wiedwald and P. Ziemann

© 2010 Wiedwald et al; licensee Beilstein-Institut.
License and terms: see end of document.

Abstract

Monatomic (Fe, Co) and bimetallic (FePt and CoPt) nanoparticles were prepared by exploiting the self-organization of precursor loaded reverse micelles. Achievements and limitations of the preparation approach are critically discussed. We show that self-assembled metallic nanoparticles can be prepared with diameters d = 2–12 nm and interparticle distances D = 20–140 nm on various substrates. Structural, electronic and magnetic properties of the particle arrays were characterized by several techniques to give a comprehensive view of the high quality of the method. For Co nanoparticles, it is demonstrated that magnetostatic interactions can be neglected for distances which are at least 6 times larger than the particle diameter. Focus is placed on FePt alloy nanoparticles which show a huge magnetic anisotropy in the $L1_0$ phase, however, this is still less by a factor of 3–4 when compared to the anisotropy of the bulk counterpart. A similar observation was also found for CoPt nanoparticles (NPs). These results are related to imperfect crystal structures as revealed by HRTEM as well as to compositional distributions of the prepared particles. Interestingly, the results demonstrate that the averaged effective magnetic anisotropy of FePt nanoparticles does not strongly depend on size. Consequently, magnetization stability should scale linearly with the volume of the NPs and give rise to a critical value for stability at ambient temperature. Indeed, for diameters above 6 nm such stability is observed for the current FePt and CoPt NPs. Finally, the long-term conservation of nanoparticles by Au photoseeding is presented.

Introduction

Magnetic nanoparticles have been the focus of research for over 60 years [1,2]. These investigations were prompted by both, fundamental aspects of the magnetism of small particles and clusters [3,4], and an increasing interest by industry, especially in the field of data storage (first magnetic tapes and later hard disk drives) [5,6]. Other important current applications include their use in the medical field [7], e.g., in hyperthermia [8], contrast enhancing in magnetic resonance imaging [9,10] or the

use as cell markers [9] which in-turn can be read out by highly-sensitive devices like TMR-sensors [11]. Moreover, magnetic NPs are thought to improve a variety of catalytic reactions [12,13]. Note that in this case the magnetic properties are in the background, rather fine tuning electronic properties of metallic surfaces is in the principle focus directed towards the catalytic activity of the NPs [14].

Various methods have been used to prepare magnetic NPs with diameters of 1–30 nm. Possibly the simplest approach is ball milling of the corresponding bulk materials. This mostly yields a rather broad size distribution, which, in turn, often hinders the study of size-dependent properties [15]. A better defined physical approach is inert-gas condensation where NPs are formed by sputtering atoms from a specific target which then agglomerate into clusters in a continuous gas flow before landing on a support [16,17]. This method has the advantage of full processing under vacuum conditions and, moreover, monodisperse NPs can be prepared by size selection during flight [18,19]. One general drawback is the random deposition of NPs on the substrate. When properties of individual NPs are of interest, then only low coverage of NPs is necessary before agglomerates are formed on the support. Note that by landing on a polymer matrix [20] or alternatively, on a biotemplate [21] it is possible to avoid the latter drawback to some extent.

The impressive progress in organometallic chemistry, however, has revolutionized the field of small particles for more than a decade [22,23]. Surfactant-mediated growth [24] of NPs with narrow size distributions from metal precursors in solution opened the field of self-assembly, which allows the formation of large-scale ordered arrays of NPs on a support [25-27]. Over the years this method has been optimized by many groups to prepare NPs with tunable diameters, small size distributions with small nm interparticle spacings and additionally, the flexibility to produce monatomic [28] as well as bimetallic NPs [24,29,30]. However, due to the preparation technique the NPs are covered by surfactants which may alter the magnetic properties of NPs [31].

Common to all the mentioned approaches is that oxides are formed when the NPs are exposed to ambient conditions. Thus, much effort has been spent on the removal of organic cover layers leading to naked particles on a support and subsequent reduction of NPs to yield, ultimately, purely metallic species [32,33]. It was shown that subsequent processing by oxygen and hydrogen plasmas is the key to obtain individual metallic particles [34]. On the other hand, embedding the NPs in an antiferromagnetic matrix may lead to modified magnetic properties due to exchange bias giving rise to thermal stability at ambient temperature with NPs having intrinsically low anisotropies [35].

Parallel to the so-called colloidal approach where NPs are formed within a liquid, the preparation of precursor loaded reverse micelles has been developed [36,37]. Here, precursor filled di*block*-co-polymers are used to form hexagonally ordered arrays on different substrates by dip-coating [38]. In a second step, NPs are formed on the substrates by exposure to oxygen plasma which etches the polymers and simultaneously forms metal-oxide NPs [39]. On subsequent hydrogen plasma treatment the formed NPs can be converted into their metallic state. This approach succeeded in the preparation of monatomic Au [40], Pt [41], Fe, Co NPs as well as bimetallic NPs such as FePt, CoPt [42] (and this present contribution) to mention only a few. Unlike all other preparation methods, the micelle approach leads to supported NPs with significantly larger interparticle distances (D > 20 nm) which is especially appealing for two reasons: (i) the magnetostatic interaction of NPs is very small and consequently, individual magnetic properties can by extracted, and (ii) the larger distance between NPs allows their annealing as opposed to colloidal NPs where extended heat treatment leads to agglomeration [43]. This aspect is especially useful for systems which undergo a phase transition and thereby improves their magnetic properties such as in the cases of FePt or CoPt NPs which are of technological interest due to their high magnetocrystalline anisotropy in the $L1_0$ phase. However, it has mostly been observed that the as-prepared particles exhibit the chemically disordered A1 (fcc) phase, while annealing at typically 600–700 °C the NPs are partially transformed into the chemically ordered $L1_0$ phase [23].

Besides the large interparticle distance, the preparation route presented in this contribution allows the systematic variation of particle diameters with narrow size distributions [44]. Thus, possible size-effects [45], e. g., of the effective magnetic anisotropy, can be investigated. In the literature, the achieved hard magnetic properties of FePt NPs and thin films after annealing vary widely [46], since the structure [47], chemical composition [48,49] and the degree of chemical order [50] have to be optimized. Ideally, each particle should be single-crystalline at equiatomic composition and perfectly $L1_0$ ordered. Meeting these three premises, however, is difficult.

One remarkable concept is the salt-annealing technique [51] in which colloidal particles are dispersed at low concentration in a salt matrix which allows high-temperature annealing without NP coalescence. After removal of the salt matrix and recovery of NPs applying surfactants as spacers, the particles show size-dependent degrees of chemical order, coercive fields, saturation magnetizations, and Curie temperatures. Technologically important is the report of the last noted group, that after annealing of FePt NPs as small as 4 nm, ferromagnetic behavior is observed even at ambient temperature corresponding to

magnetic anisotropies close to those of the bulk material [52]. To the best of our knowledge, this result has, so far, not been reproduced by other groups. In contrast, most reports find reduced anisotropies in $L1_0$ ordered NPs compared to their bulk counterpart [53], which mostly is ascribed to surface effects or defects and twins in the NP structure [47]. Consequently, a systematic investigation of possible size-dependent properties of FePt NPs is highly desirable and may lead to further insights on the ordering process. Such an investigation requires, however, a reproducible route towards ensembles of FePt NPs with as narrow as possible diameter distributions. The presently introduced micellar route, which offers control of both particle size and interparticle distance, fulfills this requirement to a considerable extent.

Results and Discussion

In this article we address the preparation of magnetic NPs by precursor loaded reverse micelles on different supports (section 1). The formation of metallic NPs by means of plasma etching was investigated in more detail by X-ray photoelectron spectroscopy as described in section 2. Moreover, the structure of FePt alloy NPs was determined by high resolution transmission electron microscopy and their tendency for Pt segregation in the metallic state by annealing as well as their stability in ambient conditions are discussed. Section 3 focuses on the magnetic properties of Co, CoPt and FePt NPs. We show that magnetostatic interactions can be neglected for micelle-based NPs, which is used in a step where the effective anisotropy K_{eff} of FePt and CoPt is determined by simple Stoner–Wohlfarth approach using a bimodal distribution of K_{eff}. Finally in section 4, the first results on Au photoseeding of Co NPs are presented.

1. Preparation of supported nanoparticles

1.1 General preparation route based on micelles

As already mentioned in the introduction, a vast variety of preparation approaches have been developed and more or less successfully tested for their application to fabricate ferromagnetic metal NPs. Success, in this context, may not be an appropriate term, since it critically hinges on the specific requirements on the NPs, which, in turn, depend on the particular application. For example, magnetic data storage using NPs demands non-interacting particles which immediately translates into a lower limit of the interparticle distances. Furthermore, retrieving the stored information requires well-defined spatial particle arrangements, for example periodic NP arrays. Yet another application driven requirement might be to keep the variance of magnetic properties within a given particle ensemble within a pre-defined narrow range. This again can be translated into corresponding requirements on size and shape as well as the chemical composition of the magnetic NPs.

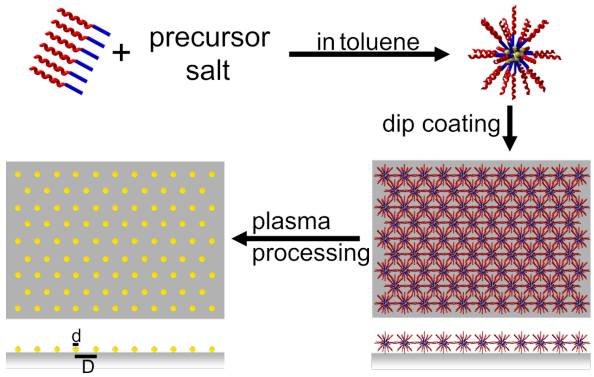
Thus, before giving a success judgment of the following preparation route based on the self-organization of micelles, the various desired criteria for magnetic particles are listed below:

- Homogeneously shaped NPs (e. g., spheres)
- Narrow size distributions (throughout this article, size will be expressed by an average diameter)
- Spatially ordered arrays of NPs, in the ideal case a 2-dimensional periodic lattice of NPs.

In addition to these NP related requirements, any fabrication process should offer high versatility with respect to the desired species of NPs such as various elemental or alloyed systems as well as control of pre-defined NP size and interparticle distance. Finally, since in the following NPs are addressed which are exclusively supported on a substrate, the preparation process should be applicable to supports with different chemical properties.

The basic idea of how to approach all those aims given above may be addressed as “carrier-principle”: A macromolecular carrier is sought which can be prepared in a liquid solvent and which exhibits a genuine tendency towards self-organization into an ordered array on top of a given substrate. In the case of spherical carriers that tend to close packing, after evaporation of the solvent a supported hexagonal arrangement may be expected. In addition, the carrier has to provide a loading mechanism to allow the chemically bonded precursor material to penetrate its interior. With those two prerequisites in mind, a suitable precursor for the planned species of NPs is loaded into the carriers during their formation or presence in the solution and, subsequently, is transported by them to the ordered positions defined by the self-organization of the carrier. In the next, most delicate step of the fabrication procedure, the organic carriers are completely removed by a plasma process and, simultaneously, the loaded precursor material is transformed into NPs of the desired material whilst conserving their original carrier position. In this way, the order of the self-organized carrier array is mapped onto the finally obtained spatial arrangement of the NPs. This basic idea of preparation and the different steps involved are summarized in the schematics shown in Scheme 1.

The first experimental realization of the above approach was demonstrated by the preparation of hexagonally ordered arrays of Au NPs [54]. In this case inverse spherical micelles formed from di*block*-co-polymers in anhydrous toluene were used as carriers. It was shown that polystyrene-*block*-poly(2-vinylpyridine) (PS-*b*-P2VP) or polystyrene-*block*-poly(4-vinylpyridine) (PS-*b*-P4VP) di*block*-co-polymers with the hydrophilic P2VP block formed the core of the micelles in the apolar solvent and



Scheme 1: Preparation of NPs by a reverse micelle technique. PS-*b*-P2VP or PS-*b*-P4VP is dispersed in anhydrous toluene. After adding a metal precursor salt and continuous stirring for about one week, reverse micelles are homogeneously loaded with the precursor material. By dip coating a hexagonal arrangement of loaded micelles can be obtained. This micelle monolayer is exposed successively to oxygen and hydrogen plasmas for (i) removal of the polymer and particle nucleation and (ii) the reduction of the metal oxide particles, respectively.

the hydrophobic PS block the surrounding shell. Loading of precursor material is selectively provided by the pyridine groups of the core. This micellar approach has been continuously improved over recent years [55,56] and is the focus of the present contribution. It is worth noting, however, that in the interim the carrier principle has also been transferred to spherical colloidal polystyrene (PS) particles which can be loaded with various metal precursors by emulsion and miniemulsion methods [57,58].

1.2 Polymers and precursors

In the following we will concentrate exclusively on the fabrication of ordered arrays of magnetic NPs based on the self-organization of precursor-loaded micelles. Application of this approach to obtain magnetic NPs has been previously reported [34]. Continuous optimization and simplification of the process, however, including replacement of the 'home-made' [54] co-polymers by commercially available ones, suggest it might be possible to obtain some supplementary information on the present state-of-the-art. For this purpose, we follow the sequence of the micellar process steps and start with the presently used polymer and precursor materials.

Commercially available di*block*-co-polymers were used exclusively (Polymer Source Inc., Canada) of the type PS(x)-*b*-P2VP(y) or PS(x)-*b*-P4VP(y), where x and y denote the number of monomers per block and, thus, determine the length of each block. Due to the hydrophobicity of the PS- and hydrophilicity of PVP-block, the co-polymers form reverse spherical micelles in apolar solvents such as the solvent used here, i.e., toluene. Empirically, however, in order to obtain stable spherical micelles, the block length of PS, x, should be significantly larger than the PVP length y. In practice, when $x \geq 2y$, the optimized spherical micelles are obtained.

On the other hand, the parameter y indicates the number of pyridine moieties per co-polymer which serve as binding sites for the precursor units. In the simplest approximation, the number of pyridine sites per micelle scales linearly with the volume of the finally expected NPs. Furthermore, the center-to-center distance of the spherical micelles should be proportional to (x + y) which parameterizes the total length of the co-polymer strand. From all the above, it becomes clear that the final size d of the NPs is not completely independent of the interparticle distance D (cf. Figure 1). Assuming $D \approx 2(x + y)$ and $x \geq 2y$, one finds the estimate $y \leq D/6$. If y^3 is proportional to the final volume V, it follows directly that y is proportional to the nanoparticle diameter d. Thus, an estimate of the correlation of the particle diameter d and the interparticle distance D may be given by $6d \leq D$. The validation of this relation is shown in the next section.

Once a suitable di*block*-co-polymer has been chosen, the corresponding solution is prepared by stirring the polymer in toluene for typically one week at ambient temperature. This period can be shortened to overnight stirring by increasing the temperature to 50 °C. In this case, however, the long-time stability of the micelles appears to be significantly reduced. Some additional practical caveats may be worth mentioning:

- It appears good practice to re-check the length distributions of the co-polymers, e.g., by size-exclusion chromatography (SEC) to make sure there is only one dominating peak.
- If toluene is used as solvent, care should be taken to keep it anhydrous.
- Most of the metal precursor salts are sensitive to humidity and, consequently, exposure to ambient conditions should be avoided or at least minimized.

Despite all of the above, the use of a glove box did not prove necessary for obtaining optimized NPs.

The other important components for the micellar recipe, besides the co-polymers forming the carriers, are the various precursor materials. This issue will be addressed by distinguishing between elemental and bi-metallic magnetic NPs.

Elemental NPs: Here our focus is on Fe and Co NPs and the related standard precursors are $FeCl_3$, and $CoCl_2$, respectively (purities 99.99% and 99.999% as given by Alfa Aesar). In all cases, loading of the micelles is accomplished by adding the precursor to the micellar solution and stirring for a couple of

days until no more metal salt residues are visible. Homogenous loading of micelles is observed up to precursor concentrations of 0.5 precursor units per P2VP monomer unit. Above this limit, it was observed that not all of the precursor salt is solved to the cores of the micelles.

Bimetallic NPs: Here the situation is more complicated, since besides the right choice of the individual metal precursors and their amount, the sequence of their addition to the micelle solution plays a crucial role. For instance, for FePt NPs the Pt-precursors H_2PtCl_6, $PtCl_4$ and $K[PtCl_3C_2H_4]\cdot H_2O$ ('Zeise salt') were investigated as well as the Fe-precursors $FeCl_2$ and $FeCl_3$. It transpired that, on the basis of the criteria of homogeneity and completeness of loading the micelles, the combination of Zeise salt and $FeCl_3$ gave the optimum results. To obtain optimized FePt NPs, however, the Pt-precursor must be added first to the micelle solution, stirred until loading is complete and only then the addition of $FeCl_3$ should be started and stirred continuously until no salt residues are visible. Similarly, for the preparation of CoPt NPs the precursor sequence, Zeise salt first followed by $CoCl_2$, gave the best results. Precursor salts were adjusted to the targeted 1:1 composition of the final NPs keeping the upper total loading limit of 0.5 precursor units per P2VP monomer.

1.3 Deposition of loaded micelles onto various substrates

The magnetic NPs, which are the focus of the present work, have been deposited onto various, mostly planar, substrates. Standard combinations are Co and Fe NPs on Si/SiO_2 or Pt as well as FePt on MgO, Si and sapphire. The latter substrates were single crystalline materials with (001) and (0001) orientations, respectively, while, in case of Pt, (111)-textured thin films (50 nm) were used which were obtained by pulsed laser deposition (PLD) at ambient temperature on MgO(001) or (100)-oriented films (80 nm) epitaxially grown by PLD on (001) strontium titanate ($SrTiO_3$) crystals at 400 °C. In all cases, no special pre-treatment of these substrates was employed prior to the deposition of the loaded micelles.

The deposition itself was made by dip-coating. For this purpose, the substrate was immersed into the micelle solution and then pulled out under ambient conditions in a controlled way at a fixed velocity. This velocity is a critical parameter as it systematically influences the inter-micelle distance on the substrate [55]. The effect was demonstrated on $CoCl_2$-loaded micelles (polymer type: PS(1779)-*b*-P2VP(857)) deposited onto Si/SiO_2 substrates by using a variety of dip-coating velocities in the range 1–90 mm/min. The corresponding results are presented in Figure 1, where the two top panels show scanning electron microscopy (SEM) images of identical micelles deposited at different velocities of (a) 5 mm/min and (b) 45 mm/min, respectively. The corresponding different areal densities of the micelles are clearly visible. Analyzing the SEM images in more detail shows the related distributions of the inter-micelle distances (Figure 1(c)), which can be approximated by Gaussian distributions (dashed curves). From such distributions the average distances are determined and plotted against the 3rd

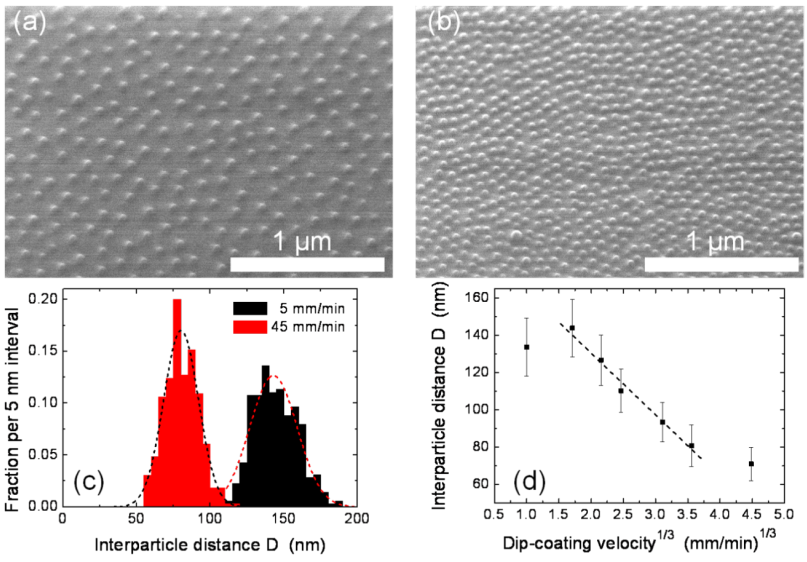


Figure 1: $CoCl_2$ loaded PS(1779)-b-P2VP(857) reverse micelles deposited at different dip-coating velocities; (a) and (b) show the SEM micrographs at dip-coating velocities of 5 mm/min and 45 mm/min, respectively. The corresponding distributions of the interparticle distance D and Gaussian fits are shown in (c). Panel (d) shows the interparticle distance as function of the 3rd root of the dip-coating velocity in the range of 1–90 mm/min. The dashed line is a linear fitting of the five central points.

root of the dip-coating velocity. Similar to previous results with Au loaded micelles [55,59], within a relatively broad range of velocities a linear relationship is obtained in accord with theoretical considerations related to the thickness of the liquid solvent film adhering to the substrate as a function of its velocity [60,61]. Thus, besides the added block lengths of the di*block*-co-polymer forming the micelles, the dip-coating velocity adds yet another possibility to fine-tune the final intermicelle distance of substrate supported carriers. In the case of $CoCl_2$-loaded PS(1779)-*b*-P2VP(857) micelles, the interparticle distance can be tuned to between 80 nm and 140 nm.

In the previous section we derived the relationship between the final particle diameter and the interparticle distance $6d \leq D$ from the simplest considerations. The closest interparticle distance observed in Figure 1 is about $D = 70$ nm while the final particle after etching (discussed below) is found to be $d = 8$ nm. Thus, the ratio $D/d = 8.75$ confirms our estimate. Similar experiments with shorter polymers ($CoCl_2$-loaded PS(312)-*b*-P2VP(71) micelles, not shown) revealed a smallest interparticle distance of $D = 18$ nm at a final particle diameter of about 3 nm, in line with the given estimate of the correlation of interparticle distance and final particle diameter.

The deposition of arrays of micelles and subsequent NP fabrication is by no means restricted to planar substrates. This is demonstrated in Figure 2 where the SEM image shows Co NPs (average diameter 8 nm), prepared on the triangular pyramid surfaces of a Si AFM-tip (an overview of the tip shape is shown in the inset at the lower left of the figure). Even in this case, laterally quite homogeneous particle arrays could be realized.

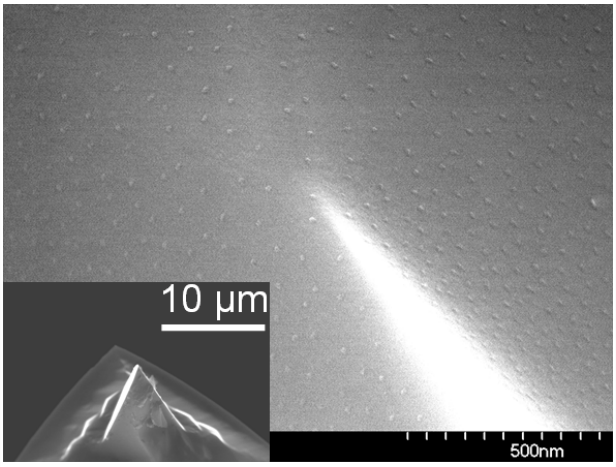


Figure 2: Co NPs prepared from $CoCl_2$-loaded PS(1779)-*b*-P2VP(857) reverse micelles deposited on a Si AFM-tip by dip coating. The SEM image shows the base of the pyramid where Co particles homogeneously cover the root side (top part) as well as the side surfaces of the pyramid (lower part). The inset shows the AFM tip on the cantilever.

Note that the most homogeneous coverage is obtained when the AFM tip points upwards during the dip-coating process. In order to enhance the material contrast in SEM investigations, oxygen plasma is used for particle nucleation and for the removal of the polymers. This procedure is discussed below in greater detail.

1.4 Plasma-assisted particle nucleation and reduction

Once the micellar carriers have self-organized into hexagonally ordered arrays during the dip-coating process on a substrate like those presented in Figure 1 (a, b), their role to provide an as high as possible degree of order is finished. The next decisive step is the complete removal of the organic carrier material and, simultaneously, to transfer the precursor into NPs without losing the previously established hexagonal order. The way to accomplish this involves exposure of the deposited loaded micelles to various plasma conditions [32,34]. For this purpose, a cluster of vacuum recipients consisting of a plasma (base pressure 10^{-8} mbar), analysis (base pressure 10^{-10} mbar), film deposition (base pressure 10^{-8} mbar) and sample storage chamber (base pressure 10^{-10} mbar) was designed and installed, all interconnected by transfer systems. Especially, the in situ transfer from the plasma into the analysis chamber allows an immediate X-ray photoelectron spectroscopy (XPS) investigation of the prepared NPs giving information on their chemical composition as well as on the presence of residues of the micelle matrix or on possible contaminations. It is worth noting that the plasma chamber together with its transfer system can be hooked up to a high-field end station at beam line PM3 at BESSY II synchrotron facility (Berlin), Germany and the 350 keV ion accelerator at Ulm University allowing full in situ sample manipulation.

After positioning the micelle containing substrate via a load lock system within the plasma chamber, an oxygen rf-plasma is ignited (frequency 13.56 MHz, operating pressure $4 \cdot 10^{-2}$ mbar, power 50 W resulting in a dc self-bias of –500 V with the sample holder grounded). Simultaneously, a sample heater is started bringing the substrate temperature up to 250 °C or 300 °C for small or large micelles, respectively. This heating proved advantageous for the nucleation and growth process of the desired NPs. After an exposure time of typically 30 min, the oxygen plasma and heat treatment were stopped and the plasma chamber pumped down to its base pressure. Since the oxygen plasma treatment leads to oxidized NPs, for all magnetic NPs discussed in the present work an additional hydrogen plasma step was applied to reduce the particles into the metallic state. For this purpose, a hydrogen working pressure of 0.1 mbar was established in the plasma chamber and the plasma ignited. Again supported by heating the substrate up to 250 °C, the NPs

were exposed to the hydrogen plasma for typically 20 min. Immediate transfer and XPS analysis revealed completely reduced metallic NPs. In the case of subsequent ex situ magnetic measurements on the NPs, they were coated in situ by thermal evaporation of SiO until a 10–20 nm thick layer had formed giving excellent protection against re-oxidation. It should be noted, however, that the NPs might as well be brought to ambient conditions to allow, e. g., their SEM characterization. In that case, the analysis is, of course, performed on oxidized particles, which has to be taken into consideration when determining their size. The particles, however, can be completely reduced to their metallic state by submitting them to the above described hydrogen plasma process. Once this state is established, all subsequent measurements have to be performed in situ or, alternatively, a protection layer has to be provided before exposing the NPs to ambient conditions.

1.5 Preparation summary: Achievements and Limitations

In the preceding subsections details are given on how the "carrier principle" can be realized to obtain finally ordered arrays of metallic NPs. Although this preparation route is quite general, in the present contribution magnetic NPs are exclusively the focus. Accordingly, in Figure 3 examples are presented for arrays of elemental Fe and Co NPs demonstrating the high control of the procedure over particle size, interparticle distance and hexagonal order: The left panels show Fe NPs and the right panels Co NPs. The particles shown in the upper panels have been prepared from PS(312)-P2VP(71) resulting in about 3 nm particles whilst for the ca. 8 nm particles in the lower panels PS(1779)-P2VP(857), reverse micelles were used. Note, that the SEM images in Figure 3 show NP arrays obtained directly after the oxygen plasma treatment; consequently fully oxidized particles are shown. The corresponding interparticle distances of the NPs differ between the small and large NPs as can be seen from the different scale bars for the upper and lower panels, respectively. The sizes and interparticle distances found are within the general range accessible by the micellar method:

$2\ \text{nm} \leq \text{particle diameters } d \leq 12\ \text{nm}$

$20\ \text{nm} \leq \text{interparticle distances } D \leq 140\ \text{nm}$

These parameter ranges hold for alloy particles such as FePt or CoPt and they represent natural limitations of the approach mainly related to the limited number of pyridine moieties within the core of single micelles [62] as well as to a maximum length of the PS-blocks without losing their spherical shape. SEM images in Figure 4 clearly reveal a short range hexagonal order of the nanoparticles for FePt NPs as previously proven [34]. The NP arrays, however, do not exhibit long range hexagonal ordering. The lower panels in Figure 4 show the corresponding AFM height distributions of the NP ensembles. NP height and its distribution were calculated from Gaussian peak fitting of

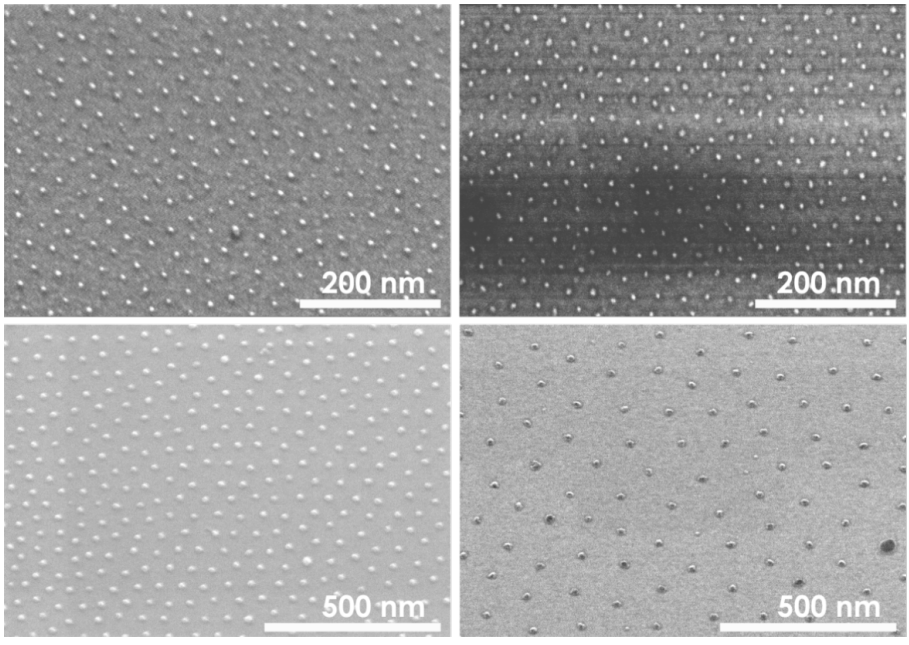


Figure 3: Fe (left column) and Co (right column) NPs prepared from PS(312)-P2VP(71) (upper panels) and PS(1779)-P2VP(857) (lower panels) reverse micelles. Note different scale bars.

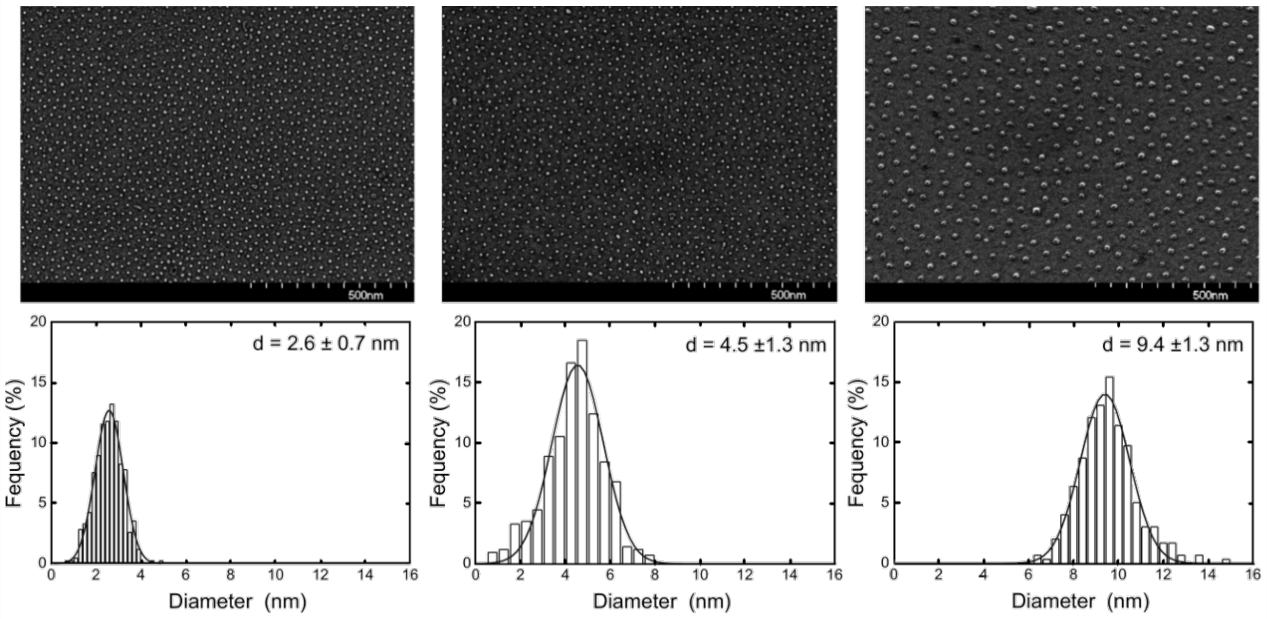


Figure 4: SEM micrographs of FePt NPs with 2.6 nm, 4.5 nm, and 9.4 nm diameter (top panels) and their AFM height distributions (lower panels). Details of the polymers employed and the interparticle spacing can be found in Table 1.

AFM histograms. It has been shown previously that the shape of the particles can be assumed to be spherical [63]. FePt NPs were prepared with diameters in the range 2.5–10.5 nm and narrow size distributions as summarized in Table 1. Besides the polymer chain length, periodicity of particles, the NP diameter, the average number of atoms per NP and the average NP composition (measured by XPS) are shown. The number of atoms per particle was calculated from the average diameter and bulk FePt lattice constant assuming perfect spheres. The integral composition of all NP batches as determined by XPS show Fe and Pt content close to the equiatomic composition and well within a range in which $L1_0$ order of FePt is favored in the bulk (40–55% of Fe). From Table 1 it is striking that identical polymers, i.e., PS(1779)-*b*-P2VP(695) may form different-sized hydrophilic cores and consequently, the resulting particle sizes differ from one another. The effect is ascribed to the preparation under ambient conditions. Generally, we find larger final particle diameters during summer when air humidity is higher when some water may enter the toluene based micelle solution.

Though the nanoparticle preparation via salt-loaded reverse micelles has been successfully performed on various types of substrates – dielectric and metallic, single crystalline and amorphous – some further restrictions related to their materials should be mentioned. First of all, to obtain NPs exposure to oxygen and/or hydrogen plasmas is necessary and the substrates must be able to withstand this etching procedure. In this context, among dielectric materials especially, oxides such as MgO, sapphire, $SrTiO_3$, quartz were found to be suitable, as well as materials forming thin oxide layers such as Si. Furthermore, adhesion of the NPs is an issue. For the magnetic metal particles studied here, the following hierarchy of adhesion

Table 1: Number of monomer PS-*b*-P2VP units, periodicity observed on Si/SiO_2 after dip coating at an emerging velocity 15 mm/min, diameter of FePt NPs after nucleation, resulting number of atoms per NP and integral composition of the samples as determined by XPS.

Polymer PS[x]-P2VP[y]	Periodicity [nm]	Diameter [nm]	No. of atoms	Composition
266-41	30 ± 5	2.6 ± 0.7	570	$Fe_{48}Pt_{52}$
312-74	26 ± 5	2.7 ± 0.9	720	$Fe_{47}Pt_{53}$
266-41	28 ± 6	4.5 ± 1.3	3300	$Fe_{44}Pt_{56}$
1779-695	48 ± 11	5.8 ± 2.6	7200	$Fe_{49}Pt_{51}$
528-177	43 ± 10	6.3 ± 1.4	9200	$Fe_{50}Pt_{50}$
1779-695	55 ± 12	6.6 ± 1.7	10500	$Fe_{48}Pt_{52}$
1779-695	61 ± 12	9.4 ± 1.3	30400	$Fe_{44}Pt_{56}$
1779-857	68 ± 14	10.5 ± 2.5	42400	$Fe_{56}Pt_{44}$

strengths was observed: sapphire < MgO < SiO_x (native Si-oxide). To arrive at this sequence, the force necessary to move the particles by the tip of an AFM was determined. In all cases, however, the supported particles could be annealed up to 700 °C without losing their positional order, i.e., no Ostwald ripening was observed.

A last remark addresses the effect of the hydrogen plasma treatment on NPs with a propensity for hydride formation such as in case of Co. Though the consequences of CoH_x formation on the corresponding magnetic properties are by no means clear-cut [64], one nevertheless has to take this into consideration. Indeed, close inspection of in situ X-ray absorption spectra (XAS) on Co NPs immediately after reduction in a hydrogen plasma revealed a significant shoulder 2 eV above the Co-$L_{3,2}$ absorption maxima caused by hydrogen uptake. In this particular case, however, the hydrogen could be expelled by annealing at 650 °C for 5 min [65], and led to complete disappearance of the above XAS shoulder. However, there is no general rule on this issue and hydrogen uptake during the reduction step must be checked individually for each type of NP.

2 Structural and chemical analyses

When the magnetic properties of NPs are investigated, the question immediately arises if and how the observation differs from the bulk properties and, moreover, how the observations can be correlated to (i) the structure of the particles and (ii) to the chemical state. Advanced analytical tools such as aberration-corrected high-resolution transmission electron microscopy (HRTEM) and related techniques as well as X-ray photoelectron spectroscopy (XPS) give important additional information on the atomic and electronic structure of the sample. Moreover, due to its surface sensitivity, XPS can be used to obtain information on surface oxidation, phase separation and segregation both in films and in particles [66]. In this section some important findings are discussed which have impact on the interpretation of the magnetic characterization.

2.1 Characterization of the particle nucleation

In order to gain some insight of the particle nucleation and reduction processes by means of plasma treatment, as discussed in section 1.4, a series of C-1s and Co-2p XP spectra after different etching steps were measured for $CoCl_2$ loaded PS(1779)-P2VP(857) reverse micelles. All spectra shown in Figure 5 are normalized to the total Si-2p signal intensity of the substrate. In the initial state PS-P2VP molecules dominate the survey scan proving the continuous coverage of the Si substrate by reverse micelles. The Co precursor material located in the cores of the micelles is not detected as a result of the surface sensitivity of XPS. Additionally, the development of the C and Co signals after different etching steps is shown in Figure 5. It is obvious that the C-1s intensity, which is predominantly related to the micelle shell, strongly decreases relative to the Si substrate even after oxygen exposure for only 30 s. After 5 min exposure time, the C-1s intensity dropped below the detection limit, while after 10 min a clear Co^{2+} spectrum can be observed. At this stage the particles simultaneously nucleate to form Co oxide NPs. To guarantee removal of the (small) volume between each nanoparticle and the substrate, which principally remains undetected by XPS, the etching time is typically tripled at temperatures up to 250 °C. After this etching period, the SEM images presented above were taken. In a final step, subse-

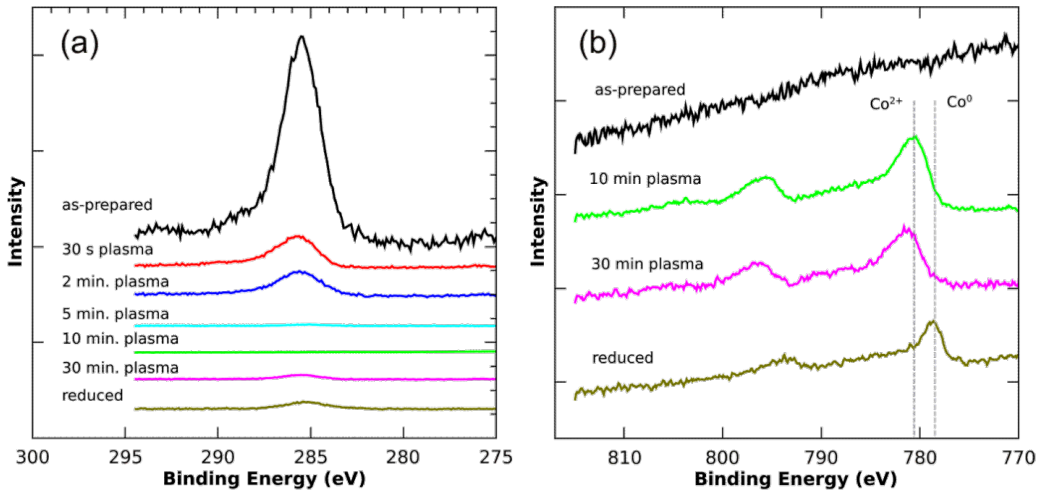


Figure 5: Photoelectron spectroscopy of Co-precursor loaded PS(1779)-P2VP(857) reverse micelles after different O and H plasma treatments. Details are given in the text; (a) and (b) show C-1s and Co-2p levels, respectively. All spectra are normalized to the Si-2p substrate signal intensity (not shown) and vertically off-set relative to each other for clarity.

quent hydrogen plasma treatment (20 min) allows the reduction of the NPs into the metallic state as indicated by the Co-2p peak shift towards the position of metallic Co. Finally, it is worth noting that the small C-1s signal visible in the reduced state is due to the necessarily long acquisition time for the XPS spectra. For example, to arrive at a reasonable signal-to-noise ratio for the Co-2p peaks, a data acquisition time of 12 h is required. Even under UHV conditions such a long exposure of a sample surface to X-rays results in the built-up of a small amount of carbon contamination, which, by covering the Co particles, may result in a slightly reduced Co-2p signal.

2.2 Oxidation of FePt nanoparticles

Degradation of magnetic properties due to oxidation is an important issue especially for applications. For naked 3d elemental nanomagnets (Fe, Co, Ni) as well as for alloys (e.g. FePt or CoPt) one can expect a strong deterioration of the targeted magnetic properties under ambient conditions [67,68]. For FePt alloy NPs, we recently investigated the oxidation behavior in more detail by XPS and signal modeling taking into account the spherical shape of NPs [66]. Here, we briefly summarize the results.

Figure 6 shows Pt-4f and Fe-2p XP spectra of (9.8 ± 0.6) nm FePt NPs in the metallic state and after 24 h exposure to air. Oxidation in ambient air becomes obvious by a clear energy shift of the Fe $2p_{3/2}$ core level to about 711 eV with a shoulder at the metal position still present. By comparison with literature data the main peak can be assigned to the Fe^{3+} oxidation state [69]. Interestingly, Pt-4f levels reveal no significant indication of oxide formation, proving the chemical state of the Pt atoms remains practically unchanged during oxidation of the FePt particles. This finding is astonishing, since it is well known that a thin Pt oxide layer forms on pure Pt under ambient conditions [70,71]. Although Pt-4f spectra have not been normalized before and after the oxidation process, e. g., to the total Fe-2p intensity, there appears to be a reduction of Pt-4f intensity which might easily be explained by the formation of a thin Fe oxide overlayer damping the Pt intensity. More details can be found in [66], in which we quantified the degree of oxidation by XPS line fitting using linear combinations of reference spectra measured under identical experimental conditions. The Fe^0 spectrum was obtained from a reduced and, thus, completely metallic FePt thin film sample, while the Fe^{3+} spectrum is measured on pure (99.5%) bulk Fe after complete oxidation in oxygen plasma. The outcome of such fitting is also shown in Figure 6 by the green solid lines.

More detailed investigations on the relative amount of Fe oxide formed after exposure to molecular oxygen and air for differently sized nanoparticles in the as-prepared metallic state have

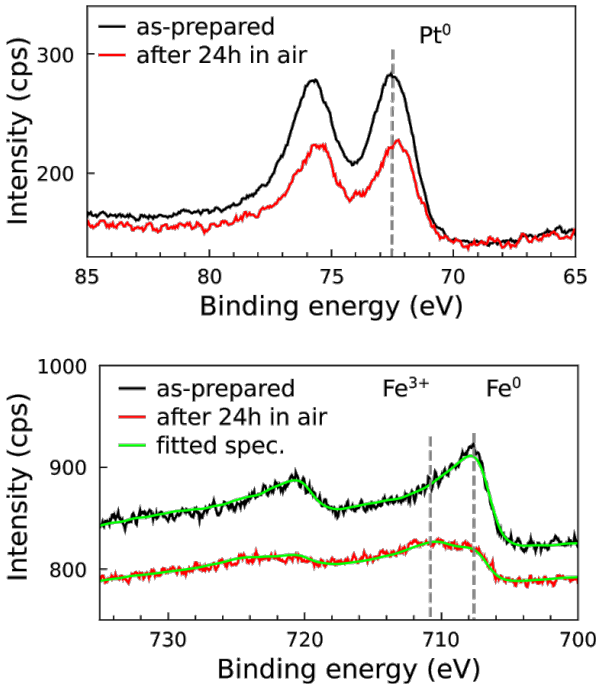


Figure 6: Pt-4f and Fe-2p XPS spectra of 9.8 nm FePt particles before and after exposure to ambient air for 24 h (Fe-2p spectrum is vertically off-set for clarity). After exposure the majority of Fe atoms are found in the Fe^{3+} state, while Pt atoms remain metallic. All spectra were smoothed by 3-point moving window averaging and no further normalization was performed. Green solid curves through Fe-2p spectra in the lower panel are fits based on Fe^0 and Fe^{3+} reference spectra.

shown that a minimum oxygen dose of 10^6–10^7 L is necessary to observe a Fe^{3+} signal above the detection limit. Higher gas exposures result in a logarithmic increase of the ratio of Fe^{3+} to Fe^0 intensities [66].

After annealing at 650 °C for 90 min of 9.8 nm and 11.5 nm NPs, thus partially $L1_0$ ordered, the oxidation rate drastically decreased. More quantitatively, annealed FePt NPs withstand 100–1000 times longer exposures to molecular oxygen than their non-annealed counterparts. A completely different oxidation behavior was displayed by 4.9 nm FePt NPs for which only low oxygen doses were needed to obtain the oxidized state and the oxidation rates were practically identical for as-prepared or annealed NPs [66]. Both types of oxidation behavior as exhibited by larger or smaller FePt NPs can be consistently described by Pt segregation towards the particle surface.

2.3 Pt segregation in FePt nanoparticles

For icosahedral FePt NPs, recent HRTEM observations have indicated a systematic increase of the lattice parameter towards the periphery of the particles starting with the bulk value in their interior [72,73]. This finding strongly points to Pt segrega-

tion towards the particle surface. A more direct way of testing for such Pt segregation is the application of an element-specific surface sensitive technique such as XPS.

Based on a FePt core–Pt shell model, the observed Pt-4f and Fe-2p spectral intensities can be analyzed quantitatively to confirm Pt segregation and give for 4.9 nm FePt NPs a value of the Pt surface enrichment of less than an equivalent of 0.1 nm pure Pt. Experimentally, we observed that after annealing 9.8 nm FePt NPs at 650 °C for 90 min the intensity ratio I(Fe)/I(Pt) droped to almost half the value observed for the as-prepared sample [66]. From this, Pt shell thicknesses of 0.2 nm and 0.3 nm were obtained for 11.5 nm and 9.8 nm NPs, respectively, while for a FePt reference film the value was 0.27 nm. Thus, the larger particles and the film gave similar results. These findings immediately suggest that in case of the film and the larger NPs, a Pt surface layer approximately one monolayer thick was formed which, in turn, strongly impedes further oxidation. For 4.9 nm FePt NPs (and smaller) this Pt surface layer is no longer complete and thereby loses its protecting effect. This latter behavior may have its origin in the strong compositional change within the interior of the particle induced by Pt segregation. As an example, for 4.9 nm NPs, a complete Pt shell with thickness of one monolayer segregated from the interior would shift the atomic composition of the core from $Fe_{53}Pt_{47}$ to $Fe_{68}Pt_{32}$. According to the FePt bulk phase diagram, such a compositional change would lead to a structural transformation into the Fe_3Pt phase. In this case, the driving force of a decreasing total surface energy due to Pt segregation is probably overcompensated by the energy needed to form Fe_3Pt from FePt.

2.4 Structure of FePt nanoparticles

Since the magnetic hardness of FePt alloys strongly depends on the chemical order parameter, we investigated the structure of individual particles by aberration corrected HRTEM. While HRTEM and electron diffraction does not provide absolute quantification of the ordering parameter as can be achieved by scanning (S)TEM at atomic resolution at its mass sensitive contrast [74], it allows a relatively fast way to distinguish between ordered and disordered phases. For the purpose of HRTEM investigations, 3 nm and 8 nm FePt NPs were prepared on Si/SiO_2 substrates. (Partial) chemical order was established by annealing at typically 650 °C for 90 min. Prior to TEM investigations, selected samples were covered with a protective layer of about 10 nm SiO_2 to avoid oxidation and mechanical damage due to TEM lamella preparation. The samples were cut into pieces (diamond wire saw), mechanically ground, dimpled, and polished to a thickness of <5 μm (Gatan dimple grinder). Low angle (10°) argon ion etching with energies of 5 to 1 keV (Fischione 1010 ion mill) was used to achieve electron transparency with lamella thicknesses smaller than 100 nm. TEM

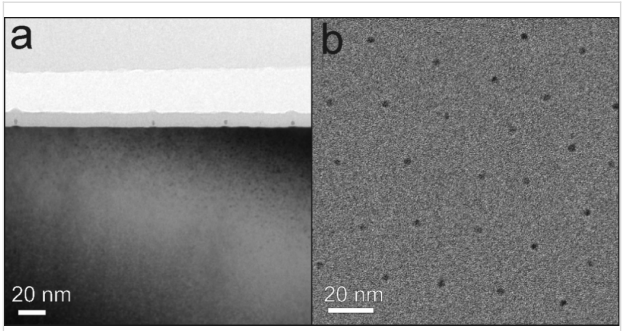


Figure 7: TEM images of 3 nm FePt NPs on Si/SiO_2 after annealing at 650 °C for 90 min. (a) Bright-field TEM image of FePt nanoparticles in cross section view. The NPs are in situ covered by a thin layer (10 nm) of SiO_2 to avoid oxidation and mechanical damage after annealing. (b) Bright-field TEM image of FePt NPs in plane view. The hexagonal ordering can be clearly seen.

investigations were carried out using a FEI Titan 80-300 microscope operating at 300 kV equipped with a CEOS type imaging aberration corrector and a slow scan CCD camera system. The aberrations were corrected up to the 3rd order resulting in a phase plate of 20 mrad (π/4 criterion) and a point to point resolution down to 0.1 nm.

Figure 7 shows overview TEM images of 3 nm FePt on Si/SiO_2 in cross section (a) and plane view geometry (b) after annealing at 650 °C for 90 min. The hexagonal 2D ordering of the particles is clearly visible in Figure 7 (b) and compares well with the SEM imaging in Figure 4.

The structure as well as the crystallographic orientation relative to the beam direction of NPs was determined by aberration corrected HRTEM when the remaining substrate/embedding film thickness made them accessible. $L1_0$ ordering of 3 nm FePt NPs is demonstrated in Figure 8. Here, two examples are presented in which the NPs are oriented along [100] direction. The presence of superlattice planes along the [001] axis proves the presence of $L1_0$ phase. Moreover, the particle in Figure 8(a) appears nearly spherical exhibiting no obvious defects, twins or

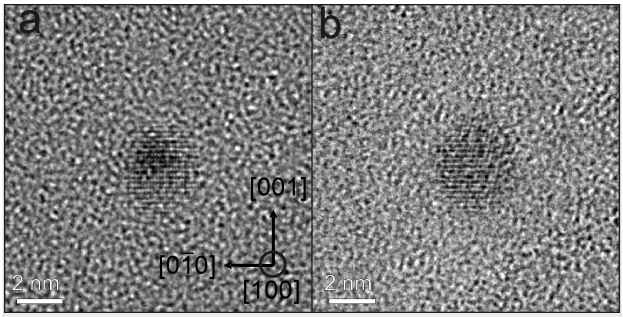


Figure 8: Aberration corrected HRTEM images of FePt particles seen along [100] direction. The $L1_0$ ordering along [001] axis can be identified by the super lattice planes.

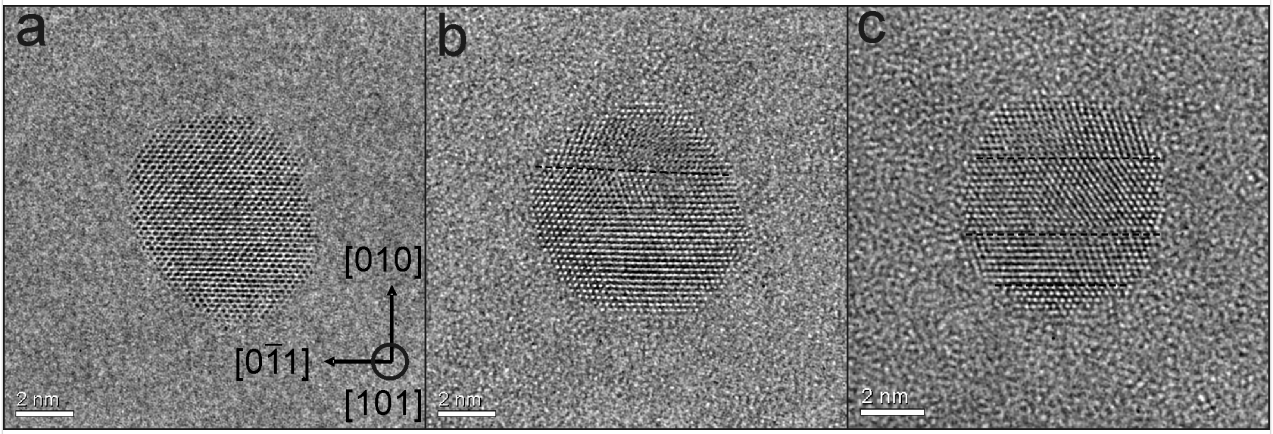


Figure 9: Aberration corrected HR-TEM images of about 8 nm FePt NPs in [101] orientation. Crystal defects such as twins or stacking faults can clearly be seen along [101] projection (defects are marked by the broken line in (b,c)). Only few particles such as in (a) do not exhibit stacking faults. Most particles contain one (b) or more (c) stacking faults.

stacking faults while the NP in Figure 8(b) shows $L1_0$ order at the left as well as a strongly distorted region (right).

The presence of possible crystal defects such as twin and stacking faults reducing the degree of chemical order and, as a consequence, leading to a reduced magnetic anisotropy, were easiest to see along the [101] direction. Figure 9 demonstrates that especially larger particles (8 nm) can exhibit twins (Figure 9(b)) and stacking faults (Figure 9(c)). Particles without defects, however, were also present (Figure 9(a)). The statistical analysis of in total 70 NPs (3 nm) shows that 38 FePt NPs exhibit defects along the [101] direction. From this result and the fact that additional defects may exist which cannot be seen in the [101] projection, it can be concluded that for the majority of particles crystal defects are a common feature. For 8 nm FePt NPs defect-free NPs are rare. In turn, this finding already suggests that the effective magnetic anisotropy energy density may be lowered compared to bulk FePt single crystals. In section 3.3.2 this issue will be addressed.

3 Magnetic properties

3.1 General remarks on the magnetic characterization

The principal difficulty in investigating the magnetic properties of NPs prepared by reverse micelles poses is having to deal with small magnetic signals composed of contributions from both, the NPs as well as the supporting mostly diamagnetic substrate. For example, 8 nm Co NPs with a bulk saturation magnetization of 1.73 μ_B per atom and interparticle distances of 100 nm on a 5 × 5 mm^2 substrate produce a total magnetic moment of only 10^{-9} Am^2 (10^{-6} emu). Although state-of-the-art SQUID-magnetometry is able to detect the related small signals, the response of the diamagnetic substrate has to be taken into account as well delivering for the typically applied external fields signals of the same order of magnitude as the particles, however, of opposite sign. Thus, the magnetic responses from the NPs and the substrate cancel each other at external fields between 20–200 mT depending on the volume of the substrate and diamagnetic susceptibility. Consequently, SQUID-magnetometry on supported micelle-based NPs is strongly hampered and often not reproducible. Moreover, prior to an ex situ characterization, the as-prepared particles have to be in situ coated, e.g., by SiO_2 to avoid oxidation under ambient conditions. Even then, further sample processing such as the annealing of the covered NPs appears unfavorable due to the possible occurrence of chemical reactions. If, however, all these problems are carefully considered, SQUID-magnetometry can provide valuable information.

The drawback of a strong diamagnetic substrate contribution in SQUID-magnetometry can be circumvented to some extent by use of a paramagnetic film to compensate for the temperature-independent diamagnetic contribution. In Figure 10(a) this approach is demonstrated. Once the diamagnetic response of the substrate has been determined or evaluated from susceptibility data, the necessary thickness of a paramagnetic film can be easily calculated. Note that the calculation only gives an estimate and the actual sample compensation temperature has to be determined separately for each sample due to slight variations in the substrates, film thicknesses and possible impurities.

3.2 Co nanoparticles on Pt films

The approach of compensating diamagnetic substrate signals by paramagnetic films is demonstrated by paramagnetic Pt(111) films on top of MgO(001) substrates. Pt films were deposited under UHV conditions at ambient temperature by pulsed laser deposition (PLD). For this purpose a 193 nm ArF laser was employed hitting a Pt target (purity 99.99%) at typical areal

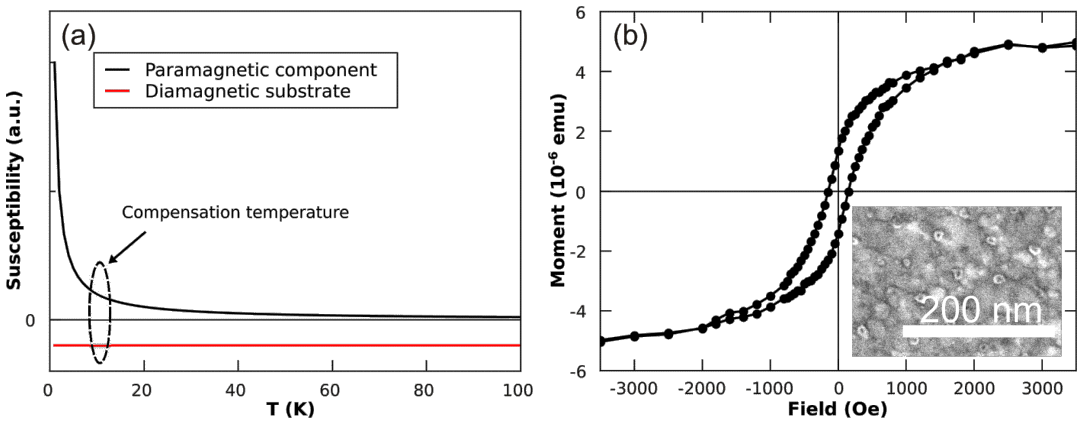


Figure 10: (a) Schematics of the compensation approach: Temperature dependence of the magnetic susceptibility of diamagnetic substrate and paramagnetic thin film deposited on the sample. At a certain temperature, which can be adjusted by the film thickness of a paramagnetic film, the two components compensate each other. (b) In-plane hysteresis loop of 8 nm Co particles deposited on a polycrystalline 50 nm Pt(111) film on MgO(001). The compensation temperature of film and substrate is found at T = 29 K. The inset shows a SEM image of Co particles prepared on the Pt(111) film.

energy densities of 8 J/cm^2. Details of the setup are described elsewhere [63,75]. The 50 nm polycrystalline Pt films exhibited a (111)-texture and a mean grain size of about 10 nm. Subsequent micelle deposition and plasma etching (details are given in section 1.4) led to Co NPs with an average particle height of 8 ± 1 nm (measured by AFM) with an interparticle distance $D \approx 60$ nm (see inset of Figure 10 (b)). The measured hysteresis loop showed a sample saturation moment, remanent magnetization and a coercive field of $M_S = 5{\cdot}10^{-6}$ emu, M_R = 26%, H_C = 150 Oe, respectively. This value of the coercive field is typical for Co NPs [32]. An M_R of 26%, which is only about half the value expected for Stoner-Wohlfarth NPs, suggests that already a significant amount of NPs is in the superparamagnetic state at $T = 29$ K. Comparing the saturation moment with the considerations mentioned above, we expected a total sample magnetic moment of $2.8{\cdot}10^{-9}$ Am^2 ($2.8{\cdot}10^{-6}$ emu) taking into account the NPs density at an average distance of 60 nm. Although this estimate is 44% lower than the experimental value, this deviation is acceptable taking the error bar of the volume of NPs into account.

Alternatively, NP ensembles exhibiting a remanent magnetization, i.e., the blocked state, can be characterized in zero external fields leading to vanishing substrate and film signals. The combination of DC-demagnetization (DCD) and isothermal remanent magnetization (IRM) [76,77] can give additional information of possible magnetic interaction of the NPs. Figure 11 (a) presents such a measurement on 8 nm Co particles at $T = 29$ K. The external field was applied in the substrate plane. The remanent magnetization is plotted as function of

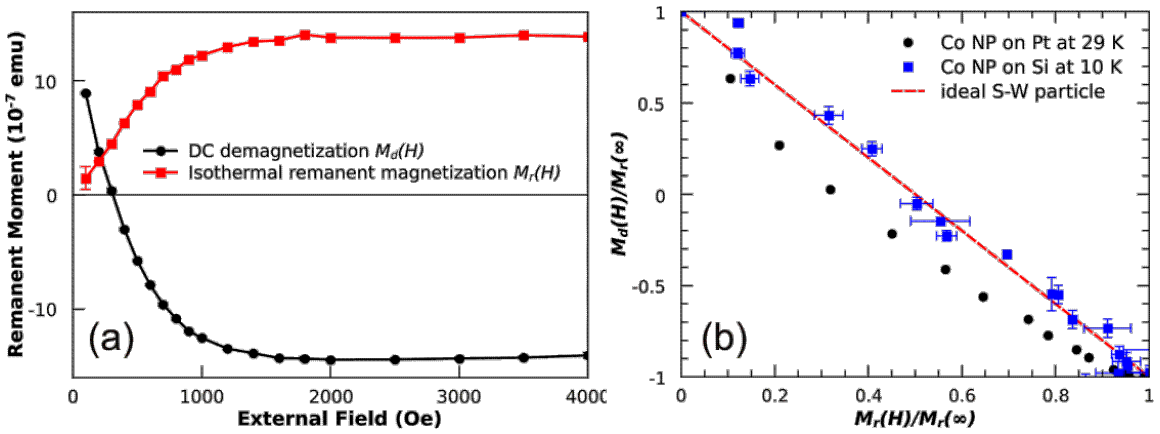


Figure 11: (a) DC-demagnetization and isothermal remanent magnetization of 8 nm Co particles measured by SQUID-magnetometry at $T = 29$ K in in-plane geometry; (b) shows the so-called Henkel plot of the Co NPs on Pt(111) film on Si (black dots) and the result obtained for Co NPs on a Si substrate at $T = 10$ K (blue squares). The expectation for ideal Stoner–Wohlfarth particles (red line) at $T = 0$ K is also included.

external field applied before measuring in zero fields the DCD and IRM dependencies. By combining the two measurements, a corresponding Henkel plot can be obtained. For ideal Stoner–Wohlfarth NPs the Henkel plot would yield a straight line with slope of –2. The result of 8 nm Co NPs on the Pt film was found to be below this Stoner–Wohlfarth limit. This deviation can be understood within the framework of thermal excitation as previously shown [76]. From a qualitative standpoint, the thermal energy gives rise to a reduced switching field of NPs and thus a steeper slope of the DCD and a lowered increase in the IRM curves, respectively. As a consequence, the Henkel plot for non-interacting particles measured at finite temperatures runs below the one expected for ideal Stoner–Wohlfarth NPs (straight line in Figure 11 (b)). For comparison, the Henkel plot of 8 nm Co NPs on Si substrates is also included in Figure 11 (b) which nicely demonstrates the validity of the approach. Note that the larger error bars of Co NPs on Si substrate are due to the lower saturation magnetization of the sample (10^{-9} Am^2).

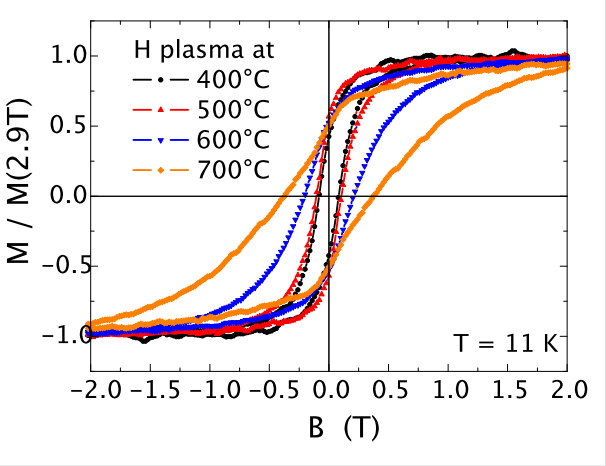


Figure 12: Element-specific magnetic hysteresis loops of 5.8 nm FePt NPs taken at the Fe-L_3 edge at T = 11 K after different annealing steps for 30 min annealing time in hydrogen plasma. Note that hysteresis loops are normalized to the magnetization at B = 2.9 T (maximum field).

3.3 FePt alloy particles

For the magnetic characterization of FePt alloy particles we chose X-ray magnetic circular dichroism (XMCD) which provides information on (i) the chemical state of sample, (ii) element-specific magnetic moments and (iii) element-specific hysteresis loops. The results presented below were measured at beamline PM-3 of the BESSY II synchrotron facility in Berlin, Germany. The total electron yield was recorded as function of photon energy in external fields up to 3 T and at variable temperatures between 11 K and 300 K [78]. Due to its surface sensitivity, it becomes possible to measure X-ray absorption spectra and hysteresis loops with high precision, even of NPs. Note that the XMCD and hysteresis loops were always measured in out-of-plane geometry. Moreover, our home-built plasma etching system can be attached to the high-field endstation which allows full in situ sample manipulation and characterization [32].

3.3.1 Tracking the phase transition in FePt nanoparticles

The setup described above enabled us to study the impact of chemical ordering on the magnetism of FePt alloy particles. For this purpose, element-specific hysteresis loops of FePt particles with an average diameter of 5.8 nm were recorded at T = 11 K after different annealing steps in hydrogen plasma. The hysteresis was extracted from the total electron yield signal as previously described [78]. It is important to note that the size distribution does not change due to annealing (for details see e.g. [79]) and thus changes of magnetic hysteresis can be attributed to changes of the effective magnetic anisotropy energy density K_{eff} originating from variations of the chemical order within the particles. Figure 12 shows the experimental results for successive annealing steps on the same sample from 400 °C to 700 °C in 100 K steps. It is obvious that the initial annealing steps at 400 °C and 500 °C do not significantly change the magnetism of the FePt particles. The coercive field $\mu_0 H_C$ is around 0.1 T while the particles remain superparamagnetic at T = 300 K (not shown). After annealing at 600 °C (700 °C), $\mu_0 H_C$ gradually increases to 0.2 T (0.38 T) proving the increasing chemical order. Interestingly, the remanent magnetization M_R is found at (50 ± 5)% of the saturation magnetization for all annealing steps. This value is expected for non-interacting Stoner–Wohlfarth particles with randomly oriented, uniaxial anisotropy axes [1]. In section 3.3.2 we make use of this model to deduce K_{eff} from hysteresis loops.

Changes of the magnetic hysteresis of FePt NPs were also investigated as function of particle diameter. For this purpose NPs were prepared on Si/SiO_2 substrates by reverse micelles. See Figure 4 and Table 1 for details. Figure 13 shows the experimental coercive field as function of FePt NP diameter at T = 15 K (inset) and T = 300 K after annealing at T_A = 700 °C for 30 min. At low temperature, the coercive field H_C was found between 1.6 kOe and 10.1 kOe thus scattering to high extent. Leaving the experimental points at 5.8 nm and 6.3 nm for a moment, a continuous increase of H_c as function of NP diameter was found. The excluded 5.8 nm and 6.3 nm FePt NPs exhibit a significantly different shape of their hysteresis curves with a notably narrow waist corresponding to significantly reduced H_c values. This feature will be discussed in the next section in more detail. More importantly, at 300 K the coercive field follows a similar dependence on the NP diameter. Small NPs are superparamagnetic and only for diameters larger than 6

nm a non-zero coercive field was observed at T = 300 K. For 6.6 nm, 9.2 nm, and 10.5 nm FePt NPs large coercive fields of 1.6 kOe, 1.9 kOe, and 2.2 kOe at ambient temperature, respectively, were found.

These results directly imply that the magnetic blocking of NPs is size-dependent at 300 K. For applications, a standard requirement for the orientation stability of blocked particle magnetizations is given by 30 $k_BT \leq K_{eff} \cdot V$ assuming the time window of the XMCD-based hysteresis measurement (600 s). With the results from Figure 13 which indicate that only FePt NPs above ca. 7 nm show strong hysteretic behavior, it is possible to calculate the minimum K_{eff} yielding blocked NPs. In this way, a value of K_{eff} = 0.69 MJ/m^3 at T = 300 K was found which is about one order of magnitude smaller than the bulk FePt anisotropy constant. Moreover, it is interesting that the observed H_c values strongly scatter around a NP diameter of 6 nm at T = 15 K. This finding, however, cannot be attributed to integral composition variation of FePt NPs as indicated by the XPS results in Table 1. Rather, the compositional variation of individual particles may cause the observed behavior. Changes in the shape of hysteresis loops are discussed in the next section in more detail.

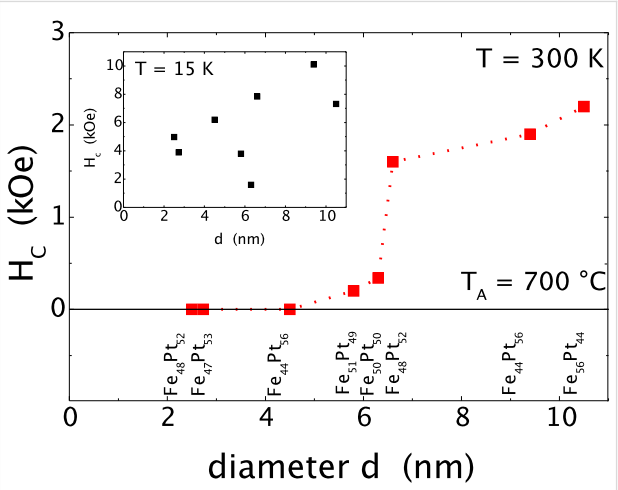


Figure 13: Coercive field at T = 300 K as function of the diameter of FePt NPs after annealing for 30 min at T = 700 °C. The dotted line serves as a guide to the eye. The particle compositions as determined by XPS are noted for each array of particles. The inset shows the coercive fields at T = 15 K.

3.3.2 Magnetic anisotropy of FePt nanoparticles

The direct determination of magneto-crystalline anisotropy energy densities K_{MC} from experiments can be carried out by several techniques: ferromagnetic resonance (FMR), XMCD or alternatively, SQUID magnetometry using magnetic hysteresis loops or zero-field/field cooling (ZFC/FC) temperature scans. In all cases advanced models must be applied to fit the experimental data correctly. Generally, ferromagnetic resonance [80] appears as the simplest and most reliable technique in case the sample can be saturated during a full angular scan varying in-plane and out-of-plane angles Φ and θ, respectively. Note, that also the first and second K_{MC}-constants should be rather small (just as for the elemental magnets Fe, Co, and Ni) to observe resonances close to the magnetic hard axis in accessible external fields of a standard electromagnet. If a magnetic film has been grown epitaxially with a well defined single crystalline structure, it becomes possible to determine anisotropy constants with high precision in different crystallographic directions [81]. XMCD relies on the precise determination of the anisotropy of orbital magnetic moments $\Delta\mu_L$ in the direction of easy and hard axes of magnetization. It has been shown both by theory [82] and experiment [83], that $\Delta\mu_L$ can be linked to K_{MC}-constants. Both techniques, however, are more difficult to apply on systems with random distribution of anisotropy axes as in case of NPs discussed in this article [84]. However, some efforts have been undertaken to obtain information on an effective anisotropy constant K_{eff} in which all possible contributions such as surface effects [85] or composition effects [53] to anisotropy are combined in a single, effective constant [86].

It is well known that ZFC/FC measurements can be used for an estimate of K_{eff} [53] employing the total anisotropy energy by $E_{aniso} = K_{eff} \cdot V$. In other words, for the volume of NPs a distribution is assumed while K_{eff} is taken as a constant. For monatomic NPs this procedure appears quite successful and could easily be extended to small particles where surface anisotropy plays an important role using $E_{aniso} = K_V \cdot V + K_S S$, where S is the surface area [85].

In case of magnetic alloy NPs such as FePt or CoPt, however, compositional distributions as well as distributions of the degree of chemical order may significantly determine the magnetic properties. Thus, these parameters have to be considered for estimates of K_{eff}. Practically, a K_{eff} distribution is included into fit formulas of ZFC/FC measurements as recently shown [53]. Alternatively, for non-interacting NPs with uniaxial anisotropy, the combination of low temperature experimental hysteresis loops and simulations along the Stoner–Wohlfarth model [1] introducing a K_{eff} distribution can be applied. As opposed to ZFC/FC measurements this approach does not include thermal energies to which E_{aniso} is compared. Moreover, K_{eff} and its distribution are the fitting parameters for simulations of magnetic hysteresis loops and volume distributions do not enter.

The above described approach is tested first on hysteresis loops of 5.8 nm NPs. Initially, a Gaussian shaped distribution of K_{eff} was assumed in-line with a recent report by others [53]. It turned out, however, that this approach delivered a satisfactory

description of the hysteretic behavior only for as-prepared FePt NPs immediately after in situ reduction, i.e., for fcc NPs exhibiting a low anisotropy. In contrast, after annealing it is not possible to fit the experimental hysteresis loops by a single Gaussian for K_{eff}. This finding is most naturally explained by the presence of two types of NPs: (i) a low anisotropy component accounting for particles which do not reach high K_{eff} values by annealing. The low K_{eff} for a (small) portion of NPs could be attributed to composition variations larger than the window in which $L1_0$ order is favoured; (ii) the desired high anisotropy component that shifts to larger values by the annealing induced formation of the ordered $L1_0$ phase. Consequently, a bimodal Gaussian-shaped distribution is applied for the simulation:

$$p(K) = A \cdot \exp\left(-\frac{(K-K_L)^2}{\sigma_L^{\,2}}\right) + B \cdot \exp\left(-\frac{(K-K_H)^2}{\sigma_H^{\,2}}\right) \quad (1)$$

Here $p(K)$ is the probability to find a value K for anisotropy, A and B account for peak weights of the two Gaussians centered at K_L and K_H while $\sigma_{L,H}$ denote the corresponding standard deviations. Simulations with varying parameters are applied until a reasonable congruence has reached. Figure 14 presents two examples of the results of such fitting for FePt NPs after annealing at T_A = 400 °C and 700 °C. Notably, the experimental data are nicely reproduced when using a bimodal Gaussian distribution.

Encouraged by the quality of the bimodal Gaussian simulation, the procedure was extended to differently sized FePt NPs. Figure 15 shows both, the distributions of K_{eff} used to fit the experimental data as well as (see insets) the resulting hysteresis curves for 2.6 nm, 4.5 nm, 6.3 nm, and 10.5 nm NPs. In all cases, excellent agreement between experimental and simulated results was obtained. Common to all loops is a waist of the hysteresis loops at low external fields which is most obvious for the 6.3 nm NPs. In the simulation, this characteristic shape of the hysteresis requires a low-anisotropy component that is, accordingly, most prominent for 6.3 nm NPs in the K_{eff} distributions. Table 2 summarizes the results of the fitting for all NP diameters. Since a bimodal Gaussian distribution and particularly the weight of low and high K_{eff} is varied to match the experiments, the median of the total distribution was also determined and listed in Table 2. Note that the low anisotropy component is centered at 1.0–1.5·10^5 J/m^3 for all NP batches, while the high anisotropy components peak in the range 1.0–1.9·10^6 J/m^3 which is 3–6 times smaller than the bulk FePt

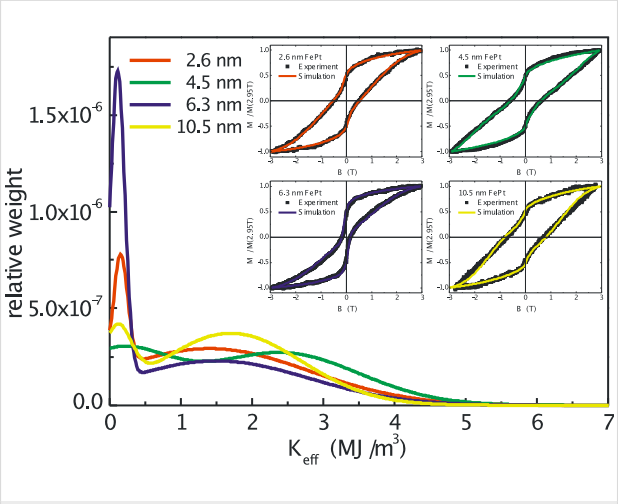


Figure 15: Distributions of the effective anisotropy K_{eff} for arrays of differently sized NPs used for simulating the experimental low temperature (15 K) hysteresis loops (insets) after annealing at 700 °C. The total area of distributions is normalized to unity. Details are discussed in the text.

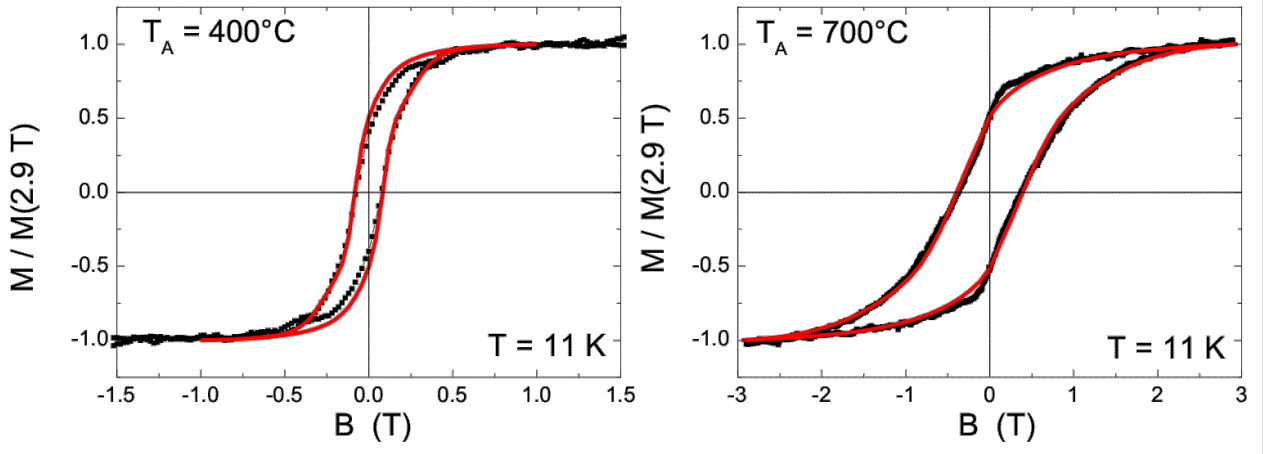


Figure 14: Experimental hysteresis loops of 5.8 nm FePt NPs at 11 K and simulations using a bimodal Gaussian K_{eff} distribution (as discussed in the text) after annealing at T_A = 400 °C and T_A = 700 °C, respectively.

Table 2: Summary of the K_{eff} evaluation of FePt NPs batches using a Stoner–Wohlfarth approach. Diameter d, the median effective magnetic anisotropy constant K_{eff} and the peak value K_L and K_H for the two components are listed (details are given in the text).

Diameter (nm)	2.6	2.7	4.5	5.8	6.3	6.6	9.4	10.5
K_{eff} (MJ/m^3)	1.71	1.14	1.93	0.56	0.92	1.57	1.81	1.69
K_L (MJ/m^3)	0.15	0.11	0.10	0.10	0.11	0.10	0.10	0.10
K_H (MJ/m^3)	1.40	1.03	2.40	0.75	1.50	1.90	1.90	1.80

anisotropy value. Within these two parameter ranges, all the differently waist-shaped hysteresis curves can be described by adjusting the relative weights of high and low K_{eff} components.

The values of K_{eff} presented in Table 2 appear quite consistent. For example, neglecting the NP batches exhibiting a huge low anisotropy component (2.7 nm, 5.8 nm, and 6.3 nm), the median of K_{eff} is found in the range of 1.6–1.9·10^6 J/m^3 after annealing at T_A = 700 °C. For these samples the experimental hysteresis loops in Figure 15 exhibit similar shapes (2.6 nm, 4.5 nm and 10.5 nm NPs). Averaging over the NP batches with larger K_{eff} medians yields K_{eff} = 1.74 MJ/m^3. Taking into account the time window of the XMCD experiment (600 s) we made use of the expression $30k_BT_B = K_{eff} \cdot V_C$ to calculate blocking temperatures. We found a critical diameter of d_c = 5.2 nm for nanoparticle blocking at ambient temperature. This value is fully in-line with the experiments in Figure 13 showing superparamagnetic response at 4.5 nm, while at 5.8 nm an open hysteresis was found although the low anisotropy portion in this batch is dominant. Compared to an earlier evaluation of anisotropy of 0.7 MJ/m^3 for slightly off-stoichiometric FePt NPs, the micelle-based NPs show an approximately 2.5 times larger K_{eff} [87].

3.3.3 Lowering the phase transition temperature by ion irradiation

For technological applications phase transition temperatures above 600 °C are not favorable due to the high energy consumption as well as the time required to reach the $L1_0$ phase. Moreover, high annealing temperatures restrict the usability of various substrates, e. g., due to degradation of the substrate or chemical reactions between the deposited particles and their support, e. g., silicide formation. Consequently, it is desirable to reduce the phase transition temperature. In the recent literature, two routes have been proposed to achieve this goal: The incorporation of a third element to function as a diffusion agent [88,89]. This approach, however, has often the undesired side effect that the pseudobinary alloys formed have a significantly reduced anisotropy compared to the corresponding pure system [90]. If the third element can be driven out, e.g., by phase separation, a huge number of vacancies and interstitials within the particles yielding lowered activation energies for diffusion can be created. Alternatively, the number of vacancies within the particles may also be strongly enhanced by ion irradiation. Previous experiments bombarding thin FePt films by He^+ ions have clearly shown that defects formed while sputtering of atoms can be safely neglected [91].

The latter approach has been successfully applied to reduce the FePt phase transition temperature by more than 100 K [79]. In detail, 7 nm FePt alloy particles were prepared on Si(001)/SiO_2 substrates by reverse micelles and bombarded with 350 keV He^+ ions up to a fluence of 10^{16} ions/cm^2 at 10^{-7} mbar and 300 K. For these conditions, SRIM simulations for a 7 nm FePt film yield an average number of displacements per FePt atom of 0.08 dpa. On the other hand, the average projected range of such He^+ ions is found to be in the order of 1.5 µm, i.e., much larger than the particle diameter. Consequently, practically all projectiles penetrate through the NPs, produce defects there, and get stopped only deep in the substrate.

The influence of this irradiation process on the magnetic hysteresis loop can be compared to a non-irradiated reference sample after both have been stepwise annealed in the range 300–775 °C. The upper panel of Figure 16 shows the evolution of the coercive fields at low (11 K) and ambient temperatures as function of annealing temperature, which is maintained for 30 min at each step for both samples. Starting from small values of the coercive field related to the low-anisotropy fcc phase, increasing annealing temperatures result in a clear enhancement of H_C at 11 K in the case of the bombarded sample as opposed to the non-irradiated reference which exhibits such a significant enhancement only after annealing at 600 °C. First hysteretic behavior at ambient temperature is observed after annealing at T_A around 600 °C for the ion irradiated sample while annealing at 700 °C is necessary for the reference. The complete set of measurements of the ion bombarded sample appears shifted by more than 100 K towards lower annealing temperatures T_A as compared to the non-irradiated counterpart. For comparison, the results of long time (270 min) annealing experiments at T_A = 775 °C are included in Figure 16. Note that for huge anisotropy values (H_C > 5 kOe) the maximum experimentally available field is not sufficient to drive the sample into saturation. Thus, the coercive fields are underestimated for annealing temperatures above 700 °C.

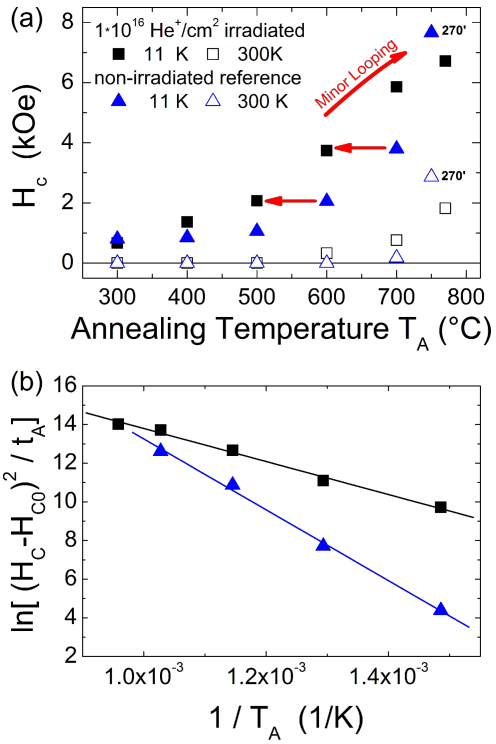


Figure 16: (a) Coercive fields at T = 11 K and T = 300 K as function of 30 min annealing time at temperature T_A for a He^+ ion irradiated and a non-bombarded reference sample. The effect of a long annealing time (270 min) at 775 °C is added for comparison. (b) Arrhenius plot of normalized coercive fields with respect to the as-prepared state. From the linear fitting activation energies of 0.7 eV and 1.6 eV are derived for the irradiated and reference sample, respectively.

The lower annealing temperature sufficient to form partially ordered FePt NPs after ion bombardment can be understood in terms of reduced activation energy for diffusion E_D. Assuming ideal Fickian diffusion, the characteristic diffusion length λ depends on the diffusion coefficient D and the annealing time t_A leading to $\lambda = (D\,t_A)^{1/2}$ with $D = D_0 \exp(-E_D/(k_B T_A))$ where D_0 is the pre-exponential factor and k_B the Boltzmann constant. For alloys with huge magnetocrystalline anisotropy, experiments have demonstrated that the anisotropy constant has a linear dependence on the degree of chemical order S [92,93]. Assuming Stoner–Wohlfarth type particles showing H_C proportional to the ratio of anisotropy K and magnetization M, the coercive field is directly proportional to S. Using the above assumptions, it becomes possible to estimate the activation energy for diffusion E_D from the hysteresis loops of non-interacting, uniaxial, isotropically distributed FePt particles assuming $(H_C - H_{C0})/H_{C0}$ is proportional to S while this quantity is proportional to λ, where H_{C0} denotes the initial coercive field. Note these assumptions only hold for S<<1. Figure 16 (b) shows the Arrhenius plots of the quantity $((H_C - H_{C0})/H_{C0})^2/t_A$. From the linear fitting we derived activation energies E_D of 0.7 eV and 1.6 eV for the ion irradiated and reference sample, respectively. The observed energies are significantly smaller compared to the volume activation energy of 3.0 eV/atom reported for Pt in FePt [47]. This finding may point to additional surface diffusion which is expected to play a significant role in NPs.

3.4 CoPt alloy particles

The CoPt bulk system behaves quite similar compared to FePt system [83]. $L1_0$ chemical order can also be achieved in a relatively wide composition range around the equiatomic ratio. Although the anisotropy energy density of bulk CoPt K = 5 MJ/m^3 [94] lies slightly below the one of FePt K = 7 MJ/m^3 at low temperatures, CoPt particles should reach blocking temperatures above 300 K when the $L1_0$ phase is at least partially formed. Consequently, it was worth preparing CoPt alloy particles for comparison purposes.

CoPt NPs were prepared by reverse micelles as described above. Thus, Zeise salt as Pt precursor and $CoCl_2$ were dissolved in PS(1779)-*b*-P2VP(695) reverse micelles formed in anhydrous toluene. After plasma etching, the particle height was determined as d = (5.6 ± 2.0) nm on Si/SiO_2 substrates by AFM. The average particle composition was $Co_{56}Pt_{44}$ as measured by XPS. For XMCD characterization in out-of-plane geometry, the particles were reduced in hydrogen plasma at T = 300 °C followed by an annealing step at T = 700 °C for 90 min in hydrogen at $p = 10^{-3}$ mbar. After cooling and pumping the plasma chamber, the sample was transferred to the XMCD chamber for magnetic characterization. Figure 17 shows Co-$L_{3,2}$ XAS and XMCD spectra achieved for circularly polarized light at a degree of circular polarization of 93% in external fields of ± 3 T at 300 K. For each direction of external field at

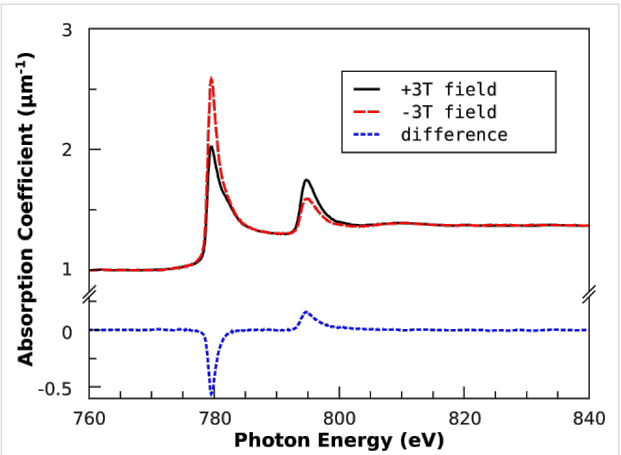


Figure 17: Co-$L_{3,2}$ XA and XMCD spectra of 5.6 nm $Co_{56}Pt_{44}$ NPs after annealing at 700 °C taken at external fields of ± 3 T and T = 300 K. Absorption spectra are rescaled to the absolute absorption coefficient as function of energy taking into account self-absorption corrections. Details are given in the text.

least two measurements were merged before further data processing. Spectra were rescaled to the linear absorption coefficient of bulk CoPt [95] at pre- and post-edge energies before self-absorption correction was applied using the method recently reported [96,97]. Finally, spin and orbital magnetic moments of Co were calculated according to the magneto-optical sum rules, see, e.g., [98] using the number of Co-3d holes of n_h = 2.628 [83].

Absorption spectra in Figure 17 clearly revealed metallic Co after particle reduction and annealing. Analysis of XMCD spectra lead to the Co spin and orbital moments listed in Table 3. Note that at B = 3 T, the sample is not fully saturated for all temperatures as can be seen from the hysteresis loops in Figure 18. The lack of magnetization, however, should be smallest at T = 11 K since all particles can be assumed to be ferromagnetic as opposed to higher temperatures where the smaller particles exhibit superparamagnetism. For the two lower temperatures, we observed constant spin and orbital moments within the error bars, while at ambient temperature a significant portion of the particles is superparamagnetic (the bump around zero external field in Figure 18) and cannot be saturated in 3 T at 300 K. The ratio of orbital and spin moments is not temperature-dependent and can be directly compared to previous reports. For an at least partially-ordered $L1_0$ epitaxial CoPt film (40 nm) on MgO(001) substrates, the Co saturation spin moment has been determined to 1.76 μ_B (at the magic angle, see [83] for details). The spin magnetic moment of $Co_{56}Pt_{44}$ NPs of 1.6 μ_B (this article) is 9% smaller compared to the CoPt thin film [83] which is ascribed to an insufficient external field to reach saturation for highly anisotropic NPs.

Table 3: Summary of spin and orbital Co magnetic moments of 5.6 nm $Co_{56}Pt_{44}$ alloy NPs after annealing at T = 700 °C for 90 min. Error bars are estimated from variations of the $L_{3,2}$ cut energy. The ratio of orbital-to-spin magnetic moments is also listed.

T (K)	μ_S^{eff} (μ_B)	μ_L (μ_B)	μ_L / μ_S^{eff}
11	1.60 ± 0.16	0.19 ± 0.04	0.13 ± 0.02
100	1.56 ± 0.19	0.15 ± 0.04	0.10 ± 0.03
300	1.26 ± 0.01	0.15 ± 0.01	0.11 ± 0.01

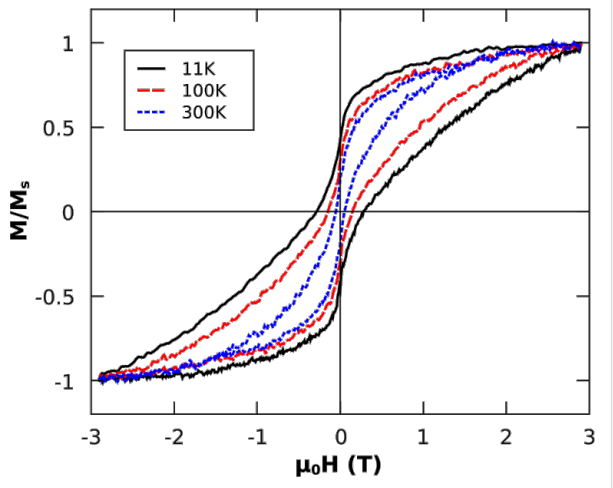


Figure 18: Element-specific magnetic hysteresis loops of 5.8 nm $Co_{56}Pt_{44}$ NPs taken at the Co-L_3 edge maximum dichroic signal at T = 11 K, 100 K and 300 K after annealing at T = 700 °C for 90 min in out-of-plane geometry. Note that hysteresis loops are normalized to the magnetization at B = 2.9 T (maximum field).

The anisotropy of the orbital moment turned out to be μ_L = 0.26 μ_B in CoPt(001) direction (easy axis) and μ_L = 0.11 μ_B at θ = 60° measured to the surface normal yielding μ_L/μ_S ratios of 0.06-0.15 in CoPt thin films [83]. Note that the in-plane ratio is still smaller but cannot be determined due to experimental limitations. For ensembles of non-interacting particles with random distribution of anisotropy axes, however, only an integral value of the orbital moment can be measured. Recently, such experiments have been undertaken for gas-phase prepared 3 nm CoPt NPs deposited in an amorphous carbon matrix [53]. After annealing at 650 °C for 2 h, the authors observed a ratio μ_L/μ_S = 0.094. Our experiments on naked $Co_{56}Pt_{44}$ NPs (5.6nm) gave an average μ_L/μ_S = 0.11 and are thus in-line with the reported experiments taking into account the experimental differences and uncertainties, e.g., diameter, annealing conditions and the effect of the carbon matrix [53].

The corresponding hysteresis loops of $Co_{56}Pt_{44}$ NPs are shown in Figure 18. Similar to the results on the FePt NPs discussed above, we observed an open hysteresis loop with a coercive field $\mu_0 B$ around 50 mT at T = 300 K. The remanent magnetization, however, is strongly reduced compared to the hysteresis at T = 11 K showing almost 50% remanent magnetization. To get an estimate of the effective anisotropy energy density, K_{eff} evaluation from the hysteresis loops at T = 11 K was applied in-line with the model described in section 3.3.2. The median of the distribution of K_{eff} is found at 1.5 MJ/m^3 which is 29% of the CoPt bulk value. Compared to FePt NPs the same trend, i.e., strongly reduced K_{eff} for NPs, was observed. For detailed comparison to FePt NPs, additional experiments on different sized particles in the A1 and the $L1_0$ phase must be carried out.

4 Long-term conservation of particles

The results discussed above have been exclusively accomplished by in situ characterization techniques. For applications, however, long-term stability at ambient conditions is a critical issue. Most magnetic systems in use tend to oxidize fast at least on the surface as shown in section 2. In other words, magnetic NPs below 10 nm always significantly oxidize when exposed to

ambient conditions and thereby often lose the desired magnetic properties. Thus, encapsulation of NPs in a protective matrix or alternatively, the preparation of thin protective shells around individual particles is often necessary to prevent oxidation. Moreover, the surface functionalization of NPs is difficult and also alters the magnetism compared to naked particles. Noble metal shells provide long-term stability due to chemical inertness along with a relatively small change of the magnetism of the magnetic cores. Additionally, noble metal shells can be designed to provide distinct optical properties, e.g., by tuning the plasma frequency [99]. Last but not least the biocompatibility of Au shells has been demonstrated by many groups: Furthermore these shells provide specific molecular binding sites at the NP surface [100,101].

Recently, we have shown that Pt and FePt NPs can be covered by a thin Au shell by photochemical seeding [102,103] over macroscopic areas (10×5 mm^2) in a parallel process. We therefore wished to know whether Co-based NPs could also be covered by this process. For this purpose 8 nm Co NPs were prepared on Si substrates (see section 1 for details). For photoseeding, however, the NPs were exposed to air since it is well known that Co particles form a 2–3 nm oxide shell when exposed to ambient conditions [104]. Thus, it was possible to study if and under what surface conditions Co-based NPs could catalyze the growth of Au shells around them.

Two different initial conditions of the 8 nm Co NPs were prepared: (i) fully oxidized Co NPs after oxygen plasma particle nucleation, and (ii) metallic Co particles after subsequent hydrogen plasma reduction. After release of the vacuum, all subsequent steps were conducted in parallel to allow direct comparison. For photoseeding a 5 mM $HAuCl_4$ solution was prepared in a chemically inert optical immersion liquid (No. 1160, Cargille Laboratories). After deposition of a 20 µl droplet completely wetting the Si substrates, the solution was irradiated homogeneously with the collimated beam of an Hg lamp for 30 min (Osram; spectral emission range between 350 and 450 nm; 10.2 mW cm^{-2}). After irradiation the samples were rinsed in acetone and isopropanol baths.

The top panel of Figure 19 shows a SEM image of NPs after oxygen plasma nucleation. Note that about 10% of particles were not nucleated to single particles. In judging the growth of Au shells, however, this finding may give additional information. The photoseeding process in this fully oxidized state completely failed (not shown). In contrast, when starting from reduced NPs which form a thin Co oxide shell after about 15 min in ambient air, selective Au deposition on the NPs was possible as shown in Figure 19 (b,c). At lower magnification the homogeneity over large sample areas is clearly demonstrated.

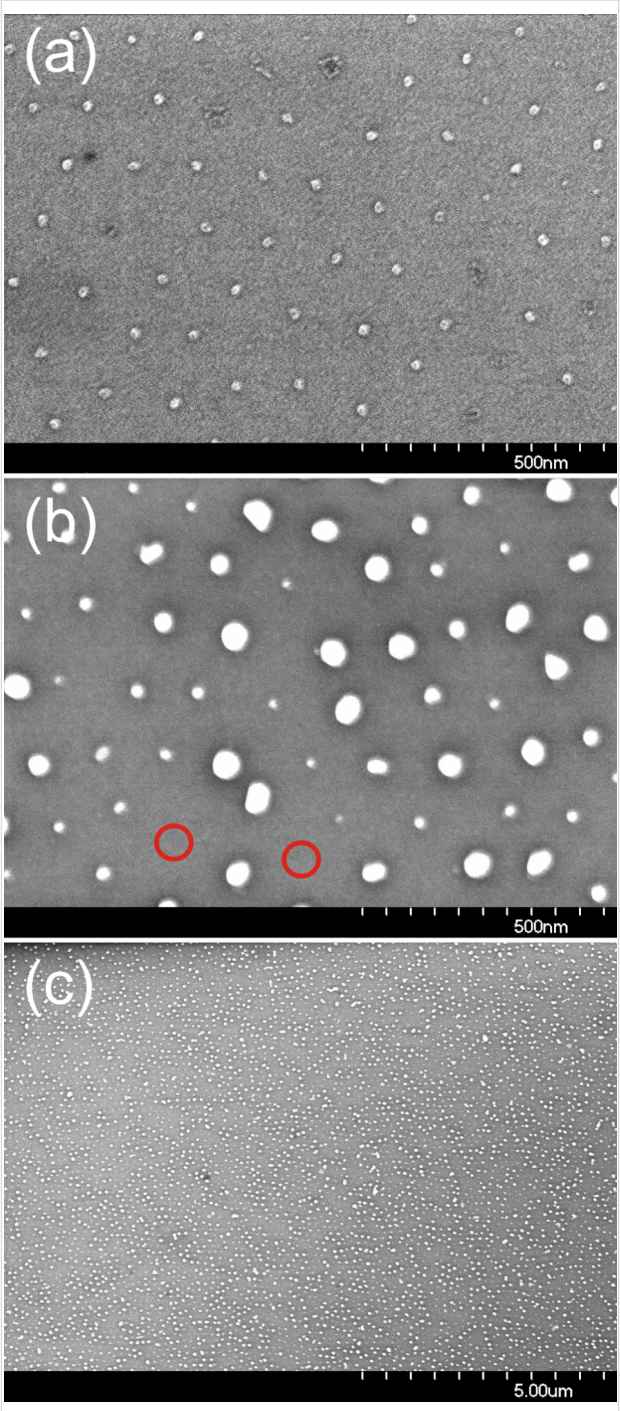


Figure 19: SEM images of 8 nm Co-based NP after oxygen plasma (a) and after Au photoseeding of reduced particles (b,c) at different magnifications.

At higher magnification it is striking that (i) two different sizes of particles are observed with 10–15 nm and 30–50 nm NP diameter after Au photoseeding and (ii) some positions where NPs were expected appear void as indicated by the red circles in Figure 19 (b). The latter can be attributed to the initially incomplete particle nucleation. When several small particles were

formed from a single micelle, these rapidly oxidize in air and consequently cannot catalyze the Au shell growth similar to the fully oxidized NPs discussed above.

The growth of Au shells around Co-based NPs with bimodal size distribution is harder to understand. Although the small particles in Figure 19 (b) appear to be of similar size as in Figure 19 (a), it can be concluded from the comparable SEM contrast of small and large particles that a thin Au shell has formed on all particles in Figure 19 (b). Growth rates of Au shells of less than 0.2 nm per minute for small particles and of about 1 nm per minute for large particles suggest different initial conditions. One reason might be a slightly different oxide shell thickness of the two species. Here, however, additional experiments with defined Co oxides thickness are necessary for detailed understanding of growth modes.

Conclusion

In the present article we describe the growth, chemical and structural parameters as well as the magnetic properties of two-dimensional ordered arrays of magnetic NPs with emphasis on monatomic Co and FePt alloy NPs. The preparation route of reverse micelles, based on commercial PS-P2VP and PS-P4VP di*block*-co-polymers, leads to spherical NPs with controllable diameters d = 2–12 nm and narrow size distributions at a tunable interparticle spacing D = 20–140 nm. In all cases the ratio D/d was found being larger than 6. Micelles are successfully deposited on various planar substrate such as Si/SiO_2, MgO, or Pt(111) textured films and, moreover, on top of AFM tips while the interparticle spacing can be additionally adjusted by the variation of dip-coating velocities. Subsequent processing by oxygen plasma forming NPs from precursor loaded reverse micelles followed by hydrogen plasma for NP reduction result in purely metallic NPs.

A host of NP systems such as Fe, Co, FePt, and CoPt NPs, were prepared and the structural, electronic as well as the magnetic properties characterized by XPS, HRTEM, SQUID-magnetometry and XMCD. For Co NPs, the formation of NPs were investigated in detail by XPS and proved the formation of Co oxide NPs after nucleation and metallic NPs after subsequent reduction in hydrogen plasma. Co NPs were successfully prepared on both, Si/SiO_2 and Pt(111) textured films. The latter was used to compensate the diamagnetic signal of the MgO substrate at T = 29 K improving the application of SQUID-magnetometry and allowing direct measurement of the hysteresis loop of 8 nm Co NPs at 29 K. Moreover, DCD and IRM investigations combined in the Henkel plot deliver prove that magnetostatic interactions between particles can be neglected. Finally, Au photoseeding was accomplished on partially oxidized Co NPs extending our previous results on Pt and FePt NPs (forming a thin Pt shell). The bimodal thickness distributions of grown Au shells around Co NPs, however, still lacks a clear explanation and further experiments are required to reveal such details.

FePt alloy NPs at approximately equiatomic composition were prepared and thoroughly investigated by XMCD and HRTEM. From XMCD-hysteresis loops, the A1-$L1_0$ phase transition could be tracked and compared after annealing at T = 700 °C for 30 min as function of FePt NP size. At T = 15 K hysteresis loops with a huge coercive field up to $\mu_0 H$ = 1 T were obtained, while at T = 300 K only NPs with average diameter larger than 6 nm exhibited hysteretic behavior and whilst the smaller NPs are superparamagnetic. The experimental data at T = 15 K could be fitted by a bimodal Gaussian size distribution of the effective magnetic anisotropy constant K_{eff} in a Stoner–Wohlfarth approach to account for low and high anisotropy distributions probably arising from (i) NPs out of the stoichiometric range in which $L1_0$ order is favored and (ii) NPs forming at least partial chemical order. This fitting approach allows the determination of the median of the anisotropy distribution K_{eff} which was evaluated as $1.6–1.9 \cdot 10^6$ J/m^3 independent of NP diameter. Such values are 3–4 times smaller than that of FePt bulk in the $L1_0$ phase. Some NP batches, however, showed even more strongly reduced median K_{eff} values due to a larger amount of low anisotropy NPs. Reasons for the reduced K_{eff} values in NPs are elucidated by HRTEM investigations. The majority of NPs show a rather high degree of chemical order, but at the same time a variety of defects, crystallographic twins and stacking faults over different NPs were observed. Consequently, the reduced K_{eff} values were primarily attributed to crystalline defects.

Finally, 5.6 nm $Co_{56}Pt_{44}$ alloy NPs were produced to compare to FePt NPs. After annealing at 700 °C, we observed strong hysteretic behavior at T = 11 K. At ambient temperature the coercive field has been obtained to 0.5 kOe comparable to FePt NPs of similar size. The median of the K_{eff} was found at 1.5 MJ/m^3 which is 29% of the CoPt bulk value.

The similarity of the magnetic behavior of FePt and CoPt leads to an important conclusion: Materials which derive their high magnetocrystalline anisotropy and, thus, their magnetic attractiveness for applications from a chemically ordered state, such as the $L1_0$ in the present case, appear to exhibit strongly deteriorated magnetic properties when prepared as NPs with a monotonous decrease of, e.g., the coercive field with decreasing particle diameter. As a consequence, significantly larger NPs are required to guarantee temporal stability of their inscribed magnetization at ambient temperatures than what is hoped for on the basis of the materials bulk behavior. Part of this problem

may be attributed to crystalline defects present in the NPs as demonstrated by HRTEM revealing also the existence of particles comprised of two or three sub-particles with different orientations. In such a case, considering projections of the easy axes onto the field direction immediately could explain the reduced H_c values. Additionally, the local chemical order may be disturbed in vicinity of a defect also leading to a depressed H_c. It is interesting to note that in case of Co, no significant H_c depression was observed for NPs though defects are also expected for such particles. If defects are exclusively responsible for the depressed H_c values in $L1_0$ NPs, the prospect of their application is definitely restricted. Recent work, however, indicated that FePt NPs may be only partially ordered due to a non-optimized annealing temperature leading to the observed H_c depression. The underlying mechanism is related to the theoretically predicted size dependence of the ordering temperature [105] with its monotonous decrease with decreasing particle diameter. As a consequence, at the most employed annealing temperatures of typically 700 °C an only partially ordered state may be stable or, in the worst case, the smallest NPs may be stable in the completely disordered fcc phase. This scenario offers a more optimistic prospect, since for smaller NPs the annealing temperature only has to be reduced, however, this must be accompanied by a correspondingly elongated annealing time to compensate for the reduced kinetics. Whether such compensation can be accomplished is not clear at the moment and the necessary experiments are under way.

Acknowledgements

The work of this article has been conducted by the help of many people in our laboratory over the last few years. We would like to thank our former and current diploma, master, and PhD students Birgit Kern, Dr. Andreas Klimmer, Barat Kuerbanjan, Dr. Anitha Ethirajan, Lianchen Shan, and Moritz Trautvetter. Prof. Dr. Hans-Gerd Boyen (University Hasselt) significantly contributed to the route of preparation and the design of the optimized the plasma etching system together with Dr. Frank Weigl, Dr. Gerd Kästle, and Dr. Klaus Zürn. Fruitful discussions with Dr. Alfred Plettl are gratefully acknowledged. We thank Axel Seidenstücker and Pavan Muralidhar for the Au photoseeding as well as Prof. Dr. Paul Walther for giving training to the students on scanning electron microscopy as well as almost unlimited access to the SEM. Synchrotron-based measurements were performed by using the high-field endstation of Prof. Dr. K. Fauth (University Würzburg). We also thank him for stimulating discussions about magnetic moment analysis and anisotropy of small particles. Beamline support by Dr. Thorsten Kachel and Helmut Pfau at beamline PM-3 of Bessy II synchrotron facility in Berlin, Germany is gratefully acknowledged. Finally, we acknowledge financial support by the Deutsche Forschungsgemeinschaft via SFB 569 and the Baden-Württemberg Stiftung via Kompetenznetz Funktionelle Nanostrukturen.

References

1. Stoner, E. C.; Wohlfarth, P. *Philos. Trans. R. Soc. London* **1948,** *A240,* 599.
2. Néel, L. *Ann. Geophys.* **1949,** *5,* 99.
3. Brown, W. F. *Phys. Rev.* **1963,** *130,* 1677–1686. doi:10.1103/PhysRev.130.1677
4. Bucher, J. P.; Douglass, D. C.; Bloomfield, L. A. *Phys. Rev. Lett.* **1991,** *66,* 3052–3055. doi:10.1103/PhysRevLett.66.3052
5. Weller, D.; Moser, A.; Folks, L.; Best, M. E.; Lee, W.; Toney, M. F.; Schwickert, M.; Thiele, J.-U.; Doerner, M. F. *IEEE Trans. Magn.* **2000,** *36,* 10–15. doi:10.1109/20.824418
6. Naito, K. *Chaos* **2005,** *15,* 047507. doi:10.1063/1.2127147
7. Berry, C. C.; Curtis, A. S. G. *J. Phys. D: Appl. Phys.* **2003,** *36,* R198. doi:10.1088/0022-3727/36/13/203
8. Pankhurst, Q. A.; Connolly, J.; Jones, S. K.; Dobson, J. *J. Phys. D: Appl. Phys.* **2003,** *36,* R167. doi:10.1088/0022-3727/36/13/201
9. Lewin, M.; Carlesso, N.; Tung, C.-H.; Tang, X.-W.; Cory, D.; Scadden, D. T.; Weissleder, R. *Nat. Biotechnol.* **2000,** *18,* 410–414. doi:10.1038/74464
10. Ito, A.; Shinkai, M.; Honda, H.; Kobayashi, T. *J. Biosci. Bioeng.* **2005,** *100,* 1–11. doi:10.1263/jbb.100.1
11. Reiss, G.; Brückl, H.; Huetten, A.; Schotter, J.; Brzeska, M.; Panhorst, M.; Sudfeld, D.; Becker, A.; Kamp, P. B.; Puehler, A.; Wojczykowski, K.; Jutzi, P. *J. Mater. Res.* **2005,** *20,* 3294–3302. doi:10.1557/jmr.2005.0409
12. Chen, W.; Kim, J.; Sun, S.; Chen, S. *Phys. Chem. Chem. Phys.* **2006,** *8,* 2779–2786. doi:10.1039/b603045a
13. Kim, J.; Lee, Y.; Sun, S. *J. Am. Chem. Soc.* **2010,** *132,* 4996–4997. doi:10.1021/ja1009629
14. Stamenkovic, V. R.; Mun, B. S.; Mayrhofer, K. J. J.; Ross, P. N.; Markovic, N. M. *J. Am. Chem. Soc.* **2006,** *128,* 8813–8819. doi:10.1021/ja0600476
15. Wang, Y.; Li, Y.; Rong, C.-B.; Liu, J. P. *Nanotechnology* **2007,** *18,* 465701. doi:10.1088/0957-4484/18/46/465701
16. Binns, C. *Surf. Sci. Rep.* **2001,** *44,* 1–49. doi:10.1016/S0167-5729(01)00015-2
17. Bansmann, J.; Baker, S. H.; Binns, C.; Blackman, J. A.; Bucher, J.-P.; Dorantes-Dávila, J.; Dupuis, V.; Favre, L.; Kechrakos, D.; Kleibert, A.; Meiwes-Broer, K.-H.; Pastor, G. M.; Perez, A.; Toulemonde, O.; Trohidou, K. N.; Tuaillon, J.; Xie, Y. *Surf. Sci. Rep.* **2005,** *56,* 89–275. doi:10.1016/j.surfrep.2004.10.001
18. Edmonds, K. W.; Binns, C.; Baker, S. H.; Thornton, S. C.; Norris, C.; Goedkoop, J. B.; Finazzi, M.; Brookes, N. B. *Phys. Rev. B* **1999,** *60,* 472–476. doi:10.1103/PhysRevB.60.472
19. Lau, J. T.; Föhlisch, A.; Nietubyc, R.; Reif, M.; Wurth, W. *Phys. Rev. Lett.* **2002,** *89,* 057201. doi:10.1103/PhysRevLett.89.057201
20. Terheiden, A.; Rellinghaus, B.; Stappert, S.; Acet, M.; Mayer, C. *J. Chem. Phys.* **2004,** *121,* 510. doi:10.1063/1.1760077
21. Queitsch, U.; Mohn, E.; Schäffel, F.; Schultz, L.; Rellinghaus, B.; Blüher, A.; Mertig, M. *Appl. Phys. Lett.* **2007,** *90,* 113114. doi:10.1063/1.2713163
22. Sun, S.; Murray, C. B.; Weller, D.; Folks, L.; Moser, A. *Science* **2000,** *287,* 1989–1992. doi:10.1126/science.287.5460.1989
23. Sun, S. *Adv. Mater.* **2006,** *18,* 393–403. doi:10.1002/adma.200501464

24. Lu, A.-H.; Salabas, E. L.; Schüth, F. *Angew. Chem., Int. Ed.* **2007,** *46,* 1222–1244. doi:10.1002/anie.200602866
25. Verdesa, C.; Chantrell, R. W.; Satoh, A.; Harrell, J. W.; Nikles, D. E. *J. Magn. Magn. Mater.* **2006,** *304,* 27. doi:10.1016/j.jmmm.2006.01.123
26. Yang, X.; Liu, C.; Ahner, J.; Yu, J.; Klemmer, T.; Johns, E.; Weller, D. J. *Vac. Sci. Technol., B: Microelectron. Nanometer Struct.* **2004,** *22,* 31–34. doi:10.1116/1.1633283
27. Barick, K. C.; Bahadur, D. *J. Nanosci. Nanotechnol.* **2010,** *10,* 668–689. doi:10.1166/jnn.2010.1734
28. Puntes, V. F.; Krishnan, K. M.; Alivisatos, A. P. *Science* **2001,** *291,* 2115–2117.
29. Amiens, C.; Chaudret, B. *Mod. Phys. Lett. B* **2007,** *21,* 1133–1141. doi:10.1142/S0217984907013833
30. Howard, L. E. M.; Nguyen, H. L.; Giblin, S. R.; Tanner, B. K.; Terry, I.; Hughes, A. K.; Evans, J. S. O. *J. Am. Chem. Soc.* **2005,** *127,* 10140–10141. doi:10.1021/ja051669e
31. Sahoo, S.; Hucht, A.; Gruner, M. E.; Rollmann, G.; Entel, P.; Postnikov, A.; Ferrer, J.; Fernández-Seivane, L.; Richter, M.; Fritsch, D.; Sil, S. *Phys. Rev. B* **2010,** *82,* 054418. doi:10.1103/PhysRevB.82.054418
32. Wiedwald, U.; Fauth, K.; Heßler, M.; Boyen, H.-G.; Weigl, F.; Hilgendorff, M.; Giersig, M.; Schütz, G.; Ziemann, P.; Farle, M. *ChemPhysChem* **2005,** *6,* 2522–2526. doi:10.1002/cphc.200500148
33. Gao, Y.; Zhang, X. W.; Yin, Z. G.; Qu, S.; You, J. B.; Chen, N. F. *Nanoscale Res. Lett.* **2010,** *5,* 1–6. doi:10.1007/s11671-009-9433-4
34. Ethirajan, A.; Wiedwald, U.; Boyen, H.-G.; Kern, B.; Han, L.; Klimmer, A.; Weigl, F.; Kastle, G.; Ziemann, P.; Fauth, K.; Cai, J.; Behm, R. J.; Romanyuk, A.; Oelhafen, P.; Walther, P.; Biskupek, J.; Kaiser, U. *Adv. Mater.* **2007,** *19,* 406–410. doi:10.1002/adma.200601759
35. Skumryev, V.; Stoyanov, S.; Zhang, Y.; Hadjipanayis, G.; Givord, D.; Nogués, J. *Nature* **2003,** *423,* 850–853. doi:10.1038/nature01687
36. Spatz, J. P.; Herzog, T.; Mößmer, S.; Ziemann, P.; Möller, M. *Adv. Mater.* **1999,** *11,* 149–153. doi:10.1002/(SICI)1521-4095(199902)11:2<149::AID-ADMA149>3.0.CO;2-W
37. Spatz, J. P.; Chan, V. Z. H.; Mößmer, S.; Möller, M.; Kamm, F.-M.; Plettl, A.; Ziemann, P. *Adv. Mater.* **2002,** *14,* 1827–1832. doi:10.1002/adma.200290011
38. Kästle, G.; Boyen, H.-G.; Weigl, F.; Ziemann, P.; Riethmüller, S.; Hartmann, Ch.; Spatz, J. P.; Möller, M.; Garnier, M. G.; Oelhafen, P. *Phase Transitions* **2003,** *4–5,* 307–313. doi:10.1080/0141159021000051479
39. Boyen, H.-G.; Kästle, G.; Zürn, K.; Herzog, T.; Weigl, F.; Ziemann, P.; Mayer, O.; Jerome, C.; Spatz, J. P.; Möller, M.; Garnier, M. G.; Oelhafen, P. *Adv. Funct. Mater.* **2003,** *13,* 359–364. doi:10.1002/adfm.200304319
40. Klimmer, A.; Ziemann, P.; Biskupek, J.; Kaiser, U.; Flesch, M. *Phys. Rev. B* **2009,** *79,* 155427. doi:10.1103/PhysRevB.79.155427
41. Seidel, Y. E.; Lindstrom, R.; Jusys, Z.; Cai, J.; Wiedwald, U.; Ziemann, P.; Behm, R. J. *Langmuir* **2007,** *23,* 5795–5801. doi:10.1021/la063295o
42. Qu, S.; Zhang, X. W.; Yin, Z. G.; You, J. B.; Chen, N. F. *Chin. Phys. Lett* **2007,** *24,* 3520. doi:10.1088/0256-307X/24/12/063
43. Dai, Z. R.; Sun, S.; Wang, Z. L. *Nano Lett.* **2001,** *1,* 443–447. doi:10.1021/nl0100421
44. Boyen, H.-G.; Kästle, G.; Weigl, F.; Koslowski, B.; Dietrich, C.; Ziemann, P.; Spatz, J. P.; Riethmüller, S.; Hartmann, C.; Möller, M.; Schmid, G.; Garnier, M. G.; Oelhafen, P. *Science* **2002,** *297,* 1533–1536. doi:10.1126/science.1076248
45. Vargas, J. M.; Zysler, R. D.; Socolovsky, L. M.; Knobel, M.; Zanchet, D. *J. Appl. Phys.* **2007,** *101,* 023903. doi:10.1063/1.2409620
46. Christodoulides, J. A.; Bonder, M. J.; Huang, Y.; Zhang, Y.; Stoyanov, S.; Hadjipanayis, G. C.; Simopoulos, A.; Weller, D. *Phys. Rev. B* **2003,** *68,* 054428. doi:10.1103/PhysRevB.68.054428
47. Rellinghaus, B.; Mohn, E.; Schultz, L.; Gemming, T.; Acet, M.; Kowalik, A.; Kock, B. F. *IEEE Trans. Magn.* **2006,** *42,* 3048–3050. doi:10.1109/TMAG.2006.880087
48. Rong, C.-B.; Li, Y.; Ping Liu, J. *J. Appl. Phys.* **2007,** *101,* 09K505. doi:10.1063/1.2709739
49. Ulmeanu, M.; Antoniak, C.; Wiedwald, U.; Farle, M.; Frait, Z.; Sun, S. *Phys. Rev. B* **2004,** *69,* 54417. doi:10.1103/PhysRevB.69.054417
50. Colak, L.; Hadjipanayis, G. C. *Nanotechnology* **2008,** *19,* 235703. doi:10.1088/0957-4484/19/23/235703
51. Rong, C.-b.; Li, D.; Nandwana, V.; Poudyal, N.; Ding, Y.; Wang, Z. L.; Zeng, H.; Liu, J. P. *Adv. Mater.* **2006,** *18,* 2984–2988. doi:10.1002/adma.200601904
52. Liu, J. P.; Elkins, K.; Li, D.; Nandwana, V.; Poudyal, N. *IEEE Trans. Magn.* **2006,** *42,* 3036–3041. doi:10.1109/TMAG.2006.880155
53. Tournus, F.; Blanc, N.; Tamion, A.; Hillenkamp, M.; Dupuis, V. *Phys. Rev. B* **2010,** *81,* 220405(R). doi:10.1103/PhysRevB.81.220405
54. Spatz, J. P.; Mössmer, S.; Hartmann, C.; Möller, M.; Herzog, T.; Krieger, M.; Boyen, H.-G.; Ziemann, P. *Langmuir* **2000,** *16,* 407–415. doi:10.1021/la990070n
55. Bansmann, J.; Kielbassa, S.; Hoster, H.; Weigl, F.; Boyen, H. G.; Wiedwald, U.; Ziemann, P.; Behm, R. J. *Langmuir* **2007,** *23,* 10150–10155. doi:10.1021/la7012304
56. Eyrich, M.; Kielbassa, S.; Diemant, T.; Biskupek, J.; Kaiser, U.; Wiedwald, U.; Ziemann, P.; Bansmann, J. *ChemPhysChem* **2010,** *11,* 1430–1437. doi:10.1002/cphc.200900942
57. Manzke, A.; Pfahler, C.; Dubbers, O.; Plettl, A.; Ziemann, P.; Crespy, D.; Schreiber, E.; Ziener, U.; Landfester, K. *Adv. Mater.* **2007,** *19,* 1337–1341. doi:10.1002/adma.200601945
58. Kobitskaya, E.; Ekinci, D.; Manzke, A.; Plettl, A.; Wiedwald, U.; Ziemann, P.; Biskupek, J.; Kaiser, U.; Ziener, U.; Landfester, K. *Macromolecules* **2010,** *43,* 3294–3305. doi:10.1021/ma902553a
59. Roldan Cuenya, B.; Baeck, S. H.; Jaramillo, D. M.; McFarland, E. W. *J. Am. Chem. Soc.* **2003,** *125,* 12928–12934. doi:10.1021/ja036468u
60. Darhuber, A. A.; Troian, S. M.; Davis, J. M.; Miller, S. M.; Wagner, S. *J. Appl. Phys.* **2000,** *88,* 5119. doi:10.1063/1.1317238
61. Wilson, S. D. R. J. *Eng. Math.* **1982,** *16,* 209–221. doi:10.1007/BF00042717
62. Förster, S.; Antonietti, M. *Adv. Mater.* **1998,** *10,* 195–217. doi:10.1002/(SICI)1521-4095(199802)10:3<195::AID-ADMA195>3.0.CO;2-V
63. Krieger, M.; Plettl, A.; Steiner, R.; Boyen, H.-G.; Ziemann, P. *Appl. Phys. A* **2004,** *78,* 327–333. doi:10.1007/s00339-003-2353-8
64. Antonov, V. E.; Antonova, T. E.; Baier, M.; Grosse, G.; Wagner, F. E. *J. Alloys Compd.* **1996,** *239,* 198–202. doi:10.1016/0925-8388(96)02188-3
65. Zürn, K., Ph.D. Thesis, Ulm University, 2009.
66. Han, L.; Wiedwald, U.; Kuerbanjiang, B.; Ziemann, P. *Nanotechnology* **2009,** *20,* 285706. doi:10.1088/0957-4484/20/28/285706

67. De la Presa, P.; Rueda, T.; Hernando, A.; Ramallo-Lopez, J. M.; Giovanetti, L. J.; Requejo, F. G. *J. Appl. Phys.* **2008,** *103,* 103909. doi:10.1063/1.2931947
68. Anders, S.; Toney, M. F.; Thomson, T.; Thiele, J.-U.; Terris, B. D.; Sun, S.; Murray, C. B. *J. Appl. Phys.* **2003,** *93,* 7343. doi:10.1063/1.1543864
69. Graat, P. C.; Somers, M. A. *Appl. Surf. Sci.* **1996,** *100,* 36.
70. Kim, K. S.; Winograd, N.; Davis, R. E. *J. Am. Chem. Soc.* **1971,** *93,* 6296–6297. doi:10.1021/ja00752a065
71. Bancroft, G. M.; Adams, I.; Coatsworth, L. L.; Bennewitz, C. D.; Brown, J. D.; Westwood, W. D. *Anal. Chem.* **1975,** *47,* 586–588. doi:10.1021/ac60353a050
72. Wang, R.; Dmitrieva, O.; Farle, M.; Dumpich, G.; Ye, H. Q.; Poppa, H.; Kilaas, R.; Kisielowski, C. *Phys. Rev. Lett.* **2008,** *100,* 017205. doi:10.1103/PhysRevLett.100.017205
73. Wang, R.; Dmitrieva, O.; Farle, M.; Dumpich, G.; Acet, M.; Mejia-Rosales, S.; Perez-Tijerina, E.; Yacaman, M. J.; Kisielowski, C. *J. Phys. Chem. C* **2009,** *113,* 4395–4400. doi:10.1021/jp811280k
74. Biskupek, J.; Jinschek, J. R.; Wiedwald, U.; Bendele, M.; Han, L.; Ziemann, P.; Kaiser, U. *Ultramicroscopy* **2010,** *110,* 820–825. doi:10.1016/j.ultramic.2010.02.043
75. Trautvetter, M.; Wiedwald, U.; Paul, H.; Minkow, A.; Ziemann, P. *Appl. Phys. A* **2010,** in press. doi:10.1007/s00339-010-5972-x.
76. Garcia-Otero, J.; Porto, M.; Rivas, J. *J. Appl. Phys.* **2000,** *87,* 7376. doi:10.1063/1.372996
77. Harrell, J. W.; Wang, S.; Nikles, D. E.; Chen, M. *Appl. Phys. Lett.* **2001,** *79,* 4393. doi:10.1063/1.1427751
78. Goering, E.; Fuss, A.; Weber, W.; Will, J.; Schütz, G. *J. Appl. Phys.* **2000,** *88,* 5920. doi:10.1063/1.1308095
79. Wiedwald, U.; Klimmer, A.; Kern, B.; Han, L.; Boyen, H.-G.; Ziemann, P.; Fauth, K. *Appl. Phys. Lett.* **2007,** *90,* 062508. doi:10.1063/1.2472177
80. Farle, M. *Rep. Prog. Phys.* **1998,** *61,* 755. doi:10.1088/0034-4885/61/7/001
81. Farle, M.; Mirwald-Schulz, B.; Anisimov, A. N.; Platow, W.; Baberschke, K. *Phys. Rev. B* **1997,** *55,* 3708–3715. doi:10.1103/PhysRevB.55.3708
82. Bruno, P. *Phys. Rev. B* **1989,** *39,* 865–868. doi:10.1103/PhysRevB.39.865
83. Grange, W.; Galanakis, I.; Alouani, M.; Maret, M.; Kappler, J.-P.; Rogalev, A. *Phys. Rev. B* **2000,** *62,* 1157–1166. doi:10.1103/PhysRevB.62.1157
84. Wiedwald, U.; Lindner, J.; Spasova, M.; Frait, Z.; Farle, M. *Phase Transitions* **2005,** *78,* 85–104. doi:10.1080/01411590412331316672
85. Respaud, M.; Broto, J. M.; Rakoto, H.; Fert, A. R.; Thomas, L.; Barbara, B.; Verelst, M.; Snoeck, E.; Lecante, P.; Mosset, A.; Osuna, J.; Ould Ely, T.; Amiens, C.; Chaudret, B. *Phys. Rev. B* **1998,** *57,* 2925–2935. doi:10.1103/PhysRevB.57.2925
86. Antoniak, C.; Lindner, J.; Farle, M. *EPL* **2005,** *70,* 250. doi:10.1209/epl/i2004-10485-9
87. Wu, X. W.; Guslienko, K. Y.; Chantrell, R. W.; Weller, D. *Appl. Phys. Lett.* **2003,** *82,* 3475. doi:10.1063/1.1576501
88. Dmitrieva, O.; Acet, M.; Dumpich, G.; Kästner, J.; Antoniak, C.; Farle, M.; Fauth, K. *J. Phys. D: Appl. Phys.* **2006,** *39,* 4741. doi:10.1088/0022-3727/39/22/001
89. Kang, S.; Harrel, J. W.; Nikles, D. E. *Nano Lett.* **2002,** *2,* 1033–1036. doi:10.1021/nl025614b
90. Meyer, G.; Thiele, J. U. *Phys. Rev. B* **2006,** *73,* 214438. doi:10.1103/PhysRevB.73.214438
91. Ravelsona, D.; Chappert, C.; Mathet, V.; Bernas, H. *Appl. Phys. Lett.* **2000,** *76,* 236. doi:10.1063/1.125713
92. Kanazawa, H.; Lauhoff, G.; Suzuki, T. *J. Appl. Phys.* **2000,** *87,* 6143.
93. Okamoto, S.; Kikuchi, N.; Kitakami, O.; Miyazaki, T.; Shimada, Y.; Fukamichi, K. *Phys. Rev. B* **2002,** *66,* 024413. doi:10.1103/PhysRevB.66.024413
94. Tournus, F.; Tamion, A.; Blanc, N.; Hannour, A.; Bardotti, L.; Prével, B.; Ohresser, P.; Bonet, E.; Epicier, T.; Dupuis, V. *Phys. Rev. B* **2008,** *77,* 144411. doi:10.1103/PhysRevB.77.144411
95. X-Ray Form Factor, Attenuation and Scattering Tables. NIST http://www.nist.gov/physlab/data/ffast/index.cfm (accessed July 18, 2010).
96. Fauth, K. *Appl. Phys. Lett.* **2004,** *85,* 3271. doi:10.1063/1.1804600
97. Kleibert, A.; Meiwes-Broer, K.-H.; Bansmann, J. *Phys. Rev. B* **2009,** *79,* 125423. doi:10.1103/PhysRevB.79.125423
98. Stohr, J.; Siegmann, H. C. *Magnetism: From Fundamentals to Nanoscale Dynamics;* Springer: Berlin, 2007.
99. Liz-Marzán, L. M. *Langmuir* **2006,** *22,* 32–41. doi:10.1021/la0513353
100. Ji, T.; Lirtsman, V. G.; Avny, Y.; Davidov, D. *Adv. Mater.* **2001,** *13,* 1253–1256. doi:10.1002/1521-4095(200108)13:16<1253::AID-ADMA1253>3.0.CO;2-T
101. Lyon, J. L.; Fleming, D. A.; Stone, M. B.; Schiffer, P.; Williams, M. E. *Nano Lett.* **2004,** *4,* 719–723. doi:10.1021/nl035253f
102. Härtling, T.; Seidenstücker, A.; Olk, P.; Plettl, A.; Ziemann, P.; Eng, L. M. *Nanotechnology* **2010,** *21,* 145309. doi:10.1088/0957-4484/21/14/145309
103. Härtling, T.; Uhlig, T.; Seidenstücker, A.; Bigall, N. C.; Olk, P.; Wiedwald, U.; Han, L.; Eychmüller, A.; Plettl, A.; Ziemann, P.; Eng, L. M. *Appl. Phys. Lett.* **2010,** *96,* 183111. doi:10.1063/1.3425670
104. Wiedwald, U.; Spasova, M.; Salabas, E. L.; Ulmeanu, M.; Farle, M.; Frait, Z.; Fraile Rodriguez, A.; Arvanitis, D.; Sobal, N. S.; Hilgendorff, M.; Giersig, M. *Phys. Rev. B* **2003,** *68,* 064424. doi:10.1103/PhysRevB.68.064424
105. Lu, H. M.; Cao, Z. H.; Zhao, C. L.; Li, P. Y.; Meng, X. K. *J. Appl. Phys.* **2008,** *103,* 123526. doi:10.1063/1.2946724

License and Terms

This is an Open Access article under the terms of the Creative Commons Attribution License (http://creativecommons.org/licenses/by/2.0), which permits unrestricted use, distribution, and reproduction in any medium, provided the original work is properly cited.

The license is subject to the *Beilstein Journal of Nanotechnology* terms and conditions: (http://www.beilstein-journals.org/bjnano)

The definitive version of this article is the electronic one which can be found at: doi:10.3762/bjnano.1.5

Beilstein Journal of Nanotechnology

Uniform excitations in magnetic nanoparticles

Steen Mørup*[1], Cathrine Frandsen[1] and Mikkel Fougt Hansen[2]

Review

Open Access

Address:
[1]Department of Physics, Building 307, Technical University of Denmark, DK-2800 Kongens Lyngby, Denmark and [2]Department of Micro- and Nanotechnology, DTU Nanotech, Building 345 East, Technical University of Denmark, DK-2800 Kongens Lyngby, Denmark

Email:
Steen Mørup* - morup@fysik.dtu.dk

* Corresponding author

Keywords:
collective magnetic excitations; Mössbauer spectroscopy; neutron scattering; spin waves; superparamagnetic relaxation

Beilstein J. Nanotechnol. **2010,** *1,* 48–54.
doi:10.3762/bjnano.1.6

Received: 17 September 2010
Accepted: 10 November 2010
Published: 22 November 2010

Guest Editors: U. Wiedwald and P. Ziemann

© 2010 Mørup et al; licensee Beilstein-Institut.
License and terms: see end of document.

Abstract

We present a short review of the magnetic excitations in nanoparticles below the superparamagnetic blocking temperature. In this temperature regime, the magnetic dynamics in nanoparticles is dominated by uniform excitations, and this leads to a linear temperature dependence of the magnetization and the magnetic hyperfine field, in contrast to the Bloch $T^{3/2}$ law in bulk materials. The temperature dependence of the average magnetization is conveniently studied by Mössbauer spectroscopy. The energy of the uniform excitations of magnetic nanoparticles can be studied by inelastic neutron scattering.

Review

Introduction

One of the most important differences between magnetic nanoparticles and the corresponding bulk materials is that the magnetic dynamics differ substantially. The magnetic anisotropy energy of a particle is proportional to the volume. For very small particles at finite temperatures it may therefore be comparable to the thermal energy. This results in superparamagnetic relaxation, i.e., thermally induced reversals of the magnetization direction. For a particle with a uniaxial anisotropy energy $E(\theta)$ given by the simple expression in Equation 1, the superparamagnetic relaxation time τ is given by Equation 2 [1,2].

$$E(\theta) = KV \sin^2 \theta \tag{1}$$

$$\tau = \tau_0 \exp\left(\frac{KV}{k_B T}\right) \tag{2}$$

Here K is the magnetic anisotropy constant, V is the particle volume, θ is the angle between an easy axis and the (sublattice) magnetization vector, k_B is Boltzmann's constant and T is the

temperature. The value of τ_0 is in the range 10^{-13}–10^{-9} s. When the superparamagnetic relaxation time is long compared to the timescale of the experimental technique, the instantaneous magnetization is measured, but in the case of fast relaxation, the average value of the magnetization is measured. The superparamagnetic blocking temperature (T_B) is defined as the temperature at which the superparamagnetic relaxation time equals the timescale of the experimental technique used for the study of the magnetic properties.

Below T_B, superparamagnetic relaxation can be considered negligible, but the magnetization direction may still fluctuate in directions close to the easy axes at θ = 0° and θ = 180°. These fluctuations have been termed "collective magnetic excitations" [3-5]. The magnetic excitations in a nanoparticle are illustrated schematically in Figure 1.

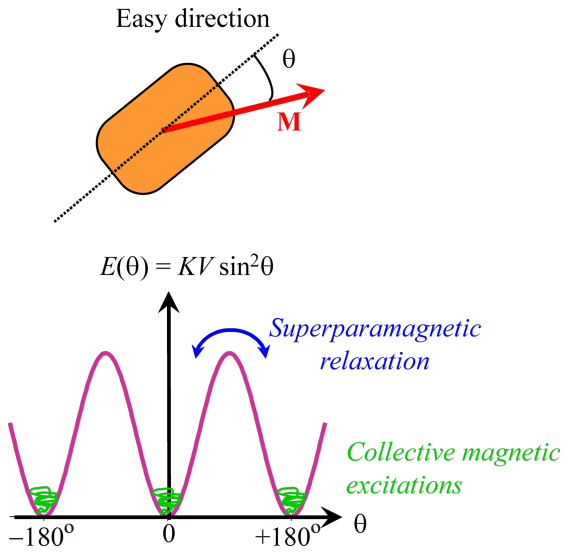


Figure 1: Schematic illustration of magnetic fluctuations in a nanoparticle. At low temperatures the direction of the magnetization vector **M** fluctuates near one of the easy directions (collective magnetic excitations). At higher temperatures the thermal energy can be comparable to the height, *KV*, of the energy barrier separating the easy directions, and the magnetization can fluctuate between the easy directions (superparamagnetic relaxation).

The magnetic dynamics well below the Curie or Néel temperature in both bulk materials and nanoparticles can be described by excitation of spin waves, but the spin wave spectrum of small particles is size-dependent and this can have a substantial influence on the temperature dependence of the magnetization in nanoparticles. In this paper we give a short review of the spin dynamics in non-interacting nanoparticles below the blocking temperature.

Ferromagnetic and ferrimagnetic nanoparticles

First, we consider a ferromagnetic or ferrimagnetic material with cubic crystal structure and lattice constant a_0. The dispersion relation for spin waves, i.e., the spin wave energy $\hbar\omega_q$ as a function of the value of the wave vector q, can for $a_0 q << 1$ be written as [6,7]

$$\hbar\omega_q = 2JSa_0^2q^2 + g\mu_B B_A. \quad (3)$$

Here ω_q is the angular frequency of a spin wave with wave vector q, J is the exchange constant, S is the atomic spin, g is the Landé factor, μ_B is the Bohr magneton, and $B_A = 2K/M_0$ is the anisotropy field, where M_0 is the saturation magnetization. If surface effects are negligible, the allowed values of the wave vector in a cubic nanoparticle with side length d are given by [7-10]

$$q = n\pi/d, \quad n = 0,1,2,3,... \quad (4)$$

In a macroscopic crystal, the energy difference between adjacent spin wave states is small and the quantized states are well approximated by a continuous distribution of energies. Furthermore, the magnetic anisotropy is usually neglected in the calculations [9,10]. In ferromagnetic and ferrimagnetic materials at low temperatures, spin wave excitations result in a temperature dependence of the magnetization given by [10,11]

$$M(T) = M(0)\left[1 - \frac{0.0587}{\upsilon}\left(\frac{k_B T}{2SJ}\right)^{3/2}\right], \quad (5)$$

where υ is an integer, which equals 1, 2, or 4 for simple cubic, bcc or fcc lattices, respectively. Equation 5 is known as the Bloch $T^{3/2}$ law.

In a nanoparticle, the value of d is small, and according to Equation 3 and Equation 4 this results in large energy gaps between spin wave modes with different q-values. The energy gap between the n = 0 and n = 1 modes is given by [7]

$$\Delta = \frac{2\pi^2 JSa_0^2}{d^2}. \quad (6)$$

This energy gap can be on the order of 10 K or larger.

In the spin wave modes with n > 0, the atomic spins precess such that adjacent spins form a small angle with each other. However, in the uniform (n = 0) spin-wave mode the atomic spins precess in unison, as illustrated in Figure 2. Due to the

energy gap, given by Equation 6, the uniform mode is predominant in nanoparticles at low temperatures [8]. In the uniform mode, $q = 0$, and the energy of a particle in an excited uniform precession state is governed by the magnetic anisotropy and is given by

$$E_0 = \left(n_0 + \tfrac{1}{2}\right) g\mu_B B_A, \tag{7}$$

where n_0 can assume the values 0, 1, 2, …

At low temperatures, the average number $\langle n_0 \rangle$ is given by [8]

$$\langle n_0 \rangle \approx \frac{k_B T}{\hbar\omega_0} = \frac{k_B T}{g\mu_B B_A}. \tag{8}$$

The anisotropy field may be on the order of 0.1 T or smaller. The z-components of the magnetic moments of neighboring precession states of the uniform mode with slightly different precession angles differ by $g\mu_B$, and the z-component of the magnetization at the temperature T is given by

$$\langle M \rangle \cong M_0 - \frac{g\mu_B}{V}\langle n_0 \rangle \cong M_0\left[1 - \frac{k_B T}{2KV}\right]. \tag{9}$$

According to Equation 9, the temperature dependence of the magnetization in nanoparticles at low temperatures is independent of the exchange interaction, in contrast to bulk materials (Equation 5). Furthermore, the magnetization depends linearly on temperature, in contrast to the Bloch $T^{3/2}$ law for bulk materials, as illustrated schematically in Figure 2.

The magnetic dynamics in nanoparticles at low temperatures can be described in terms of excitations of the uniform mode in combination with transitions between excited states with different values of n_0, i.e., with different precession angles. These dynamics have also been termed "collective magnetic excitations" [4,5]. The contribution from the uniform mode to the temperature dependence of the magnetization of bulk materials is negligible, because of the dependence of the magnetization on the volume in Equation 9.

The temperature dependence of the magnetization of a nanoparticle can also be derived by considering the particle as a macrospin, which can be treated as a classical magnetic moment, i.e., it is assumed that the magnetization vector can point in any direction [3-5]. Below T_B, the magnetization direction remains near one of the minima and the temperature dependence of the magnetization can be calculated by use of Boltzmann statistics:

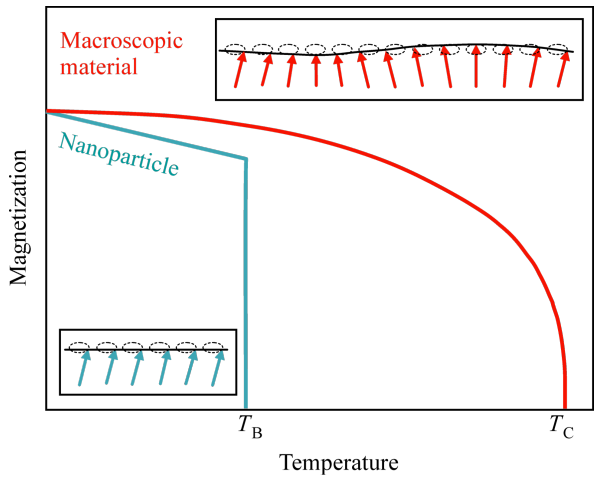


Figure 2: Schematic illustration of spin waves in macroscopic crystals (red arrows) and uniform excitations in nanoparticles (blue arrows) and the corresponding temperature dependence of the magnetization. T_B is the superparamagnetic blocking temperature and T_C is the Curie temperature.

$$\begin{aligned}\langle M(T) \rangle &= M_0 \frac{\int_{-\pi/2}^{+\pi/2} \exp\left[-E(\theta)/k_B T\right] \cos\theta \sin\theta \, d\theta}{\int_{-\pi/2}^{+\pi/2} \exp\left[-E(\theta)/k_B T\right] \sin\theta \, d\theta}, \\ &\approx M_0\left[1 - \frac{k_B T}{2KV}\right],\end{aligned} \tag{10}$$

where $E(\theta)$ is given by Equation 1, and the latter approximation is valid at low temperatures. The linear temperature dependence of the magnetization in nanoparticles was first observed by Mössbauer spectroscopy studies of magnetite (Fe_3O_4) nanoparticles [3], but it has later been studied in nanoparticles of several other magnetic materials.

In Mössbauer spectroscopy studies, the magnetic hyperfine field is measured, which is proportional to the magnetization. If the magnetic fluctuations near an energy minimum are fast compared to the timescale of the technique, which is on the order of a few nanoseconds for Mössbauer spectroscopy, then the average magnetic hyperfine field is measured. The relaxation times for transitions between states with different values of n_0 are much shorter than the pre-exponential factor τ_0 in Equation 2 [12,13], which is on the order of 10^{-13}–10^{-9} s. Thus, it is a good approximation to assume that the relaxation is fast compared to the timescale of Mössbauer spectroscopy, and the observed magnetic hyperfine field is then given by

$$\langle B_{hf} \rangle \cong B_0\left[1 - \frac{k_B T}{2KV}\right], \tag{11}$$

where B_0 is the saturation hyperfine field. Figure 3 shows the temperature dependence of the magnetic hyperfine field of three samples of magnetite (Fe_3O_4) nanoparticles with different average sizes [3]. From the slopes of the fitted straight lines one can estimate the values of the magnetic anisotropy constants K. It was found that K increases with decreasing particle size. This is in accordance with the expected increase of the surface contribution to the total magnetic anisotropy [14]. A similar size dependence of the magnetic anisotropy constant has been found by Mössbauer studies in other nanoparticles, for example, maghemite (γ-Fe_2O_3) [15], hematite (α-Fe_2O_3) [16] and metallic iron (α-Fe) [17].

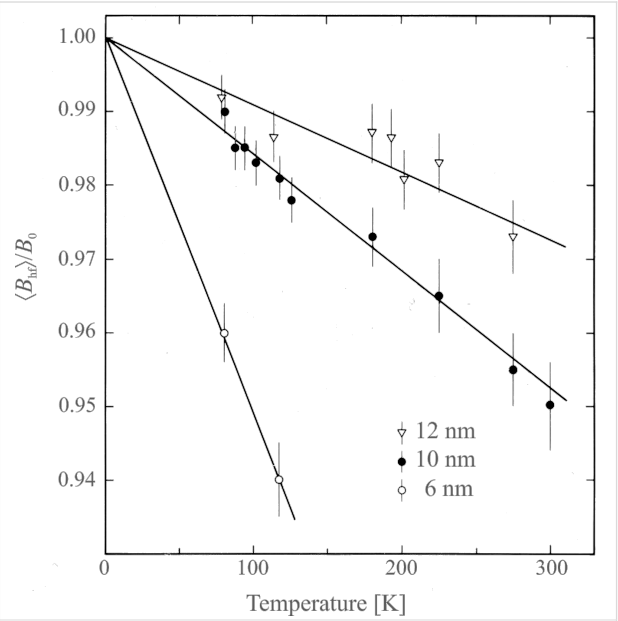


Figure 3: The reduced average magnetic hyperfine field $\langle B_{hf}\rangle/B_0$ as a function of temperature for particles of magnetite with sizes of 6 nm, 10 nm and 12 nm. The solid lines are the best linear fits to the experimental data in accordance with Equation 11. [Reprinted with permission from Mørup, S.; Topsøe, H. Mössbauer Studies of Thermal Excitations in Magnetically Ordered Microcrystals, *Appl. Phys.* **1976,** *11,* 63-66. Copyright (1976) by Springer Science + Business Media.]

If a sufficiently large magnetic field B is applied, such that $B >> B_A$, the anisotropy field in Equation 7 and Equation 8 should be replaced by the applied field. This leads to a temperature and field dependence of the magnetization given by [18]

$$\langle M\rangle \cong M_0\left[1-\frac{k_B T}{M_0 V B}\right], \tag{12}$$

which also can be derived as the high-field approximation to the Langevin function [18]. The temperature and field dependence of the magnetic hyperfine field is given by an equivalent expression.

The timescale of inelastic neutron scattering is on the order of picoseconds, i.e., much shorter than that of Mössbauer spectroscopy, and inelastic neutron scattering can be used to measure the energy difference between adjacent uniform precession states in nanoparticles [19-22]. In inelastic neutron studies of magnetic dynamics of ferrimagnetic particles one can measure the energy distribution of neutrons that are diffracted at a scattering angle corresponding to a magnetic diffraction peak. This energy distribution is usually dominated by a large peak at zero energy, due to elastically scattered neutrons. The energy difference between neighboring precession states in the uniform mode results in satellite peaks in the energy distribution at energies $\pm\varepsilon_0$. These peaks are associated with transitions of the type $n_0 \rightarrow n_0 \pm 1$. The energy ε_0 is given by [20]

$$\varepsilon_0 = \hbar\omega_0 = g\mu_B B_A. \tag{13}$$

Anisotropy fields on the order of 0.1 T correspond to $\varepsilon_0 \approx 0.01$ meV. Using a neutron spectrometer with an energy resolution on the order of 0.1 meV, the satellite peaks are therefore difficult to observe, but they may be visible if a large magnetic field B is applied, because they are then shifted to higher energies [20]. For $B >> B_A$, the energy is approximately given by an expression similar to Equation 13 with B_A replaced by B. The relative intensity of the satellite peaks is for $M_0VB >> k_BT$ given by [20]

$$R_{in} \approx \frac{2k_B T}{M_0 V B}; \tag{14}$$

i.e., it decreases with increasing field because the uniform excitations are suppressed by the applied magnetic field. The temperature dependence of R_{in} is in accordance with the expected increase of the population of the uniform precession mode with increasing temperature.

In Figure 4, data obtained from inelastic neutron scattering studies of 4.0 nm maghemite particles [20] is shown. Figure 4a demonstrates that the energy of the satellite peaks varies almost linearly with the magnitude of the applied magnetic field, indicating that the anisotropy field is almost negligible for $B > 1$ T. By a detailed analysis of the data, B_A was estimated to be on the order of 0.3 T. Panels (b) and (c) in Figure 4 show the relative area, R_{in}, of the satellite peaks as a function of the applied field at 300 K and as a function of temperature at $B = 2$ T, respectively, and the lines are fits by using Equation 14.

Antiferromagnetic nanoparticles

The magnetic dynamics of nanoparticles of antiferromagnetic particles differs in several ways from that of ferro- and ferri-

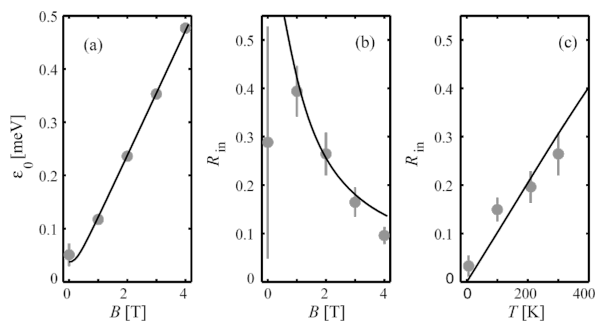


Figure 4: Parameters derived from inelastic neutron scattering data for 4.0 nm particles of maghemite: (a) Energy of the satellite peaks as a function of the applied magnetic field at 300 K; (b) the relative area of the inelastic peaks as a function of the applied field at 300 K; (c) the relative area of the inelastic peaks as a function of temperature at B = 2 T. [Reprinted with permission from Lefmann, K.; Bødker, F.; Klausen, S. N.; Hansen, M. F.; Clausen, K. N.; Lindgård, P.-A.; Mørup, S. A neutron scattering study of spin precession in ferrimagnetic maghemite nanoparticles *Europhys. Lett.* **2001,** *54*, 526–532. Copyright (2001) by EDP Sciences.]

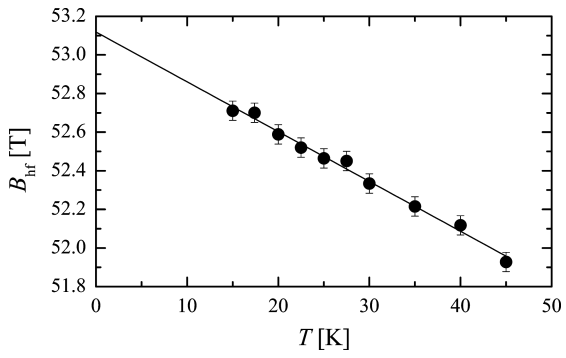


Figure 5: The observed median hyperfine field for 20 nm hematite nanoparticles as a function of temperature. The line is a fit in accordance with Equation 11. [Adapted from Hansen, M. F.; Bender Koch, C.; Mørup, S. The magnetic dynamics of weakly and strongly interacting hematite nanoparticles, *Phys. Rev. B* **2000,** *62,* 1124–1135. Copyright (2000) by the American Physical Society.]

magnetic nanoparticles [23]. In an antiferromagnetic material with uniaxial anisotropy, the dispersion relation for spin waves is given by [10]

$$\hbar\omega_q = g\mu_B\left[\left(B_E + B_A\right)^2 - B_E^2\left(1-\frac{2q^2a_0^2}{z}\right)\right]^{1/2}, \qquad (15)$$

where $B_A = K/M_s$ is the anisotropy field for an antiferromagnetic material with sublattice magnetization M_s, B_E is the exchange field and z is the number of nearest neighbor atoms. The exchange fields of antiferromagnetic materials may be larger than 100 T, i.e., much larger than the anisotropy field. Therefore, in antiferromagnetic nanoparticles, the energy gap between the uniform mode at n = 0 and the n =1 mode is much larger than in ferro- or ferrimagnetic materials. However, in spite of the differences in the excitation energies of ferro- or ferrimagnetic particles and antiferromagnetic particles, the temperature dependence of the sublattice magnetization and the magnetic hyperfine field in antiferromagnetic nanoparticles are still given by Equation 10 and Equation 11 [8].

As an example, Figure 5 shows the temperature dependence of the magnetic hyperfine field of 20 nm hematite nanoparticles [24]. From the slope of the linear fit of the data for the non-interacting particles, the value of the magnetic anisotropy constant can be estimated with Equation 11.

The energy difference between neighboring precession states in the uniform (q = 0) mode is given by [6,10,19,25]

$$\varepsilon_0 = \hbar\omega_0 = g\mu_B\sqrt{B_A^2 + 2B_EB_A} \approx g\mu_B\sqrt{2B_EB_A}, \qquad (16)$$

where the last approximation is valid for $B_E >> B_A$. Because the exchange fields of typical antiferromagnetic materials are much larger than the anisotropy fields, the energy, ε_0, can be much larger than in ferro- and ferrimagnetic nanoparticles and can more easily be resolved in inelastic neutron scattering experiments in zero applied field [19,21,22].

Figure 6 shows inelastic neutron scattering data from a sample of 15 nm α-Fe_2O_3 nanoparticles. The data were obtained from neutrons, scattered at the scattering vector with Q = 1.50 Å^{-1}, corresponding to the purely magnetic hexagonal (101) peak [21]. Data obtained in zero applied field as a function of temperature are shown in Figure 6a, whereas Figure 6b shows data obtained in different applied magnetic fields at 200 K. In Figure 6a, inelastic satellite peaks at energies $\pm\varepsilon_0 \approx \pm 1.1$ meV are seen on both sides of the intense quasielastic peak. As in the data for ferrimagnetic maghemite (Figure 4) the relative area of the inelastic peaks increases with increasing temperature. At low temperatures the relative area of the inelastic peaks in zero applied field is given by [23]

$$R_{in} \approx \frac{k_BT}{KV}. \qquad (17)$$

When magnetic fields are applied at 200 K, the inelastic peaks are shifted to higher energies, and their relative intensity decreases as for ferrimagnetic maghemite nanoparticles (Figure 4).

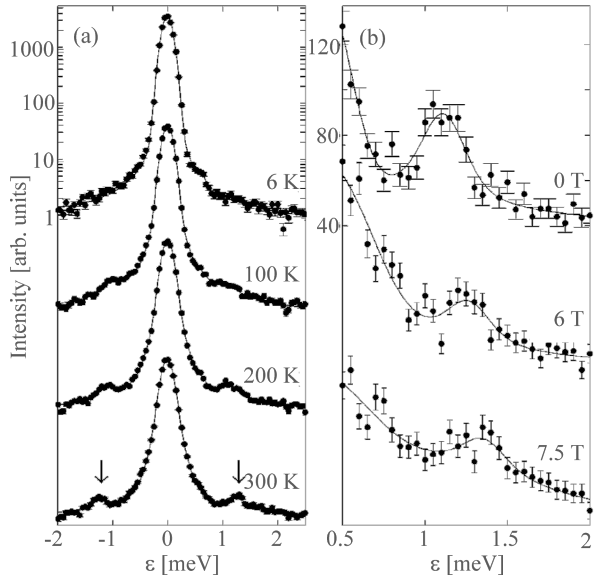


Figure 6: Inelastic neutron scattering data for 15 nm hematite particles measured at the scattering vector Q = 1.50 Å^{-1}: (a) Data obtained in zero applied magnetic field at the indicated temperatures; (b) data obtained at 200 K with the indicated applied magnetic fields. [Reprinted from Klausen, S. N.; Lefmann, K.; Lindgård, P.-A.; Kuhn, L. T.; Frandsen, C.; Mørup, S.; Roessli, B.; Cavadini, N. Quantized spin waves and magnetic anisotropy in hematite nanoparticles. *Phys. Rev. B* **2004**, *70*, 214411. Copyright (2004) by the American Physical Society.]

The energy of the uniform excitations in antiferromagnetic materials, Equation 16, was derived assuming that the antiferromagnetic material had zero net magnetization, but nanoparticles of antiferromagnetic materials usually have a magnetic moment because of uncompensated spins, for example, in the surface [23,26]. This can have a large influence on the excitation energy [25,27]. For example, an uncompensated magnetic moment of only around 1% of the sublattice magnetic moment can result in a decrease of the excitation energy by a factor of two [27]. Neutron studies of hematite nanoparticles [28] have shown that the effect is significant in 8 nm hematite particles, which have relatively large uncompensated moments.

In antiferromagnetic materials, excitation of the uniform mode has interesting consequences. The spins of the two sublattices precess around the easy axis in such a way that they are not strictly antiparallel, but form different angles, θ_A and θ_B, with respect to the easy axis. This is illustrated in Figure 7. For $B_A << B_E$ the two angles are related by [29]

$$\frac{\sin\theta_A}{\sin\theta_B} \cong 1 \pm \sqrt{2\frac{B_A}{B_E}}. \qquad (18)$$

Therefore, the magnetic moments of the two sublattices do not cancel, and the nanoparticle has a net magnetic moment, which increases with increasing temperature. The contribution to the initial susceptibility from this thermoinduced magnetization is given by [30]

$$\chi_i \approx \frac{8k_BT}{V}\left(\frac{g\mu_B}{\hbar\omega_0}\right)^2. \qquad (19)$$

Several studies of the magnetization of antiferromagnetic nanoparticles have demonstrated an apparent increase of the magnetization with increasing temperature, which is in accordance with the model for thermoinduced magnetization [30]. However, magnetization curves of samples of antiferromagnetic nanoparticles can be significantly influenced by the distribution of magnetic moments due to uncompensated spins [31] and by the magnetic anisotropy [32], and these effects may be difficult to distinguish from the contribution from the thermoinduced magnetization.

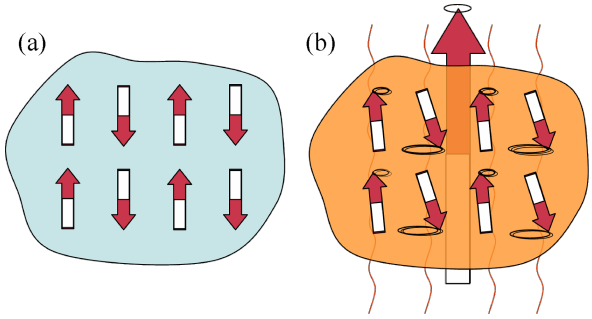


Figure 7: Schematic illustration of the uniform mode in antiferromagnetic nanoparticles: (a) At low temperatures the spins in the two sublattices are essentially antiparallel; (b) at higher temperatures the two sublattices are not antiparallel, but precess around an easy axis with different precession angles. This leads to a non-zero magnetic moment of the nanoparticle.

Conclusion

After the discovery of superparamagnetism much of the research in the field of magnetic nanoparticles has focused on superparamagnetic relaxation while the magnetic dynamics below T_B has attracted less attention. However, the quantization of the spin-wave spectrum, especially the large energy gap between the lowest (q = 0) excitation state and the states with q > 0, results in a predominance of the uniform mode in nanoparticles. This results in a linear temperature dependence of the magnetization and the magnetic hyperfine field, in contrast to the Bloch $T^{3/2}$ law in bulk materials. Mössbauer spectroscopy is useful for studies of the temperature depend-

ence of the magnetization of nanoparticles, whereas inelastic neutron scattering studies can give information on the energy of the uniform excitations.

References

1. Néel, L. *Ann. Geophys. (C. N. R. S.)* **1949,** *5,* 99–136.
2. Brown, W. F., Jr. *Phys. Rev.* **1963,** *130,* 1677–1686. doi:10.1103/PhysRev.130.1677
3. Mørup, S.; Topsøe, H. *Appl. Phys.* **1976,** *11,* 63–66. doi:10.1007/BF00895017
4. Mørup, S.; Topsøe, H.; Lipka, J. *J. Phys., Colloq.* **1976,** *37,* C6-287–C6-290. doi:10.1051/jphyscol:1976658
5. Mørup, S. *J. Magn. Magn. Mater.* **1983,** *37,* 39–50. doi:10.1016/0304-8853(83)90350-5
6. Yosida, K. *Theory of Magnetism*. Cardona, M.; Fulde, P.; von Klitzing, K.; Queisser, H. J., Eds.; Springer Series in Solid-State Sciences, Vol. 122; Springer: Berlin, 1996.
7. Kodama, R. H. *J. Magn. Magn. Mater.* **1999,** *200,* 359–372. doi:10.1016/S0304-8853(99)00347-9
8. Mørup, S.; Hansen, B. R. *Phys. Rev. B* **2005,** *72,* 024418. doi:10.1103/PhysRevB.72.024418
9. Hendriksen, P. V.; Linderoth, S.; Lindgård, P.-A. *Phys. Rev. B* **1993,** *48,* 7259–7273. doi:10.1103/PhysRevB.48.7259
10. Martin, D. H. *Magnetism in Solids;* MIT Press: Cambridge, U.S.A., 1967.
11. Coey, J. M. D. *Magnetism and Magnetic Materials;* Cambridge University Press: U.K., 2010.
12. Jones, D. H.; Srivastava, K. K. P. *Phys. Rev. B* **1986,** *34,* 7542–7548. doi:10.1103/PhysRevB.34.7542
13. Van Lierop, J.; Ryan, D. H. *Phys. Rev. B* **2001,** *63,* 064406. doi:10.1103/PhysRevB.63.064406
14. Néel, L. *J. Phys. Radium* **1954,** *15,* 225–239. doi:10.1051/jphysrad:01954001504022500
15. Tronc, E. *Nuovo Cimento Soc. Ital. Fis., D* **1996,** *18,* 163–180.
16. Bødker, F.; Mørup, S. *EPL* **2000,** *52,* 217–223. doi:10.1209/epl/i2000-00426-2
17. Bødker, F.; Mørup, S.; Linderoth, S. *Phys. Rev. Lett.* **1994,** *72,* 282–285. doi:10.1103/PhysRevLett.72.282
18. Mørup, S.; Clausen, B. S.; Christensen, P. H. *J. Magn. Magn. Mater.* **1987,** *68,* 160–170. doi:10.1016/0304-8853(87)90270-8
19. Hansen, M. F.; Bødker, F.; Mørup, S.; Lefmann, K.; Clausen, K. N.; Lindgård, P.-A. *Phys. Rev. Lett.* **1997,** *79,* 4910–4913. doi:10.1103/PhysRevLett.79.4910
20. Lefmann, K.; Bødker, F.; Klausen, S. N.; Hansen, M. F.; Clausen, K. N.; Lindgård, P.-A.; Mørup, S. *EPL* **2001,** *54,* 526–532. doi:10.1209/epl/i2001-00279-7
21. Klausen, S. N.; Lefmann, K.; Lindgård, P.-A.; Kuhn, L. T.; Frandsen, C.; Mørup, S.; Roessli, B.; Cavadini, N. *Phys. Rev. B* **2004,** *70,* 214411. doi:10.1103/PhysRevB.70.214411
22. Hansen, M. F.; Bødker, F.; Mørup, S.; Lefmann, K.; Clausen, K. N.; Lindgård, P.-A. *J. Magn. Magn. Mater.* **2000,** *221,* 10–25. doi:10.1016/S0304-8853(00)00372-3
23. Mørup, S.; Madsen, D. E.; Frandsen, C.; Bahl, C. R. H.; Hansen, M. F. *J. Phys.: Condens. Matter* **2007,** *19,* 213202. doi:10.1088/0953-8984/19/21/213202
24. Hansen, M. F.; Bender Koch, C.; Mørup, S. *Phys. Rev. B* **2000,** *62,* 1124–1135. doi:10.1103/PhysRevB.62.1124
25. Kittel, C. *Phys. Rev.* **1951,** *82,* 565. doi:10.1103/PhysRev.82.565
26. Néel, L. *C. R. Hebd. Seances Acad. Sci.* **1961,** *252,* 4075–4080.
27. Bahl, C. R. H.; Garde, J.; Lefmann, K.; Jensen, T. B. S.; Lindgård, P.-A.; Madsen, D. E.; Mørup, S. *Eur. Phys. J. B* **2008,** *62,* 53–57. doi:10.1140/epjb/e2008-00122-1
28. Kuhn, L. T.; Lefmann, K.; Bahl, C. R. H.; Klausen, S. N.; Lindgård, P.-A.; Frandsen, C.; Madsen, D. E.; Mørup, S. *Phys. Rev. B* **2006,** *74,* 184406. doi:10.1103/PhysRevB.74.184406
29. Chikazumi, S. *Physics of Ferromagnetism;* Clarendon Press: Oxford, 1997.
30. Mørup, S.; Frandsen, C. *Phys. Rev. Lett.* **2004,** *92,* 217201. doi:10.1103/PhysRevLett.92.217201
31. Silva, N. J. O.; Amaral, V. S.; Carlos, L. D. *Phys. Rev. B* **2005,** *71,* 184408. doi:10.1103/PhysRevB.71.184408
32. Madsen, D. E.; Mørup, S.; Hansen, M. F. *J. Magn. Magn. Mater.* **2006,** *305,* 95–99. doi:10.1016/j.jmmm.2005.11.033

License and Terms

This is an Open Access article under the terms of the Creative Commons Attribution License (http://creativecommons.org/licenses/by/2.0), which permits unrestricted use, distribution, and reproduction in any medium, provided the original work is properly cited.

The license is subject to the *Beilstein Journal of Nanotechnology* terms and conditions: (http://www.beilstein-journals.org/bjnano)

The definitive version of this article is the electronic one which can be found at: doi:10.3762/bjnano.1.6

Beilstein Journal of Nanotechnology

Flash laser annealing for controlling size and shape of magnetic alloy nanoparticles

Damien Alloyeau*[1], Christian Ricolleau[1], Cyril Langlois[1], Yann Le Bouar[2] and Annick Loiseau[2]

Full Research Paper

Open Access

Address:
[1]Matériaux et Phénomènes Quantiques, UMR 7162, Bâtiment Condorcet, Case 7021, Université Paris 7 / CNRS, 75205 Paris Cedex 13, France, Phone : +33 1 57 27 69 83 and [2]Laboratoire d'Etude des Microstructures – Unité mixte ONERA / CNRS, BP 72, 92322 Châtillon Cedex, France

Email:
Damien Alloyeau* - damien.alloyeau@univ-paris-diderot.fr

* Corresponding author

Keywords:
magnetic alloy nanoparticles; nanoparticle morphology; nanosecond pulsed laser annealing; order-disorder transformation

Beilstein J. Nanotechnol. **2010,** *1,* 55–59.
doi:10.3762/bjnano.1.7

Received: 27 July 2010
Accepted: 28 October 2010
Published: 22 November 2010

Guest Editors: U. Wiedwald and P. Ziemann

© 2010 Alloyeau et al; licensee Beilstein-Institut.
License and terms: see end of document.

Abstract

We propose an original route to prepare magnetic alloy nanoparticles with uniform size and shape by using nanosecond annealing under pulsed laser irradiation. As demonstrated here on CoPt nanoparticles, flash laser annealing gives an unprecedented opportunity to control the size and the shape of bimetallic nanoparticles without changing their composition. The mechanisms involved in the complete reshaping of the nanoparticle thin films are discussed and it is also shown that order-disorder phase transformations occur under laser irradiation. This technique is then very interesting for magnetic alloy nanoparticles studies and applications because it opens up a new way to fabricate size-controlled spherical nanoparticles with narrow size dispersion.

Introduction

Future high-density recording systems require 10 nm magnetic grains with a high magnetic anisotropy (K_u) to insure their thermal stability [1]. CoPt and FePt nanoparticles (NPs) in the chemically ordered $L1_0$ structure [2] are very promising materials for such magnetic applications, because of their 10 times larger K_u as well as the larger saturation magnetization compared to CoCr-based alloys used nowadays in the recording systems [3-5]. However the understanding of their size-dependant properties and their future applications depend on the ability to synthesize NPs with a very good control over the size distribution and the chemical composition. Up to now, only chemical synthesis is able to produce monodisperse CoPt [6] and FePt [7,8] NPs with a polydispersity (that is, standard deviation divided by the mean size) as small as 10%. However, chemically prepared monodisperse bimetallic NPs are limited to sub-10 nm diameter, and postsynthesis thermal treatments used

to increase NPs size, inevitably widen size dispersion. Vapour phase homogenous nucleation allows the fabrication of sub-10 nm and sup-10 nm particles, but their polydispersity varies from 30% to 60% with cluster size. This broad size distribution makes the study of the structural and magnetic properties of NPs complicated, because it drastically influences the results of commonly used analysis techniques, such as X-ray diffraction and SQUID. For that reason, single NP analysis techniques are necessary to understand size effects on the NP properties [9-11].

In this article, we propose an original route to prepare CoPt bimetallic NPs with uniform size and shape by using nanosecond annealing with pulsed laser radiation at 248 nm. This technique has already been successfully applied to Ag [12-14] and Au [15-20] NPs in solution, or on a substrate, by using laser energy in the UV range or at the plasmon resonant wavelength of the metal. We will show here that similar results can be obtained on bimetallic NPs by using a nanosecond pulsed laser beam, without changing the NPs composition. These developments open up a new way to design magnetic alloys NPs with ideal morphologies and size for magnetic studies and applications.

Results and Discussion

CoPt NP thin films on amorphous alumina (a-Al_2O_3) were produced by pulsed laser deposition (PLD) in a high vacuum chamber [21,22]. a-Al_2O_3 and the metals are deposited by PLD using a KrF excimer laser at 248 nm with a pulse duration of 25 ns at a repetition rate of 5 Hz. Substrates were commercial transmission electron microscopy (TEM) grids on which an amorphous carbon layer with a thickness of 10 nm was deposited. On the top of the amorphous carbon, a 3 nm layer of a-Al_2O_3 was deposited. Then, cobalt and platinum were alternatively deposited using pure Co and Pt targets irradiated with an energy density of 4.4 J/cm^2 in order to obtain $Co_{50}Pt_{50}$ NPs. The crystalline structure of as-grown NPs can be controlled with the substrate temperature [21,22]. Two samples with a nominal thickness of 2.5 nm were prepared, with a substrate temperature of 550 °C and 650 °C, leading to the formation of a disordered face centered cubic (FCC) and $L1_0$ ordered structures, respectively. On both samples, a 3 nm-thick layer of a-Al_2O_3 was deposited over the NPs to protect them from air oxidation.

After the synthesis, the sample was irradiated by using the same laser as the one used for the PLD experiment. A pulse frequency of 1 Hz was used and the laser energy was chosen well below the ablation threshold of CoPt and Al_2O_3 in order to avoid the vaporization of the sample. For that purpose, a focusing lens is placed between the laser and the sample. The experimental setup is schematically illustrated in Figure 1. The energy density on the sample is controlled by the distance D between the back focal plane of the lens and the sample. In our experiment, samples were irradiated with a fluence of 47 mJ/cm^2. The evolution of the NPs size and shape was studied by TEM. TEM experiments were carried out on a JEM-2010F field-emission electron microscope operating at 200 kV and equipped together with a high-resolution pole piece and a PGT energy dispersive X-Ray (EDX) analyser.

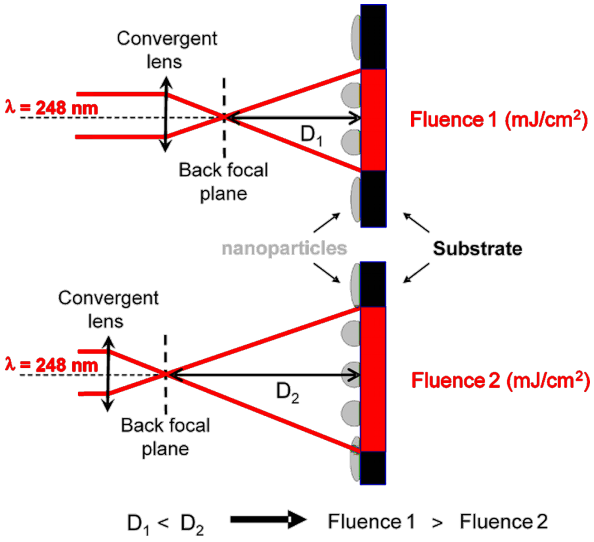


Figure 1: Schematic representation of the experimental setup: the sample is placed behind the back focal plane of a convergent lens. The fluence in the substrate plane is then fixed by the distance D between the sample and the back focal plane of the lens. The longer is D, the lower is the fluence on the substrate.

The morphology of as-grown CoPt NPs is shown in Figure 2a. NPs have irregular shapes elongated in the substrate plane due to coalescence processes during the synthesis. The morphological changes induced by the laser irradiation as a function of the number of laser pulses is presented in Figure 2b and Figure 2c. After the first pulse, we can already observe a partial reshaping of the NPs towards rounded shapes and smooth surfaces, but a significant number of elongated NPs remains. After 7 laser pulses, the shape and the size distribution of bimetallic NPs have completely changed. First of all, the morphology of the particles evolves from a flat to spherical shape, as indicated by the higher intensity levels of the NPs in Figure 2c. At the same time, the mean size, the polydispersity, and the coverage ratio of the NPs decrease (Table 1), changing the broad size dispersion of as-grown NPs into a Gaussian distribution (Figure 2). This technique allows the fabrication of 10 to 15 nm size NPs with a polydispersity as low as 20%. In good agreement with previous studies on monometallic NPs [23,24], we have shown that similar effects are obtained with CoPt thin films near the

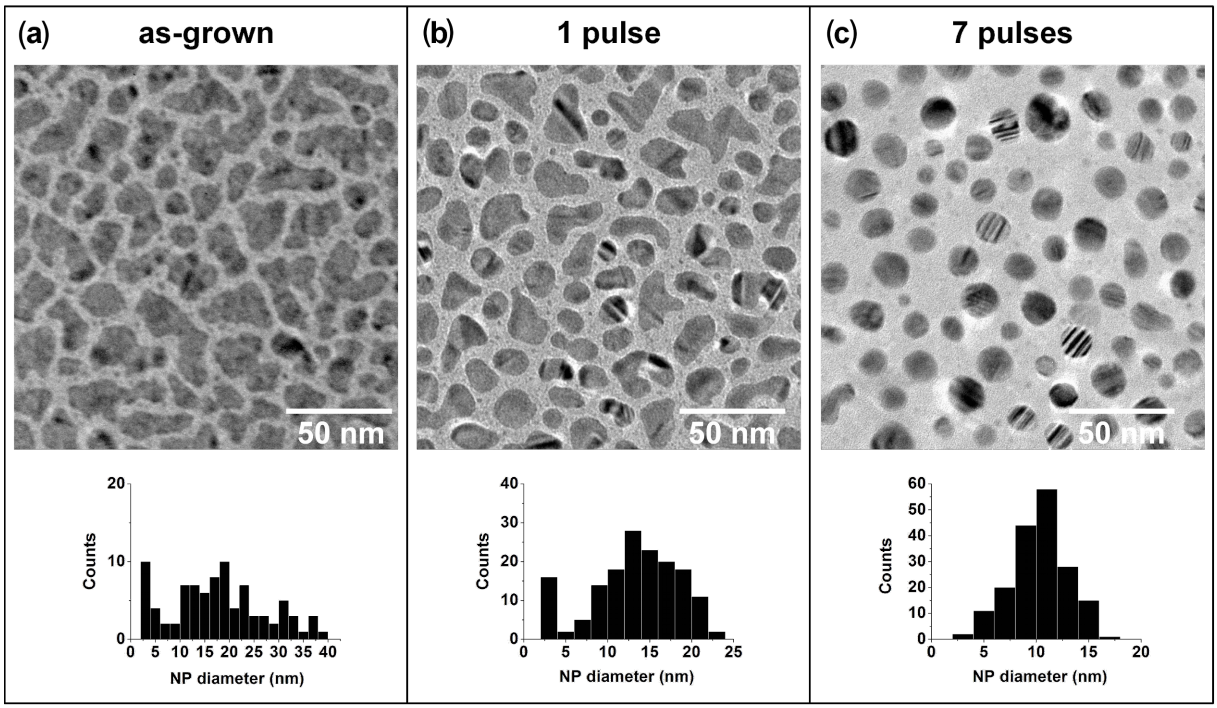


Figure 2: Evolution of the CoPt NPs size and shape as a function of the number of laser pulses. TEM images and the corresponding NPs size dispersion, (a) before laser irradiation, (b) after 1 laser pulse, (c) after 7 laser pulses.

Table 1: Evolution of the NPs mean size, polydispersity, and coverage ratio as a function of the number of laser pulses.

	As-grown	1 pulse	7 pulses
Mean size	16.6 nm	13.4 nm	10.3 nm
Polydispersity	61%	38%	25%
Coverage ratio	60%	53%	32%

percolation threshold, indicating that the morphological transformations does not depend on the as-grown film morphology. If flash laser annealing experiments always result in spherical and monodisperse NPs, the nominal thickness of the as-grown film can be used to control the final size of the irradiated NPs.

NPs composition was measured by EDX analysis. Despite the complete change of the NP morphology, their composition was found to be $Co_{50}Pt_{50}$ (±2 at. %) before and after irradiation experiments. Therefore flash laser annealing does not influence the composition of bimetallic cluster which is a *sine qua non* condition for the use of this technique on magnetic alloy NPs. The conservation of NPs composition indicates that if metal atoms evaporate from CoPt NPs thin films during flash laser annealing, the evaporation rates of Co and Pt atoms are similar. This property of alloys is sometimes exploited for controlling the composition of NPs synthesized by PLD, since the irradiation of alloy targets often leads to the formation of NPs with the same stoichiometry as the target [25,26].

The laser energy can be absorbed either by the NPs or by the substrate since both materials absorb at the laser wavelength. For the NPs, this absorption results in the increase of their temperature and induces desorption of Co and Pt atoms. The absorption cross section of the UV radiation varies as d^3, where d is the diameter of the NPs [13,27]. Desorption phenomena are then more effective on the biggest particles leading to the reduction of the particle size and polydispersity (Table 1). This process can be described, as an "inverse" Ostwald ripening [28], since energetic factors cause small NPs to grow, drawing materials from the bigger clusters, which shrink. In addition, NPs polydispersity is also reduced by the disappearance of the sub-3 nm clusters, which are unstable under laser irradiation because of their lower melting temperature [29]. After a few laser pulses, all the particles are large enough to remain stable under laser irradiation, and their narrow size dispersion tends to equilibrate the laser-induced fluxes of atoms between the clusters.

In parallel, the temperature increase due to the laser intensity induces a solid-liquid transition of the alloy leading to a complete reshaping of the particles. This solid-liquid transition

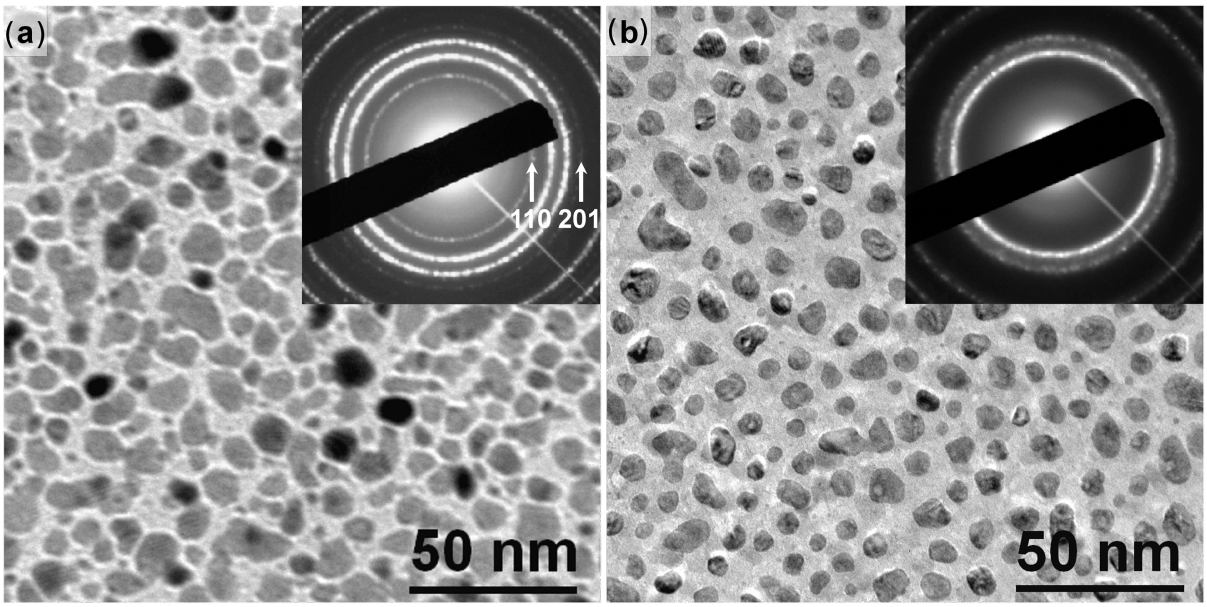


Figure 3: Evolution of the CoPt NPs size, shape, and crystalline structure during flash laser annealing. TEM images and the corresponding diffraction pattern (inset), (a) as-grown CoPt NPs in the $L1_0$ ordered structure, (b) after 3 laser pulses, CoPt NPs in the FCC disordered structure.

is demonstrated by the rounded shape of the particles similar to small water droplets on clean glass substrate. The formation of twin boundaries observed on Figure 2c, is characteristic of rapid solidification processes following NPs melting. These laser-induced phenomena tend to reduce the surface energy of the NPs [19] and spherical shape is the energetically favourable configuration. Evidence of NPs melting has been also reported for irradiated Au NPs [15,30].

Bulk CoPt alloy has a phase transition at 825 °C between the $L1_0$ ordered structure at low temperature and the disordered FCC structure at high temperature. As previously reported [9], this phase transition temperature decreases with particle size; however, such a size effect only occurs in sub-3 nm CoPt NPs. It can then be considered that the phase transition temperature for NPs larger than 10 nm is similar to the bulk phase transition temperature. Figure 3 shows that flash laser annealing experiments performed on $L1_0$ ordered CoPt NPs result in FCC clusters. This phase transformation is demonstrated by the disappearance of the 110 and 201 superstructure reflections, characteristic of chemically ordered structures, on the diffraction pattern of the NPs (Figure 3b). This result proves that the temperature inside the NPs is at least higher than 825 °C. Moreover, this disordering is similar to a quenching of the NPs from a high temperature phase and demonstrates the very fast thermalisation of the NPs, during which the substrate probably acts as a heat sink.

Of course, FCC disordered NPs are not usable for information storage applications because of their superparamagnetic state. However, we have previously reported [21] that between 600 °C and 700 °C, the temperature is high enough to transform FCC NPs into chemically ordered NPs and low enough to prevent NPs coalescence. Using classical annealing procedures $L1_0$ ordered NPs can then be obtained without changing their shape.

In conclusion, flash laser annealing is a method of choice to fabricate 10 to 15 nm size magnetic alloy NPs with spherical shape and low polydispersity (~20%). Indeed, in this range of size, conventional chemical and physical syntheses do not allow the fabrication of NPs with such narrow size dispersion. This technique gives an unprecedented opportunity to control the size and the shape of bimetallic NPs without changing their composition. It can also be used to produce organized CoPt or any bimetallic NPs on a substrate, by using an accurate patterning of the light field intensity designed by masks or gratings lithography [14,31].

References

1. Yu, M.; Liu, Y.; Sellmyer, D. J. *J. Appl. Phys.* **2000,** *87,* 6959–6961. doi:10.1063/1.372899
2. Le Bouar, Y.; Loiseau, A.; Finel, A. *Phys. Rev. B* **2003,** *68,* 224203. doi:10.1103/PhysRevB.68.224203
3. Sakuma, A. *J. Phys. Soc. Jpn.* **1994,** *63,* 3053–3058. doi:10.1143/JPSJ.63.3053

4. Klemmer, T.; Hoydick, D.; Okumura, H.; Zhang, B.; Soffa, W. A. *Scr. Metall. Mater.* **1995,** *33,* 1793–1805. doi:10.1016/0956-716X(95)00413-P
5. Ariake, J.; Chiba, T.; Watanabe, S.; Honda, N.; Ouchi, K. *J. Magn. Magn. Mater.* **2005,** *287,* 229–233. doi:10.1016/j.jmmm.2004.10.037
6. Park, J. I.; Kim, M. G.; Jun, Y. W.; Lee, J. S.; Lee, W. R.; Cheon, J. *J. Am. Chem. Soc.* **2004,** *126,* 9072–9078. doi:10.1021/ja049649k
7. Sun, S.; Murray, C. B.; Weller, D.; Folks, L.; Moser, A. *Science* **2000,** *287,* 1989–1992. doi:10.1126/science.287.5460.1989
8. Liu, C.; Wu, X.; Klemmer, T.; Shukla, N.; Yang, X.; Weller, D.; Roy, A. G.; Tanase, M.; Laughlin, D. *J. Phys. Chem. B* **2004,** *108,* 6121–6123. doi:10.1021/jp0312971
9. Alloyeau, D.; Ricolleau, C.; Mottet, C.; Oikawa, T.; Langlois, C.; Le Bouar, Y.; Braidy, N.; Loiseau, A. *Nat. Mater.* **2009,** *8,* 940–946. doi:10.1038/nmat2574
10. Alloyeau, D.; Ricolleau, C.; Oikawa, T.; Langlois, C.; Le Bouar, Y.; Loiseau, A. *Ultramicroscopy* **2008,** *108,* 656–662. doi:10.1016/j.ultramic.2007.10.006
11. Alloyeau, D.; Ricolleau, C.; Oikawa, T.; Langlois, C.; Le Bouar, Y.; Loiseau, A. *Ultramicroscopy* **2009,** *109,* 788–796. doi:10.1016/j.ultramic.2009.02.002
12. Takami, A.; Yamada, H.; Nakano, K.; Koda, S. *Jpn. J. Appl. Phys.* **1996,** *35,* L781–L783. doi:10.1143/JJAP.35.L781
13. Bosbach, J.; Martin, D.; Stietz, F.; Wenzel, T.; Träger, F. *Appl. Phys. Lett.* **1999,** *74,* 2605–2607. doi:10.1063/1.123911
14. Haro-Poniatowski, E.; Fort, E.; Lacharme, J. P.; Ricolleau, C. *Appl. Phys. Lett.* **2005,** *87,* 143103. doi:10.1063/1.2061857
15. Takami, A.; Kurita, H.; Koda, S. *J. Phys. Chem. B* **1999,** *103,* 1226–1232. doi:10.1021/jp983503o
16. Inasawa, S.; Sugiyama, M.; Koda, S. *Jpn. J. Appl. Phys.* **2003,** *42,* 6705–6712. doi:10.1143/JJAP.42.6705
17. Yang, D. Q.; Meunier, M.; Sacher, E. *J. Appl. Phys.* **2004,** *95,* 5023–5026. doi:10.1063/1.1689751
18. Aguirre, C. M.; Moran, C. E.; Young, J. F.; Halas, N. J. *J. Phys. Chem. B* **2004,** *108,* 7040–7045. doi:10.1021/jp036222b
19. Resta, V.; Siegel, J.; Bonse, J.; Gonzalo, J.; Afonso, C. N.; Piscopiello, E.; Van Tenedeloo, G. *J. Appl. Phys.* **2006,** *100,* 084311.
20. Ito, S.; Mizuno, T.; Yoshikawa, H.; Masuhara, H. *Jpn. J. Appl. Phys.* **2007,** *46,* L241–L243. doi:10.1143/JJAP.46.L241
21. Alloyeau, D.; Langlois, C.; Ricolleau, C.; Le Bouar, Y.; Loiseau, A. *Nanotechnology* **2007,** *18,* 375301. doi:10.1088/0957-4484/18/37/375301
22. Langlois, C.; Alloyeau, D.; Le Bouar, Y.; Loiseau, A.; Oikawa, T.; Mottet, C.; Ricolleau, C. *Faraday Discuss.* **2008,** *138,* 375–391. doi:10.1039/b705912b
23. Kawasaki, M.; Hori, M. *J. Phys. Chem. B* **2003,** *107,* 6760–6765. doi:10.1021/jp034768s
24. Inasawa, S.; Sugiyama, M.; Yamaguchi, Y. *J. Phys. Chem. B* **2005,** *109,* 3104–3111. doi:10.1021/jp045167j
25. Belouet, C. *Appl. Surf. Sci.* **1996,** *96–68,* 630–642. doi:10.1016/0169-4332(95)00535-8
26. Rousset, J. L.; Cadete Santos Aires, F. J.; Sekhar, B. R.; Melinon, P.; Prevel, B.; Pellarin, M. *J. Phys. Chem. B* **2000,** *104,* 5430–5435. doi:10.1021/jp994391j
27. Kreibig, U.; Vollmer, M. *Optical properties of metal clusters;* Springer: Berlin, 1995; Vol. 25.
28. Lifshitz, I. M.; Slyozov, V. V. *J. Phys. Chem. Solids* **1961,** *19,* 35–50. doi:10.1016/0022-3697(61)90054-3
29. Buffat, P.; Borel, J. P. *Phys. Rev. A* **1976,** *13,* 2287–2298. doi:10.1103/PhysRevA.13.2287
30. Inasawa, S.; Sugiyama, M.; Yamaguchi, Y. *J. Phys. Chem. B* **2005,** *109,* 9404–9410. doi:10.1021/jp0441240
31. Vollmer, M.; Weidenauer, R.; Hoheisel, W.; Schulte, U.; Träger, F. *Phys. Rev. B* **1989,** *40,* 12509–12512. doi:10.1103/PhysRevB.40.12509

License and Terms

This is an Open Access article under the terms of the Creative Commons Attribution License (http://creativecommons.org/licenses/by/2.0), which permits unrestricted use, distribution, and reproduction in any medium, provided the original work is properly cited.

The license is subject to the *Beilstein Journal of Nanotechnology* terms and conditions: (http://www.beilstein-journals.org/bjnano)

The definitive version of this article is the electronic one which can be found at: doi:10.3762/bjnano.1.7

Beilstein Journal of Nanotechnology

Review and outlook: from single nanoparticles to self-assembled monolayers and granular GMR sensors

Alexander Weddemann*[1], Inga Ennen[1,2], Anna Regtmeier[1], Camelia Albon[1], Annalena Wolff[1], Katrin Eckstädt[1], Nadine Mill[1], Michael K.-H. Peter[3], Jochen Mattay[3], Carolin Plattner[4], Norbert Sewald[4] and Andreas Hütten[1]

Review

Open Access

Address:
[1]Department of Physics, Thin Films and Physics of Nanostructures, Bielefeld University, 33615 Bielefeld, Germany, [2]Institute of Solid State Physics, Vienna University of Technology, A-1040 Vienna, Austria, [3]Department of Chemistry, Organic Chemistry I, Bielefeld University, 33615 Bielefeld, Germany and [4]Department of Chemistry, Organic Chemistry III, Bielefeld University, 33615 Bielefeld, Germany

Email:
Alexander Weddemann* - weddeman@physik.uni-bielefeld.de

* Corresponding author

Keywords:
bottom-up particle synthesis; dipolar particle coupling; granular giant magnetoresistance sensor; magnetic nanoparticles; self-assembly

Beilstein J. Nanotechnol. **2010,** *1,* 75–93.
doi:10.3762/bjnano.1.10

Received: 05 August 2010
Accepted: 28 October 2010
Published: 22 November 2010

Guest Editors: U. Wiedwald and P. Ziemann

© 2010 Weddemann et al; licensee Beilstein-Institut.
License and terms: see end of document.

Abstract

This paper highlights recent advances in synthesis, self-assembly and sensing applications of monodisperse magnetic Co and Co-alloyed nanoparticles. A brief introduction to solution phase synthesis techniques as well as the magnetic properties and aspects of the self-assembly process of nanoparticles will be given with the emphasis placed on selected applications, before recent developments of particles in sensor devices are outlined. Here, the paper focuses on the fabrication of granular magnetoresistive sensors by the employment of particles themselves as sensing layers. The role of interparticle interactions is discussed.

Introduction

Magnetic nanoparticles have been thoroughly studied during the last decades due to their many promising applications in chemical, physical and medical fields [1]. A common example is their employment in microfluidic devices: Due to their permanent magnetic moment, they can be controlled via external, inhomogeneous magnetic fields [2] and also be detected by magnetoresistive sensors [3] which allows for the magneto-based monitoring of magnetically labeled biomolecules.

The interaction between several particles is also of high practical relevance: Due to different types of coupling, magnetic nanoparticles assemble in superstructures. Various technological applications such as their employment in data storage devices, where every particle represents one bit of information [4], have been a strong driving force for the development of new methods for the well-defined deposition of superstructures on a substrate. In this regard, the different morphologies of

nanoparticles have also become of interest as they offer additional degrees of freedom.

Within such assemblies, magnetic nanoparticles themselves may act as magnetoresistive sensor devices: Surrounded by a non-magnetic matrix, various spin-dependent transport phenomena have been observed [5-9]. Contrary to formerly used metallurgic preparation techniques, nanoparticle fabrication by bottom-up chemical syntheses offer significant advantages: The systematic adjustment of the self-organization process by, e.g., the employment of ligands with different alkyl chain lengths, allows for the independent variation of the particle-matrix volume fraction and the inter-particle distances between the magnetic granules and, therefore, enables a systematic study of granular resistive effects. These systems have promising applications of high technological relevance such as the realization of printable magnetoresistive sensor devices by the employment of colloidal magnetic spheres dispersed in a conductive paste.

However, the controlled preparation of highly ordered assemblies of magnetic nanoparticles requires a strong understanding of all steps involved and remains challenging due to the high degree of interdisciplinary influences. In this work, we give an overview of different preparation techniques, the resulting particles and the possibilities to control particle properties such magnetism of morphology by varying parameters in the synthesis process. The governing dynamics during the self-assembly process and within the static particle configuration are discussed, and we further analyze different properties of granular giant magnetoresistance sensors based on their spin-dependent transport properties.

Review

1. Particle preparation

In principle, two different strategies for the synthesis of nanoparticles may be pursued. The top-down method starts from the bulk material which is decomposed by mechanical influences into decreasingly smaller fragments. The resulting objects have a mean diameter of about 100 nm and show a very wide size distribution. Therefore, such an approach is usually not suitable for the manufacturing of particles with a well-defined geometrical configuration.

The bottom-up method may be understood as an approach from the opposite direction: A small precursor, commonly an organometal compound or a salt, is decomposed by either thermal or optical excitation, which separates the metal atom from the organic residue, or by a reducing agent. Via the nucleation of numerous metal atoms, particles with a diameter of 1 to 50 nm and a narrow size distribution are formed. Due to the advantage of highly defined particle morphology, the bottom-up method is preferred in the works reported throughout this paper. However, a firm control of such properties for the design of particles tailored to specific applications requires a detailed understanding of different influences during the synthesis which are discussed in the following sections.

1.1 Thermolysis

A very commonly used method is thermolysis, which was originally introduced by Puntes et al. [10,11]. Tensides such as oleic acid, oleylamine, TOPO (tri-*n*-octylphosphine oxide), dendrimers or proteins are dissolved in airless conditions in an organic solvent and subsequently heated to reflux. By adding different organ metal compounds such as metal acetyl acetate [$M(acac)_n$] or metal carbonyls, the formation of nucleation seeds is initiated. After formation, seeds absorb free metal atoms and continue to grow. The role of the tensides will be discussed below, however at this point, it is sufficient to know that they act as stabilizers for the particles; the resulting nanoobjects have a shell of the corresponding molecules. The particle growth dynamics can be explained in the frame of the LaMer model [12] which describes the growth process in two separate steps (Figure 1, blue line): above a critical concentration of free metal atoms, nucleation seeds are formed. Once the concentration drops below a critical threshold, the number of seeds remains constant and the existing seeds continue to grow.

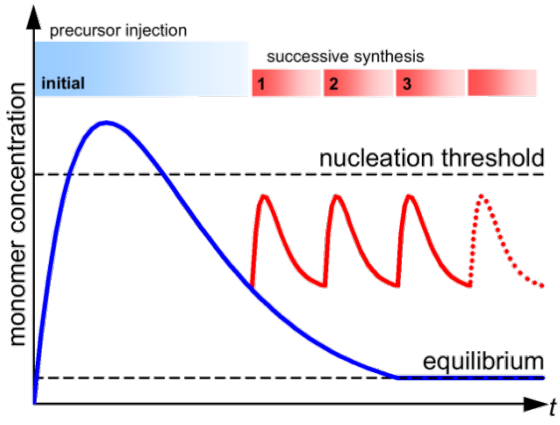


Figure 1: Schematic representation of the precursor concentration according to the LaMer model. The blue line represents the situation of a single injection; the particle size is limited by the precursor concentration. The red line shows the successive approach in order to increase the resulting particle size. During successive injection, the monomer concentration may not exceed the nucleation threshold.

From a thermodynamic point of view, nucleation seeds are formed once the nucleation energy barrier is exceeded. The free enthalpy ΔG is composed of surface contributions G_S and the bulk enthalpy G_V:

$$\Delta G = G_S + G_V = 4\pi R^2\gamma + \frac{4}{3}\pi R^3 \Delta G_V \quad (1)$$

where R denotes the particle radius. The first summand describes the influence of the surface with γ the specific free surface energy. We always have $\gamma > 0$ and, thus, the nucleation process cannot be initiated due to surface effects. The second term refers to volume contributions with ΔG_V the free enthalpy difference between the solved monomer and the unit volume crystal. If $\Delta G_V > 0$, solved monomers are energetically more favorable and, therefore, no nucleation seeds will be formed. For the synthesis of nanoparticles, it is, therefore, necessary to have $\Delta G_V < 0$ such that $G_S < |G_V|$. By introducing the degree of saturation S, ΔG_V may be rewritten as

$$\Delta G_V = -\frac{C_R T \ln S}{V_m} \quad (2)$$

with C_R the Rydberg constant, T the absolute temperature and V_m the molar volume of the crystal. S reaches the value 1 for a completely saturated solution. At higher (supersaturated) concentrations, $S > 1$ and, consequently, also $\Delta G_V < 0$. An analysis of the free enthalpy ΔG with respect to the particle radius R reveals that there is a maximum at

$$R_C = -\frac{2\gamma}{\Delta G_V} = \frac{2\gamma V_m}{C_R T \ln S} \quad (3)$$

Below this critical radius, nucleation seeds can be formed, however, they immediately decay into smaller objects which are energetically more favorable. Therefore, the corresponding R-value R_c at the maximum of ΔG is the minimum size of a nucleation seed. The equations given above require the enthalpy difference ΔG_V and the specific surface energy γ to be constants. However, in the case of nanoparticles, this is no longer valid: Both values may strongly depend on the particle size and also different mechanisms of energy minimization such as rearrangement of the crystallographic phase may occur which are not included in Equation 1. Therefore, the critical size (Equation 3) is only an approximation.

Based on the LaMer model, the particle size can be controlled in different ways. Nucleation processes are initiated once the precursor concentration exceeds a critical concentration threshold. During the nucleation and in the subsequent seed growth, the concentration drops again below this boundary and no further seeds are formed. From this point onwards, the remaining free metal atoms contribute to the growth of the existing seeds. Therefore, the resulting particles are larger the less seeds have been formed during the nucleation events. Thus, particles with a large radius can be obtained by adjusting the precursor concentration to exceed the nucleation threshold by as little as possible which result in a small number of nucleation events. An alternative approach is indicated in Figure 1, red line, which is known as successive particle synthesis [13]. During the growth process, repeated injection of precursor concentration below the nucleation threshold results in a continuous growth without the formation of any new seeds. However, this method often leads to a broad size distribution.

In most synthesis processes, tensides form a basic requirement for particle stabilization: Due to their steric demand, they control the minimal distance between particles (see Section 2.1). If no tensides are present during the process, the synthesis will result in bulk material instead of nanoparticles. However, their interaction with the particle surface also proves key in the modification of particle properties: The interaction between a tenside and the particle surface can occur in many ways and are mainly based on dipole–dipole-, hydrogen bond- or van der Waals interactions. They do usually not show covalent characteristics.

Tensides can be characterized by their head groups via which they interact with metal atoms on the surface of the particles. We distinguish between tensides such as TOPO which has a phosphine oxide head group and can only bind in a single motif to the surface (Figure 2(a)) and tensides such as oleic acid where different binding motifs are possible (Figure 2(b)): In the monodentrate structure, only one oxygen atom binds to a metal atom, the second is not integrated. If both oxygen atoms are involved in the binding process, they form complexes with either two different metal atoms or a single one. These motifs are referred to as bridged and chelating, respectively (Figure 2(b)). Experimentally, the actual binding motif may be

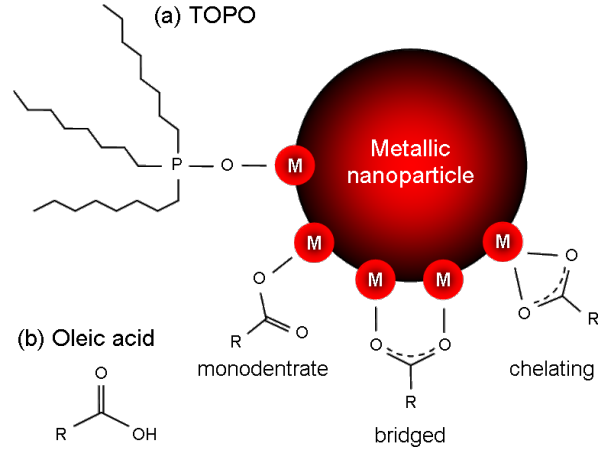


Figure 2: Interaction of different ligands with the surface of a metallic nanoparticle. There is only a single binding motif for TOPO (a) but three for ligands such as oleic acid (b).

distinguished by IR spectroscopy due to a characteristically shifted carbonyl band [14]. Which motif is dominating for a specific tenside–particle pair depends on the properties of the metal surface and the structure of the head group of the absorbed tenside. In particular, lattice constants and crystallographic planes involved play an important role.

The strength of the coupling between ligand and particle strongly affects the growth behavior of the metal cluster: The absorption of free metal atoms to the seed surface and, therefore, the continuation of growth is only possible at those areas where no complexes are present. A measure for the detachment of ligands is given by the dissociation constant D_e. A small value of D_e corresponds to a hard to break bond between the metal surface and the ligand and, consequently, in reduced particle growth. The size of the dissociation constant may strongly vary, depending on the above mentioned binding affinities to different crystal planes. Crystals with a simple cubic symmetry result in an isotropic value which entails spherical particles (Figure 3(a)). However, if non-cubic crystal lattices are present, the dissociation constants may depend on the crystal plane and growth in specific directions is promoted [10,15-17].

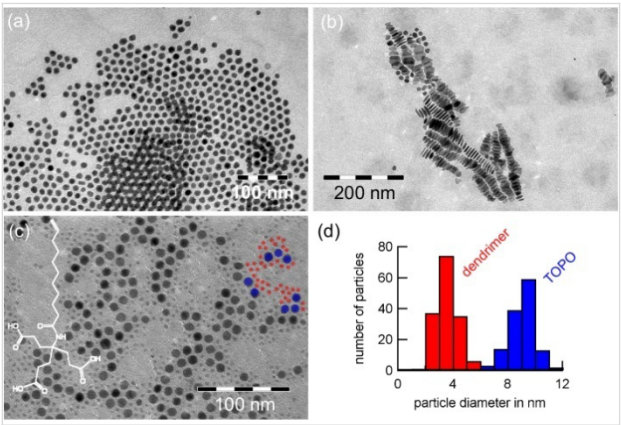


Figure 3: Transmission electron microscopy (TEM) images of Co particles of various sizes and morphologies synthesized under the influence of (a) TOPO, (b) oleic acid and oleylamine and (c) a dendrimer and TOPO which results in two distinct particle sizes (d).

Such effects are shown in Figure 3: The subplots present particles synthesized in *ortho*-dichlorobenzene employing dicobalt octacarbonyl as a precursor. As a ligand (a) TOPO, (b) a mixture of oleic acid and oleylamine and (c) a mixture of TOPO and a dendrimer of the first generation is present. The single binding motive of TOPO results in a constant dissociation along the particle surface and, thus, an isotropic growth. The multiple binding motives of the ligand mixture (b) lead to different binding affinities along different crystal planes. Therefore, the growth in specific directions is enhanced which can result in disk-shaped nanocrystals. In subplot (c), a bimodal particle distribution can be found. The two distinct sizes as shown in (d) result from different binding affinities of the tensides to the metal surface: Smaller particles are mainly stabilized by the dendrimer, larger ones by TOPO. The dendrimer has a very high dissociation constant which results in a strong binding to the metal atoms and, therefore, in a slow growth.

1.2 Alternative methods

1.2.1 Micro emulsion and magnetotactic bacteria

Another method for the synthesis of nanoparticles is the micro emulsion technique which is based on a thermally stabile, isotropic dispersion of two immiscible solvents, in which the micro domains of one or both solvents are stabilized by tensides on the boundary layer. Such behavior is well known from tensides in water which form micelles due to hydrophilic head groups and hydrophobic tails. Such micelles have a size of 1 to 50 nm depending on the tenside concentration [18]. The precursor is confined within these defined droplets which may, thus, act as nanoreactors in which particle growth is initiated. A typical result obtained by the use of an isopropanol/water emulsion and cetyltrimethylammonium bromide (CTAB) as a tenside is shown in Figure 4(a); the reducing agent is sodium borohydride.

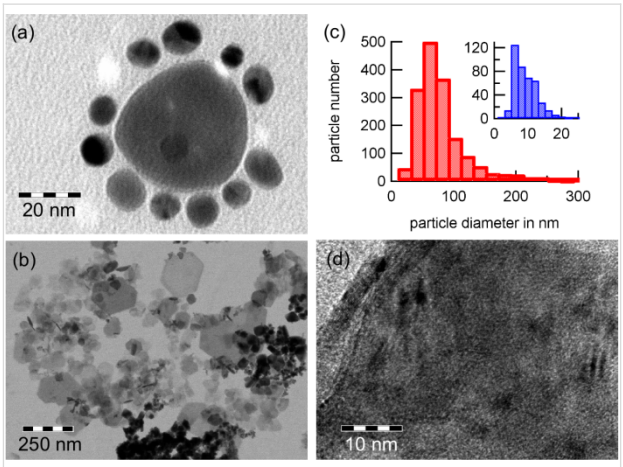


Figure 4: (a) Nanoparticles synthesized by micro emulsion approach and (b) by employment of the synthetic protein c25-mms6 after 15 days. The latter approach results in two different particle species of different sizes (c). Within a single particle, crystallites of different orientation can be found (d).

While micro emulsion allows for much lower temperatures during the synthesis, stabilizing tensides usually need to be injected after the actual growth. Therefore, the additional control of the particle morphology by tensides is available. However, as shown by Tan et al. [19], it is still possible to synthesize nanoparticles of different shapes, materials or phases [20,21]. The major disadvantages of this technique are a broad

distribution of size and morphology. Furthermore, much solvent is necessary for the synthesis which leads to a low efficiency in comparison to the thermolysis.

A very similar mechanism can be found with magnetotactic bacteria which produce ferrite nanoparticles under mild conditions as part of their metabolism. The biomineralization process within such bacteria is not yet well understood. Recent studies indicate specific genes and proteins play a major role [22]. As shown in Figure 5, the growth dynamic is believed to be a multistep process [22,23]:

1. *Invagination of cytoplasmic membrane*: The cytoplasmic membrane invaginates for vesicle formation. These vesicles later serve as precursors of the nanoparticle membrane. It is believed that a 16 kDa protein Mms16 (small GT-Pase) assists with the vesicle formation. A second protein Mms 24 (24 kDa) may also be required [24].
2. *Accumulation of ferrous irons*: External iron ions are transported into the vesicle. Ferric iron Fe^{3+} appears to be reduced on the cell surface and transported into the vesicle as ferrous iron Fe^{2+}. This conversion is required so the iron ions can pass the cytoplasmic membrane, a detailed description can be found in [25]. A protein magA appears to be involved in this transport process. The oxidation level within the vesicles is controlled by an oxidation–reduction system.
3. *Nucleation*: Several proteins are believed to regulate the morphology. Mms5, Mms6, Mms7 and Mm13 are tightly bound to the magnetic nanoparticle. All these proteins are amphiphilic. Their *N*-terminal is hydrophilic while their *C*-terminal is hydrophilic. The hydrophilic *C*-terminal of Mms6 is believed to be the iron binding site [26].

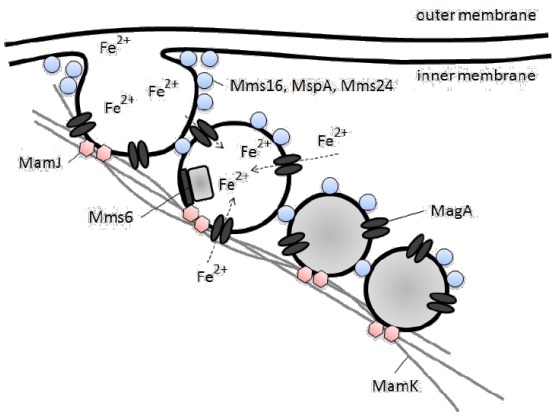


Figure 5: Hypothesized particle formation during the biomineralization process in magnetotactic bacteria (in analogy to [22]).

Recent studies within our group showed that nanoparticles can be synthesized in vitro by the use of a shorter synthetic version of the protein Mms6 called c25-mms6. This polypeptide consists of 25 amino acids from the *C*-terminal region of Mms6. In this study, cobalt ferrite nanoparticles not known to occur in magnetotactic bacteria were synthesized. Cobalt and iron salts were added to the c25-mms6 mixture and incubated at 4 °C. The mixture was stirred under argon flux until it reached room temperature and then left for 15 to 28 days to allow for crystal growth. The nanoparticles obtained can be divided into Co_2FeO_4 and $CoFe_2O_4$ particles, Figure 4(b,c), which consist of small phase separated crystallites, Figure 4(d). The majority of larger particles is hexagonally or truncated hexagonally shaped and constitute the Co rich phase. A control experiment without c25-mms6 showed that the nucleation is not triggered by the protein but that it regulates shape and morphology and, therefore, the physical properties of the nanoparticles.

1.2.2 Bimetallic nanoparticles

Bimetallic nanoparticles [27,28] form an important area in the field of nanoparticles based on their interesting properties which provide various advantages in comparison to monometallic nanocrystals. An example can be found with CoFe particles which have a strongly increased magnetic moment per atom in comparison to pure Co particles [29]. Bimetallic particles can be classified into 5 groups [30]:

1. *Stoichiometrical compounds* with well defined crystal structures. Examples are CdSe semiconductor particles or magnetic FePt particles [31].
2. *Undefined mixtures*. Two compounds are completely miscible. This situation occurs if the bulk metals have similar structures with a mismatch of below 10%. SiGe [32] and AuAg [33] are systems of this type.
3. *Undefined structure with a concentration gradient*. The requirements are similar to the second class but the component distribution is controlled kinetically. CoFe is a well known example [30] (see Figure 6).
4. *Core shell particle*. Based on two immiscible materials, one compound in the center (core-phase) is coated by the second (shell phase) [34].
5. *All other two phase systems* which are not in class 4. Similar requirements as in class 4 need to be met [35].

Thermodynamic and kinetic properties influence the type of particle which results from the synthesis. Depending on the miscibility of the two compounds, either a single phase system (1–3) for high miscible or a two phase particle (4,5) in case of immiscible components is obtained. A first estimation on the miscibility can be concluded from the phase diagrams of the bulk materials.

In order to illustrate the growth dynamics and material distribution along the particle volume, we consider two miscible compounds, A_1 and A_2, such as iron and cobalt carbonyl. The result should fall into the classes 1 to 3. Precursors decay at different decay rates k_i which entails a high concentration of the less stable precursor in the particle center and a bimetallic particle of class 3 [13]. According to the LaMer model, precursors decay and free monomers B are formed. If concentration and initial concentration are denoted by [•] and $[\bullet]_0$, respectively, the equations of evolution are given by

$$\frac{d[\mathrm{A_i}]}{dt} = -k_\mathrm{i}[\mathrm{A_i}] \tag{4}$$

$$\frac{d[\mathrm{B}]}{dt} = k_1[\mathrm{A_1}] + k_2[\mathrm{A_2}] - k_3[\mathrm{B}] \tag{5}$$

with the solutions (Figure 6)

$$[\mathrm{A_i}] = [\mathrm{A_i}]_0 e^{-k_i t}$$

$$[\mathrm{B}] = \frac{(k_2 - k_3)k_1[\mathrm{A}]_0 + (k_1 - k_3)k_2[\mathrm{B}]_0}{(k_1 - k_3)(k_2 - k_3)} e^{-k_3 t} - \frac{k_1[\mathrm{A_1}]_0}{k_1 - k_3} e^{-k_1 t} - \frac{k_2[\mathrm{A_2}]_0}{k_2 - k_3} e^{-k_2 t}$$

The absolute concentration of the material absorbed by nucleation seeds is $[\mathrm{S}] = [\mathrm{A_1}]_0 + [\mathrm{A_2}]_0 - [\mathrm{B}] - [\mathrm{A_1}] - [\mathrm{A_2}]$ and, therefore, the particle growth rate is given by $v(t) = d[\mathrm{S}]/dt$. Further, the ratio $x = \mathrm{A_1}/\mathrm{A_2}$ of material absorbed at time t

$$x(t) = \left(\frac{d[\mathrm{A_1}]}{dt}\right)\left(\frac{d[\mathrm{A_2}]}{dt}\right)^{-1} = \frac{k_1[\mathrm{A_1}]}{k_2[\mathrm{A_2}]}$$

with the relative compound ratios

$$a_2(t) = \frac{1}{x(t)+1}$$

and

$$a_1(t) = 1 - a_2(t)$$

allows for determination of the inner distribution of the two compounds via integration of the individual growth rates $a_i v$, with respect to time.

In a different approach, monometallic particles are synthesized in a first step and subsequently coated by a second metallic compound which can be realized, e.g., with the successive method described in the LaMer model, by changing the precursor solution during the injections. This approach results in core–shell nanoparticles [36]. Also, it is possible to protect the core of a magnetic particle by different materials, e.g., in order to stabilize the material against oxidation or to allow for the employment of toxic materials in biomedical applications [37,38].

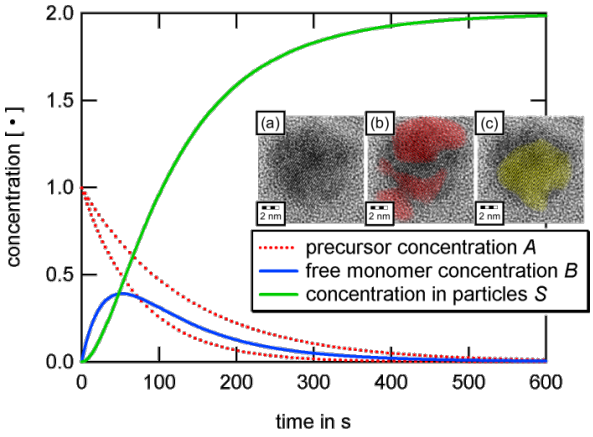


Figure 6: Dynamic evolution of different concentrations for the decay rates k_1 = 0.00753 s^{-1} and k_2 = 0.0136 s^{-1} and k_3 = 0.03 s^{-1} for the respective precursors A_1 and A_2 and the free monomer B. The insets show a high resolution TEM image of a $Fe_{0.47}Co_{0.53}$ nanoparticle (a) which has been synthesized via such an approach. The particle is oriented in bcc (100) direction. The center of the particle consists of a Co enriched alloy ($Fe_{0.44}Co_{0.56}$, marked by a yellow sublattice (c)) while the surface shows a higher Fe content ($Fe_{0.63}Co_{0.37}$, red lattice (b)).

1.3 Magnetic properties

In the subsequent sections, we will mainly focus on magnetic properties of assemblies of nanoparticles. As the components of such assemblies, it is necessary to understand the properties of individual nanoparticles themselves. In comparison to macroscopic objects, nanoparticles have a very high 'surface to volume' ratio and are on the size scale where quantum mechanical effects are increasingly of more importance. Therefore, the magnetization of nanoparticles is dominated by finite size and surface effects [39,40].

The magnetic structure of macroscopic magnetic materials is divided into magnetic domains. Along these domains, magnetic moments have a parallel alignment, different domains are separated by domain walls. In comparison to a homogeneously magnetized object, the formation of domains decreases the magnetostatic energy of the system proportional to the sample volume. However, a certain amount of energy is required for the creation of the domain wall, which is proportional to the domain interface. With the reduction of the sample size, interface effects gain importance until below a critical diameter d_c,

the formation of domains is energetically less favorable. For spherical particles, this critical diameter d_c depends on various material properties such as the exchange constant A, the effective anisotropy constant K_{eff} and the saturation magnetization M_S, and is given by

$$d_c = 18\frac{\sqrt{AK_{eff}}}{\mu_0 M_S^2}$$

where μ_0 is the vacuum permeability.

In this work, we focus on particles of sizes between 5 to 20 nm; the single domain limits of cobalt and iron nanocrystals are on this size scale. The crystalline microstructure introduces energetically favorable easy axes and directions of high energy, hard axes. The magnetization of a free particle aligns with one of the easy axes. In order to switch the magnetization into a different state, a certain energy barrier needs to be overcome. If this energy originates from thermal energy, particles are called superparamagnetic. There are no longer stable magnetization configurations but the magnetic moment permanently switches between different orientations. For uniaxial crystal anisotropy, the superparamagnetic size limit needs to meet

$$k_B T \gg K_{uni} V_{part} \quad (6)$$

where k_B is the Boltzmann constant, T the absolute temperature, K_{uni} the first anisotropy constant and V_{part} the particle volume. In particular, we can directly derive the superparamagnetic radius R_{spm}

$$R_{spm} = \left(\frac{75 k_B T}{4\pi K_{uni}}\right)^{1/3} \quad (7)$$

below which superparamagnetic behavior can be found. For spherical hcp Co particles, this is expected at a diameter of 7.8 nm [13]. Superparamagnetic particles show no hysteresis; their magnetization response to an external magnetic field resembles the Langevin behavior of paramagnetic materials but with the high susceptibility and magnetization values of the ferromagnetic materials they are composed of, compare Figure 7.

With even smaller particles, surface effects become dominant and a fully quantum mechanical treatment is necessary for their description. For example, 60% of all spins of the 1.6 nm fcc Co particles analyzed by Batlle et al. are surface spins [39]. Particles in this size scale lie outwith the scope of this work. We will only consider particles, where the semi-classical treatment is a good approximation.

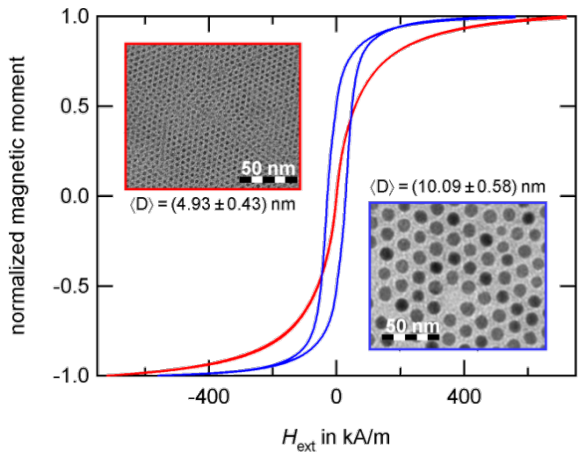


Figure 7: Co particles with a diameter of 4.9 and 10 nm measured at room temperature shortly after the preparation of particles. With the superparamagnetic limit at 7.8 nm [13], the larger particle species (blue) shows a hysteresis while the small particles (red) are superparamagnetic at room temperature.

2. Self-assembled particle structures

The ability of nanoparticles to self-assemble on a substrate has opened the way to many applications such as sputtering masks, magnetic data storage media or sensor devices [41-44]. This interesting phenomena can result in highly ordered regions ranging from monolayers of hexagonally or cubically ordered arrays with sizes between a few square nanometers up to the square micron scale [13,45-47] and to three dimensional superlattices of several cubic millimeters [48,49] as shown in Figure 8. For many applications, a high degree of order on a large scale is essential; we will see an example for this later on in Section 4. In order to obtain such highly symmetric particle patterns, a narrow particle size distribution is essential; the stan-

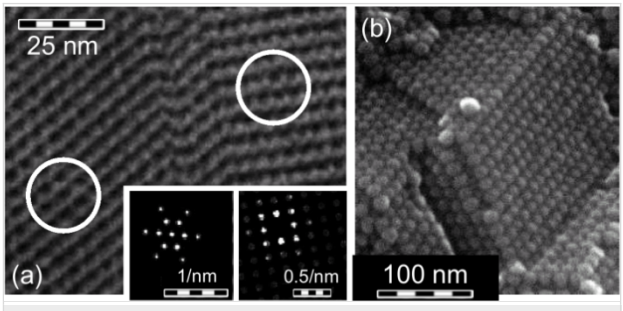


Figure 8: Self-assembled FeCo nanoparticles with different dimensions: (a) The 2D-monolayer of 4.6 nm sized spherical FeCo nanocrystals shows a phase transition from a hexagonal to a cubic lattice symmetry. The FFT patterns are taken from the marked areas. (b) SEM image of a millimetre sized 3D supercrystal composed of FeCo particles with a diameter of 15 nm. The crystal has been broken to show the high degree of order inside. (Figure (b): Reprinted by permission from Macmillan Publishers Ltd: Nature Materials, ref. [48], copyright 2005, http://www.nature.com/naturematerials)

dard deviation should not exceed 10% of the mean value [50-52]. As already mentioned in the preliminary section, bottom-up synthesis methods are well suited for these requirements. In addition, particle size distributions can be further refined via sedimentation or by magnetic separation subsequent to chemical synthesis [15].

2.1 Driving forces to self-assemblies

The organization process is driven by a superposition of interparticle interactions and external forces [47-53]. Interparticle forces act on the nanocrystals in the liquid phase of a particle solution as well as during the assembly process on a substrate. Different forces may have major impact on the resulting assemblies: An attractive potential is given by the van der Waals interaction which is caused by induced electric dipoles and acts along the connection line between them. For two interacting solid spheres Hamaker derived the expression

$$E_{\mathrm{vdW}} = -\frac{A}{12}\left(\frac{4R^2}{(\delta+2R)^2-4R^2}+\frac{4R^2}{(\delta+2R)^2} +2\ln\frac{(\delta+2R)^2-4R^2}{(\delta+2R)^2}\right) \quad (8)$$

for the interaction potential [50-52] with A the Hamaker constant, and R and δ the particle radius and the interparticle distance, respectively (compare Figure 9 (a)).

Repulsive force contributions originate either from electric Coulomb forces or steric repulsion, depending on the nature of the particle stabilization. For instance, spherical particles which are surrounded by a dense ligand shell with non-polar end groups result in a short ranged repulsive potential that can be calculated by the equation of de Gennes [54]

$$E_{\mathrm{steric}} = \frac{100RL^3}{\delta\pi s^3}k_{\mathrm{B}}T_{\mathrm{prep}}\exp\left(-\frac{\pi\delta}{L}\right) \quad (9)$$

where L is the thickness of the ligand shell, s the distance of two neighboring ligand headgroups on the surface of the particle core, T_{prep} the absolute temperature during preparation and k_{B} the Boltzmann constant. This potential strongly depends on the properties of the employed ligand. Therefore, ligands do not only play a key role for the geometrical properties of individual particles but also for the organization of ensembles in superstructures. Figure 9(b) shows the different potential contributions calculated according to Equation 8 and Equation 9, if the parameters of oleic acid stabilized Co nanoparticles with a diameter of 3.3 nm are assumed (T = 400 K, L = 1.17 nm, s = 0.51 nm). The superposition of both potentials results in a total potential with a global minimum. In the example, the particles will assemble at a distance of about δ = 3.6 nm.

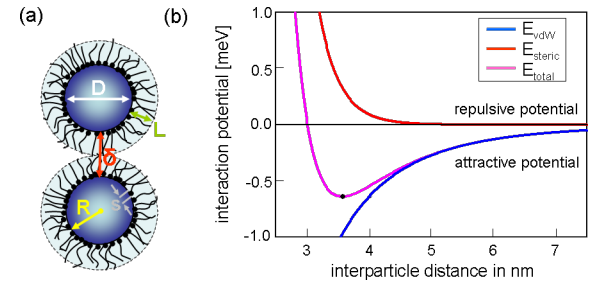


Figure 9: (a) Scheme of two particles with a metallic core of radius R surrounded by a ligand shell of the thickness L, s denotes the required distance of two neighboring ligand head groups on the surface of the particle cores and δ the surface distance between the metallic cores. (b) Total interaction potential calculated from the contributions of the steric repulsion (red) and the attractive van der Waals potential (blue) for two Co nanoparticles of a diameter of 3.3 nm stabilized with oleic acid (L = 1.17 nm, s = 0.51 nm).

For magnetic particles with sizes above the superparamagnetic limit (Equation 7), dipole–dipole interactions between adjacent particles can play a major role during self-assembly. Such ferromagnetic particles mutually align their magnetic dipole moments which entails an attractive coupling and may result in different geometrical patterns such as particle chains or rings [55,56]. An example of a dipole interaction dominated arrangement is shown in Figure 10(a): Co particles with a bimodal size distribution show varying behavior depending on their size. The hcp Co particles of a diameter of 12 nm are above the superparamagnetic limit and self-assemble in chain superstructures while the smaller particles are superparamagnetic and favour a hexagonal ordering.

Recent developments on the directed assembly of nanoparticles under external influences have attracted much interest. Such constraints may arise during the self-assembly process on a substrate or by exerting the particle solution to external electromagnetic fields. Since this topic is not quite within the focus of this work, we will only show a few possibilities.

Convective particle flux may be induced by a hydrodynamic velocity field within the solvent on top of a substrate. The effect is shown in Figure 10(d): a droplet of particle solution with heptane as a solvent was placed on a SiO_2 surface. The spreading of the droplet results in a force onto the particles which entails the assembly close to air–liquid boundary. This allows for a controlled positioning of the particle monolayer within a specified target region (on top of magnetoresistive sensors, between contacts for measurements of electrical transport properties etc.) if the drop parameters such as volume–diameter relation for a specific solvent-substrate combination are

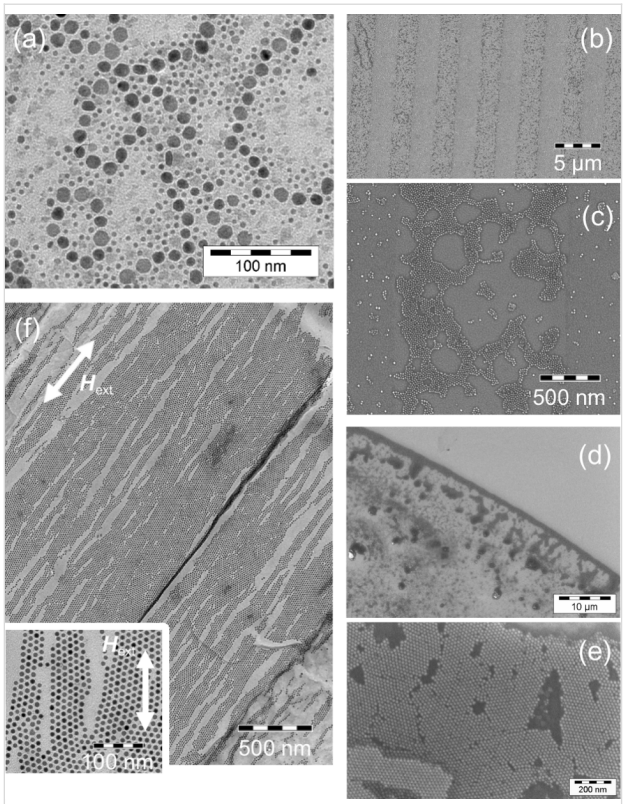


Figure 10: Images of self-assembled spherical Co nanoparticles: (a) TEM image of a bimodal distribution; large particles with a diameter of about 12 nm are ferromagnetic and assemble in ring-shaped superstructures. (b) Influence of the surface properties on the self-assembly; Co particles are predominately arranged along areas which were previously covered with photo resist and (c) detailed image of the particle ordering. (d) SEM images of assemblies under the combined influence of hydrodynamic and capillary forces; the edge of the drop mainly consists of a particle monolayer. (e) Detailed image of the hexagonal network formed by the particles within the monolayer. (f) Particles deposited under the influence of an external magnetic field. The nanocrystals are organized in lines oriented parallel to the direction of the applied field. The inset shows a detailed image of the distorted hexagonal order.

known. Further, capillary forces improve the ordering of the particle monolayer along the edge (Figure 10(e)). This attractive force is caused by the Laplace pressure which arises when a curved meniscus is formed around two adjacent particles during the evaporation of the solvent. Due to the linear dependence of the capillary force on the particle diameter, the action is stronger the larger the particles. Therefore, although suspended in the same solvent, smaller particles show a lower degree of order [49].

Additionally, friction and shear forces can arise between the particles on the one hand and between particles and substrate on the other hand [57,58]. In the latter case, the forces strongly depend on the surface properties such as structure and roughness. Thus, the choice of substrate is another crucial factor for the preparation of homogeneously ordered superlattices on large scales. The influence of different surface conditions is shown in Figure 10(b): A photo resist mask of 2.5 µm wide strips created on top of a Ta layer by optical lithography was employed. After removal of the mask, the substrate was dipped into a particle suspension. Along the formerly resist covered area, a higher particle density can be observed. This effect can be attributed to a strengthened adhesion within the strips due to a modified surface roughness and energy.

In order to obtain a magnetically structured sample, a suspension of ferromagnetic particles can be placed on the substrate in the presence of an external magnetic field. For manufacturing of particle layers, a homogeneous magnetic field needs to be employed; inhomogeneous fields result in the accumulation of nanoparticles along the area where high field gradients can be found [59]. An example of ferromagnetic Co nanocrystals arranged under the influence of a homogeneous magnetic field of 120 kA/m parallel to the substrate plane is shown in Figure 10(f): Particles arrange along lines parallel to the external field which is in contrast to free self-assembly (Figure 10(a)). The magnetic orientation within the nanocrystals is dominated by the external field which results in a distortion of the hexagonal ordering due to repulsive forces between adjacent lines of particles perpendicular to the field direction.

2.2 Influence of the particle geometry

As already discussed in the preliminary section, the particle morphology can be controlled by appropriate ligands. In contrast to spheres, nanocrystals with the shape of (truncated) triangles, facetted particles or hexangular disks have additional rotational degrees of freedom. Figure 11(a) shows a sample of Co particles with a broad distribution of different shapes. In particular, the disk-shaped objects show interesting behavior: They are mainly arranged in long rows of up to 40 disks, stacked face-to-face and standing on their edges. Within the two-dimensional TEM image, disks resemble the shape of rods. However, on tilting the sample, they may easily be identified as nanodisks [10,15]. A more detailed analysis of the rows reveals a size gradient along the superstructures; disks of larger radius are placed further towards the center [51]. Individual rows of disks propagate in a random direction and adherent rows tend to align with each other in areas of high concentration [10,60].

The arrangement of disks is not yet completely understood. The minimization and size dependence of the van der Waals contribution are supposed to be the main driving forces for the spatial arrangement [15,51] and the size distribution along the chains [51]. Bao et al. explained the formation of disk rows by a hydrophobic interaction between the ligand tails, thus, minimizing exposure to air by maximizing the contact between the

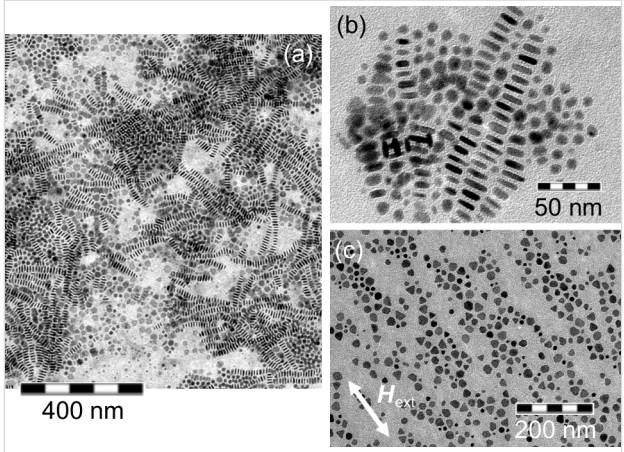


Figure 11: TEM images of self-assembled Co particles with different morphologies. Nanodisks exhibit a typical thickness to diameter ratio of 1:3 and organize mainly in rows of standing disks. Three-dimensional superstructures can be observed when two rows of disks cross each other (a). Assemblies of Co nanodisks deposited on a TEM grid (b) without and (c) under the influence of an external magnetic field of H_{ext} = 160 kA/m applied parallel to the substrate plane.

ligand tails [60]. Due to the magnetic nature of the Co disks, a magnetic origin for the formation of rows is also under discussion. Under the influence of strong shape anisotropy, the magnetization direction is confined within the disk plane which was believed to entail an antiferromagnetic configuration in order to minimize the magnetic stray field along a particle row [15,46]. However, in 2006, Gao et al. [61] performed electron holography experiments on magnetic Co disks which reveal a spiral-like arrangement of individual moment vectors around the row propagation axis.

Similar to the situation of spherical magnetic particles, the orientation of such disks can be controlled by the application of an external field during the deposition [15]. Figure 11(b) shows a typical arrangement of nanodisks if no external field was applied during the self-assembly. By applying an in-plane magnetic field of 160 kA/m, the configuration shown in Figure 11(c) is obtained. This allows for several conclusions: a) The disk plane coincides with the magnetically easy plane of the nanocrystals and b) the driving forces responsible for the self-organization process may be overcome by the magnetic interactions induced by the homogeneous external field.

3. Magnetically interacting nanoparticles

As already demonstrated in the preliminary section, different types of interactions entail self-organization processes of magnetic nanoparticles in chains or monolayers depending on the geometry of magnetic objects and external constraints. However, once the geometric configuration has reached an equilibrium state, remagnetization processes along the assembly become the dominating dynamics. Since small magnetic objects do not have an inner magnetic substructure but the magnetization is homogeneously distributed along the volume, the stray field at a point **r** of a magnetic nanoparticle with magnetic moment **m** situated in the origin is given by the dipolar expression [62]

$$\mathbf{H}_{\text{dipole}} = \frac{1}{4\pi}\left(\frac{3\langle \mathbf{m},\mathbf{r}\rangle \mathbf{r}}{|\mathbf{r}|^5} - \frac{\mathbf{m}}{|\mathbf{r}|^3}\right) \tag{10}$$

with $\langle \bullet , \bullet \rangle$ the Euclidean inner product. A schematic representation is shown in Figure 12(a). Adjacent particles influence each other via their dipolar coupling. Strong interactions can be found in such assemblies which even cause agglomerations of superparamagnetic components to show hysteretic behavior.

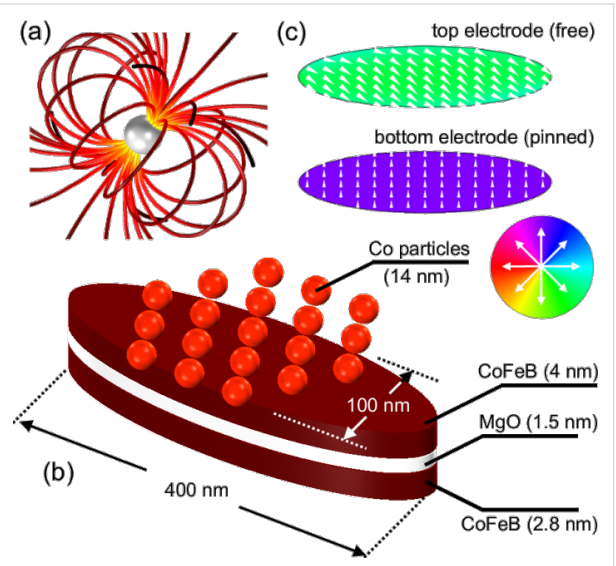


Figure 12: Schematic representation of the tunnel magnetoresistance (TMR) sensor setup for the detection of multiple Co nanoparticles of 14 nm diameter: (a) Stray field of a homogeneously magnetized particle, (b) TMR-sensor with particles on top, (c) magnetic equilibrium state of the ferromagnetic electrodes.

3.1 Direct observation of dipolar coupling

In order to analyze the magnetic properties of assemblies of magnetic nanoparticles, tunneling magnetoresistive (TMR) sensors are employed. The schematic configuration of a TMR sensor is shown in Figure 12(b): Two thin ferromagnetic films are separated by an insulating barrier [63]. If the TMR sensor is positioned in an external magnetic field and a bias voltage is applied across the stack, then a quantum mechanical tunneling current flows across the insulator barrier. The resistance of the TMR sensor depends on the relative orientation of the magnetization within the two ferromagnetic layers [64]. A perturbation field introduced by a single magnetic particle or by an assembled monolayer of them entails a variation of the magnetization

distributions in both electrodes which leads to a change of the measured resistance. Depending on the resistance change, different conclusions on the configuration on top of the sensor surface may be drawn. In order to enhance the effect and to allow for a wide range of applications, the top electrode is usually chosen magnetically soft to be easily influenced by magnetic field variations to be detected, while the bottom (reference) layer is magnetically hard and, ideally, cannot be switched by external perturbations.

The experimental setup employed here consists of two CoFeB layers that are separated by an MgO barrier. The geometric and magnetic configuration of the sensor is chosen to allow for a precise measurement of single magnetic beads and nanoscale objects: We employ elliptically shaped sensors with longitudinal and lateral dimensions of 400 and 100 nm, respectively. The magnetic configuration within the top electrode is free to rotate while magnetization of the lower CoFeB layer is fixed by an artificial antiferromagnet. From micromagnetic simulations, we can conclude the equilibrium magnetic configuration of the free sensing layer: Without any external influences, the magnetization would align parallel to the long ellipse axis. However, due to the stray field of the pinned bottom electrode the magnetization orientation is tilted towards an antiparallel configuration with respect to the reference layer (Figure 12(c)). For a more detailed description on the sensor configuration, fabrication and properties, see [65,66]. The interplay between geometrical shape anisotropy and stray field coupling of the layers entails a resistance change which is linearly connected to the strength of an external magnetic field in a field range of ±40 kA/m. Thus, such sensors are well suited for the detection of multiple particles. Due to the linearity in the response, we expect a signal proportional to the number of particles deposited on top of the sensor surface.

For the experimental realization, 14 nm Co particles were deposited on top of the sensor via a dropping procedure which results in random particle distributions along the surface. In order to compare different sensors, we analyze the relative change

$$\Delta\mathrm{TMR} = \frac{R_{\mathrm{particle}} - R_{\mathrm{sensor}}}{R_{\mathrm{sensor}}} \qquad (11)$$

with the respective resistances R_{particle} and R_{sensor} for the situations with and without particles on top. The experimental measurements are shown in Figure 13(a) (red markers). For a very small number of particles, the measured signal is below the electric noise ratio of the device and no detection is possible. Once a critical detection threshold is exceeded, a linear

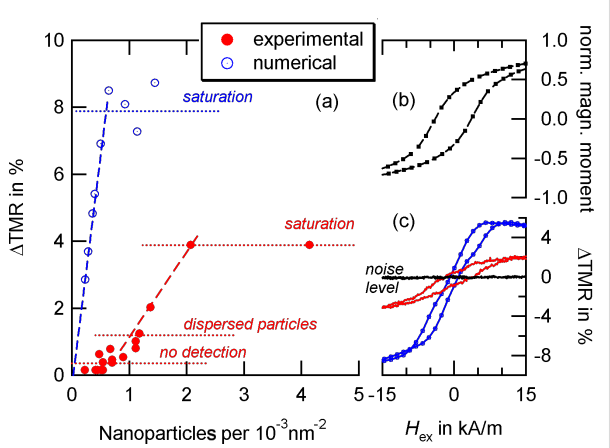


Figure 13: Properties of the magnetoresistive sensors. (a) Comparison between experimental and numerical data. The magnetic properties of the 14 nm Co particles obtained by AGM measurements (b). The coercive field H_C = 3.76 kA/m entails a hysteretic ΔTMR-signal (c) due to the detection of nanoparticles that interact by dipolar coupling.

increase, corresponding to the degree of coverage, can be reported, as expected. With the dipolar coupling strength decaying by $1/r^3$, the distance between nanoparticles proves crucial for the observed behavior. In particular, if particles are freely dispersed on the top of the sensor and sufficiently far apart from each other, the induced magnetic moment resembles the intrinsic anisotropy of the nanoparticle [67]. The detected signal shows no hysteresis which reveals the superparamagnetic nature of the nanoparticles. Moreover, the intensity of the detected signal increases linearly with the number of particles situated on the sensor surface; similar results have been reported by Wang and Li [68]. With decreasing particle distances, the significance of dipolar coupling increases. A manifestation of this type of interaction is the induced hysteresis in the detection signal. The coercive field of the ΔTMR-hysteresis loop coincides with the coercive field measured by an alternating gradient magnetometer (AGM). Once a second critical value is exceeded, no further increase can be reported; the signal remains constant.

In order to understand the experimental observations, the findings are compared to numerical simulations: Particles are assumed to be organized along a hexagonal grid on top of the sensor as shown in Figure 12(b); the surface concentration is modified via the adjustment of the lattice parameter. The magnetodynamics of N homogeneously magnetized particles are governed by a set of ordinary differential equations [69,70]

$$(\mathbf{Id} - \alpha\mathbf{M})\frac{\partial \tilde{\mathbf{m}}}{\partial t} = \gamma\mathbf{M}\tilde{\mathbf{H}}_{\mathrm{eff}} \qquad (12)$$

where **Id** is the $3N \times 3N$ identity matrix, γ the gyromagnetic ratio, α the empirical damping coefficient and further the block diagonal matrix **M**

$$\mathbf{M} = \begin{pmatrix} M_1 & & 0 \\ & \ddots & \\ 0 & & M_N \end{pmatrix}$$

where $M_n = \varepsilon_{ijk}\hat{m}_{n,j}$, $n = 1, \ldots, N$, and the vectors

$$\frac{\partial \tilde{\mathbf{m}}}{\partial t} = \frac{\partial}{\partial t}(\hat{m}_{x,1}, \hat{m}_{y,1}, \hat{m}_{z,1}, \hat{m}_{x,2}, \ldots)^{\mathrm{T}}$$

$$\tilde{\mathbf{H}}_{eff} = (H_{eff,x,1}, H_{eff,y,1}, H_{eff,z,1}, H_{eff,x,2}, \ldots)^{\mathrm{T}}$$

.

For the effective magnetic field, we restrict our analysis to pure dipolar coupling. Therefore, each magnetic moment evolves under the influence of the superposed stray fields of adjacent particles. Due to a $1/r^3$-decay, it is sufficient to neglect the interaction of particles with a distance more than five times the average particle radius [71]. By integrating Equation 12 and employing the solution of the equilibrium configuration for micromagnetic simulations of the free sensing layer, the data shown in Figure 13(a) (blue markers) are obtained.

In qualitative agreement to the experimental observation, a linear increase for low surface coverage can be found while for high concentrations the signal becomes stationary (Figure 13(a)). Further, the ΔTMR-response shows a hysteretic behavior (Figure 13(c), blue line). Quantitatively, the numerical data predict a sensor response which is about double the value at half the particle concentration in comparison to the experimental findings. Also, the hysteretic signal observed in the experiments is about double the theoretical value. These particular deviations may be attributed to the highly idealized particle distribution on top of the sensor: According to the preliminary section, (ferro-)magnetic particles form self-assembled structures and agglomerations in the liquid phase (Figure 10(a)). Therefore, the degree of clustered nanocrystals is much higher in the experimental situation, in particular, if a high number of particles is deposited on top of the sensor surface.

This observation allows for different conclusions: a) A linear increase in the ΔTMR-response originates from dispersed particles which are sufficiently far away from other objects and, therefore, their magnetism is dominated by external fields prior to interparticle coupling. b) In the high concentration regime, dipolar coupling plays the major role for the dynamic processes and the equilibrium configuration of magnetic particles assembled in monolayers.

3.2 Transport properties

By embedding magnetic nanoparticles in non-magnetic matrices, they form the components of granular systems which reveal spin-dependent transport phenomena. Depending on the material of the interparticle matrix, different effects may occur: Conducting matrices result in giant magnetoresistance (GMR), the use of an insulating material in tunneling magnetoresistance effects. Ever since the discovery of the GMR-effect in granular Co/Cu-systems in 1992 by Xiao et al. [72] and Berkowitz et al. [73], numerous preparation methods have been introduced. Typically, granular materials are prepared by top-down methods such as co-sputtering or co-evaporation of matrix and precipitated materials as well as by metallurgic techniques [74-78].

A first bottom-up approach for the preparation of granular structures is based on the simultaneous deposition of particles, which are prefabricated in the gas phase, and the matrix material on a cold surface [79]. This approach has allowed for the avoidance of paramagnetic impurities within the matrix material and for the investigation of the dependence of the magnetoresistance effects on the particle size and volume ratios for different material systems [79-81]. Recently, Tan et al. showed that chemically synthesized, ligand stabilized nanoparticles can also be used for a bottom-up preparation of granular TMR systems [8,9]. An electrically isolating ligand shell acts as a tunneling barrier. TMR amplitudes of up to 3000% at low temperatures have been reported in such granular three-dimensional self-assembled supercrystals consisting of FeCo nanparticles (compare Figure 8(b)).

In our work, we focus on the resulting transport properties of two-dimensional monolayers of Co nanocrystals embedded in a conducting matrix. Therefore, 8 nm Co particle assemblies have been created in a dropping procedure as described in Section 2. After the self-assembly process, the insulating ligand shells were removed by heating the particles for approximately 4 h at 400 °C in a reducing gas atmosphere. Subsequently, a thin Cu layer was deposited on top of the nanocrystals. The measurements were taken at room temperature via a four-point-measurement geometry; the results are shown in Figure 14: A GMR-amplitude of about 4% was observed with a bell shaped measurement characteristic.

In order to get a first qualitative understanding of the observed behavior, AGM measurements on the particles were carried out to determine the magnetic properties of the nanocrystals. As shown in Figure 14, the Co particles mainly exhibit a superparamagnetic behavior, their response to an external magnetic field

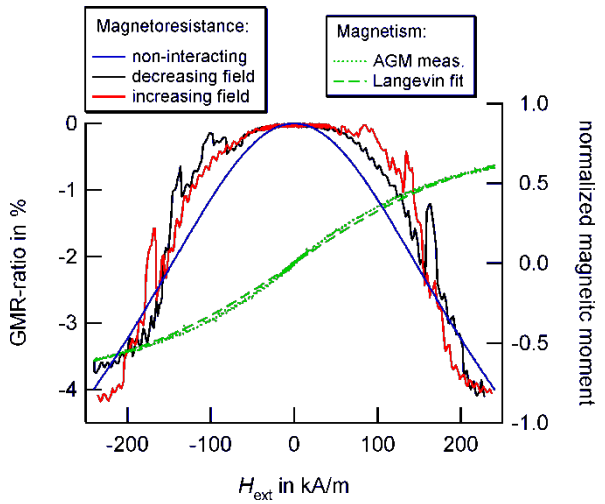


Figure 14: GMR response of a monolayer consisting of 8 nm Co particles covered by a thin Cu film. Measurements were taken at room temperature with a sample current of 1 mA and an in-plane external magnetic field. In comparison to the prediction of non-interacing particles, the experiments show additional features at field values of about ±176 kA/m, ±136 kA/m and ±88 kA/m.

follows the Langevin function. For non-interacting particles, the magnetization reversal may be employed to deduce the expected magnetoresistance characteristic in granular structures by

$$\mathrm{GMR} = -A\left(\frac{M}{M_\mathrm{S}}\right)^2 \qquad (13)$$

where A is the effect amplitude [78]. By comparison of the expected behavior according to Equation 13 and the experimental results (see Figure 14), additional features can be found in the measurements. Such features appear symmetrically for in- and decreasing external field strength and may be attributed to a dipolar coupling induced magnetic reversal of large coupled areas and, thus, the inner magnetic structure of the particle assemblies.

As we will see in Section 4, the orientations of magnetic moments in such two-dimensional assemblies are correlated along domains with an antiparallel orientation similar to ferromagnetic materials. Consequently, the evolution of the magnetic configuration strongly depends on the history of the magnetic pattern and repeated measurements made under identical conditions may result in significantly deviating findings. An example obtained from a self-assembly of ferromagnetic Co nanocrystals (see Figure 10(e)) is shown in Figure 15: The first measurement (Figure 15(a)) resembles the behavior of non-interacting particles. On the microscopic level, the degree of

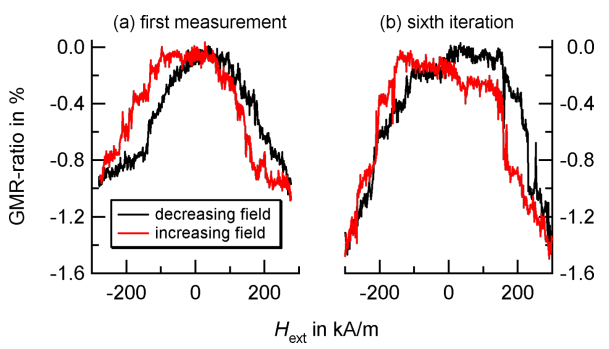


Figure 15: Magnetoresistance measurements at room temperature on a granular system consisting of Co nanoparticles with a mean diameter of ‹D› = (14.9 ± 0.4) nm covered with a 4 nm thick Cu-layer. The measurements have been taken from a series (a) at the very beginning and (b) after six runs.

correlation is very low and each magnetic moment exhibits a Langevin-like behavior. Due to the induced formation of domains, subsequent measurement increase the degree of dipolar coupling which entails a strong correlation between adjacent moments. The changes in the GMR-ratio occur stepwise, in particular, a broad plateau around $H_{ext} = 0$ may be reported. This observation corresponds to an antiparrallel arrangement of magnetic moments which maintains stability against external influences.

4. Particle based magnetoresistive sensors

In a similar way as a small magnetoresistive sensor opens techniques for the design of a magnetic microscope in order to detect magnetic beads and particles and to evaluate spatial coordinates [82], an analogous approach should be possible for two-dimensional assemblies of magnetic nanoparticles. The principal idea in both strategies is very similar: An undisturbed reference configuration is exerted to some sort of perturbation which results in a variation of the magnetic configuration and, consequently, in a measurable resistance change. Since the measured signal depends on the magnetic field along the sensor area, it is possible to conclude the properties of the source. The key difference between the two approaches is a direct consequence of the governing Equation 12 for the evolution of discrete magnetic moments and the continuous equations for micromagnetic systems [83,84]: As shown in Figure 16, four discrete magnetic moments arranged along the corners of a square tend to align in a vortex-like state in order to minimize the total stray field energy of the system. Such behavior is not possible for ferromagnetic systems on the nanoscale. The interatomic exchange energy entails a strong confinement between neighboring spins which results in a strong magnetic stiffness on the mesoscale. Therefore, magnetic domains can only be found above a certain geometrical size scale; this is also the reason why the electrodes of the sensors discussed in Section

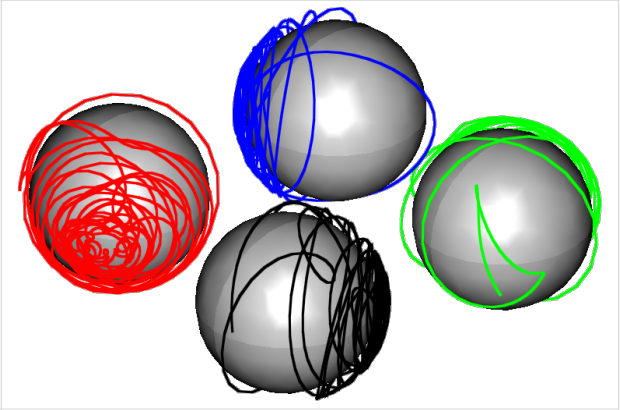


Figure 16: Magnetization evolution of four interacting magnetic dipoles arranged in the corners of a square with side length a = 15 nm. Dipole strengths are chosen equivalent to nanoparticles of radius R = 5 nm and M_S = 200 kA/m, the damping constant is set to α = 0.02. The stable equilibrium is reached after a timescale of 100 ns and is comparable to a vortex state which entails a very low stray field energy.

3.1 show no domain substructure. Due to such stiffness, elements are no longer sensitive to small field variations, which is one of the major challenges to overcome when downscaling magnetoresistive sensors below the micron range [85]. By employing assemblies of superparamagnetic particles, the confinement is broken in the most intuitive way - by spatial separation. Each particle forms its own magnetic domain, coupled to particles nearby via dipolar interactions [86]. This setup allows for localized switching of single magnetic moments and, therefore, forms a promising strategy for the design of increasingly smaller sensors. However, in order to guide future experiments and design new applications, a thorough analysis of the resulting properties is necessary. Therefore, in this final paragraph, we will study the response properties of these assemblies by solving the micromagnetic equations.

4.1 Equilibrium states and response functions

As already demonstrated in the preliminary sections, individual magnetic moments are coupled to their neighbors via their dipolar stray fields. In contrast to the exchange coupling within a ferromagnetic material, such electromagnetic interaction entails an antiparallel correlation within the 10 × 10-particle array as shown in Figure 17 for the example of a cubic and a hexagonal grid: The out-of-plane components of the equilibrium moment distribution may be neglected. Therefore, the color code resembles the in-plane direction of the magnetic moment of each individual particle. The degree of local ordering varies between the two different grid types: A cubic symmetry decomposes into vortex-like substructures as shown in Figure 16. Close to the cluster edges, antiparallel moment loops are formed with the moment direction orthogonal to the boundary normal. Such elementary vortices are very stable against external influences which results in a hysteretic magnetization response as shown in Figure 17(c). Contrary, hexagonal assemblies show almost no hysteresis which is due to a different equilibrium state. Within the hexagonal lattice, magnetic domains are formed (Figure 17(b), highlighted areas) similar to the domain formation in ferromagnetic materials. However, the correlation leads to an antiparallel alignment where the magnetization direction follows lines of adjacent neighbors; the geometrical symmetry introduces a magnetic anisotropy. Consequently, the response of such setups to an external perturbation strongly depends on the direction of the applied magnetic field. Figure 18 shows the dependency of the susceptibility χ on the direction of an in-plane magnetic field for small particle assemblies. For cubic symmetry, the magnetically soft axes correspond to the grid vectors. Similar to the GMR measurements shown in Figure 14 where features occurred symmetrically for in- and decreasing field strengths,

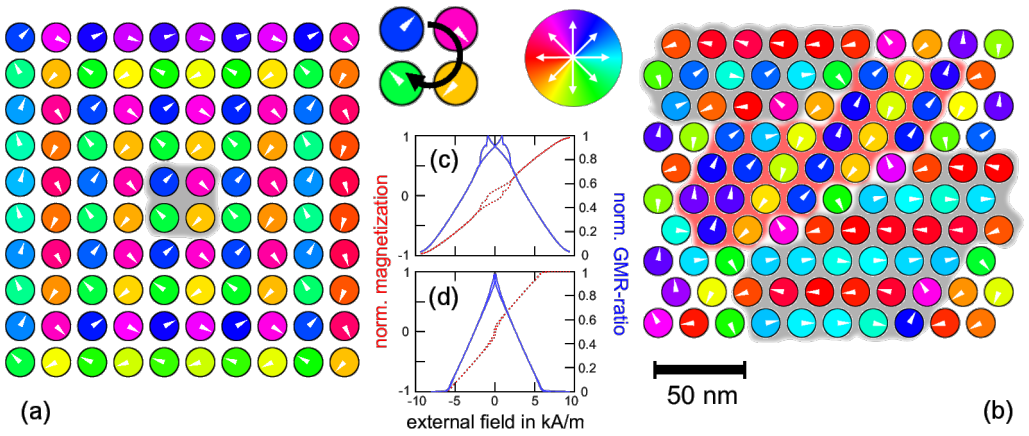


Figure 17: Equilibrium states of 10 × 10-particle arrays with cubic and hexagonal symmetry. Magnetic moments in cubic particle assemblies align in vortex-like 2 × 2-states while hexagonal symmetries entail domains of antiparallel ordering. The stability of the vortex states against external perturbations result in a hysteretic magnetization/GMR behavior, while hexagonal arrays have a linear behavior.

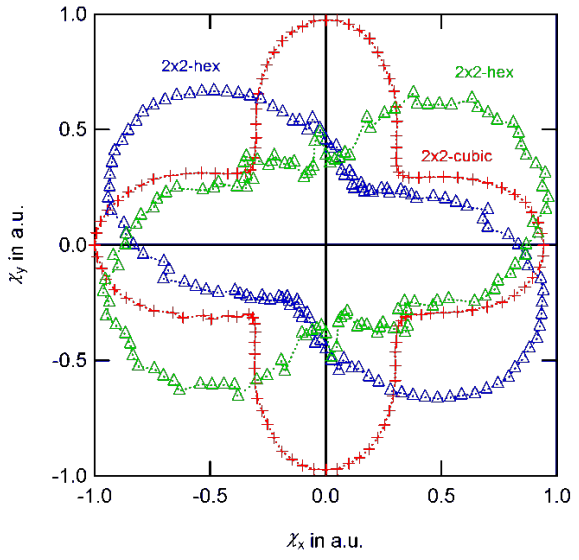


Figure 18: Direction dependent responses of different small particle assemblies to an external magnetic field. 2 × 2-grids align their magnetic moments in vortex-like states as shown in Figure 16. For cubic symmetry, the susceptibility is "degenerated" and independent of the vortex orientation. For hexagonal grids clock- and counter clockwise orientation entail different responses.

the response function χ is conserved and under a field rotation of 180°. For larger patterns, geometrical properties such as spatial configuration, the shape of the boundary or lattice distortions as well as the internal magnetic structure have a major impact and may result in various features.

The GMR ratio of such a magnetic pattern may be calculated according to V. Wiser as [87]

$$\mathrm{GMR} = 1 - \frac{C}{2}\langle 1 + \cos\theta \rangle^2 \qquad (14)$$

where the constant C is a measure for the spin dependence of electron scattering and θ the angle between adjacent magnetic moments. For the sake of simplicity, we will set $C = 1$ in the following. Due to the antiparallel alignment and domain formation, a high degree of magnetic disorder is obtained if there is no external magnetic field applied. Therefore, the equilibrium state entails a high resistance according to Equation 14. Under the influence of a magnetic field, a configuration of increasing order and decreasing resistance is obtained as we already learnt from the above transport measurements.

These observations form the conceptional basis of a granular giant magnetoresistance (gGMR) sensor. The stray field of a magnetic bead outside the assembly results in the partial alignment of the magnetic moment vectors; the degree of alignment depends on the position and the material parameters of the external object.

4.2 Spatial resolution properties

In order to analyze the capability of a two-dimensional particle assembly as a gGMR sensor, we consider a similar hexagonal particle patch as shown in Figure 17. The equilibrium state of the magnetization is calculated by solving Equation 13 under the influence of an additional probe particle P modeled by Equation 10. We denote the centre coordinates of P by $\mathbf{r}_P$, the radius by R_P and the magnetization by M_P. For the evaluation of the position influence, the particle centre is placed along the nodes of a discrete grid, with grid nodes at

$$x_P = \{-200\ \mathrm{nm} + i \bullet 8\ \mathrm{nm},\ i = 0, \ldots, 50\}$$

$$y_P = \{-200\ \mathrm{nm} + j \bullet 8\ \mathrm{nm}, j = 0, \ldots, 50\}$$

$$z_p = 100\ \mathrm{nm}$$

For a first analysis of the response properties, we make two simplifying assumptions: a) we can manipulate the magnetism of the probe particle without influencing the particle assembly itself and b) we can directly deposit the particle at a certain node point. The first assumption is legitimate if a magnetization perpendicular to the sensor plane is imposed. From simulations, we learn that the susceptibility χ_z is very small; an external magnetic field employed to bring particles into saturation only has a small effect on the magnetization distribution within the particle assembly due to the strong in-plane confinement. For in-plane components, this is no longer true. Therefore, these simulations may only be taken as a first estimation on the expected behavior. Further, the second assumption is not valid in the experimental situation. The iterative measurements on identical systems have revealed a strong dependency on the history of the magnetic state (Figure 15). We will not use this simplification in Section 4.3 in order to estimate the impact of hysteresis within these setups.

By solving Equation 12 for the probe particle at a certain grid point the respective GMR value can be calculated from the solution according to Equation 14. The results are shown in Figure 19 for a 10 × 10-hexagonal gGMR sensor consisting of $R = 8$ nm particles of a magnetization $M = 1000$ kA/m; values in between the discrete nodes are obtained by linear interpolation. The probe particle is chosen with radius $R_p = 50$ nm and a magnetization half, identical and double to sensor components. By such variation of the perturbation strength, we may identify two different characteristic behaviors/measuring modes of the granular sensor:

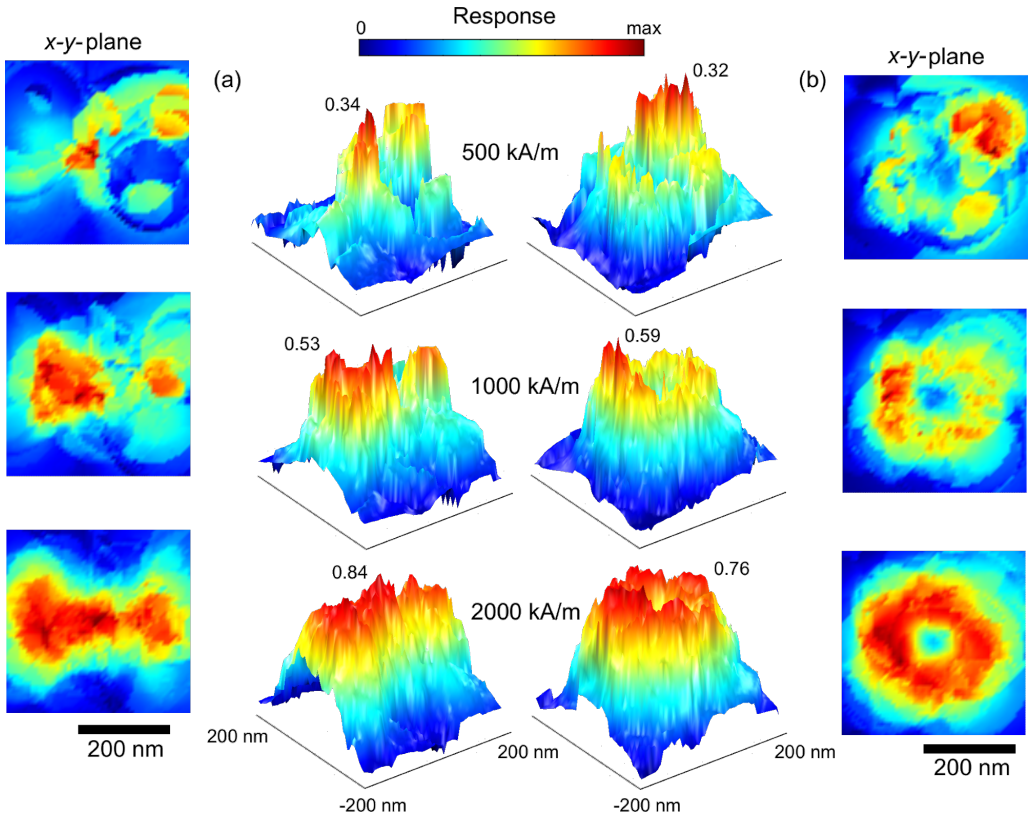


Figure 19: Response maps of a 10 × 10-hexagonal gGMR sensor for a probe particle with R_p = 50 nm and M_p = 500 (top), 1000 (middle) and 2000 kA/m (bottom); (a) shows the response for $\mathbf{m}_p \parallel \hat{\mathbf{x}}$ and (b) the results for $\mathbf{m}_p \parallel \hat{\mathbf{z}}$.

For a magnetic particle with a sufficiently strong magnetic moment (Figure 19, bottom), the response surface resembles the crosscut of the particle stray field. The influence of the particle is strong enough to overcome the interparticle dipolar coupling within the sensor which results in global switching of the entire plane and, consequently, in very high response ratios. For very low particle strengths (equivalent to particles very far away from the sensor), the coupling within the particle plane remains dominant. The imprint of the stray field may still be identified but in common with MR sensors, it will fall below the noise value of the device. However, here the major advantage is revealed. Along the sensor, regions of high response sensitivity are present which enable the detection of much smaller magnetic fields.

Further, the results also reveal that the reduced stiffness is bought at a certain cost: In contrast to similar response maps for TMR sensors [65], the gGMR maps are not smooth. The discrete particle assembly entails an inherent "deterministic" noise contribution which was also present in the experimental realization (compare Figure 14 and Figure 15). These additional features originate from localized switching events and the discrete spatial structure of the gGMR sensor.

4.3 Hysteretic particle monitoring

A major advantage of the gGMR sensor lies in the strong capability of the magnetization distribution to perform local switching. Therefore, the assumption of directly placing the particle at a certain node point allows for a first qualitative understanding of the expected results but will not resemble the quantitative situation particularly well. In order to obtain a first estimation on the importance of hysteretic behavior, we assume the probe particle to travel from one side of the sensor the other one along

$$x_P = \{-250\ \text{nm} + i \bullet 2.5\ \text{nm},\ i = 0, \ldots, 200\}$$

$$y_P = 0\ \text{nm}$$

$$z_p = 100\ \text{nm}$$

The resulting set of equations is solved in same way as before. The results are shown in Figure 20. Intuitively, it could be expected that memory effects gain importance, the higher the magnetic moment of the source to be detected. In general, the numerical results show that this assumption is not true (compare Figure 20, 2000 kA/m). Instead, above a critical threshold,

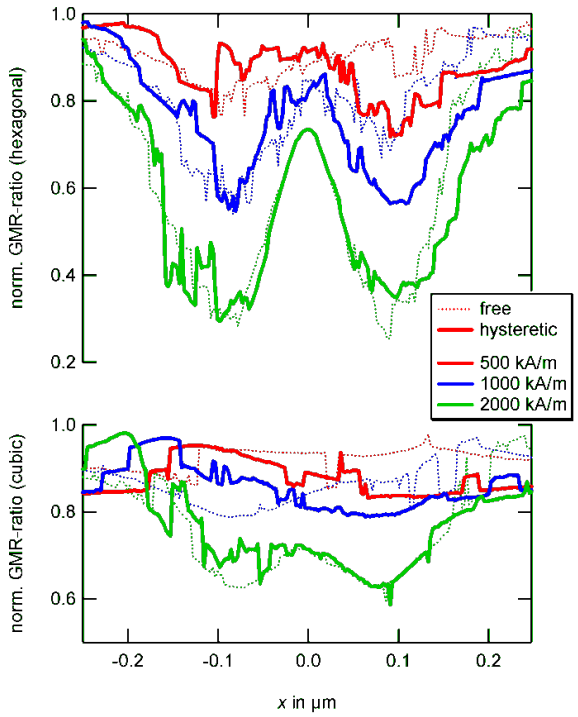


Figure 20: Comparison between free (dotted) and hysteretic (line) sensor behavior for cubic and hexagonal symmetries. Due to stable vortex-like states, the overall effect is smaller for the cubic assemblies. For high particle moments, hysteretic and non-hysteric responses show only small deviations.

interparticle coupling is diminished and the hysteretic behavior resembles the non-hysteretic situation. Independent of the particle position, a switching along large areas of the sensor takes place.

A different observation can be made for lesser source impacts: If the particle migrates along a path where no areas of enhanced sensitivity are crossed, only small deviations in the hysteretic and non-hysteretic response can be found. However, by passing a hot spot in the gGMR map, a permanent change in the magnetic configuration is entailed and consequently, a discontinuous jump in the gGMR response is the result (compare Figure 20, cubic, 500 kA/m; 1000 kA/m); the measured value evolves from there on along a different branch.

Conclusion

We have shown how magnetic particles synthesized by bottom-up methods may form the components for granular GMR sensors. Due to their narrow size distribution, various preparation methods allow for the manufacturing of long scale, highly symmetric monolayers of magnetic nanocrystals. Along these assemblies, dipolar coupling is the dominating driving force for their magnetic properties and the resulting behavior of the ensemble. Embedded in a non-magnetic matrix, a spin-dependent transport occurs which forms the conceptional basis of the gGMR sensor. Due to spatial separation of individual nanoparticles and the entailed missing of exchange coupling, the magnetic stiffness of ferromagnetic thin film systems is overcome and areas of enhanced sensitivity are introduced along the sensor surface. A thorough analysis of these hot spots and the different possible switching states will prove key in the future development of the gGMR approach to the design of nanoscale detection devices.

Acknowledgements

The authors affiliated with Bielefeld University would like to thank the SFB613 and the FOR 945 for financial support in the framework of the project K3 and 3, respectively. Furthermore, the authors would like to acknowledge H. Rösner (INT, Forschungszentrum Karlsruhe) for the high-resolution TEM analysis of the FeCo nanoparticles.

References

1. Reiss, G.; Hütten, A. *Nat. Mater.* **2005,** *4,* 725–726. doi:10.1038/nmat1494
2. Pamme, N. *Lab Chip* **2006,** *6,* 24–38. doi:10.1039/b513005k
3. Loureiro, J.; Ferreira, R.; Cardoso, S.; Freitas, P. P.; Germano, J.; Fermon, C.; Arrias, G.; Pannetier Lecoeur, M.; Rivadulla, F.; Rivas, J. *Appl. Phys. Lett.* **2009,** *95,* 034104. doi:10.1063/1.3182791
4. Sun, S.; Weller, D. J. *Magn. Soc. Jpn.* **2001,** *25,* 1434.
5. Wang, S.; Yue, F. J.; Wu, D.; Zhang, F. M.; Zhong, W.; Du, Y. W. *Appl. Phys. Lett.* **2009,** *94,* 012507. doi:10.1063/1.3059571
6. Zeng, H.; Black, C. T.; Sandstrom, R. L.; Rice, P. M.; Murray, C. B.; Sun, S. *Phys. Rev. B* **2006,** *73,* 020402. doi:10.1103/PhysRevB.73.020402
7. Wen, T.; Liu, D.; Luscombe, C. K.; Krishnan, K. M. *Appl. Phys. Lett.* **2009,** *95,* 082509. doi:10.1063/1.3213561
8. Tan, R. P.; Carrey, J.; Desvaux, C.; Grisolia, J.; Renaud, P.; Chaudret, B.; Respaud, M. *Phys. Rev. Lett.* **2007,** *99,* 176805. doi:10.1103/PhysRevLett.99.176805
9. Tan, R. P.; Carrey, J.; Respaud, M.; Desvaux, C.; Renaud, P.; Chaudret, B. *J. Magn. Magn. Mater.* **2008,** *320,* L55–L59. doi:10.1016/j.jmmm.2007.11.010
10. Puntes, V. F.; Krishnan, K. M.; Alivisatos, A. P. *Science* **2001,** *291,* 2115–2117.
11. Puntes, V. F.; Krishnan, K. M.; Alivisatos, A. P. *Appl. Phys. Lett.* **2001,** *78,* 2187. doi:10.1063/1.1362333
12. LaMer, V. K.; Dinegar, R. H. *J. Am. Chem. Soc.* **1950,** *72,* 4847–4854. doi:10.1021/ja01167a001
13. Hütten, A.; Sudfeld, D.; Ennen, I.; Reiss, G.; Hachmann, W.; Heinzmann, U.; Wojczykowski, K.; Jutzi, P.; Saikaly, W.; Thomas, G. *J. Biotechnol.* **2004,** *112,* 47–63. doi:10.1016/j.jbiotec.2004.04.019
14. Nakamoto, K. *Infrared Spectra of Inorganic and Coordination Compounds;* Wiley: New York, 1963.
15. Puntes, V. F.; Zanchet, D.; Erdonmez, C.; Alivisatos, A. P. *J. Am. Chem. Soc.* **2002,** *124,* 12874–12880. doi:10.1021/ja027262g
16. Peng, X.; Manna, L.; Yang, W.; Wickham, J.; Scher, E.; Kadavanich, A.; Alivisatos, A. *Nature* **2000,** *404,* 59–61. doi:10.1038/35003535

17. Soulantica, K.; Maisonnat, A.; Senocq, F.; Fromen, M. C.; Casanove, M. J.; Chaudret, B. *Angew. Chem.* **2001,** *113,* 3071–3074. doi:10.1002/1521-3757(20010817)113:16<3071::AID-ANGE3071>3.0.CO;2-Q
18. Langevin, D. *Annu. Rev. Phys. Chem.* **1992,** *43,* 341–369. doi:10.1146/annurev.pc.43.100192.002013
19. Tan, W.; Santra, S.; Zhang, P.; Tapec, R.; Dobson, J. Coated Nanoparticles. U.S. Patent 6,548,264 B1, April 15, 2003.
20. Carpenter, E. E.; Seip, C. T.; O'Connor, C. J. *J. Appl. Phys.* **1999,** *85,* 5184. doi:10.1063/1.369118
21. Liu, C.; Zou, B.; Rondinone, A. J.; Zhang, Z. J. *J. Phys. Chem. B* **2000,** *104,* 1141–1145. doi:10.1021/jp993552g
22. Arakaki, A.; Nakazawa, H.; Nemoto, M.; Mori, T.; Matsunaga, T. *J. R. Soc. Interface* **2008,** *5,* 977–999. doi:10.1098/rsif.2008.0170
23. Bazylinski, D. A.; Schüler, D. *Microbe* **2009,** *4,* 124–130.
24. Bazylinski, D. *Chem. Geol.* **1996,** *132,* 191–198. doi:10.1016/S0009-2541(96)00055-1
25. Matsunaga, T.; Okamura, Y. *Trends Microbiol.* **2003,** *11,* 536–541. doi:10.1016/j.tim.2003.09.008
26. Matsunaga, T.; Arakaki, A.; Webb, J. *J. Biochem.* **2003,** *278,* 8745–8750. doi:10.1074/jbc.M211729200
27. Bönnemann, H.; Brijoux, W.; Joußen, T. *Angew. Chem.* **1990,** *102,* 324–326. doi:10.1002/ange.19901020327
28. Bönnemann, H.; Brijoux, W. Catalytically Active Metal Powders and Colloids. In *Active metals: preparation, characterization, applications;* Fürstner, A., Ed.; VCH: Weinheim, Germany, 1996; pp 339–379. doi:10.1002/9783527615179.ch09
29. Entel, P.; Gruner, M. E. *J. Phys.: Condens. Matter* **2009,** *21,* 064228. doi:10.1088/0953-8984/21/6/064228
30. Wojczykowski, K. Untersuchungen zur Synthese und Stabilisierung metallischer Nanopartikel. Ph.D. Thesis, Universität Bielefeld, Germany, 2006.
31. Sun, S. *Adv. Mater.* **2006,** *18,* 393–403. doi:10.1002/adma.200501464
32. Asaduzzaman, A.; Springborg, M. *Phys. Rev. B* **2006,** *74,* 165406. doi:10.1103/PhysRevB.74.165406
33. Chimentao, R. J.; Cota, I.; Dafinov, A.; Medina, F.; Sueras, J. E.; de la Fuenta, J. L.; Cesteros, Y.; Salagre, P. *J. Mater. Res.* **2006,** *21,* 105–111. doi:10.1557/jmr.2006.0014
34. Park, J. I.; Cheon, J. *J. Am. Chem. Soc.* **2001,** *123,* 5743–5746. doi:10.1021/ja0156340
35. Yasuda, H.; Mitsuishi, K.; Mori, H. *Phys. Rev. B* **2001,** *64,* 094101. doi:10.1103/PhysRevB.64.094101
36. Cheng, G.; Hight Walker, A. R. *J. Magn. Magn. Mater.* **2007,** *311,* 31–35. doi:10.1016/j.jmmm.2006.11.164
37. Seo, W. S.; Lee, J. H.; Sun, X.; Suzuki, Y.; Mann, D.; Liu, Z.; Terashima, M.; Yang, P. C.; McConnell, M. V.; Nishimura, D. G.; Dai, H. *Nat. Mater.* **2006,** *5,* 971–976. doi:10.1038/nmat1775
38. Wang, D.; He, J.; Rosenzweig, N.; Rosenzweig, Z. *Nano Lett.* **2004,** *4,* 409–413. doi:10.1021/nl035010n
39. Batlle, X.; Labarta, A. *J. Phys. D: Appl. Phys.* **2002,** *35,* R15. doi:10.1088/0022-3727/35/6/201
40. Sorensen, C. M. In *Nanoscale Materials in Chemistry;* Klabunde, K. J., Ed.; Wiley: New York, 2001.
41. Bayati, M.; Patoka, P.; Giersig, M.; Savinova, R. *Langmuir* **2010,** *26,* 3549–3554. doi:10.1021/la904287t
42. Murray, C. B.; Sun, S.; Gaschler, W.; Doyle, H.; Betley, T. A.; Kagan, C. R. *IBM J. Res. Dev.* **2001,** *45,* 47–56. doi:10.1147/rd.451.0047
43. Sun, S.; Murray, C.; Weller, D.; Folks, L.; Moser, A. *Science* **2000,** *287,* 1989–1992. doi:10.1126/science.287.5460.1989
44. Boyen, H.-G.; Fauth, K.; Stahl, B.; Ziemann, P.; Kästle, G.; Weigl, F.; Banhart, F.; Hessler, M.; Schütz, G.; Gajbhiye, N. S.; Ellrich, J.; Hahn, H.; Büttner, M.; Garnier, M. G.; Oelhafen, P. *Adv. Mater.* **2005,** *17,* 574–578. doi:10.1002/adma.200400748
45. Yang, H.; Sheng, C. M.; Su, Y. K.; Yang, T. Z.; Gao, H. J.; Wang, Y. G. *Appl. Phys. Lett.* **2003,** *82,* 4729. doi:10.1063/1.1586481
46. Gao, Y.; Bao, Y.; Beermann, M.; Yasuhara, A.; Shindo, D.; Krishnan, K. M. *Appl. Phys. Lett.* **2004,** *86,* 3361. doi:10.1063/1.1723687
47. Petit, C.; Taleb, A.; Pileni, M. P. *J. Phys. Chem. B* **1999,** *103,* 1805–1810. doi:10.1021/jp982755m
48. Desvaux, C.; Amiens, C.; Fejes, P.; Renaud, P.; Respaud, M.; Lecante, P.; Snoeck, E.; Chaudret, B. *Nat. Mater.* **2005,** *4,* 750–753. doi:10.1038/nmat1480
49. Richardi, J.; Pileni, M.-P. Self-Organization of Magnetic Nanocrystals at the Mesoscopic Scale: Example of Liquid–Gas Transitions. In *Nanocrystals Forming Mesoscopic Structures;* Pileni, M.-P., Ed.; Wiley-VCH, 2005; pp 75–87.
50. Korgel, B.; Fullam, S.; Connolly, S.; Fitzmaurice, D. *J. Phys. Chem. B* **1998,** *102,* 8379–8388. doi:10.1021/jp981598o
51. Ohara, P. C.; Leff, D. V.; Heath, J. R.; Gelbart, W. M. *Phys. Rev. Lett.* **1995,** *75,* 3466–3469. doi:10.1103/PhysRevLett.75.3466
52. Motte, L.; Courty, A.; Ngo, A.-T.; Lisiecki, I.; Pileni, M.-P. Self Organization of Inorganic Nanocrystals. In *Nanocrystals Forming Mesoscopic Structures;* Pileni, M.-P., Ed.; Wiley-VCH, 2005; pp 1–31.
53. Min, Y.; Akbulut, M.; Kristiansen, K.; Golan, Y.; Israelachvili, X. *Nat. Mater.* **2008,** *7,* 527–538. doi:10.1038/nmat2206
54. de Gennes, P. G. *Adv. Colloid Interface Sci.* **1987,** *27,* 189–209. doi:10.1016/0001-8686(87)85003-0
55. Ghazali, A.; Levy, J. *Phys. Rev. B* **2003,** *67,* 064409. doi:10.1103/PhysRevB.67.064409
56. Levesque, D.; Weis, J. J. *Phys. Rev. E* **1994,** *49,* 5131–5140. doi:10.1103/PhysRevE.49.5131
57. Carpick, R. W.; Agrait, N.; Ogletree, F.; Salmeron, M. *Langmuir* **1996,** *12,* 3334–3340. doi:10.1021/la9509007
58. Landmann, U.; Luedtke, W. D.; Burnham, N. A.; Colton, R. J. *Science* **1990,** *248,* 454–461. doi:10.1126/science.248.4954.454
59. Ennen, I.; Höink, V.; Weddemann, A.; Hütten, A.; Schmalhorst, J.; Reiss, G.; Waltenberg, C.; Jutzi, P.; Weis, T.; Engel, D.; Ehresmann, A. *J. Appl. Phys.* **2007,** *102,* 013910. doi:10.1063/1.2752146
60. Bao, Y.; Beerman, M.; Krishnan, K. M. *J. Magn. Magn. Mater* **2004,** *272–276* (Suppl. 1), E1367–E1368. doi:10.1016/j.jmmm.2003.12.219
61. Gao, Y.; Bao, Y.; Pakhomov, A.; Shindo, D.; Krishnan, K. *Phys. Rev. Lett.* **2006,** *96,* 137205. doi:10.1103/PhysRevLett.96.137205
62. Jackson, J. D. *Classical electrodynamics,* 2nd ed.; Wiley: New York, 1975.
63. Julliere, M. *Phys. Lett. A* **1975,** *54,* 225–226. doi:10.1016/0375-9601(75)90174-7
64. Schepper, W.; Schotter, J.; Brückl, H.; Reiss, G. *J. Biotechnol.* **2004,** *112,* 35–46. doi:10.1016/j.jbiotec.2004.04.032
65. Albon, C.; Weddemann, A.; Auge, A.; Rott, K.; Hütten, A. *Appl. Phys. Lett.* **2009,** *95,* 023101. doi:10.1063/1.3179241
66. Weddemann, A.; Auge, A.; Albon, C.; Wittbracht, F.; Hütten, A. *New J. Phys.* **2009,** *11,* 113027. doi:10.1088/1367-2630/11/11/113027
67. Kodama, R. H. *J. Magn. Magn. Mater.* **1999,** *200,* 359–372. doi:10.1016/S0304-8853(99)00347-9
68. Wang, S. X.; Li, G. *IEEE Trans. Magn.* **2008,** *44,* 1687–1702. doi:10.1109/TMAG.2008.920962

69. Laroze, D.; Vargas, P.; Cortez, C.; Gutierrez, G. *J. Magn. Magn. Mater.* **2009,** *320,* 1440–1448. doi:10.1016/j.jmmm.2007.12.010
70. Weddemann, A.; Auge, A.; Kappe, D.; Wittbracht, F.; Hütten, A. *J. Magn. Magn. Mater.* **2010,** *322,* 643–646. doi:10.1016/j.jmmm.2009.10.031
71. Schaller, V.; Wahnström, G.; Sanz-Velasco, A.; Enoksson, P.; Johansson, P. *J. Magn. Magn. Mater.* **2009,** *321,* 1400–1404. doi:10.1016/j.jmmm.2009.02.047
72. Xiao, J. Q.; Jiang, J. S.; Chien, C. L. *Phys. Rev. Lett.* **1992,** *68,* 3749–3752. doi:10.1103/PhysRevLett.68.3749
73. Berkowitz, A. E.; Mitchell, J. R.; Carey, M. J.; Young, A. P.; Zhang, S.; Spada, F. E.; Parker, F. T.; Hütten, A.; Thomas, G. *Phys. Rev. Lett.* **1992,** *68,* 3745–3748. doi:10.1103/PhysRevLett.68.3745
74. Milner, A.; Gerber, A.; Groisman, B.; Karpovsky, M.; Gladkikh, A. *Phys. Rev. Lett.* **1996,** *76,* 475–478. doi:10.1103/PhysRevLett.76.475
75. Wang, J. Q.; Dao, N.; Kim, N. H.; Whittenburg, S. L. *J. Appl. Phys.* **2004,** *95,* 6762. doi:10.1063/1.1664171
76. Mebed, A. M.; Howe, J. M. *J. Appl. Phys.* **2006,** *100,* 074310. doi:10.1063/1.2354419
77. Chen, Y. Y.; Ding, J.; Si, L.; Cheung, W. Y.; Wong, S. P.; Wilson, I. H.; Suzuki, T. *Appl. Phys. A: Mater. Sci. Process.* **2001,** *73,* 103–106. doi:10.1007/s003390100524
78. Chien, C. L.; Xiao, J. Q.; Jiang, J. S. *J. Appl. Phys.* **1993,** *73,* 5309. doi:10.1063/1.353765
79. Dupuis, V.; Tuaillon, J.; Prevel, B.; Perez, A.; Melinon, P.; Guiraud, G.; Parent, F.; Steren, L. B.; Morel, R.; Barthelemy, A.; Fert, A.; Mangin, S.; Thomas, L.; Wernsdorfer, W.; Barbara, B. *J. Magn. Magn. Mater.* **1997,** *165,* 42–45. doi:10.1016/S0304-8853(96)00469-6
80. Holdenried, M.; Hackenbroich, B.; Micklitz, H. *J. Magn. Magn. Mater.* **2001,** *231,* 13–19. doi:10.1016/S0304-8853(01)00143-3
81. Rubin, S.; Holdenried, M.; Micklitz, H. *J. Magn. Magn. Mater.* **1999,** *203,* 97–99. doi:10.1016/S0304-8853(99)00200-0
82. Weddemann, A.; Albon, C.; Auge, A.; Wittbracht, F.; Hedwig, P.; Akemeier, D.; Rott, K.; Meißner, D.; Jutzi, P.; Hütten, A. *Biosens. Bioelectron.*, in press. doi:10.1016/j.bios.2010.06.031
83. Landau, L. D.; Lifshitz, E. *Phys. Z. Sowjetunion* **1935,** *8,* 153–169.
84. Kronmüller, H.; Parkin, S., Eds. *Handbook of Magnetism and Advanced Materials;* Wiley: New York, 2007; Vol. 2.
85. Weddemann, A.; Auge, A.; Albon, C.; Wittbracht, F.; Hütten, A. *J. Appl. Phys.* **2010,** *107,* 104314. doi:10.1063/1.3427549
86. Wiser, N. *J. Magn. Magn. Mater.* **1996,** *159,* 119–124. doi:10.1016/0304-8853(95)00613-3
87. Altbir, D.; d'Albuquerque e Castro, J.; Vargas, P. *Phys. Rev. B* **1996,** *54,* R6823–R6826. doi:10.1103/PhysRevB.54.R6823

License and Terms

This is an Open Access article under the terms of the Creative Commons Attribution License (http://creativecommons.org/licenses/by/2.0), which permits unrestricted use, distribution, and reproduction in any medium, provided the original work is properly cited.

The license is subject to the *Beilstein Journal of Nanotechnology* terms and conditions: (http://www.beilstein-journals.org/bjnano)

The definitive version of this article is the electronic one which can be found at: doi:10.3762/bjnano.1.10

Beilstein Journal of Nanotechnology

Magnetic coupling mechanisms in particle/thin film composite systems

Giovanni A. Badini Confalonieri[*1], Philipp Szary[1], Durgamadhab Mishra[1], Maria J. Benitez[1,2], Mathias Feyen[2], An Hui Lu[2], Leonardo Agudo[3], Gunther Eggeler[3], Oleg Petracic[1] and Hartmut Zabel[1]

Full Research Paper

Open Access

Address:
[1]Institut für Experimentalphysik/Festkörperphysik, Ruhr-Universität Bochum, D-44780 Bochum, Germany, [2]Max-Planck Institut für Kohlenforschung, D-45470 Mülheim an der Ruhr, Germany and [3]Institut für Werkstoffe, Ruhr-Universität Bochum, D-44780 Bochum, Germany

Email:
Giovanni A. Badini Confalonieri[*] - giovanni.badini@rub.de

* Corresponding author

Keywords:
exchange bias; iron oxide nanoparticles; nanoparticle self-assembly; nanoparticle-thinfilm composite; super-spin glass interaction

Beilstein J. Nanotechnol. **2010,** *1,* 101–107.
doi:10.3762/bjnano.1.12

Received: 05 August 2010
Accepted: 18 October 2010
Published: 01 December 2010

Guest Editors: U. Wiedwald and P. Ziemann

© 2010 Confalonieri et al; licensee Beilstein-Institut.
License and terms: see end of document.

Abstract

Magnetic γ-Fe_2O_3 nanoparticles with a mean diameter of 20 nm and size distribution of 7% were chemically synthesized and spin-coated on top of a Si-substrate. As a result, the particles self-assembled into a monolayer with hexagonal close-packed order. Subsequently, the nanoparticle array was coated with a Co layer of 20 nm thickness. The magnetic properties of this composite nanoparticle/thin film system were investigated by magnetometry and related to high-resolution transmission electron microscopy studies. Herein three systems were compared: i.e. a reference sample with only the particle monolayer, a composite system where the particle array was ion-milled prior to the deposition of a thin Co film on top, and a similar composite system but without ion-milling. The nanoparticle array showed a collective super-spin behavior due to dipolar interparticle coupling. In the composite system, we observed a decoupling into two nanoparticle subsystems. In the ion-milled system, the nanoparticle layer served as a magnetic flux guide as observed by magnetic force microscopy. Moreover, an exchange bias effect was found, which is likely to be due to oxygen exchange between the iron oxide and the Co layer, and thus forming of an antiferromagnetic CoO layer at the γ-Fe_2O_3/Co interface.

Introduction

Recently, the study of composite magnetic nanostructures has received great interest due to the potential applications as permanent magnets or advanced data storage media [1-5]. In particular, systems where nanoparticles (NPs) represent at least one of the constituent materials [3] have generated much attention. A large number of investigations can be found that address potential technological applications, preparation methods and fundamental properties of magnetic NPs, such as in photonics

[6,7], nanomedicine [8-10], electronics [11,12] and data storage technology [13-15]. In the latter case, composites of magnetic NPs grown onto or embedded in a host matrix have received particular attention due to their potential use for hard disk drive media [13,15-17].

In most cases, magnetic NP/thin film composites are prepared by physical growth methods, such as sputtering [18,19], sequential pulsed laser deposition [20,21], sputtering gas aggregation [22] or mechanical milling [23]. In this work, we report a different approach to fabricate composite nanoparticle/thin-film materials, i.e., which combines the use of both chemical and physical growth methods. The composite material can be successfully prepared over areas larger than 100 mm^2 and is obtained by combining chemical synthesis of the NPs, their mechanical self-assembly on top of a substrate, and ion-beam sputtering of a magnetic layer. All experimental details about the fabrication of the present system are described in the last section.

While the physical properties of magnetic NPs are well documented [24-27], the collective behavior of self-assembled magnetic NPs on the one hand and their interaction with a magnetic substrate on the other hand is less well studied. The aim of our present investigation is to shed light on these various interactions.

Results and Discussion

Structural characterization

Hexagonal close packing of self-assembled NPs as a result of the spin-coating process was confirmed by means of atomic force microscopy (AFM) images in Figure 1a and scanning electron microscopy (SEM) images in Figure 1b. The monodisperse nature of the particles and their ordering can be observed in these images. Furthermore, in both images common faults can be seen which are encountered in NP monolayer samples prepared by spin-coating, such as the presence of regions with two overlapping layers, missing particles (voids), and dislocations separating domains of hexagonal order. Aside from the presence of local defects, the spin-coating technique has proven to be able to produce long range hexagonal order over areas of 10 × 10 mm^2 with a structural coherence length, as probed by scattering techniques, in the order of 200–300 nm [28].

AFM observations, shown in Figure 1a, also confirm the hexagonal close-packed ordering with an average surface roughness of the film of approximately 1.4 nm.

Ion-milling carried out at the surface of the NPs removed the oleic acid layer, flattened the NPs at the top, and reduced the surface roughness prior to the deposition of a Co layer on top.

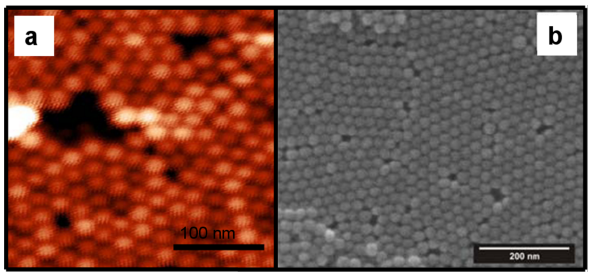


Figure 1: AFM (a) and SEM (b) images showing the self-assembly of the NPs in a close-packed hexagonal structure as a consequence of the spin-coating process.

Approximately, a 2 to 3 nm thick layer was removed from the surface during milling. Cross sectional TEM images of the samples are shown in Figure 2b. For comparison, a reference sample that has not undergone ion-milling is also depicted in Figure 2a. Without ion-milling, the Co layer replicates the topography of the NPs beneath, which is much less in the case of the Co layer on the ion-milled NPs.

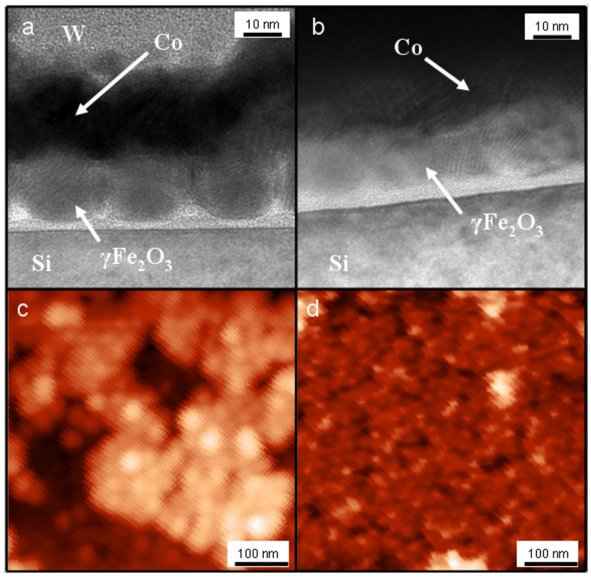


Figure 2: Top panel: High-resolution TEM cross-section images of non-ion-milled (a) and ion-milled (b) composite samples. Bottom panel: AFM images of the Co surface for the non-ion-milled (c) and ion-milled (d) samples.

AFM images of the two samples prepared with non-ion-milled (Figure 2c) and with ion-milled (Figure 2d) NPs are in good agreement with the TEM observation. In the former case the topography of the NPs is reflected on the Co surface, while, after milling the surface is flattened down with a reduction in the average roughness from 5.8 nm to 1.8 nm.

Magnetic characterization

Magnetization hysteresis loops of a monolayer film, consisting of single phased maghemite NPs as detailed in the experimental section, are shown in Figure 3a. Hysteresis loops taken at 330 K and 15 K show the expected behavior of nanosized ferrimagnetic particles, i.e., symmetric loops, with a coercivity of H_c = 280 Oe at 15 K and H_c= 40 Oe at 330 K. The large increase in coercivity at low temperature is in agreement with previous reports and with the model of superparamagnetic (SPM) particles [29,30].

After the deposition of Co on top of the NP arrays, the H_c at 15 K increases to 408 Oe and 455 Oe for the non-ion-milled (Figure 3b) and the ion-milled (Figure 3c) samples, respectively, while at 330 K the H_c values with and without the Co layer are essentially the same. The interaction between the NPs and the Co layer becomes more pronounced at low temperatures and is expressed by a further increase of the coercivity and in a change of the shape of the hysteresis loop. In addition, it should be noted that, while the hysteresis loop for the NP monolayer is symmetric, the composite systems show a significant bias. It is important to note that the bias is only observed when the sample is field cooled, implying that its origin should be ascribed to an antiferromagnetic/ferromagnetic (AF/FM) coupling [31-35].

The magnetic exchange interaction between an AF and an FM layer can usually be observed as a horizontal shift of the magnetic hysteresis loop, when cooling the material from a temperature above the Néel temperature in an applied magnetic field. This offset is defined as exchange bias (EB) field, H_b [32,33]. We find EB values at 15 K of H_b = 157 Oe and 185 Oe for the non-ion-milled and the ion-milled system, respectively.

Since the system considered here is composed of single-phase ferrimagnetic maghemite NPs and a ferromagnetic Co thin film, it is necessary to account for the presence of an extra AF component. A possible explanation is that the Co layer is partially oxidized to AF CoO. The Co layer is capped with a protective Cu layer, and therefore, oxidation is more likely to occur at the particle/film interface by oxygen exchange from both the iron oxide and the organic oleic acid to the Co layer. In the event of oxygen exchange between the iron oxide nanoparticles and the Co layer, it is reasonable to expect a change in stoichiometry of the nanoparticles, at least at the surface level, close to the interface. However, it was not possible to verify this aspect, either from direct TEM images or to infer it from magnetic measurements. Further work is necessary to clarify this point. In any case, the EB is likely due to the exchange interaction between the AF CoO interfacial layer and the FM layer.

This CoO layer is estimated to be between 1 to 4 nm thick. Although it was not possible to resolve such a CoO layer from the high-resolution TEM images (Figure 2), dark-field TEM images (Figure 4a) reveal the presence of a crystalline ~4 nm thick layer being well distinguishable from the Co layer, and thus attributed to the formation of an oxide phase in the Co film. The corresponding diffraction pattern shown in Figure 4b confirms the existence of a CoO crystal structure.

Further information about the magnetic behavior and in particular about the coupling effects between the NPs and the Co layer can be obtained from measurements of the magnetic moment vs temperature (Figure 5) after zero-field cooling (ZFC) and field cooling (FC).

Generally, the system is first cooled down from relatively high temperatures (here 380 K) in a zero field, then a magnetic field is applied and the ZFC curve is measured. The FC curve is usually obtained directly following the ZFC curve upon cooling in the same applied field.

Figure 5 shows m_{ZFC} and m_{FC} measured at 500 Oe for the three systems, i.e., the NP monolayer (green squares), non-ion-milled

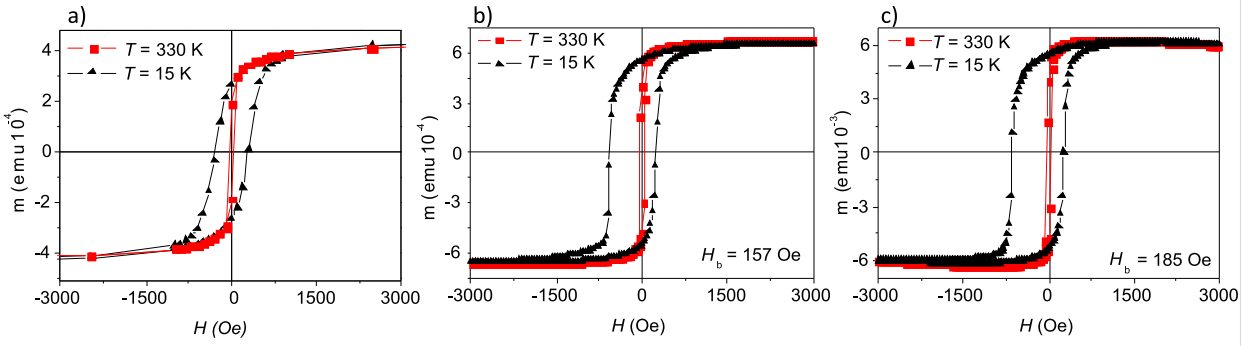


Figure 3: Magnetic hysteresis loops at 330 K and 15 K for a monolayer film of nanoparticles (a) and the composite nanoparticle/Co film non-ion-milled (b) and after ion-milling (c).

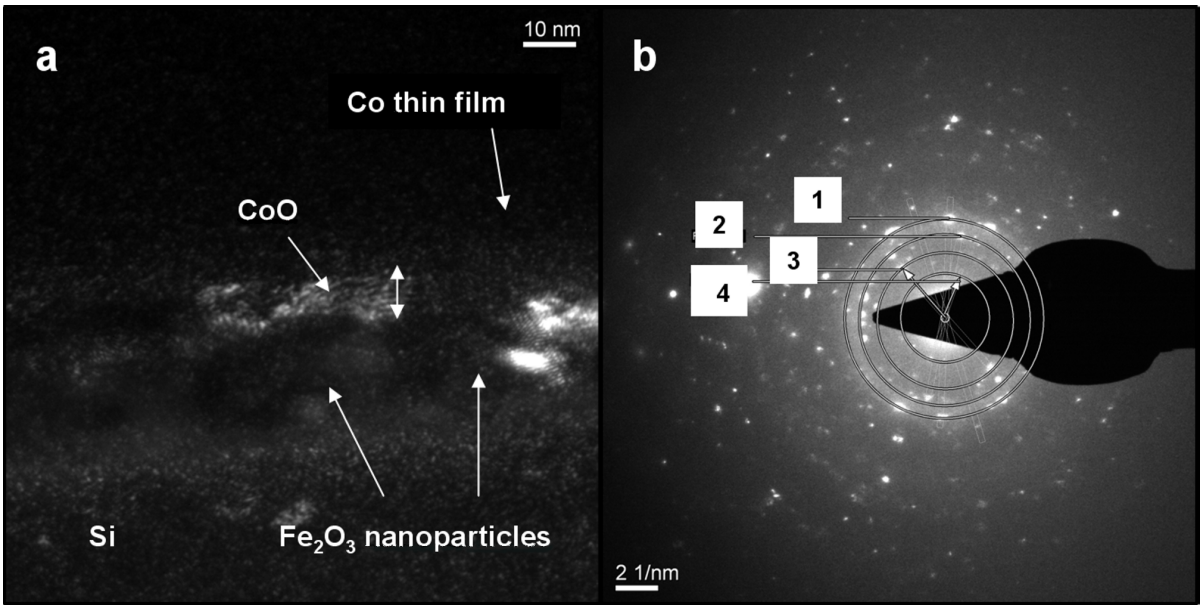


Figure 4: (a) Dark-field TEM image of the cross section NPs/thin-film system showing the CoO layer at the interface with NPs. (b) The corresponding diffraction pattern where the following phases are identified: 1) CoO (200), 2) Fe_2O_3 (311), 3) Si (111), 4) Fe_2O_3 (111).

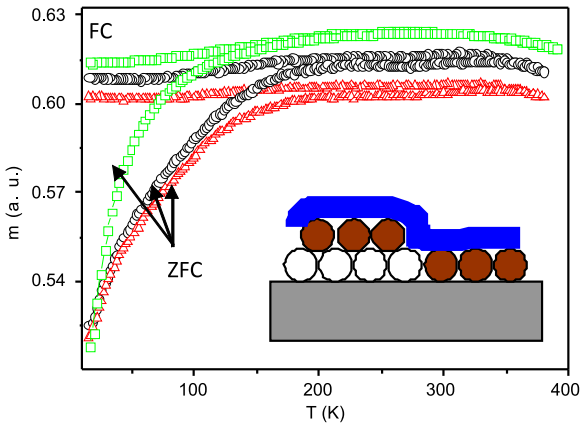


Figure 5: ZFC/FC magnetic moment vs temperature measured in 500 Oe for a NP monolayer (green squares), non-ion-milled composite (black circles) and ion-milled composite (red triangles), respectively. The curves are scaled for better clarity. The inset shows a schematic of the composite system. The Co film is depicted as a blue solid film and the NPs as circles, where two subsystems are marked: the open circles represent particles which are not in contact with the Co layer, and the filled brown circles are particles in contact with or near to the Co, respectively.

composite (black circles) and ion-milled composite (red triangles), respectively. The ZFC/FC curves for the NP monolayer show the regular behavior as expected from a SPM system, i.e., a peak in the ZFC curve marking the blocking temperature, $T_b \approx 250$ K, of the system and the splitting of the ZFC and FC curves near T_b. However, an important feature is the decrease of the magnetic moment in the FC curve for decreasing temperatures below T_b. This trend has already been recognized as indicating a collective particle behavior, a so-called super-spin glass (SSG) state [21,24,27,36,37]. The peak temperature then marks the 'blocking temperature', however, not of individual NPs, but of the entire *interacting* monolayer of NPs.

When adding a Co layer on top of the NPs, the collective behavior of the NPs is partially inhibited as found from a more shallow dip in the FC curve. Interestingly, in the composite systems the ZFC/FC curves reveal the presence of two separate T_b peaks, i.e., at ≈340 K and at ≈210 K and hence one above and one below, respectively, the blocking temperature of the NP monolayer.

There are two possible origins for the two peaks feature. In first place it might be due to the existence of two different NP subsystems as schematically depicted in the inset of Figure 5. The Co film does not cover all NPs equally, but only the top layer of NPs. In a 'monolayer' of NPs (that means one layer of particles on average) there exist not only holes and dislocations in the array but also areas with a second layer (see Figure 1). Hence, there will be NPs that are not in contact with the Co layer (open circles in the inset of Figure 5). Consequently, one might expect two magnetic subsystems, i.e., firstly NPs which are strongly magnetically coupled to the Co film or exchange biased to the CoO layer mentioned above at the NP-Co interface. These NPs are likely to produce an increased blocking temperature due to an increased energy barrier originating from the additional coupling.

Secondly, the other peak at lower temperatures is then due to NPs that are not in contact to the Co layer. These particles are weakly coupled to the other NPs by dipolar interactions. Because this subsystem consists of fewer particles than the entire NP ensemble, the collective blocking temperature of this smaller system will be reduced.

The second possible origin of the low-field peak might also arise from the CoO layer. It was in fact reported for a FM/AF coupled Fe_3O_4/CoO [38] and Fe/CoO [39] thin film systems, that the blocking temperature, in this case the temperature at which exchange bias between a FM and an AF thin film disappears, can occur at temperatures below the Néel temperature of CoO (~290 K), in the case of ultra thin films of CoO (less than 5 nm). Considering the thickness of the CoO film naturally grown in our system, it cannot be excluded that the peak at lower temperature in Figure 5 might be caused by the disappearance of the FM/AF coupling. In order to clarify this point further experimental work is necessary.

MFM was used to investigate the surface domain structure of the composite materials with the sample in the remanent state (Figure 6c and Figure 6d). For comparison, the corresponding AFM images are also shown (Figure 6a and Figure 6b). In the case of the ion-milled system no well-defined magnetic domain structure at remanence can be recognized. The stray field of the MFM tip was found to modify the magnetic contrast during scanning (see Figure 6d). In order to rule out the possibility of artificial features from the tip or from surface impurities, different scans were performed after magnetic cycling. This effect was reproducible over multiple scans. Accounting for the better contact between particles and thin film and thus stronger magnetic coupling, this phenomenon can be due to the particles collecting the magnetic flux in a mechanism similar to that exerted by soft magnetic underlayers in perpendicular recording media [13]. This effect, however, becomes reduced with increasing interface roughness, as is the case for the non-ion-milled NPs. Here a sample-tip interaction was not observed (Figure 6c). A diffuse but stable domain structure in the Co layer is observed.

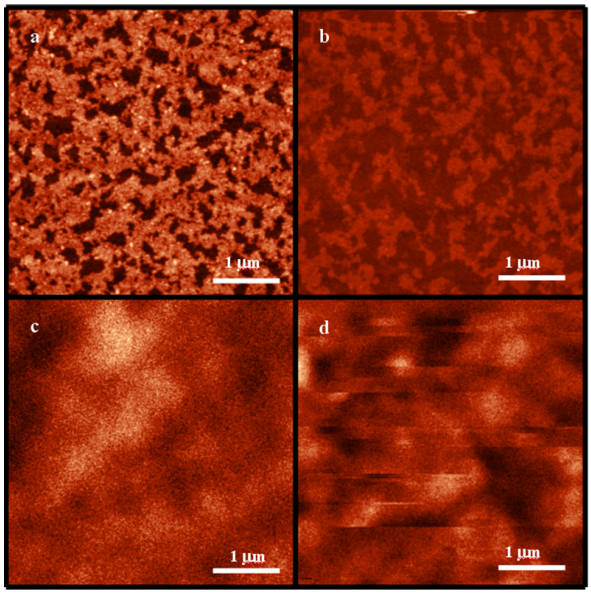


Figure 6: Top panel: AFM images of the Co surface for the non-ion-milled (a) and ion-milled (b) composite systems. Bottom panel: MFM images of the Co surface of non-ion-milled (c) and ion-milled (d) composite samples, taken with the sample in the remanent state after saturating at 1000 Oe.

Conclusion

Self assembled magnetic NP/thin film composites were prepared by a combination of spin-coating and ion-beam sputtering techniques. Ion-milling of the NP surface was used prior to Co sputtering for removing the oleic acid shell at the top of the NPs and to smooth out the interface prior to Co film deposition. This process was found to improve the coupling between the NPs and the Co layer. A shift of the hysteresis loop at low temperatures indicates an AF/FM exchange bias effect in the composite system, which is likely due to the formation of a CoO layer at the interface. The single NP layer exhibits a stretched blocking temperature, indicative of a collective behavior due to magnetic dipole interaction. The composite system shows two blocking temperatures: one above the temperature of the single NP layer, which likely is due to the interaction with the Co-layer, and one below, which we assign to small NP islands that are in contact with other NPs on top but not with the Co layer. Moreover, a 'soft magnetic underlayer' behavior of the ion-milled system was observed by MFM measurements. In conclusion, the contact of magnetic NPs with a closed thin magnetic film increases the blocking temperature of the system, i.e., it increases the potential well for thermal fluctuations. Composite systems also exhibit an enhanced coercivity and a change in the shape of the hysteresis loop at low temperature. The other two effects, exchange bias and a second lower blocking temperature, are extrinsic and depend on the particular system chosen.

Experimental

Iron oxide NPs were prepared by thermal decomposition of metal-oleate complexes [40]. As-prepared, particles with mean diameter of 20 nm and 7% size distribution were coated with a ~2 nm thick layer of oleic acid and dissolved in toluene. The NP dispersion, with a concentration of approximately 50 mg of NPs per 5 ml of toluene, was spin-coated at 3000 rpm for 30 s on top of a Si(100) substrate with a natural oxide layer. As a result of the spin-coating process, approximately one monolayer of self-

organized particles was formed having hexagonal closed-packed lateral order (see Figure 1). The samples were annealed at 170 °C for 20 min in air in order to obtain mainly single phase maghemite (γ-Fe_2O_3) NPs as reported in Ref. [41].

After heat treatment, the NP monolayer was ion-milled with neutralized Ar-ions for 4 min in order to flatten the NP array and remove the oleic acid layer. Finally, a thin cobalt film of 20 nm thickness was grown on top of the NPs by ion-beam sputtering from a Co target at 3.9×10^{-4} mbar with a base pressure of 1×10^{-8} mbar. To prevent oxidation of the Co surface, the sample was finally capped with a 3 nm thick layer of Cu. A reference composite sample was prepared for comparison, where the NPs were not ion-milled prior to the sputtering of Co.

The structure and topography of the samples were characterized by means of scanning electron microscopy (SEM) with a FEI Quanta FEG-SEM, transmission electron microscopy (TEM) with an analytical 200 kV FEG-TEM TECNAI F20 S-Twin instrument, atomic force and magnetic force microscopy (AFM, MFM) with an NT-MDT low temperature HV-Solver system. For cross sectional investigations of the composite film, TEM foils were extracted perpendicularly to the sample surface, by means of focused ion-beam technique, for which the sample had to be coated with an approximately 3 μm thick layer of tungsten. Magnetic measurements were performed by means of superconducting quantum interference device (SQUID) magnetometry (Quantum Design, MPMS) on sample areas of 7×7 mm^2, in a temperature range between 15 and 380 K, with the field applied in the plane of the sample.

Acknowledgements

This work was supported by the Ruhr-University Bochum through the Research Department IS^3/HTM. The authors would like to acknowledge M. Bienek for the invaluable help during TEM foil preparation.

References

1. Kneller, E. F.; Hawig, R. *IEEE Trans. Magn.* **1991,** *27,* 3588–3600. doi:10.1109/20.102931
2. Skomski, R.; Coey, J. M. D. *Phys. Rev. B* **1993,** *48,* 15812–15816. doi:10.1103/PhysRevB.48.15812
3. Zeng, H.; Li, J.; Liu, J. P.; Wang, Z. L.; Sun, S. *Nature* **2002,** *420,* 395–398. doi:10.1038/nature01208
4. Thiele, J. U.; Maat, S.; Fullerton, E. E. *Appl. Phys. Lett.* **2003,** *82,* 2859–2861. doi:10.1063/1.1571232
5. Wang, J. P. *Nat. Mater.* **2005,** *4,* 191–192. doi:10.1038/nmat1344
6. Lyubchanskii, I. L.; Dadoenkova, N. N.; Lyubchanskii, M. I.; Shapovalov, E. A.; Rasing, T. H. *J. Phys. D: Appl. Phys.* **2003,** *36,* R277–R287. doi:10.1088/0022-3727/36/18/R01
7. Ge, J.; Hu, Y.; Yin, Y. *Angew. Chem., Int. Ed.* **2007,** *46,* 7428–7431. doi:10.1002/anie.200701992
8. Medarova, Z.; Pham, W.; Farrar, C.; Petkova, V.; Moore, A. *Nat. Med.* **2007,** *13,* 372–377. doi:10.1038/nm1486
9. Krishnan, K. M.; Pakhomov, A. B.; Bao, Y.; Blomqvist, P.; Chun, Y.; Gonzales, M.; Grin, K.; Ji, X.; Roberts, B. K. *J. Mater. Sci.* **2006,** *41,* 793–815. doi:10.1007/s10853-006-6564-1
10. Pankhurst, Q. A.; Connolly, J.; Jones, S. K.; Dobson, J. *J. Phys. D: Appl. Phys.* **2003,** *36,* R167–R181. doi:10.1088/0022-3727/36/13/201
11. Hai, P. N.; Ohya, S.; Tanaka, M.; Barnes, S. E.; Maekawa, S. *Nature* **2009,** *458,* 489–492. doi:10.1038/nature07879
12. Black, C. T.; Murray, C. B.; Sandstrom, R. L.; Sun, S. *Science* **2000,** *290,* 1131–1134. doi:10.1126/science.290.5494.1131
13. Terris, B. D.; Thomson, T. *J. Phys. D: Appl. Phys.* **2005,** *38,* R199–R222. doi:10.1088/0022-3727/38/12/R01
14. Burda, C.; Chen, X.; Narayanan, R.; El-Sayed, M. A. *Chem. Rev.* **2005,** *105,* 1025–1102. doi:10.1021/cr030063a
15. Sun, S. H. *Adv. Mater.* **2006,** *18,* 393–403. doi:10.1002/adma.200501464
16. Yu, M.; Liu, Y.; Moser, A.; Weller, D.; Sellmyer, D. J. *Appl. Phys. Lett.* **1999,** *75,* 3992–3994. doi:10.1063/1.125516
17. Sun, M.; Zangari, G.; Shamsuzzoha, M.; Metzger, R. M. *Appl. Phys. Lett.* **2001,** *78,* 2964–2966. doi:10.1063/1.1370986
18. Yan, M. L.; Li, X. Z.; Gao, L.; Liou, S. H.; Sellmyer, D. J.; van de Veerdonk, R. J. M.; Wierman, K. W. *Appl. Phys. Lett.* **2003,** *83,* 3332–3334. doi:10.1063/1.1621071
19. Sahoo, S.; Petracic, O.; Kleemann, W.; Stappert, S.; Dumpich, G.; Nordblad, P.; Cardoso, S.; Freitas, P. P. *Appl. Phys. Lett.* **2003,** *82,* 4116–4118. doi:10.1063/1.1581002
20. Herndon, N. B.; Oh, S. H.; Abiade, J. T.; Pai, D.; Sankar, J.; Pennycook, S. J.; Kumar, D. *J. Appl. Phys.* **2008,** *103,* No. 07D515. doi:10.1063/1.2833309
21. Fei, G. T.; Barnes, J. P.; Petford-Long, A. K.; Doole, R. C.; Serna, R.; Gonzalo, J. *J. Phys. D: Appl. Phys.* **2002,** *35,* 916–922. doi:10.1088/0022-3727/35/9/313
22. Morel, R.; Brenac, A.; Bayle-Guillemaud, P.; Portemont, C.; La Rizza, F. *Eur. Phys. J. D* **2003,** *24,* 287–290. doi:10.1140/epjd/e2003-00158-9
23. Binns, C.; Trohidou, K. N.; Bansmann, J.; Baker, S. H.; Blackman, J. A.; Bucher, J.-P.; Kechrakos, D.; Kleibert, A.; Louch, S.; Meiwes-Broer, K.-H.; Pastor, G. M.; Perez, A.; Xie, Y. *J. Phys. D: Appl. Phys.* **2005,** *38,* R357. doi:10.1088/0022-3727/38/22/R01
24. Dormann, J. L.; Fiorani, D.; Tronc, E. Magnetic Relaxation in Fine-Particle Systems. In *Advances in Chemical Physics;* Prigogine, I.; Rice, S. A., Eds.; John Wiley & Sons: Hoboken, 1997; Vol. 98, pp 283–494. doi:10.1002/9780470141571.ch4
25. Batlle, X.; Labarta, A. *J. Phys. D: Appl. Phys.* **2002,** *35,* R15–R42. doi:10.1088/0022-3727/35/6/201
26. Bansmann, J.; Baker, S. H.; Binns, C.; Blackman, J. A.; Bucher, J.-P.; Dorantes-Davila, J.; Dupuis, V.; Favre, L.; Kechrakos, D.; Kleibert, A.; Meiwes-Broer, K.-H.; Pastor, G. M.; Perez, A.; Toulemonde, O.; Trohidou, K. N.; Tuaillon, J.; Xie, Y. *Surf. Sci. Rep.* **2005,** *56,* 189–275. doi:10.1016/j.surfrep.2004.10.001
27. Petracic, O. *Superlattices Microstruct.* **2010,** *47,* 569–578. doi:10.1016/j.spmi.2010.01.009
28. Mishra, D.; Benitez, M. J.; Szary, P.; Feyen, M.; Lu, A. H.; Agudo, L.; Eggeler, G.; Petracic, O.; Zabel, H. (to be published).
29. Sharrock, M. P. *J. Appl. Phys.* **1994,** *76,* 6413–6418. doi:10.1063/1.358282

30. Kumar, D.; Narayan, J.; Kvit, A. V.; Sharma, A. K.; Sankar, J. *J. Magn. Magn. Mater.* **2001,** *232,* 161–167. doi:10.1016/S0304-8853(01)00191-3
31. Meiklejohn, W. H.; Bean, C. P. *Phys. Rev.* **1956,** *102,* 1413–1414. doi:10.1103/PhysRev.102.1413
32. Nogués, J.; Schuller, I. K. *J. Magn. Magn. Mater.* **1999,** *192,* 203–232. doi:10.1016/S0304-8853(98)00266-2
33. Berkowitz, A. E.; Takano, K. J. *J. Magn. Magn. Mater.* **1999,** *200,* 552–570. doi:10.1016/S0304-8853(99)00453-9
34. Stamps, R. L. *J. Phys. D: Appl. Phys.* **2000,** *33,* R247–R268. doi:10.1088/0022-3727/33/23/201
35. Radu, F.; Zabel, H. *Springer Tracts Mod. Phys.* **2007,** *227,* 97–184. doi:10.1007/978-3-540-73462-8_3
36. Jonsson, T.; Mattsson, J.; Djurberg, C.; Khan, F. A.; Nordblad, P.; Svedlindh, P. *Phys. Rev. Lett.* **1995,** *75,* 4138–4141. doi:10.1103/PhysRevLett.75.4138
37. Parker, D.; Dupuis, V.; Ladieu, F.; Bouchaud, J.-P.; Dubois, E.; Perzynski, R.; Vincent, E. *Phys. Rev. B* **2008,** *77,* 104428. doi:10.1103/PhysRevB.77.104428
38. van der Zaag, P. J.; Ijiri, Y.; Borchers, J. A.; Feiner, L. F.; Wolf, R. M.; Gaines, J. M.; Erwin, R. W.; Verheijen, M. A. *Phys. Rev. Lett.* **2000,** *84,* 6102–6105. doi:10.1103/PhysRevLett.84.6102
39. Nowak, G.; Remhof, A.; Radu, F.; Nefedov, A.; Becker, H. W.; Zabel, H. *Phys. Rev. B* **2007,** *75,* 174405. doi:10.1103/PhysRevB.75.174405
40. Park, J.; An, K.; Hwang, Y.; Park, J.-G.; Noh, H.-J.; Kim, J.-Y.; Park, J.-H.; Hwang, N.-M.; Hyeon, T. *Nat. Mater.* **2004,** *3,* 891–895. doi:10.1038/nmat1251
41. Benitez, M. J.; Mishra, D.; Szary, P.; Feyen, M.; Lu, A. H.; Agudo, L.; Eggeler, G.; Petracic, O.; Zabel, H. *J. Phys.: Cond. Mat.* **2010,** *submitted*. ArXiv:1010.0938v1.

License and Terms

This is an Open Access article under the terms of the Creative Commons Attribution License (http://creativecommons.org/licenses/by/2.0), which permits unrestricted use, distribution, and reproduction in any medium, provided the original work is properly cited.

The license is subject to the *Beilstein Journal of Nanotechnology* terms and conditions: (http://www.beilstein-journals.org/bjnano)

The definitive version of this article is the electronic one which can be found at: doi:10.3762/bjnano.1.12

Beilstein Journal of Nanotechnology

Ultrafine metallic Fe nanoparticles: synthesis, structure and magnetism

Olivier Margeat[1,2], Marc Respaud[*3], Catherine Amiens[*1], Pierre Lecante[4] and Bruno Chaudret[1]

Full Research Paper

Open Access

Address:
[1]Université de Toulouse, LCC - CNRS, 205, route de Narbonne, 31077 Toulouse Cedex 04 - France. Tel: +33 (0) 5 61 33 31 82; Fax: +33 (0) 5 61 55 30 03, [2]Université de la Méditéranée, Faculté des Sciences, GCOM2, 163 Avenue de Luminy, 13288 Marseille Cedex 09 - France. Tel: +33 (0) 6 17 24 81 15, [3]LPCNO, INSA, 135 avenue de Rangueil, 31077 Toulouse Cedex 04 - France. Tel: +33 (0) 5 61 55 96 48; Fax: +33 (0) 5 61 55 96 97 and [4]CEMES - CNRS, 29 rue Jeanne Marvig, 31077 Toulouse Cedex 04 - France. Tel: +33 (0)5 62 25 78 51; Fax: +33 (0)5 62 25 79 99

Email:
Olivier Margeat - olivier.margeat@univmed.fr; Marc Respaud* - respaud@insa-toulouse.fr; Catherine Amiens* - amiens@lcc-toulouse.fr; Pierre Lecante - lecante@cemes.fr

* Corresponding author

Keywords:
iron nanoparticles; magnetic properties; organometallic synthesis; size effects; structure

Beilstein J. Nanotechnol. **2010,** *1,* 108–118.
doi:10.3762/bjnano.1.13

Received: 23 July 2010
Accepted: 21 October 2010
Published: 03 December 2010

Guest Editors: U. Wiedwald and P. Ziemann

© 2010 Margeat et al; licensee Beilstein-Institut.
License and terms: see end of document.

Abstract

The results of the investigation of the structural and magnetic (static and dynamic) properties of an assembly of metallic Fe nanoparticles synthesized by an organometallic chemical method are described. These nanoparticles are embedded in a polymer, monodisperse, with a diameter below 2 nm, which corresponds to a number of around 200 atoms. The X-ray absorption near-edge structure and Mössbauer spectrum are characteristic of metallic Fe. The structural studies by wide angle X-ray scattering indicate an original polytetrahedral atomic arrangement similar to that of β-Mn, characterized by a short-range order. The average magnetic moment per Fe atom is raised to 2.59 μ_B (for comparison, bulk value of metallic Fe: 2.2 μ_B). Even if the spontaneous magnetization decreases rapidly as compared to bulk materials, it remains enhanced even up to room temperature. The gyromagnetic ratio measured by ferromagnetic resonance is of the same order as that of bulk Fe, which allows us to conclude that the orbital and spin contributions increase at the same rate. A large magnetic anisotropy for metallic Fe has been measured up to $(3.7 \pm 1.0)\cdot 10^5$ J/m^3. Precise analysis of the low temperature Mössbauer spectra, show a broad distribution of large hyperfine fields. The largest hyperfine fields display the largest isomer shifts. This indicates a progressive increase of the magnetic moment inside the particle from the core to the outer shell. The components corresponding to the large hyperfine fields with large isomer shifts are indeed characteristic of surface atoms.

Introduction

Progress in both experimental techniques and theoretical calculations over the past ten years have allowed the development of precise studies on the influence of size reduction on the magnetic properties of nanoparticles (NPs) down to the nanometer scale. A first spectacular result was the observation of the enhancement of the atomic magnetic moment in NPs of classical 3d ferromagnetic metals [1-4]. More surprisingly, the study of small Rh NPs revealed a paramagnetic to ferromagnetic phase transition induced by size reduction for clusters containing less than 40 atoms [5]. Band structure calculations have investigated the role of size reduction and demonstrated that it promotes a narrowing of the magnetic bands and thus an increase of the spin polarisation, associated to an enhancement of the orbital contribution [6-9]. However, even if these tendencies are now well established, there is some disparity in the experimental results, even in the case of the ferromagnetic 3d metals. In the case of free-standing Fe clusters, Billas and coworkers have demonstrated the enhancement of the magnetic moment μ_{Fe} when the cluster contains less than 1000 atoms [2,3]. In this size range some oscillations of μ_{Fe} with cluster size have also been revealed. Similarly, supported α-Fe NPs with diameters down to 2 nm show an enhancement of the hyperfine field B_{Hyp}, indicative of enhanced μ_{Fe} [10-12]. Recent careful measurements, by X-ray magnetic circular dichroism (XMCD) [13-16], consistently indicate an increase in the ratio of the orbital magnetic moment over the spin magnetic moment. However, different values have been reported, from $\mu_L/\mu_S = 0.1$ for 2 nm size selected clusters deposited on Si substrates [15], 0.15 for size selected clusters containing less than 10 atoms deposited on a Ni surface [13] and up to $\mu_L/\mu_S = 0.3$ for Fe islands on a Au surface [16]. For all these systems, the structure of the clusters and the influence of the substrate, which could both modify the electronic band structure, remain uncertain. This could explain the disparities observed in the experimental results. The theoretical investigations carried out so far were restricted to free clusters and therefore cannot explain all these experimental results. Calculations of the orbital contribution lead to an enhanced μ_L/μ_S ratio compared to the bulk value, but this enhancement is smaller than those estimated from XMCD measurements [9]. Interestingly, calculations by Pastor et al. demonstrate that large spin moments can be found for Fe clusters, depending on their structural arrangement [6].

In summary, since the magnetic properties may be strongly influenced by both their crystal structure and interactions with the substrate, it is important to develop new synthetic approaches which could allow extensive magnetic and structural investigations. In this respect, a chemical approach could be productive enough to afford NPs for both characterization and further use. For the past ten years we have developed a new method for the synthesis of metal NPs based on an organometallic approach [17]. We have, for example, shown that cobalt NPs prepared by the decomposition of an organometallic precursor under mild conditions in the presence of a stabilising polymer exhibit physical properties similar to those of free cobalt clusters [18].

In this article, we report the chemical synthesis of well-isolated Fe NPs embedded in a polymer, with diameters of less than 2 nm. The structural and chemical properties have been investigated by transmission electron microscopy, wide angle X-ray scattering (WAXS), and X-ray absorption near-edge structure (XANES). Preliminary results of this work have already been published [19]. Here a more detailed study of the magnetic properties is presented including Mössbauer spectrometry, ferromagnetic resonance (FMR) and superconducting quantum interference device (SQUID) measurements (static and AC susceptibility).

Results and Discussion

Synthesis and structural studies

The precursor chosen for the synthesis is $\{Fe[N(SiMe_3)_2]_2\}$ (**1**), which has previously been used for preparing self-organized iron nanocubes [20]. Furthermore, upon reduction with dihydrogen, it will generate, as the sole by-product an amine, a ligand previously shown to possess no influence on the magnetic properties of small metal particles [21]. The NPs were synthesized by dissolving the precursor **1** in a solution of polydimethylphenylene oxide (PPO) in toluene. After heating at 110 °C for 12 h under 3 bar H_2, the reaction mixture turned black. The solvent and volatile byproducts were then removed at reduced pressure. The black residue consists of Fe NPs embedded in the polymer. This material, the Fe content of which can be determined by chemical analysis, may be used without further purification for physics measurements. All the samples were prepared in a glove box to prevent oxidation. The particles were characterized by transmission electron microscopy (TEM), wide angle X-ray scattering (WAXS) [22], and X-ray absorption near-edge structure (XANES). TEM micrographs show the presence of well-dispersed small particles of ca. 1.8 nm mean size with a narrow size distribution (15%). Interestingly, the WAXS diagram (Figure 1, top) and the radial distribution function (RDF, Figure 1, bottom) demonstrate that the particles do not adopt any of the bulk Fe structures (lower curves). The most peculiar points are as follows: in real space, a broad first peak, indicative of a large dispersion of metal–metal distances, and the absence of the peak at $d\sqrt{2}$ associated with octahedral sites in close-packed structures (with d the average metal–metal distance); in reciprocal space, the split-

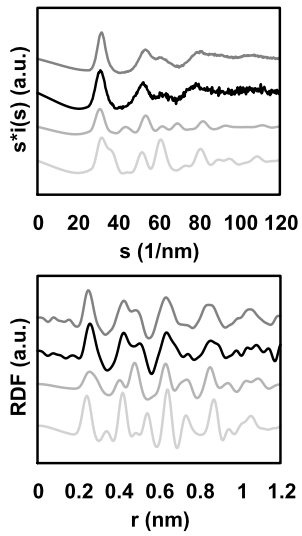


Figure 1: WAXS diagram (top) and the related RDF (bottom). Black: experimental spectra of Fe NPs taken at room temperature; dark grey (top): experimental spectra of Co NPs taken at room temperature; medium grey: α-Fe (bcc) model; light grey (bottom): γ-Fe (fcc) model.

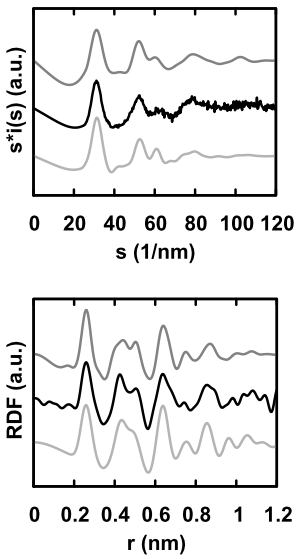


Figure 2: WAXS diagram (top) and the related RDF (bottom). Black: Fe NPs taken at room temperature; dark grey (top): Mn beta model; medium grey (bottom): van de Waal model.

ting of the second peak often observed in amorphous metals [23], including Fe [24,25], which also points to the absence of octahedral sites and thus suggests a polytetrahedral atomic arrangement with a very short periodicity.

This therefore excludes not only the close-packed fcc structure, but also many non-periodical structures commonly encountered in small particles, such as icosahedra or decahedra containing more than 50 atoms. It does not exclude the bcc structure, since the related RDF also exhibits a broad first peak and no peak at $d\sqrt{2}$. However, this function clearly does not match the experimental one over the complete range of distances (see Figure 1). In view of the WAXS diagram, the bcc structure can be also discounted since the experimental diagram does not present any intermediate peak for s in the range of 40–50 nm^{-1}.

Interestingly, both the WAXS diagram and the RDF resemble the corresponding curves obtained for Co NPs of 1.6 and 2.0 nm mean sizes prepared by a similar procedure and which were suggested to adopt a non-periodic polytetrahedral atomic arrangement. Such arrangements are locally ordered but lack the extended coherence length of regular structures. Different growth schemes lead to very close distance distributions, e.g., the shell-over-shell growth proposed for quasicrystalline alloys, or the disordered assembling of elementary icosahedra proposed for amorphous metals; both schemes adequately fit the experimental data [22]. As an illustration, Figure 2 displays the curves calculated from a van de Waal model (bottom curve). The first metal–metal distance ranges from 242.2 to 301.0 pm, leading to a structure locally more compact than in the bulk.

Interestingly, a small cluster based on the β-Mn structure leads also to a good agreement with the experimental data, both in the real (lower curve) and reciprocal spaces (upper curve) [26]. This structure, recently attributed to Co NPs (ε-Co) [27,28], displays several non-equivalent sites in distorted tetrahedral environments [26], which account for the large distribution of metal–metal distances and the splitting of the second peak observed in reciprocal space. The best fit between the calculated and experimental curves was obtained after contracting all distances occurring in the β-Mn structure by a factor of 1%, leading to metal–metal distances ranging from 236.4 to 267.9 pm, once again pointing to a locally more compact packing of iron atoms even if the overall calculated density for this model is 7.68 g/cm^3, i.e., lower than that of bulk iron.

XANES and EXAFS are other powerful tools for the study of short range order [29]. We therefore carried out these measurements at the iron K-edge at room temperature. Figure 3 shows the data obtained for the iron NPs and an iron foil used as a reference, and the first derivative is shown in the inset of Figure 3. In both cases, the K-edge absorption, determined as the energy of the maximum of the first derivative, starts at 7111 eV and 7110.5 eV for α-Fe and NPs, respectively. These values are in agreement with those reported earlier [30]. In contrast, the third curve, which corresponds to the signal recorded after exposure of the NPs to air, displays a pre-edge characteristic of an iron oxide [30-32].

For the two metallic phases, the shapes of the edge itself are however, quite different. The second shoulder and the

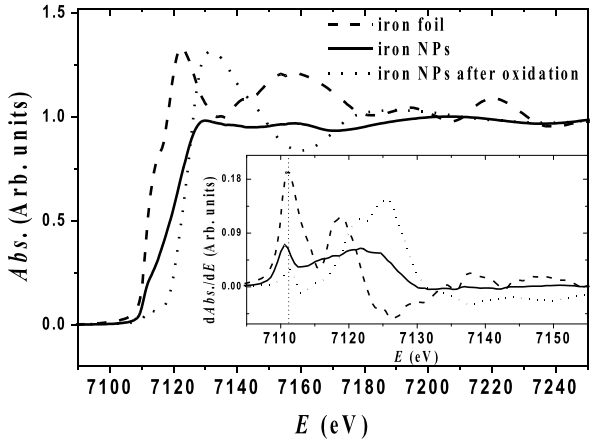


Figure 3: XANES spectra taken at room temperature for metallic Fe NPs, compared to a Fe foil reference, and intentionally oxidized Fe NPs. Inset displays the derivative of the absorption.

maximum of the absorption are shifted toward higher energies for NPs as compared to the reference. Unfortunately, the EXAFS signal is strongly damped, which prevents further analysis of the higher energy part. Notwithstanding, the results (both shape and damping) are consistent with published data on amorphous iron [31], thus exhibiting metallic NPs without long-range order. The structural determination is therefore not unequivocal. However, this study demonstrates NPs with a short-range order similar to β-Mn with a local polytetrahedral atomic arrangement with areas both more and much less dense than in bulk structures. It is noteworthy that the possible growth modes (atom per atom or cluster per cluster) are consistent with the synthetic procedure. Indeed, formation of a seed and its subsequent growth by random dense packing of atoms, generated during the hydrogenation of the iron precursor, can easily coexist in solution with a growth process involving the coalescence of small clusters. This emphasises the importance of the solution phase synthesis for the trapping of unstable intermediates and the growth of metastable structures often kinetically favoured.

Magnetic properties

A. Mössbauer spectra

The Mössbauer spectra, recorded at various temperatures between 293 K and 5 K, are shown in Figure 4. The measurements were performed with a ^{57}Co source in a Rh matrix and were calibrated against bulk α-Fe. Upon decreasing the temperature, the spectrum progressively splits but still remains broad, even at the lowest temperature. Such temperature dependence is characteristic of a superparamagnetic transition. The NPs, which have relaxation times (τ) longer than the measurement time (τ_m), give rise to a sextet (blocked NPs). The superparamagnetic NPs with a short relaxation time ($\tau < \tau_m$) show paramagnetic like behaviour. In the case of Mössbauer spectroscopy, τ_m is in the range of 10^{-8} s [33-35] and the superparamagnetic relaxation time is given by

$$\tau = \tau_0 \exp\left(\frac{K_{\text{eff}} \nu}{k_B T}\right) \quad (1)$$

where ν is the volume, K_{eff} the effective anisotropy, and τ_0 is of the order of 10^{-11}–10^{-9} s [36]. The blocking temperature of the material corresponds to the temperature where the blocked and the superparamagnetic contributions are equivalent. We estimated it to be in the range of 25 ± 5 K.

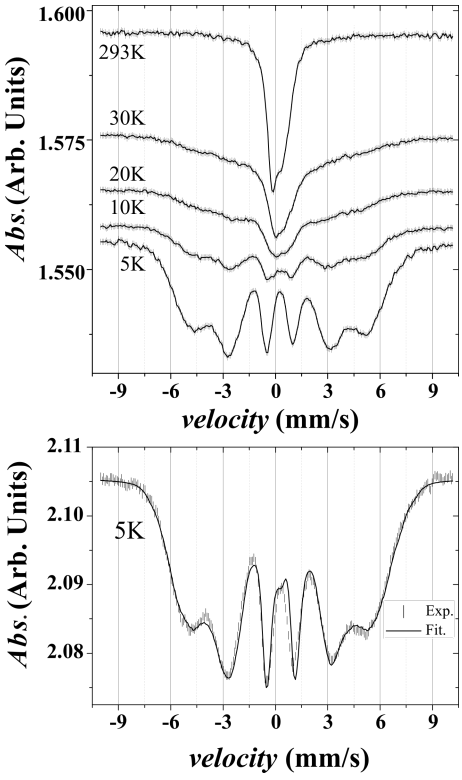


Figure 4: Top: Mössbauer spectra taken at different temperatures. Bottom: experimental spectra (symbols) taken at 5 K and the corresponding fit (solid line).

We now focus on the analysis of the low temperature spectrum. At low temperature, relaxation phenomena on the time scale of Mössbauer spectroscopy should be negligible. The large broadening of the sextet is thus indicative of a distribution of hyperfine fields (B_{hyp}). The fitting was carried out considering a distribution of hyperfine fields, with an isomer shift depending on B_{hyp} in order to adjust the experimental curve as precisely as possible. The relative areas of each component of the sextet have been constrained to the ratio of 3:2:1:1:2:3. Figure 5

displays the distributions of B_{hyp} and the corresponding isomer shifts (*IS*) used to simulate the spectrum measured at $T = 5$ K. Two distributions of B_{hyp} have been introduced. The first one, associated with a small *IS* centred on 0.05 mm/s, is composed of B_{hyp} values below 24 T. The second one has larger B_{hyp} values ranging from 20 T up to 50 T, associated with a larger *IS* centred around 0.35 mm/s. It is interesting to note that the *IS* increases with B_{hyp}.

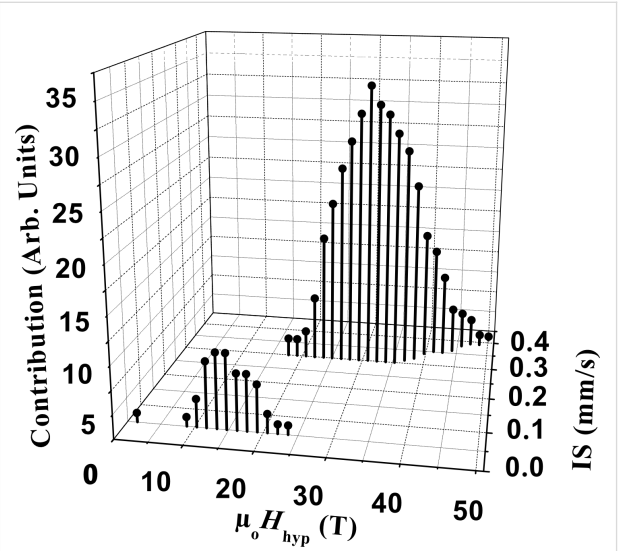


Figure 5: Distributions of the *IS* and the $\mu_0 H_{hyp}$ used to fit the experimental Mössbauer spectrum measured at 5 K.

The parameters defining the main contribution are of the same order of magnitude as those measured on slightly larger metallic NPs. For α-Fe NPs with diameters in the range of 3.7 nm, Bødker and coworkers estimated the hyperfine fields to be in the range of up to 45 T with an average *IS* of 0.5 mm/s [11,37]. Furubayashi found a smaller *IS* of 0.22–0.27 mm/s for NPs with diameters of approx. 2.0 nm [10]. Mössbauer spectra measured on 1.8 nm metallic NPs stabilised by $HN(SiMe_3)_2$ display two similar Fe contributions, except that the upper limit of hyperfine field distribution is 42 T [25]. These effects – broad B_{hyp} distribution and large *IS* – may be related to the smaller size of our NPs and to the atomic polytetrahedral arrangement, in particular the presence of many non-equivalent Fe sites compared to the conventional α-Fe phase. Band structure calculations on cubic Fe phases show a shell dependent magnetic moment with quite large differences between the core and the surface [7-9]. The enhancement of the spin and orbital magnetic moments is progressive from the core to the surface as the coordination number decreases. On the surface, as a consequence of both the reduction of the coordination number and the interface with the vacuum, there is a reduction of the s-electron density and a larger local magnetic moment, leading to, respectively, an important increase of the *IS* combined with a larger hyperfine field [9-11,37-39]. This explains well our experimental results with a simultaneous increase of the isomer shift and hyperfine field. The polytetrahedral atomic arrangement should also play a role since it leads to a reduced coordination number and a large distribution in the Fe–Fe distances, even in the core as in the case of amorphous Fe which displays the same local structure [31]. This will lead to a very different electronic structure at each site, and to a much broadened dispersion of B_{hyp}. Thus, we interpret the Mössbauer spectra as evidence of the progressive increase of the magnetic moment inside the particle from the core to the outer shell of the NP, the components corresponding to the large hyperfine fields with large isomer shifts being characteristic of surface atoms.

B. Magnetization

Magnetization measurements have been carried out with a commercial Quantum design SQUID magnetometer. Figure 6 shows the static zero-field-cooling field-cooling (ZFC-FC) magnetization curve versus temperature (*T*) in a low magnetic field of 1 mT. It exhibits a classical superparamagnetic (SP) transition with a blocking temperature $T_B = 4.9$ K.

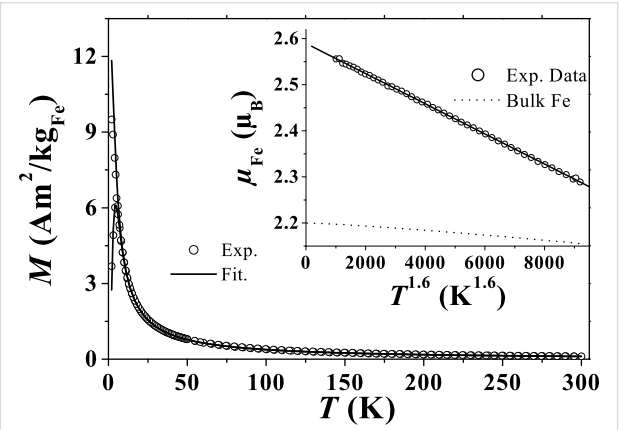


Figure 6: ZFC-FC magnetizations measured under $\mu_0 H = 1$ mT. Inset shows the extracted temperature dependence of M_S.

The measure of the AC susceptibility (χ_{AC}) shows the same superparamagnetic transition. Figure 7 displays the χ_{AC} variation versus temperature for a set of frequencies ranging from 0.1 Hz to 1000 Hz. The decrease of the measurement time τ_m induces an increase of T_B.

Figure 8 and Figure 9 display the magnetization curves measured below T_B ($T = 2$ K) and above T_B ($T = 10$ K, 25 K, 50 K, 100 K, 200 K and 300 K), respectively. At $T = 2$ K (Figure 8), the magnetization is almost saturated in a field of 5 T, with a mean magnetic moment per Fe atom $\mu_{Fe} = 2.59 \pm 0.05\ \mu_B$, well above the bulk value.

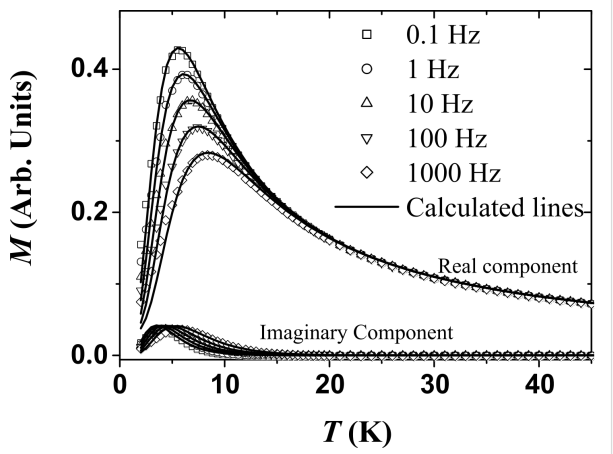


Figure 7: AC susceptibility measured for various frequencies (symbols) and their fits (solid lines).

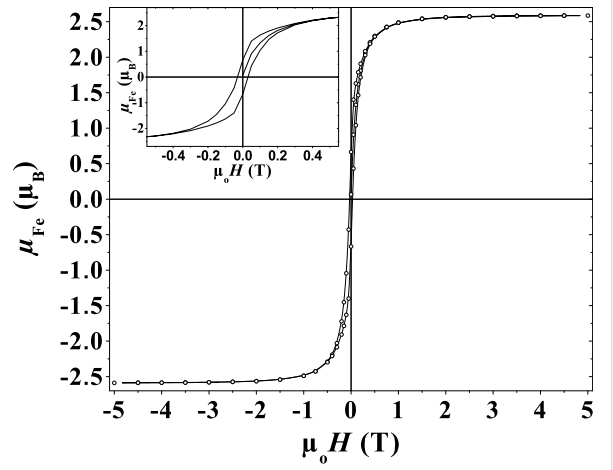


Figure 8: Hysteresis loop measured at 2 K. Inset: enlargement near zero field showing the coercive field.

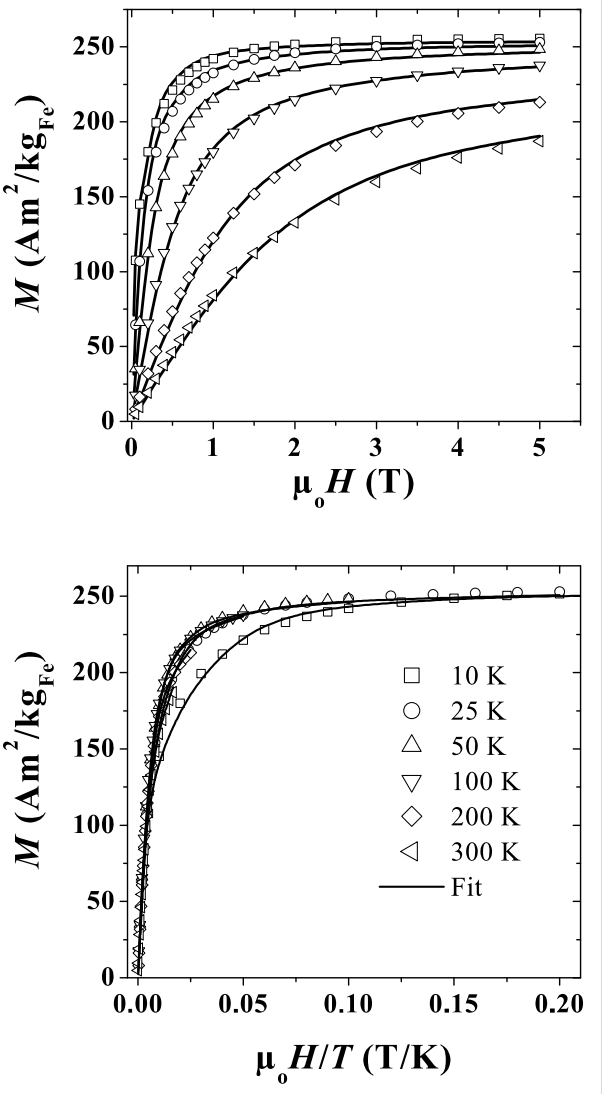


Figure 9: Magnetization curves in the superparamagnetic regime plotted versus the applied magnetic field (top) and versus the magnetic field divided by the temperature (bottom), for different temperatures.

Above T_B (Figure 9, top), the hysteretic behaviour disappears, and the magnetization measured at 5 T progressively decreases with increasing temperature. The plot of these curves as a function of H/T exhibits some deviations from the pure Langevin behaviour (Figure 9, bottom). In low fields, the slope is practically the same for temperatures up to 100 K, and then starts to decrease as a consequence of the decrease of spontaneous magnetization (M_S) with increasing temperature. Moreover, just below the magnetic saturation, some deviations arise, especially for the curve measured at $T = 10$ K ($\approx 2 \times T_B$), due to the influence of the anisotropy on the magnetization process [40].

The aim is now to determine a precise value of the effective anisotropy (K_{eff}), and the evolution of the spontaneous magnetization (M_S) with temperature. For an assembly of randomly oriented non-interacting particles in the superparamagnetic regime, the influence of the uniaxial anisotropy can be taken into account, leading to a modified Langevin function,

$$m = \frac{M_S(T)}{2}\int_0^{\pi} d\theta_b \sin\theta_b m(\theta_b) \qquad (2)$$

with

$$m(\theta_b) = \frac{N(\theta_b)}{D(\theta_b)},\ \sigma = \frac{K_{eff}(T)v}{k_B T},\ \xi = \frac{M_S(T)vH}{k_B T} \qquad (3)$$

$$N(\theta_b)=\int_0^{\pi} d\theta\ \sin\theta\ \exp\left(\xi\cos(\theta_b-\theta)+\sigma\cos^2\theta\right) \times[\sin\theta_b\sin\theta I_1(\xi\sin\theta_b\sin\theta) +\cos\theta_b\cos\theta I_0(\xi\sin\theta_b\sin\theta)] \quad (4)$$

$$D(\theta_b)=\int_0^{\pi} d\theta\sin\theta\ \exp\left(\xi\cos(\theta_b-\theta)+\sigma\cos^2\theta\right) \times I_0(\xi\sin\theta_b\sin\theta) \quad (5)$$

θ_b and θ define the angle of the applied magnetic field and magnetic moment with respect to the anisotropy axis [40], respectively. Interestingly, in low fields, for such an assembly of NPs, the susceptibility ($\chi = m/H$) versus temperature follows a Curie law independent of the anisotropy [40]. It should be noted that this expression depends on M_S and K_{eff} which are both temperature dependent.

The static ZFC-FC curves can be modelled according to the usual expressions for non-interacting NPs with a uniaxial effective anisotropy including a log-normal size distribution [18],

$$m(T)=\frac{1}{\int_0^{\infty} v\,f(v)\,dv}\left(\begin{array}{l}\int_0^{v_B(T)} m_{sup}(T)\,v\,f(v)\,dv \\ +\int_{v_B(T)}^{\infty} m_{bl}(T)\,v\,f(v)\,dv\end{array}\right) \quad (6)$$

where

$$m_{Sup}(T,\omega)=\frac{M_s^2(T)v}{3k_BT}H$$

defines the superparamagnetic contribution, and where m_{bl} is defined as

$$m_{bl}(T,\omega)=\frac{M_s^2(T)}{3K_{eff}}H \text{ and } m_{bl}(T,\omega)=\frac{\ln(\tau_m/\tau_0)M_s^2(T)}{3K_{eff}}H,$$

corresponding to the blocked contributions in the ZFC and FC experiments, respectively. $v_B(T)=\ln(\tau_m/\tau_0)k_BT/K_{eff}$ is the critical volume above (below) which the particles are in the blocked (superparamagnetic) state. This critical volume depends also on τ_o, which is extracted from the dependence of T_B versus τ_m (see below). In the superparamagnetic state, the magnetization is given by,

$$m(T)=\frac{1}{\int_0^{\infty} v\,f(v)\,dv}\int_0^{\infty}\frac{M_S^2(T)v}{3k_BT}H\,v\,f(v)\,dv = \frac{1}{\int_0^{\infty} v\,f(v)\,dv}\frac{M_S^2(T)}{3\,k_BT}H\int_0^{\infty}v^2\,f(v)\,dv \quad (7)$$

Thus, in the case of non-interacting NPs, the variation of the spontaneous magnetization versus the temperature can be extracted by plotting $(m_{Sup_Exp}\,T)^{1/2}$ versus T, where m_{Sup_Exp} corresponds to the ZFC-FC magnetization measured in the SP regime well above T_B.

Finally, the ac-susceptibility can be modelled from the following expressions [41]:

$$m(T,\omega)=\frac{1}{\int_0^{\infty} v\,f(v)dv}\int_0^{\infty} m_v(T,\omega)v\,f(v)dv, \quad (8)$$

with

$$m_v(T,\omega)=\frac{m_{Sup}(T)+i\omega\tau(T)m_{bl}(T)}{1+i\omega\tau(T)} \quad (9)$$

With these equations, it is possible to extract precisely the size distribution, the magnetic parameter $M_S(T)$ and the low temperature value of K_{eff}. We first analyse the dependence of the relaxation time on temperature. Figure 10 displays the plot of $\log(\tau_m)$ versus $1/T_B$, this curve allows the determination of the pre-exponential time τ_o of the relaxation time τ. According to Equation 1, linear behaviour is expected. Fitting the variation of $\log(\tau_m)$ versus $1/T_B$ in the range of the longest measurement times gives τ_0 = 2 ps. A deviation is observed for the

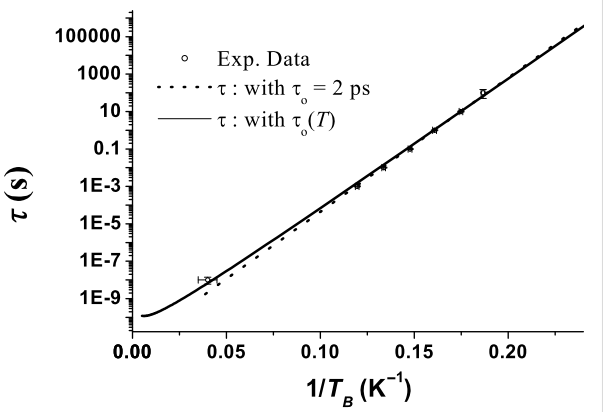


Figure 10: Relaxation time versus the inverse of temperature.

shortest measuring times corresponding to the Mössbauer experiment. This deviation is reduced when the temperature dependence of $\tau_0(T) \propto \sqrt{T}$ is taken into account [33-35,42]. This value is small compared to the expected, and usually measured, values, which are in the nanosecond range [43]. However, it is within the same range as Co NPs of similar size [44].

In a second step, we determine the temperature dependence of M_S, from the static magnetization ZFC-FC curves by plotting $M_S(T) \propto (m_{Sup_Exp}\ T)^{1/2}$ versus T^n.

As shown in the inset of Figure 6, M_S follows a $M_S(T) = M_S(T = 0)[1-\alpha T^n]$ law, where $n = 1.6 \pm 0.05$ and $\alpha = 3.27\ 10^{-5}\ K^{-1.6}$ allow the best fit. Even if the decrease of M_S is faster than in the case of bulk systems, as a result of lower surface coordination number [45], M_S remains above the bulk value, even at 300 K [46].

In a third step, knowing $\tau(T)$ and $M_S(T)$, the static ZFC-FC and the AC susceptibility curves (Figure 6 and Figure 7, respectively) are fitted with the same size distribution $f(v)$ and K_{eff}. As suggested by the narrow peak of the ZFC magnetization around T_B, the size distribution is very narrow (standard deviation of 0.15) centred on an average diameter of 1.6 nm. This magnetic size corresponds to that deduced from morphological studies by TEM. It approximately corresponds to clusters containing 150 to 200 atoms. Fitting these curves leads to an estimation of the effective anisotropy $K_{eff} = (3.7 \pm 1.0)\cdot 10^5$ J/m^3 well above the bulk value. Another estimation of K_{eff} was obtained by fitting the magnetization curves in the superparamagnetic regime. In this case, the size distribution was not taken into account since its influence can be neglected. A slightly larger value, $K_{eff} = (5.0 \pm 1.0)\cdot 10^5$ J/m^3, was obtained. Only the low temperature value of K_{eff} is accessible, since the influence of the anisotropy on the magnetization process rapidly vanishes and becomes negligible when T is above $10 \times T_B$. Thus, we cannot access the temperature dependence of K_{eff}.

In summary, the magnetization studies allow us to obtain some information on the magnetic size of these Fe NPs which contain 150–200 atoms on average. The mean magnetic moment per Fe atom $\mu_{Fe} = 2.59 \pm 0.05\ \mu_B$, is much higher than the value for bulk iron (2.2 μ_B), which well explains the strong hyperfine fields found with Mössbauer spectroscopy. The magnetic moment is higher than the one estimated by Furubayashi et al., who measured $\mu_{Fe} = 2.28\ \mu_B$ for particles with diameters around 2 nm [10], and the μ_{Fe} for Fe NPs stabilised by $HN(SiMe_3)_2$ [25]. It is, however, in good agreement with the values obtained for time-of-flight selected clusters by Billas et al. who measured μ_{Fe} in the range of 2.6–2.8 μ_B for clusters with less than 300 atoms (≤2 nm) [2]. This confirms that the synthesis using metal–organic precursors and an organic polymer as a matrix allows the growth of clusters with narrow size distributions and magnetic properties similar to those of free clusters, since the number of anchoring sites of the polymer on the surface is very small. The influence of surface coordination is thus limited. However, M_S decreases slowly with temperature in contrast to free-clusters [2]. It is difficult to interpret this latter effect, which is probably related to the structural order within the NPs. The origin of the enhancement of the magnetic moment must be related to the large surface to volume ratio. However, the adsorption during the synthesis of some hydrogen on the NP surface cannot be ruled out. Surface hydrides may form as has been demonstrated in the case of ruthenium [47]. This chemisorbed hydrogen could give a small spin contribution as evidenced with smaller clusters by Knickelbein and estimated to be 0.4 μ_B per adsorbed atom [48]. In our case, this contribution is not sufficient to explain the total magnetization per Fe atom observed, and the increase of the magnetic moment is thus related to an intrinsic effect as a consequence of the size reduction.

The value of the effective anisotropy K_{eff} in the range of $(3.7–5.0)\cdot 10^5$ J/m^3 is much higher than the bulk value, and larger than that deduced with micro-SQUID techniques from the magnetization curve of a single α-Fe NP containing 800 atoms embedded in a Nb matrix [49]. However, our result fits the diameter (Φ) dependence observed by Bødker et al., which follows $K_{eff} = K_v + 6/\Phi\ K_s$, with $K_v = 3\cdot 10^4$ J/m^3 and $K_s = 0.09$ mJ/m^2 [12]. It is quite surprising that, whatever the surface state and the crystallographic order, a magnetic anisotropy of the same order of magnitude should be obtained (for comparison $K_v \approx 7\cdot 10^4$ J/m^3 in bulk iron at low temperature). The origin of this enhancement is still an open question, since in the expression $K_{eff} = K_v + 6/\Phi\ K_s$, the second contribution has been derived considering a sphere, and a sphere should not induce any surface anisotropy. Most probably, with reduced size, deviations from sphericity become more important as a consequence of the presence of facets or incomplete surface layers, thus leading to a strong surface anisotropy.

C. FMR spectra

Ferromagnetic resonance experiments (FMR) have been performed in order to obtain some estimation of the relative contributions of the orbital and spin magnetic moments [50]. The most precise way to measure this ratio is to measure the frequency dependence of the resonant field [51,52]. We propose another approach based on the temperature dependence of the resonance field. Figure 11 displays the resonance curves, i.e., the derivative of the absorption line d(*Abs.*)/d*H,* measured at a frequency $\omega/2\pi = 9.5$ GHz for several temperatures well above

T_B in the SP regime. Upon decreasing the temperature, the absorption lines broaden, become inhomogeneous and shift toward low magnetic fields. The inset in Figure 11 displays the plot of the temperature dependence of the effective gyromagnetic ratio defined as $g_{\text{eff}} = \frac{\hbar}{\mu_B}\frac{\omega}{H_r}$.

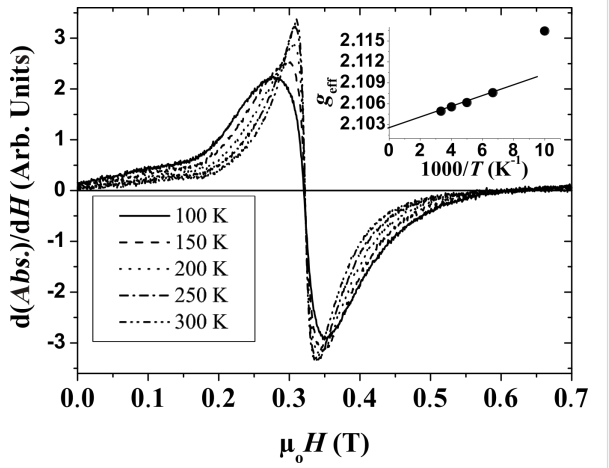


Figure 11: FMR spectra collected for various *T*. Inset displays the evolution of g_{eff} versus 1/*T*.

The resonant field (H_r) was defined as d(*Abs.*)/dH = 0. At high temperature, g_{eff} displays a linear dependence when plotted as a function of T^{-1}. Well above T_B, the anisotropy field vanishes as a consequence of the SP behaviour. Under these conditions, we can demonstrate by expanding the relation defining the resonance condition [53], that $g_{\text{eff}} = g\,(1 + A\,T^{-1})$, where A = *cte* × 2 $K_{\text{eff}}/5k_B$. *cte* is a coefficient depending on the orientation of the NP with respect to the applied field [54]. This extrapolation is only valid as long as $\xi = M_S v/k_B T$ verifies the condition $\xi < 1$, which is not fulfilled when *T* is less than 100 K. Extrapolation towards $T^{-1} = 0\ K^{-1}$ leads to the gyromagnetic ratio *g* of the NPs. The value determined is 2.103 ± 0.001, close to the bulk value of 2.09. More precise measurements, especially at different frequencies, are required in order to confirm unambiguously if there is a small increase. Using this value, we estimate the ratio μ_L/μ_S by the Kittel relation $\mu_L/\mu_S = (g - 2)/2 = 0.05$ [55]. With these data, the values of average spin and orbital magnetic moments are estimated to be 2.46 μ_B and 0.13 μ_B, respectively. This demonstrates that the enhancement of the total magnetic moment has contributions from both μ_L and μ_S.

In comparison to the estimations made on other systems using XMCD [13-16], the average total magnetic moment per Fe atom is of the same order of magnitude. But, the ratio μ_L/μ_S is smaller in our case. Band structure calculations are in relative good agreement with our estimations, for both the total magnetic moment and the ratio μ_L/μ_S. We believe that the small size of the particles compared to ours and the interactions with the substrates could lead to a stronger enhancement of μ_L/μ_S. In thin films, the magnetic anisotropy is related to the anisotropy of the orbital moment [56]. This anisotropy of μ_L cannot be measured in the case of disordered NPs randomly oriented. However, we believe that the large orbital contribution should be anisotropic, which could explain the large effective magnetic anisotropy measured in these particles. Oriented NPs would be necessary to investigate this latter phenomenon.

Conclusion

Systems of well isolated metallic Fe NPs with diameters of less than 2 nm and embedded in a polymer have been synthesized by an organometallic approach. Structural studies reveal an unusual polytetrahedral atomic arrangement leading to locally both denser and less dense regions compared to the bulk phases. The large surface to volume ratio dominates the electronic properties and thus the magnetic properties. The total magnetic moment is increased since both the spin and orbital contributions are increased. Large hyperfine fields related to surface sites have been demonstrated, showing the influence of the reduction of surface coordination on the magnetic moment. Both the spin and orbital moments are also involved in this enhancement.

Acknowledgements

We acknowledge financial support through the II-04-004 EC contract of the European Commission for the XANES measurements at Hasylab and J. Wienold for technical support on X1. We thank R. E. Benfield for valuable discussions and help during the beam time at Hasylab, and A. Marie for recording SQUID and FMR data.

References

1. Bucher, J. P.; Douglass, D. C.; Bloomfield, L. A. *Phys. Rev. Lett.* **1991,** *66,* 3052–3055. doi:10.1103/PhysRevLett.66.3052
2. Billas, I. M. L.; Becker, J. A.; Chatelain, A.; de Heer, W. A. *Phys. Rev. Lett.* **1993,** *71,* 4067–4070. doi:10.1103/PhysRevLett.71.4067
3. Billas, I. M. L.; Chatelain, A.; de Heer, W. E. *Science* **1994,** *265,* 1682–1684. doi:10.1126/science.265.5179.1682
4. Apsel, S. E.; Emmert, J. W.; Deng, J.; Bloomfield, L. A. *Phys. Rev. Lett.* **1996,** *76,* 1441–1444. doi:10.1103/PhysRevLett.76.1441
5. Cox, A. J.; Louberdack, J. G.; Apsel, S. E.; Bloomfield, L. A. *Phys. Rev. B* **1994,** *49,* 12295–12298. doi:10.1103/PhysRevB.49.12295
6. Pastor, G. M.; Dorantes-Davila, J.; Bennemann, K. H. *Phys. Rev. B* **1989,** *40,* 7642–7654. doi:10.1103/PhysRevB.40.7642
7. Franco, J. A.; Vega, A.; Aguilera-Granja, F. *Phys. Rev. B* **1999,** *60,* 434–439. doi:10.1103/PhysRevB.60.434
8. Pastor, G. M.; Dorantes-Davila, J.; Pick, S.; Dreyssé, H. *Phys. Rev. Lett.* **1995,** *75,* 326–329. doi:10.1103/PhysRevLett.75.326
9. Sipr, O.; Kosuth, M.; Ebert, H. *Phys. Rev. B* **2004,** *70,* 174423. doi:10.1103/PhysRevB.70.174423

10. Furubayishi, T.; Nakatani, I.; Saegusa, N. *J. Phys. Soc. Jpn.* **1987,** *56,* 1855–1858. doi:10.1143/JPSJ.56.1855
11. Bødker, F.; Mørup, S.; Oxborrow, C. A.; Linderoth, S.; Madsen, M. B.; Niemantsverdriet, J. M. *J. Phys.: Condens. Matter* **1992,** *4,* 6555. doi:10.1088/0953-8984/4/31/008
12. Bødker, F.; Mørup, S.; Linderoth, S. *Phys. Rev. Lett.* **1994,** *72,* 282–285. doi:10.1103/PhysRevLett.72.282
13. Lau, J. T.; Föhlisch, A.; Nietubyć, R.; Reif, M.; Wurth, W. *Phys. Rev. Lett.* **2002,** *89,* 057201. doi:10.1103/PhysRevLett.89.057201
14. Edmonds, K. W.; Binns, C.; Baker, S. H.; Thornton, S. C.; Norris, C.; Goedkoop, J. B.; Finazzi, M.; Brookes, N. B. *Phys. Rev. B* **1999,** *60,* 472–476. doi:10.1103/PhysRevB.60.472
15. Binns, C.; Baker, S. H.; Maher, M. J.; Louch, S.; Thornton, S. C.; Edmonds, K. W.; Dhesi, S. S.; Brookes, N. B. *Phys. Status Solidi A* **2002,** *189,* 339–350. doi:10.1002/1521-396X(200202)189:2<339::AID-PSSA339>3.0.CO;2-8
16. Ohresser, P.; Brookes, N. B.; Padovani, S.; Scheurer, F.; Bulou, H. *Phys. Rev. B* **2001,** *64,* 104429. doi:10.1103/PhysRevB.64.104429
17. Osuna, J.; de Caro, D.; Amiens, C.; Chaudret, B.; Snoeck, E.; Respaud, M.; Broto, J.-M.; Fert, A. R. *J. Phys. Chem.* **1996,** *100,* 14571–14574. doi:10.1021/jp961086e
18. Respaud, M.; Broto, J. M.; Rakoto, H.; Fert, A. R.; Thomas, L.; Barbara, B.; Verelst, M.; Snoeck, E.; Lecante, P.; Mosset, A.; Osuna, J.; Ely, T. O.; Amiens, C.; Chaudret, B. *Phys. Rev. B* **1998,** *57,* 2925–2935. doi:10.1103/PhysRevB.57.2925
19. Margeat, O.; Dumestre, F.; Amiens, C.; Chaudret, B.; Lecante, P.; Respaud, M. *Prog. Solid State Chem.* **2005,** *33,* 71–79. doi:10.1016/j.progsolidstchem.2005.11.002
20. Dumestre, F.; Chaudret, B.; Amiens, C.; Renaud, P.; Fejes, P. *Science* **2004,** *303,* 821–823. doi:10.1126/science.1092641
21. Cordente, N.; Amiens, C.; Chaudret, B.; Respaud, M.; Senocq, F.; Casanove, M.-J. *J. Appl. Phys.* **2003,** *94,* 6358. doi:10.1063/1.1621081
22. Dassenoy, F.; Casanove, M.-J.; Lecante, P.; Verelst, M.; Snoeck, E.; Mosset, A.; Ould Ely, T.; Amiens, C.; Chaudret, B. *J. Chem. Phys.* **2000,** *112,* 8137. doi:10.1063/1.481414
23. van de Waal, B. W. *J. Non-Cryst. Solids* **1995,** *189,* 118–128. doi:10.1016/0022-3093(95)00208-1
24. Bellissent, R.; Galli, G.; Grinstaff, M. W.; Migliardo, P.; Suslick, K. S. *Phys. Rev. B* **1993,** *48,* 15797–15800. doi:10.1103/PhysRevB.48.15797
25. Lacroix, L.-M.; Lachaize, S.; Falqui, A.; Blon, T.; Carrey, J.; Respaud, M.; Dumestre, F.; Amiens, C.; Margeat, O.; Chaudret, B.; Lecante, P.; Snoeck, E. *J. Appl. Phys.* **2008,** *103,* 07D521. doi:10.1063/1.2837625
26. Hafner, J.; Hobbs, D. *Phys. Rev. B* **2003,** *68,* 014408. doi:10.1103/PhysRevB.68.014408
27. Dinega, D. P.; Bawendi, M. G. *Angew. Chem., Int. Ed.* **1999,** *38,* 1788–1791. doi:10.1002/(SICI)1521-3773(19990614)38:12<1788::AID-ANIE1788>3.0.CO;2-2
28. Sun, S.; Murray, C. B. *J. Appl. Phys.* **1999,** *85,* 4325. doi:10.1063/1.370357
29. XANES measurements were performed on the X1 spectrometer at Hasylab in Hamburg, Germany (http://www-hasylab.desy.de/index.htm). The samples were prepared without dilution as 5 mm large, disk shaped, pellets. The measurements were done in transmission mode at room temperature using a silicon monochromator set for diffraction from (111) planes.
30. Grunes, L. A. *Phys. Rev. B* **1983,** *27,* 2111–2131. doi:10.1103/PhysRevB.27.2111
31. Long, G. J.; Hautot, D.; Pankhurst, Q. A.; Vandoarmel, D.; Grandjean, F.; Gaspard, J. P.; Briois, V.; Hyeon, T.; Suslick, K. S. *Phys. Rev. B* **1998,** *57,* 10716–10722. doi:10.1103/PhysRevB.57.10716
32. Westre, T. A.; Kennepohl, P.; DeWitt, J. G.; Hedman, B.; Hodgson, K. O.; Solomon, E. I. *J. Am. Chem. Soc.* **1997,** *119,* 6297–6314. doi:10.1021/ja964352a
33. Néel, L. *Ann. Geophys. (C. N. R. S.)* **1949,** *5,* 99.
34. Brown, W. F., Jr. *Phys. Rev.* **1963,** *130,* 1677–1686. doi:10.1103/PhysRev.130.1677
35. Aharoni, A. *Phys. Rev.* **1964,** *135,* A447–A449. doi:10.1103/PhysRev.135.A447
36. Dormann, J. L.; D'Orazio, F.; Lucari, F.; Tronc, E.; Prené, P.; Jolivet, J. P.; Fiorani, D.; Cherkaoui, R.; Nogues, M. *Phys. Rev. B* **1996,** *53,* 14291–14297. doi:10.1103/PhysRevB.53.14291
37. Bødker, F.; Mørup, S.; Oxborrow, C. A.; Madsen, M. B.; Niemantsverdriet, J. W. *J. Magn. Magn. Mater.* **1992,** *104–107,* 1695–1696. doi:10.1016/0304-8853(92)91513-S
38. Ohnishi, S.; Weinert, M.; Freeman, A. J. *Phys. Rev. B* **1984,** *30,* 36–43. doi:10.1103/PhysRevB.30.36
39. Tyson, J.; Owens, A. H.; Walker, J. C.; Bayreuther, G. *J. Appl. Phys.* **1981,** *52,* 2487. doi:10.1063/1.328976
40. Respaud, M. *J. Appl. Phys.* **1999,** *86,* 556. doi:10.1063/1.370765
41. Gittlemann, J. I.; Abeles, B.; Bozowski, S. *Phys. Rev. B* **1974,** *9,* 3891–3897. doi:10.1103/PhysRevB.9.3891
42. Coffey, W. T.; Crothers, D. S. F.; Kalmykov, Yu. P.; Massawe, E. S.; Waldron, J. T. *J. Magn. Magn. Mater.* **1993,** *127,* L254–L260. doi:10.1016/0304-8853(93)90039-5
43. Bødker, F.; Mørup, S.; Pedersen, M. S.; Svendlinh, P.; Jonsson, G. T.; Garcia-Palacios, J. L.; Lazaro, F. J. *J. Magn. Magn. Mater.* **1998,** *177–181,* 925–927. doi:10.1016/S0304-8853(97)00782-8
44. Respaud, M.; Goiran, M.; Broto, J. M.; Lionti, F.; Thomas, L.; Barbara, B.; Ould Ely, T.; Amiens, C.; Chaudret, B. *EPL* **1999,** *47,* 122. doi:10.1209/epl/i1999-00361-2
45. Hendriksen, P. V.; Linderoth, S.; Lindgård, P.-A. *Phys. Rev. B* **1993,** *48,* 7259–7273. doi:10.1103/PhysRevB.48.7259
46. Köbler, U. *J. Phys.: Condens. Matter* **2002,** *14,* 8861. doi:10.1088/0953-8984/14/38/310
47. Pery, T.; Pelzer, K.; Buntkowsky, G.; Philippot, K.; Limbach, H.-H.; Chaudret, B. *ChemPhysChem* **2005,** *6,* 605–607. doi:10.1002/cphc.200400621
48. Knickelbein, M. B. *Chem. Phys. Lett.* **2005,** *353,* 221–225. doi:10.1016/S0009-2614(02)00024-6
49. Jamet, M.; Wernsdorfer, W.; Thirion, C.; Dupuis, V.; Mélinon, P.; Pérez, A.; Mailly, D. *Phys. Rev. B* **2004,** *69,* 024401. doi:10.1103/PhysRevB.69.024401
50. Farle, M. *Rep. Prog. Phys.* **1998,** *61,* 755. doi:10.1088/0034-4885/61/7/001
51. Antoniak, C.; Lindner, J.; Farle, M. *EPL* **2005,** *70,* 250. doi:10.1209/epl/i2004-10485-9
52. Ulmeanu, M.; Antoniak, C.; Wiedwald, U.; Farle, M.; Frait, Z.; Sun, S. *Phys. Rev. B* **2004,** *69,* 054417. doi:10.1103/PhysRevB.69.054417
53. Raikher, Y. L.; Stepanov, V. I. *Soviet Physics - JETP* **1992,** *75,* 764.
54. Respaud, M. Unpublished work, 2010.
55. Kittel, C. *Phys. Rev.* **1949,** *76,* 743–748. doi:10.1103/PhysRev.76.743
56. Bruno, P. *Phys. Rev. B* **1989,** *39,* 865–868. doi:10.1103/PhysRevB.39.865

License and Terms

This is an Open Access article under the terms of the Creative Commons Attribution License (http://creativecommons.org/licenses/by/2.0), which permits unrestricted use, distribution, and reproduction in any medium, provided the original work is properly cited.

The license is subject to the *Beilstein Journal of Nanotechnology* terms and conditions: (http://www.beilstein-journals.org/bjnano)

The definitive version of this article is the electronic one which can be found at: doi:10.3762/bjnano.1.13

Beilstein Journal of Nanotechnology

Magnetic nanoparticles for biomedical NMR-based diagnostics

Huilin Shao[1], Tae-Jong Yoon[1,2], Monty Liong[1], Ralph Weissleder[*1,3] and Hakho Lee[*1]

Review

Open Access

Address:
[1]Center for Systems Biology, Massachusetts General Hospital, 185 Cambridge St, CPZN 5206, Boston, MA 02114, U.S.A., [2]Department of Applied Bioscience, CHA University, Seoul 135-081, Korea and [3]Department of Systems Biology, Harvard Medical School, 200 Longwood Av, Alpert 536, Boston, MA 02115, U.S.A.

Email:
Ralph Weissleder[*] - rweissleder@mgh.harvard.edu; Hakho Lee[*] - hlee@mgh.harvard.edu

* Corresponding author

Keywords:
biosensor; diagnostics; magnetic nanoparticle; microfluidics; nuclear magnetic resonance

Beilstein J. Nanotechnol. **2010,** *1,* 142–154.
doi:10.3762/bjnano.1.17

Received: 16 September 2010
Accepted: 17 November 2010
Published: 16 December 2010

Guest Editors: U. Wiedwald and P. Ziemann

© 2010 Shao et al; licensee Beilstein-Institut.
License and terms: see end of document.

Abstract

Rapid and accurate measurements of protein biomarkers, pathogens and cells in biological samples could provide useful information for early disease diagnosis, treatment monitoring, and design of personalized medicine. In general, biological samples have only negligible magnetic susceptibility. Thus, using magnetic nanoparticles for biosensing not only enhances sensitivity but also effectively reduces sample preparation needs. This review focuses on the use of magnetic nanoparticles for in vitro detection of biomolecules and cells based on magnetic resonance effects. This detection platform, termed diagnostic magnetic resonance (DMR), exploits magnetic nanoparticles as proximity sensors, which modulate the spin–spin relaxation time of water molecules surrounding molecularly-targeted nanoparticles. By developing more effective magnetic nanoparticle biosensors, DMR detection limits for various target moieties have been considerably improved over the last few years. Already, a library of magnetic nanoparticles has been developed, in which a wide range of targets, including DNA/mRNA, proteins, small molecules/drugs, bacteria, and tumor cells, have been quantified. More recently, the capabilities of DMR technology have been further advanced with new developments such as miniaturized nuclear magnetic resonance detectors, better magnetic nanoparticles and novel conjugational methods. These developments have enabled parallel and sensitive measurements to be made from small volume samples. Thus, the DMR technology is a highly attractive platform for portable, low-cost, and efficient biomolecular detection within a biomedical setting.

Introduction

Rapid and sensitive measurement of clinically relevant biomarkers, pathogens and cells in biological samples would be invaluable for disease diagnosis, monitoring of malignancy, and for evaluating therapy efficacy in personalized medicine. To translate such molecular measurements into clinical settings, however, an assay would need to 1) provide high sensitivity and specificity, 2) minimize sample preparation and sample volume, and 3) ideally allow concurrent detection of diverse target moieties through multiplexed measurements. Biosensing strategies based on magnetic nanoparticles (MNPs) have recently received considerable attention, since they offer unique advantages over traditional detection methods. Specifically, because biological samples exhibit negligible magnetic background, MNPs can be used to obtain highly sensitive measurements in turbid samples with reduced sample preparation. In contrast, traditional detection strategies based on optical techniques, for example, are often affected by scattering, absorption, autofluorescence, and require extensive sample purification before measurements can be made.

To detect biomarkers using MNPs, several technologies have been developed [1]. These include techniques that use magnetometers, such as superconducting quantum interference device (SQUID) [2-4], magnetoresistive sensors [5-11], and Hall sensors [12], which directly measure the magnetic fields from magnetically-labeled biological targets. Another technology that has achieved considerable success is diagnostic magnetic resonance (DMR). Based on nuclear magnetic resonance (NMR) as the detection mechanism, DMR exploits MNPs as proximity sensors, which modulate the spin–spin relaxation time of water molecules adjacent to the molecularly-targeted MNPs. The latter create a local magnetic field and induce a change in proton relaxation rate in billions of neighboring water molecules [13]. Direct detection of magnetic moments with magnetometers requires MNP-labeled targets to be closely positioned to the sensing elements. DMR assays, however, are faster and simpler since the analytical signal is generated from the entire sample volume.

By developing optimized MNPs, DMR detection sensitivities for various target moieties have been considerably improved. To date, numerous magnetic biosensors have been designed to identify and quantify a wide range of targets including DNA/mRNA, proteins, small molecules/drugs, bacteria, and tumor cells. More recently, the development of miniaturized, chip-based NMR detector systems has served to further enhance DMR technology [14-16]. Such detectors can perform highly sensitive measurements on microliter sample volumes and in a multiplexed format. With the integration of key components (i.e., microcoils, microfluidic networks, NMR electronics, and a portable magnet), the DMR systems have now demonstrated their potential for portable, sensitive and rapid operation in a point-of-care setting [14,17-19].

This review will report on various aspects of MNPs, their use in DMR sensing, assay modes, and on recent developments in improving detection sensitivities. Specific biomedical DMR applications will also be summarized.

Magnetic nanoparticles and their relaxation properties

Nanoparticles have tremendous potential in the field of biomedical applications, primarily on account of their similar size to biological molecules, and because their properties can be fine-tuned during chemical synthesis. In particular, MNPs can be synthesized in such a way as to possess unique superparamagnetic properties, to be biocompatible, and to remain inert with respect to cells and molecules of interest. As the size of magnetic objects shrinks to the nanometer scale, it becomes energetically more favorable for them to have a single magnetic domain than to form domain walls and a consequent multidomain structure [20]. The upper limit for a single domain [$\sim(A/2K)^{1/2}$] is determined by the material properties: the exchange stiffness (A) and the anisotropy constant (K). For most magnetic materials (e.g., ferrite and iron), MNPs with a diameter <20 nm will have a single domain with magnetic moments aligned in a particular direction defined by magnetic anisotropy. At sufficiently high temperatures (above blocking temperature), thermal energy can induce free rotation of the magnetic moment. Thus, when MNPs are grouped together, they display a form of paramagnetic behavior, known as superparamagnetism: MNPs assume overall magnetic moments when placed in an external magnetic field but lose their moments when the field is removed. Distinct from paramagnetism, which arises from individual spins at the atomic or molecular level, superparamagnetism applies to magnetic elements that already assume a magnetically-ordered spin state (typically ferromagnetic or ferrimagnetic). This superparamagnetic property enables MNPs to avoid spontaneous aggregation in solution, a feature that makes them suitable for many biomedical applications. In its simplest form, an MNP is comprised of an inorganic magnetic core and a biocompatible surface coating that stabilizes the particle in physiological conditions. By applying suitable surface chemistry, functional ligands can be integrated and confer the MNP with molecular specificity.

Synthesis of magnetic nanoparticles

Synthetic methods for MNPs have been recently reviewed [15,16,21-25]. A variety of chemical methods, ranging from traditional wet chemistry to high-temperature thermal decompo-

sition, have been employed to synthesize MNPs. Colloidal iron oxide nanoparticles, which are used as clinical magnetic resonance imaging (MRI) contrast agents, are generally prepared via an aqueous co-precipitation method [25,26]. During these hydrolytic processes, control of solution pH and the addition of suitable coating surfactants are critical for regulating the nanoparticle size as well as the magnetic properties. Unfortunately, depending on the synthesis procedure used, magnetization can vary significantly among nanoparticles of similar sizes.

More recently, high quality MNPs have been prepared through thermal decomposition of organometallic precursors, in non-hydrolytic organic solutions containing surfactants [15,16,27-29]. Monomers are generated via high-temperature thermal decomposition of precursors. Above a supersaturation level, these monomers then aggregate to induce nucleation and nanoparticle growth. By tuning the growth conditions during this procedure (such as precursor choice, monomer concentration, growth temperature and time), it is possible to control the size, composition, and crystallinity of the nanoparticles. While high-temperature decomposition markedly improves size control, size distribution and crystallinity of MNPs, the resulting particles are encased in a hydrophobic coating. In order to achieve nanoparticle stability in aqueous media, this approach requires additional modifications. Techniques, such as the addition of an amphiphilic polymer [30] or surfactant exchange strategies [31-33], have been examined for their ability to transfer the hydrophobic MNPs into the aqueous phase.

Magnetic relaxation mechanism

When placed in an external field, each MNP creates a local magnetic field, which increases the field inhomogeneity. When water molecules diffuse within the periphery of the MNPs, the coherent precessions of water proton spins are perturbed. The net effect is a change in the magnetic resonance signal, which is measured as a shortening of the longitudinal (T_1, spin–lattice) and transverse (T_2, spin–spin) relaxation times. The capacities of MNPs to decrease T_2 and T_1 are respectively defined as the transverse (r_2) and the longitudinal (r_1) relaxivities. Typically, because the transverse relaxivities (r_2) of MNPs are greater than their longitudinal relaxivities (r_1), T_2 is used for NMR-based biosensing applications. With a higher r_2 relaxivity, fewer numbers of nanoparticles are required to produce detectable T_2 changes.

Within an ensemble of MNPs, magnetic relaxation properties depend on more than simply the particles' relaxivities; the organizational state of the ensemble is also important. Unlike evenly dispersed MNPs, aggregates of nanoparticles (self-assembled magnetic clusters) have been shown to enhance the net rate of transverse relaxation [13,34]. This unique phenomenon, known as magnetic relaxation switching (MRSw), is a cooperative process in which the interacting nanoparticles become more efficient at dephasing the spins of neighboring water protons, leading to a decrease in T_2 relaxation time. The phenomenon can be explained by the outer-sphere theory. For a given volume fraction of MNPs in solution, T_2 of the sample is inversely proportional to the cross-sectional area of the particles [35,36]. Thus, the same amount of magnetized material is much more effective when dispersed as fewer large nanoparticles than as a greater number of smaller ones [35]. In MRSw, nanoparticles aggregate to form self-assembled clusters, and the consequent increase in cross-sectional area of the particles shortens T_2 relaxation times.

DMR assay configurations

Analogous to MRI, DMR exploits targeted MNPs to modulate the spin–spin T_2 relaxation time of biological samples. Depending on the size of the target biomarker, DMR assays can take two forms.

For small molecular targets with sizes less than or comparable to that of the MNPs, MRSw assays can be used effectively for their detection and quantification. Small molecular analytes, such as drugs, metabolites, oligonucleotides, and proteins, can cross-link MNPs to promote relaxation switching. As indicated in Figure 1a, MRSw assays can be designed to cause forward switching: a process whereby molecular targets are used as cross-linking agents to assemble MNPs into clusters, thus effecting a corresponding decrease in T_2. Alternatively, the assays can cause reverse switching, where enzymatic cleavage or competitive binding of molecular targets disassembles preformed clusters to cause an increase in T_2. Note that MRSw assays are carried out without removing excess unbound MNPs.

For larger biological structures such as bacteria, entire mammalian cells or cellular components, targeted MNPs can be used to tag cell surface markers to impart a magnetic moment (Figure 1b). The change of $1/T_2$ is proportional to the number of MNPs bound, and also indicative of the abundance of relevant surface biomarkers. Unlike MRSw assays, this magnetic tagging strategy requires washing steps to remove excess unbound MNPs from the tagged biological targets.

Optimal magnetic nanoparticles for DMR detection sensitivity

To enhance DMR detection sensitivity, MNPs should possess the following characteristics: 1) exhibit superparamagnetic properties; 2) have high stability in aqueous media to avoid spontaneous aggregation, which could mimic target-induced

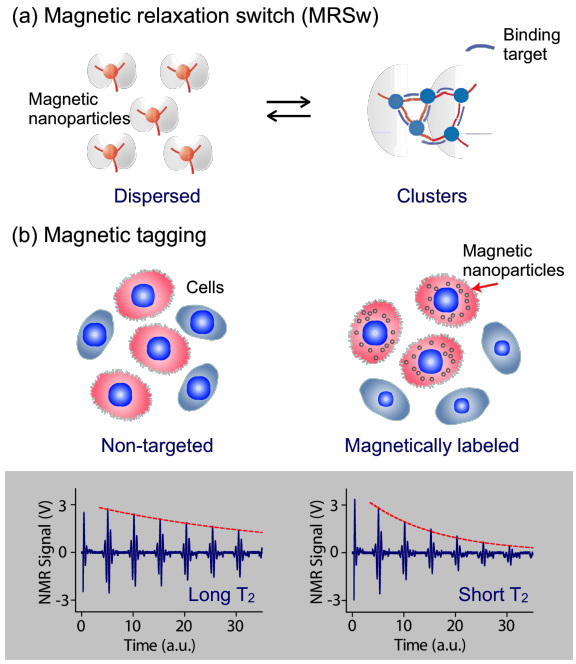


Figure 1: DMR assay configurations with magnetic nanoparticles (MNPs). (a) Magnetic relaxation switching (MRSw) assays detect the clustering of MNPs (forward switching), using a small target biomarker as a cross-linker, or the disassembly of pre-formed clusters (reverse switching) using an enzyme or competitive binding. When dispersed MNPs aggregate upon binding to targets, the self-assembled magnetic clusters become more efficient at dephasing nuclear spins of surrounding water protons, leading to a decrease in T_2 relaxation time. The reverse is true upon cluster disassembly. (b) Magnetic tagging assays detect the presence of bound MNPs on larger biological entities. Tagging of cell surface markers via targeted MNPs imparts a magnetic moment to cells, leading to a decrease in T_2 relaxation time. Unbound MNPs must be removed to ensure detection sensitivity of this assay mode. (Reproduced with permission from [13,14]. Copyright 2002, 2008 Nature Publishing Group.)

clustering; 3) have high magnetization and transverse relaxivity (r_2) to induce pronounced T_2 changes; and 4) have good surface chemistry to simplify conjugational procedures for attaching affinity molecules, such as antibodies and peptides. The MNPs and their representative strategies described below have been shown to be uniquely suited for DMR applications.

Cross-linked iron oxide nanoparticles

Cross-linked iron oxide (CLIO) nanoparticles have been widely used for DMR applications on account of their excellent stability and biocompatibility [13,37-42]. CLIO nanoparticles contain a superparamagnetic iron oxide core (3–5 nm monocrystalline iron oxide) composed of ferrimagnetic magnetite (Fe_3O_4) and/or maghemite (γ-Fe_2O_3). The metallic core is subsequently coated with biocompatible dextran, before being cross-linked with epichlorohydrin and activated by ammonia to provide primary amine group functionality. The amine groups can then be easily reacted with various agents containing anhydride, hydroxyl, carboxyl, thiol, or epoxide groups, to confer molecular specificity to the nanoparticle through bioconjugation [43]. Amine-terminated CLIO nanoparticles have an average hydrodynamic diameter of 25–40 nm, approximately 40–80 amines per nanoparticle for bioconjugation, and a r_2 of ~50 $s^{-1}{\cdot}mM^{-1}$ [Fe] [13,44]. Despite their relatively low r_2, their unique coating makes CLIO nanoparticles exceedingly robust for use in biological applications.

Doped-ferrite nanoparticles

The magnetization of ferrite nanoparticles can be further enhanced by doping the ferrite with ferromagnetic elements such as manganese (Mn), cobalt (Co) or nickel (Ni) [23,27,45]. Among the singly-doped ferrite MNPs, $MnFe_2O_4$ nanoparticles were found to exhibit the highest magnetization and r_2 value, on account of their electron spin configurations, followed by $FeFe_2O_4$, $CoFe_2O_4$, and $NiFe_2O_4$. More recently, it has been demonstrated that magnetization can be further enhanced via additional Zn^{2+} dopant control in $MnFe_2O_4$ nanoparticles [46]. In addition, nanoparticle magnetization is known to increase with particle size [33]. Ideally, each magnetic spin within a bulk magnetic material would be aligned parallel to the external magnetic field. However, in the nanoscale regime, surface spins tend to be tilted, a feature that reduces the overall magnetic moment. By increasing the MNP size, this surface effect is decreased, which in turn increases the magnetization. It has also been noted that transverse relaxivity r_2 is proportional to the cross-sectional area of the magnetic core [36]. Thus, increasing MNP size is an efficient method for enhancing r_2, since this strategy increases both the magnetization as well as the particle cross-sectional area.

Both magnetic doping and sizing strategies were recently employed by our laboratory to produce $MnFe_2O_4$ nanoparticles with superior r_2 relaxivity, for DMR biosensing applications [15]. These particles were synthesized by reacting iron(III) acetylacetonate [$Fe(acac)_3$], manganese(II) acetylacetonate [$Mn(acac)_2$] and 1,2-hexadecanediol at high temperature (300 °C). A seed-mediated growth approach was used to increase the size of the magnetic core from 10 nm to 12, 16, or 22 nm. $MnFe_2O_4$ nanoparticles with a diameter ≤16 nm were found to be highly monodisperse and superparamagnetic at 300 K (Figure 2a). The MNPs were subsequently rendered water-soluble using the small molecule, meso-2,3-dimercaptosuccinic acid (DMSA). DMSA has a terminal carboxylic acid group at one end which interacts directly with the magnetic core, and a sulfhydryl group at the other end which cross-links with other DMSA molecules to increase stability [27,33,47]. Due to DMSA's small size, the hydrodynamic diameter of $MnFe_2O_4$ nanoparticles was found to be smaller than that of CLIO nanoparticles, despite their larger magnetic core. More importantly, these $MnFe_2O_4$ nanoparticles possessed superior

relaxivities with r_2 values as high as 420 $s^{-1}{\cdot}mM^{-1}$[metal] (equal to 6×10^{-11} $s^{-1}{\cdot}$[particle/mL]$^{-1}$), more than 8 times greater than CLIO nanoparticles in metal basis (50 $s^{-1}{\cdot}mM^{-1}$[metal] or 0.7×10^{-12} $s^{-1}{\cdot}$[particle/mL]$^{-1}$) [15].

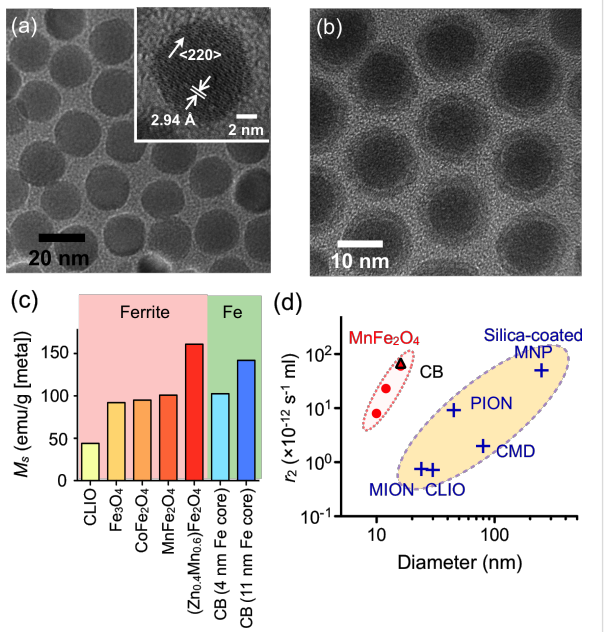


Figure 2: Higher r_2-relaxivity MNPs developed to improve detection sensitivity of in vitro diagnostics. (a) Transmission electron micrograph (TEM) images of manganese-doped ferrite nanoparticles ($MnFe_2O_4$). These nanoparticles have narrow size distribution and high crystallinity, and were synthesized by a seed-growth method to produce 10, 12, 16, and 22 nm nanoparticles. (b) TEM image of elemental iron (Fe) core/ferrite shell magnetic nanoparticles (CB; cannonballs). These particles have a large Fe core (11 nm) passivated with a thin ferrite shell (2.5 nm), resulting in high particle relaxivity. (c) Summary of published saturated magnetizations (M_s) for ferrite and Fe-based nanoparticles. Doped-ferrite and elemental Fe-based nanoparticles have improved M_s. (d) Comparison of the size and the r_2 relaxivity of various doped-ferrite and elemental Fe-based nanoparticles: CLIO, cross-linked iron oxide; MION, monocrystalline iron oxide; PION, polycrystalline iron oxide; and CMD, carboxymethyl dextran-coated MNP. (Adapted with permission from [15]. Copyright 2009 National Academy of Sciences, USA. Reproduced with permission from [16]. Copyright 2009 John Wiley and Sons, Inc.)

Elemental iron-based nanoparticles

The synthesis of elemental iron-based nanoparticles (i.e., with elemental iron rather than iron oxides) and their stable dispersion in aqueous media, has remained one of the most attractive goals in magnetic nanomaterial engineering. Elemental iron (Fe) has a higher magnetization than that of metal oxides, which consequently motivates the creation of Fe-core MNPs to achieve high r_2 relaxivities [48,49]. Because the Fe cores are extremely reactive and subject to rapid oxidation, they need to be encased by a protective shell in order to maintain their magnetic properties. Recently, a 16 nm Fe-core/ferrite shell MNP, known as "cannonball", was developed for DMR applications (Figure 2b) [16]. The cannonballs were synthesized by thermal decomposition of iron(0) pentacarbonyl [$Fe(CO)_5$] to form the Fe core. A protective ferrite shell was formed by controlled oxidation with oxygen gas; this method resulted in a thinner shell than that previously produced by chemical oxidizers [49], and thus the nanoparticles retained a larger Fe core. The cannonballs were then coated with DMSA as described above. Because of their large Fe core, superparamagnetic cannonballs showed high magnetization (139 emu·g^{-1} [Fe]) when compared to other published Fe core–shell structures (Figure 2c). The relaxivity of cannonballs is similar to that of the $MnFe_2O_4$ nanoparticles (6×10^{-11} $s^{-1}{\cdot}$[particle/mL]$^{-1}$), which is considerably higher than other commercially available or previously reported ferrite nanoparticles (Figure 2d).

Bioorthogonal nanoparticle detection

In addition to the previous strategies to improve the MNP core to enhance their relaxivities, surface modification of nanoparticles also improves their biosensing capabilities by amplifying their targeting valency for DMR applications. Bioorthogonal "click" chemistry has emerged as a novel method to label small molecules in complex biological media [50]. Most reported applications, however, rely on either the azide–alkyne cycloaddition, which requires a copper catalyst, or the strain-promoted azide–alkyne cycloaddition, which has relatively slow kinetics. Overcoming these limits, we have developed a new bioorthogonal chemistry based on the Diels–Alder cycloaddition between a 1,2,4,5-tetrazine (Tz) and a *trans*-cyclooctene (TCO). The reaction is fast, irreversible (covalent) and can be performed at room temperature without using a copper catalyst [51,52]. Recently, this chemistry has been successfully adapted to magnetic targeting, so as to improve nanoparticle binding efficiency and detection sensitivity. Termed 'bioorthogonal nanoparticle detection' (BOND), this technique provides a novel targeting platform in which Tz and TCO act as the coupling agents [53]. In a two-step labeling strategy (BOND-2; Figure 3), antibodies against biomarkers of interest are first modified with TCO, which is then used as a target to facilitate the coupling of Tz-modified nanoparticles onto mammalian cells. Because of the small size of the coupling reagents, their high multiplicity on antibodies/nanoparticles resulted in higher nanoparticle binding to cells. In comparison to alternative standard techniques, such as the avidin/biotin method, BOND-2 not only amplifies the biomarker signals but also significantly improves the detection sensitivity. Moreover, this platform is broadly-applicable and scalable for biomedical use. BOND-2 has already been successfully adapted for molecular profiling of cell samples by DMR [53], and has now established itself as a major targeting method in our laboratory. Table 1 lists a library of cellular makers tested with BOND-2 and DMR.

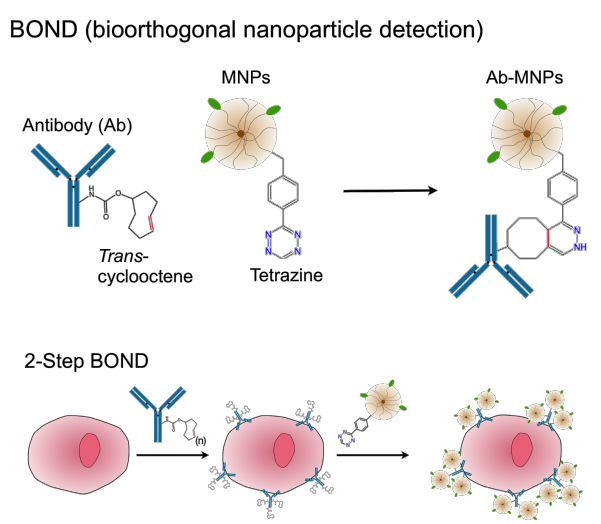


Figure 3: Bioorthogonal nanoparticle detection (BOND) strategy for DMR detection. The schematics show the conjugation chemistry between the antibody and the nanoparticle. This nanoparticle targeting platform uses a rapid, catalyst-free cycloaddition as the coupling mechanism. Antibodies against biomarkers were modified with *trans*-cyclooctene (TCO) and used as scaffolds to couple more tetrazine (Tz) modified nanoparticles onto live cells. The strategy is fast, specific, and amplifies biomarker signals. (Reproduced with permission from [53]. Copyright 2010 Nature Publishing Group.)

Miniaturized NMR systems

Nuclear magnetic resonance (NMR) can be detected with instruments such as clinical MRI scanners (routinely used for deep tissue whole body imaging), and NMR spectroscopy (used to study proteins and small molecules). Both of these techniques have been used to measure T_2 relaxation time for DMR biosensing. However, because these conventional instruments are bulky and expensive, they remain as specialized equipment in hospitals and laboratories. Benchtop relaxometers, which operate at lower NMR frequencies (100 kHz–50 MHz) with a permanent low-field magnet (<1 T), provide a lower-cost alternative for DMR biosensing [13,40]. However, these systems lack the capability for performing multiplexed measurements, and require large sample volumes (>100 μL) to achieve accurate measurements.

Chip-NMR biosensor

To overcome the limitations of conventional detectors and to address the need for fast, simple and high-throughput biosensing, our laboratory recently developed a chip-based microNMR (μNMR) device [14]. This miniaturized DMR device consists of an NMR probe containing microcoils for both radio-frequency (RF) excitation and NMR signal detection, on-board NMR electronics, a microfluidic network for sample handling, and a small permanent magnet for generating an external magnetic field.

The first μNMR prototype was designed with a 2 × 4 planar microcoil array that was lithographically patterned onto a glass substrate (Figure 4a) [14]. This array format enabled the performance of parallel measurements, and each microcoil held 5–10 μl of sample. In the second-generation μNMR, we changed our design to solenoidal coils [15,16], as such geometry provides higher signal-to-noise ratio (SNR) by producing

Table 1: List of extracellular and intracellular biomarkers tested with BOND-2 and DMR.

Tumors				Normal host cells
Extracellular		Intracellular		
A33	Glypican-3	α-fetoprotein	Cleaved PARP	anti-Fibroblast
B7H3	Hepsin	Cleaved CASP3	pH2AX	Calretinin A
B7-H4	HER2	CK5	phospho-EGFR	CD11b
CA125	HER3	CK7	phospho-p53	CD11c
CD133	Mesothelin	CK8	phospho-S6rp	CD14
CEA	MET	CK14	PSA	CD15
Claudin-1	Mucin1	CK18	PSMA	CD16
Claudin-3	Mucin16	CK19	s100A2	CD19
Claudin-7	Mucin18	CK20	s100A4	CD45
E-cadherin	P-cadherin	panCK	s100A6	CD56
EGFR	PCSA	EGFR-cytoplasmic	s100A11	CD68
EGFRv3	PSMA	gp100	s100B	CD56
EMMPRIN	PSAP	Ki-67	S6rp	CD68
EpCAM	TfR	MAGE-1	TTF-1	
FOLR1	TSPAN8	Melan-A	Tyrosinase	
FSH-R	uPAR	p53	Vimentin	
		PARP1	WT1	

more homogeneous radio-frequency magnetic fields for sample excitation. The SNR could be further increased by integrating the coil with a microfluidic channel (Figure 4b). The solenoidal coils were first wound around polyethylene tubes and subsequently immersed into a polymer (polydimethylsiloxan). Following polymer curing, the tubes were retracted to open up fluidic channels. The entire bore of the solenoid thus can be filled with sample to achieve maximal filling factor (≈1), the fraction of the coil volume occupied by the sample. Due to the larger cross-sectional area of the winding wires, the solenoidal coils also have smaller less electrical resistance than lithographically-patterned coils. With these advantages, the sample volume for DMR detection could be reduced by a factor of ~10 (to 1 μL) compared to the previous devices (~10 μL).

The microfluidic networks in the DMR system facilitate the handling of biological fluids, the effective mixing of MNPs with small sample volumes, and the distribution of small volumes to different coils for parallel sensing. The networks also serve to confine the samples to the most sensitive region of a given microcoil. Furthermore, a membrane filter can be inserted at the outlet of the solenoidal microcoil to retain large biological targets, whilst removing smaller contaminants such as unbound MNPs [16]. This configuration enables both the concentration of scant samples from large volumes, as well as the performance of on-chip washing steps.

The NMR electronics generate versatile RF pulse sequences to measure the longitudinal (T_1) and transverse (T_2) relaxation times, process raw NMR signals (amplification, frequency-conversion, filtering) for acquisition by a computer, and handle the multiplexed operation of an array of coils. In the first prototype, the NMR electronics was constructed as a tabletop system using discrete RF chips (e.g., AD9830 for RF generation and AD604 for NMR signal amplification; Analog Devices) and off-the-shelf RF components (e.g., ZAD-1 mixer, ZMSC-2 power splitter, and ZYSWA-2 RF switch; Mini-Circuits) [14]. In newer versions, these functionalities have been integrated onto a single CMOS IC chip [17,19]. This chip was designed to overcome the adverse effects associated with system miniaturization during NMR measurements, including 1) low NMR signals resulting from small sample volumes, and 2) fast signal decay due to field inhomogeneity produced by the portable magnet. These challenges were addressed by implementing low noise RF amplifiers with high voltage gain, and by developing an on-chip digital pulse generator for various pulse sequences. The latter enabled the accurate measurement of transverse (T_2) relaxation times by generating Carr–Purcell–

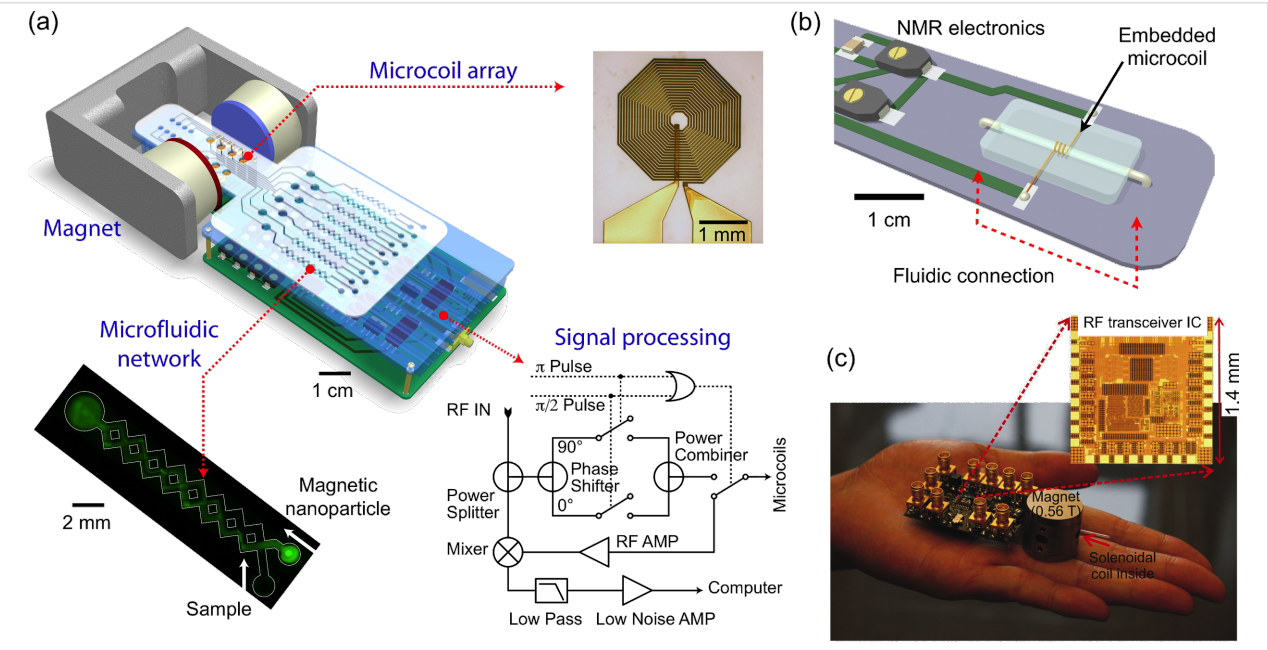


Figure 4: Miniaturized devices developed for DMR biosensing. (a) The first-generation miniaturized device to measure relaxation times of biological samples consists of an array of microcoils for NMR measurements, microfluidic networks for sample handling and mixing, miniaturized NMR electronics and a portable permanent magnet to generate a polarizing magnetic field. (b) The second-generation consists of a solenoidal coil embedded in a microfluidic device. As compared to the previous generation, this improved device has a higher filling factor, better signal-to-noise ratio, and reduced sample volume requirement to ~1 μL. (c) The latest 0.1 kg "palm" DMR system is 20× lighter and 30× smaller than previous generations. To achieve this significant size reduction, a small 0.56 T magnet was used. To compensate for the signal reduction from the smaller magnet, this device incorporates a new RF transceiver fully integrated in the 0.18 μm CMOS. (Reproduced with permission from [14]. Copyright 2008 Nature Publishing Group. Reproduced with permission from [15]. Copyright 2009 National Academy of Sciences, USA. Reproduced with permission from [19]. Copyright 2010 IEEE.)

Meiboom–Gill (CPMG) sequences to compensate for the inhomogeneity of the polarizing magnetic field.

In the latest implementation, the entire DMR system was packaged as a handheld unit for portable operation ("palm" NMR system; Figure 4c) [19]. When benchmarked against conventional NMR systems, these miniaturized devices provided both superior detection sensitivities and capabilities for multiplexed measurements on small sample volumes. In view of such advantages, the miniaturized DMR technology is well suited for fast, simple and high-throughput analysis of scant biological samples within a point-of-care setting.

DMR applications

DMR has been successfully applied to sensitively identify and quantify a wide range of biological targets including DNA/mRNA, proteins, enzyme activities, small molecules/drugs, bacteria, viruses and mammalian tumor cells, as summarized in Table 2. As described previously, the detection mode of DMR depends on the size of its target.

Table 2: Selected list of DMR assays developed to date[a].

Type	Target	MNP Sensor (MNP core diameter <20 nm)	Reference
DNA	Telomeres	$(CCCTAA)_3$-CLIO	[54]
RNA	GFP	CLIO-ATTTGCCGGTGT; TCAAGTCGCACA-CLIO	[13]
Soluble Proteins	Avidin	Biotin-CLIO	[14,55]
	GFP	Anti-GFP-CLIO	[13]
	β-HCG	Anti-HCG-CLIO	[56]
	Telomerase	Anti-telomerase-CLIO	[37]
	CA-125	Anti-CA125-CLIO	[14]
	VEGF	Anti-VEGF-CLIO	[14]
	α-fetoprotein	Anti-α-fetoprotein-CLIO	[14]
Enzyme activities	BamH1	CLIO-TTA-CGC-CTAGG-ATC-CTC; AAT-GCG-GGATCC-TAC-GAG-CLIO	[39]
	Methylase, MboI, DpnI	Methylated BamH1 CLIO	[39]
	Caspase-3	CLIO-Avidin-Biotin-GDEVDG-CLIO	[13]
	Renin	Biotin-IHPFHLVIHTK-Biotin; Avidin-CLIO	[57]
	Trypsin	Biotin-$(G)_4$RRRR$(G)_3$K-Biotin or Biotin-GPARLAIK-Biotin; Avidin-CLIO	[57]
	MMP-2	Biotin-GGPLGVRGK-Biotin; Avidin-CLIO	[57]
	Telomerase	CLIO-AATCCCAATCCC; AATCCCAATCCC-CLIO	[37,54]
	Peroxidases	Phenol-CLIO, tyrosines-CLIO	[41]
Small molecules	Drugs, enantiomers	D-Phenylalanine-CLIO	[58]
	Folate	Folate-CLIO	[59]
	Glucose	Concavalin-CLIO	[59]
	HA peptide	HA-CLIO	[59]
	Calcium	Calmodulin-CLIO; M13-CLIO or chelaters	[60,61]
	Influenza Tag peptide	Anti-Tag-CLIO	[62,63]
Pathogens	Herpes simplex virus	Anti-glycoproteinD(HSV-1)-CLIO; Anti-HSV1-CLIO	[40]
	Adenovirus-5	Anti-Adenovirus-5-CLIO	[40]
	S. aureus	Vancomycin-CLIO	[14]
	MTB/BCG	Anti-BCG-CLIO, Anti-BCG-Cannonball	[16]
Cells (Extracellular and intracellular proteins)	Tumor cell lines	Anti-Her2-CLIO, Anti-EGFR-CLIO, Anti-EpCAM-CLIO	[14]
	FNA (mouse xenograft)	Anti-Her2-$MnFe_2O_4$; Anti-EGFR-$MnFe_2O_4$, Anti-EpCAM-$MnFe_2O_4$	[15]
	Tumor cell lines (BOND amplification)	Anti-Her2-TCO, Anti-EGFR-TCO, Anti-EpCAM-TCO, Anti-Mucin1-TCO; Tz-CLIO; Many others, see Table 1	[53]

[a]BCG: Bacillus Calmette–Guérin; CLIO: cross-linked iron oxide; EGFR: epithelial growth factor receptor; EpCAM: epithelial cell adhesion molecule; FNA: fine needle aspirate; GFP: green fluorescent protein; HA peptide: hemagglutinin peptide; β-HCG: β-human chorionic gonadotropin; MMP-2: matrix metalloproteinase-2; MTB: mycobacterium tuberculosis; VEGF: vascular endothelial growth factor.

Proteins

The concept of forward MRSw sensing can be demonstrated with proteins, for example avidin, in model applications. In one early series of experiments, biotinylated MNPs were incubated with varying amounts of avidin [14]. As shown in Figure 5a, the binding of biotin to avidin resulted in clustering of MNPs and a concomitant avidin concentration-dependent change in T_2. By varying the concentration of MNPs, four orders of dynamic ranges were achieved, indicating that the system has a robust working range. Likewise, specific antibodies can also be used to perform MRSw on target protein molecules. As the second proof-of-principle analysis, green fluorescent protein (GFP)-sensitive nanoparticles were prepared by conjugating CLIO nanoparticles with anti-GFP polyclonal antibodies [13]. Using this system, GFP was rapidly and sensitivity detected in a dose-dependent manner while the addition of bovine serum albumin (BSA) protein as a control did not elicit any change in T_2 (Figure 5b). More recently, MRSw biosensors, capable of detecting soluble tumor biomarker proteins (such as CA-125, VEGF, and α-fetoprotein) were described, and used for parallel detection of multiple markers in blood samples with the μNMR device [14]. Finally, using the BOND-2 method, many other cancer proteins have been detected (Table 1).

Enzyme activities

The reverse MRSw strategy has been widely applied to the detection of enzymatic activities. Reverse sensors have been designed to detect and quantify proteases [38,64], endonucleases and methylases [39]. In these assays, the enzyme activity disassembles pre-formed clusters of MNPs; this disintegration translates the enzymatic activity into a detectable T_2 signal. In the first demonstration of this strategy, MNP aggregates were formed with the peptide sequence biotin-GDEVDGC. This sequence served as a linker, binding both an avidin-conjugated CLIO population (via the biotin/avidin interaction) as well as a second CLIO population (via the thiol provided by the terminal cysteine on the peptide) [13]. The subsequent addition of caspase-3 disassembled the aggregates by cleaving within the DEVD site, which led to a corresponding increase in T_2 relaxation time (Figure 5c). This dissociation was not observed when a specific caspase-3 inhibitor was added. A similar reverse switching strategy has been used to detect trypsin, renin, and matrix metalloproteinase 2 activities [57].

Forward MRSw assays on enzymatic activities have also been demonstrated via the assembly of nanoparticle biosensors (as a result of enzymatic reactions). For example, specific MNPs have been designed to assess human telomerase (hTERT) activity by hybridizing with the 30-base pair telomeric repeat sequences produced by hTERT activity [54]. More recently, myeloperoxidase (MPO) sensors were generated by attaching phenol-containing molecules, such as dopamine or serotonin, to CLIO nanoparticles [41]. In the presence of peroxidase activity, tyroxyl radicals were formed to cross-link the nanoparticles. Using the same assay configuration, leukocyte-derived MPO has been shown to play a critical role in the pathogenesis of atherosclerotic plaques [65].

Bacteria

Detection and quantification of large pathogens have been successfully demonstrated using the DMR platform, primarily through magnetic tagging of targets. For example, detection of

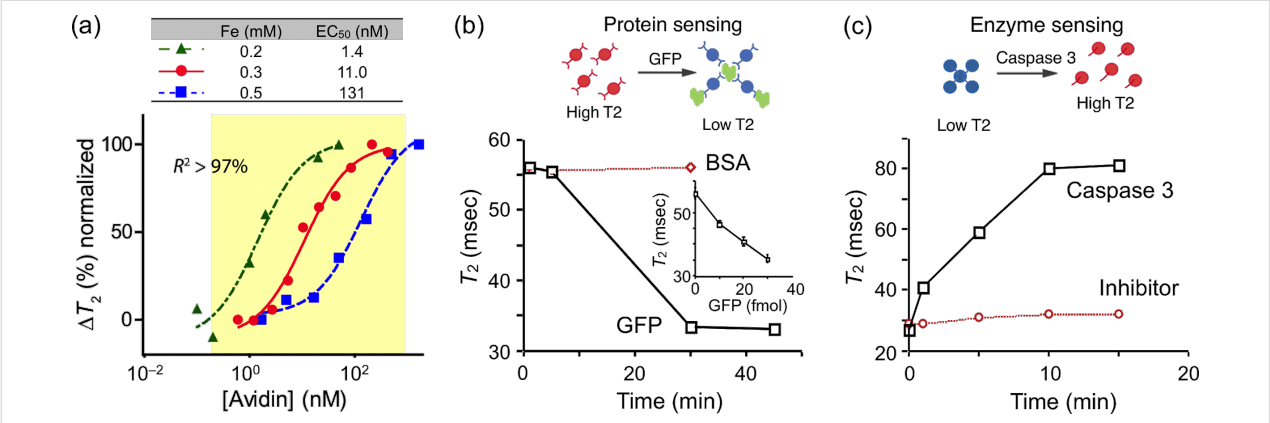


Figure 5: DMR detection of proteins and enzyme activities with MRSw sensors.
(a) Detection of avidin. Biotinylated MNPs were incubated with different amounts of avidin to cause clustering of the nanoparticles. The T_2 relaxation changes were dependent on avidin concentrations. (b) Detection of green fluorescent protein (GFP). MNPs conjugated with a polyclonal anti-GFP antibody were incubated with GFP or BSA as a control. T_2 relaxation time decreased with increasing GFP concentrations; the detection limit was down to the low femtomolar range. (c) Detection of enzyme activity of caspase-3. MNPs were clustered with a peptide linker containing the sequence DEVD and were rapidly dissociated upon the activity of caspase-3. This dissociation was not observed when a specific caspase-3 inhibitor was added. The enzyme-dependent disassembly of the MNP clusters resulted in an increase in T_2 relaxation time. (Reproduced with permission from [13,14]. Copyright 2002, 2008 Nature Publishing Group.)

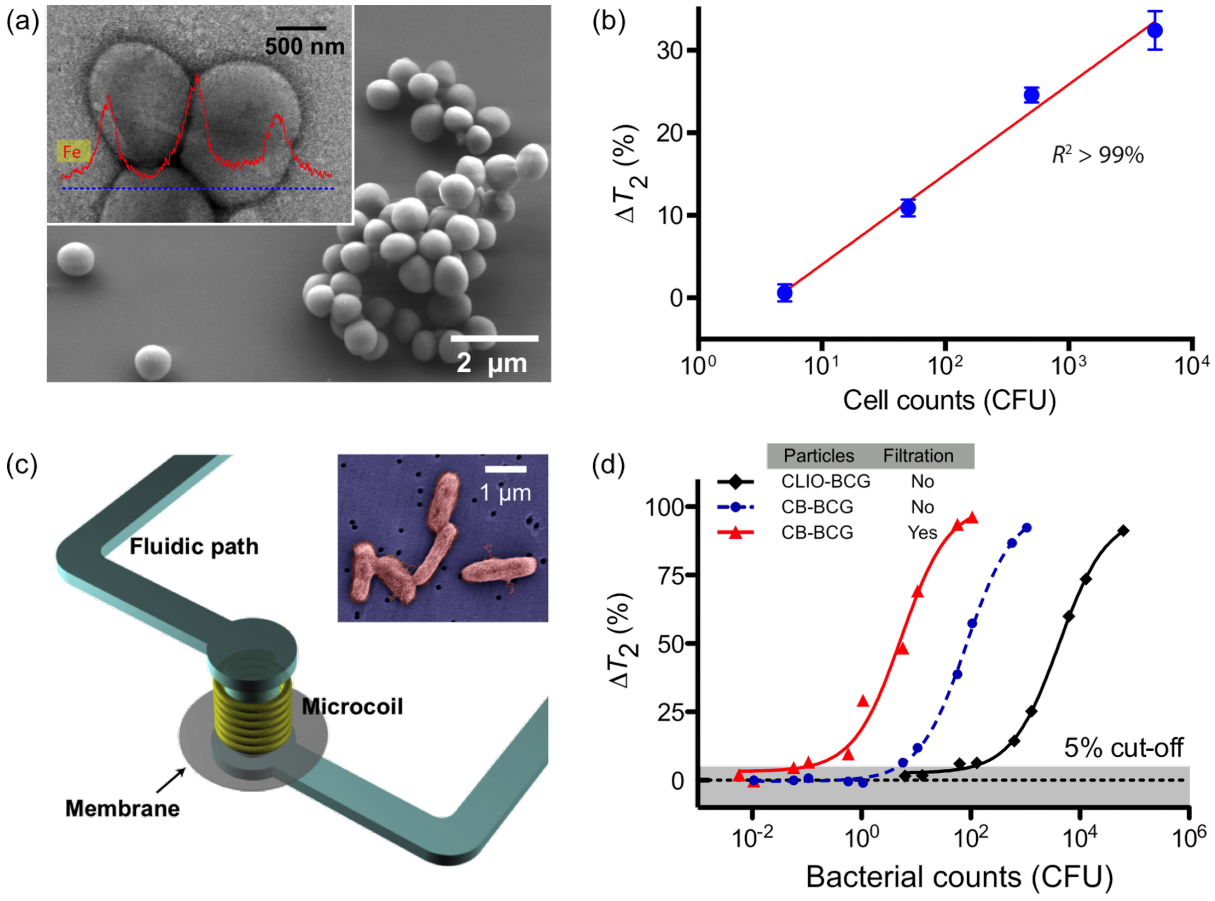


Figure 6: DMR detection of bacteria by tagging the bacterial samples with MNPs. (a) Scanning electron micrograph of *S. aureus.* Inset shows TEM of *S. aureus* targeted by CLIO conjugated with vancomycin. MNPs formed dense clusters on the bacterial wall. Elemental analysis by energy dispersive X-ray spectrometry further confirmed the binding of nanoparticles to the bacteria. (b) Changes to T_2 with varying number of *S. aureus.* The DMR system had a detection sensitivity of a few colony-forming units (CFUs) per microliter, with dynamic ranges over three orders of magnitude. (c) NMR-filter system for bacterial concentration and detection. It consists of a microcoil and a membrane filter integrated with a microfluidic channel. The membrane filter concentrates bacteria inside the NMR detection chamber to achieve high-detection sensitivity. Inset shows bacteria (Bacillus Calmette–Guérin, BCG) captured on the membrane filter after filtration. (d) Changes to T_2 with varying BCG bacterial counts. Detection limit was approximately 100 CFUs with CLIO nanoparticles and 6 CFUs with higher relaxivity cannonballs. Detection sensitivity was further increased to ~1 CFU using the built-in filtration. CLIO, cross-linked iron oxide; CB, cannonball (Fe@ferrite) MNP. (Reproduced with permission from [14]. Copyright 2008 Nature Publishing Group. Reproduced with permission from [16]. Copyright 2009 John Wiley and Sons, Inc.)

the bacterium *Staphylococcus aureus* was recently reported with the μNMR device. *S. aureus* were initially incubated with MNPs derivatized with vancomycin, a drug which binds to D-alanyl–D-alanine moieties in the bacterial cell wall to form dense clusters (Figure 6a) [14]. On account of the low sample volume required by the μNMR device, this first proof-of-concept analysis demonstrated a detection sensitivity of only a few colony-forming units (CFUs) per microliter sample (Figure 6b).

More recently, tuberculosis (TB) bacteria have been detected using DMR. In one study, the highly magnetic Fe-core/ferrite shell nanoparticles (CB; cannonballs) were used in combination with the second generation DMR device [16]. To evaluate the clinical utility of the DMR platform for TB detection, Bacillus Calmette-Guérin (BCG), used as a surrogate for *Mycobacterium tuberculosis*, was spiked into sputum samples. Following liquefaction, the biological samples were incubated with cannonballs conjugated to an anti-BCG monoclonal antibody. Unbound MNPs were then removed via a built-in membrane filter, embedded within the device (Figure 6c). This membrane (~100 nm size cut-off) not only removed excess unbound MNPs but also retained the BCG bacteria; thus was effective for both concentrating scant bacteria and removing background signal. In comparison to standard TB diagnostics, which involve time-consuming culture and acid-fast bacilli (AFB) smear microscopy, the DMR diagnostic technology showed unprecedented detection sensitivity and speed: as few

as 20 CFUs could be detected in 1 ml of sputum sample, in less than 30 minutes (Figure 6d). Currently, this detection technology is being adapted to detect infectious pathogens in clinical sputum samples.

Tumor cells

Sensitive detection and rapid profiling of tumor cell surface markers in unprocessed biological samples will undoubtedly have a significant impact on both the life sciences and clinical practice. DMR molecular profiling of Her2/*neu*, EGFR, and CD326 (EpCAM) cancer markers on mammalian cells was first demonstrated using the first-generation DMR device [14]. In these early experiments, CLIO nanoparticles were directly conjugated to monoclonal antibodies. More recently, the use of BOND-2 strategy has further advanced DMR profiling capabilities (Table 1). Cancer cells were targeted with CLIO nanoparticles via BOND-2. At a low cell count (~1000 cells per sample), parallel DMR measurements could be performed rapidly [53]. As a universal labeling approach, BOND-2 simplifies the preparation of the targeted MNPs for multiplexing and amplifies nanoparticle binding to cells.

Using the μNMR device with a solenoidal coil and the highly magnetic $MnFe_2O_4$ nanoparticles, detection sensitivity for cell sensing was remarkably improved (Figure 7a) [15]. Notably, as shown in Figure 7b, the detection threshold was reduced to approximately single-cell level, far surpassing the sensitivity seen in either previous DMR experiments or other conventional clinical methods. There was also a good correlation between DMR measurements and those obtained with flow cytometry

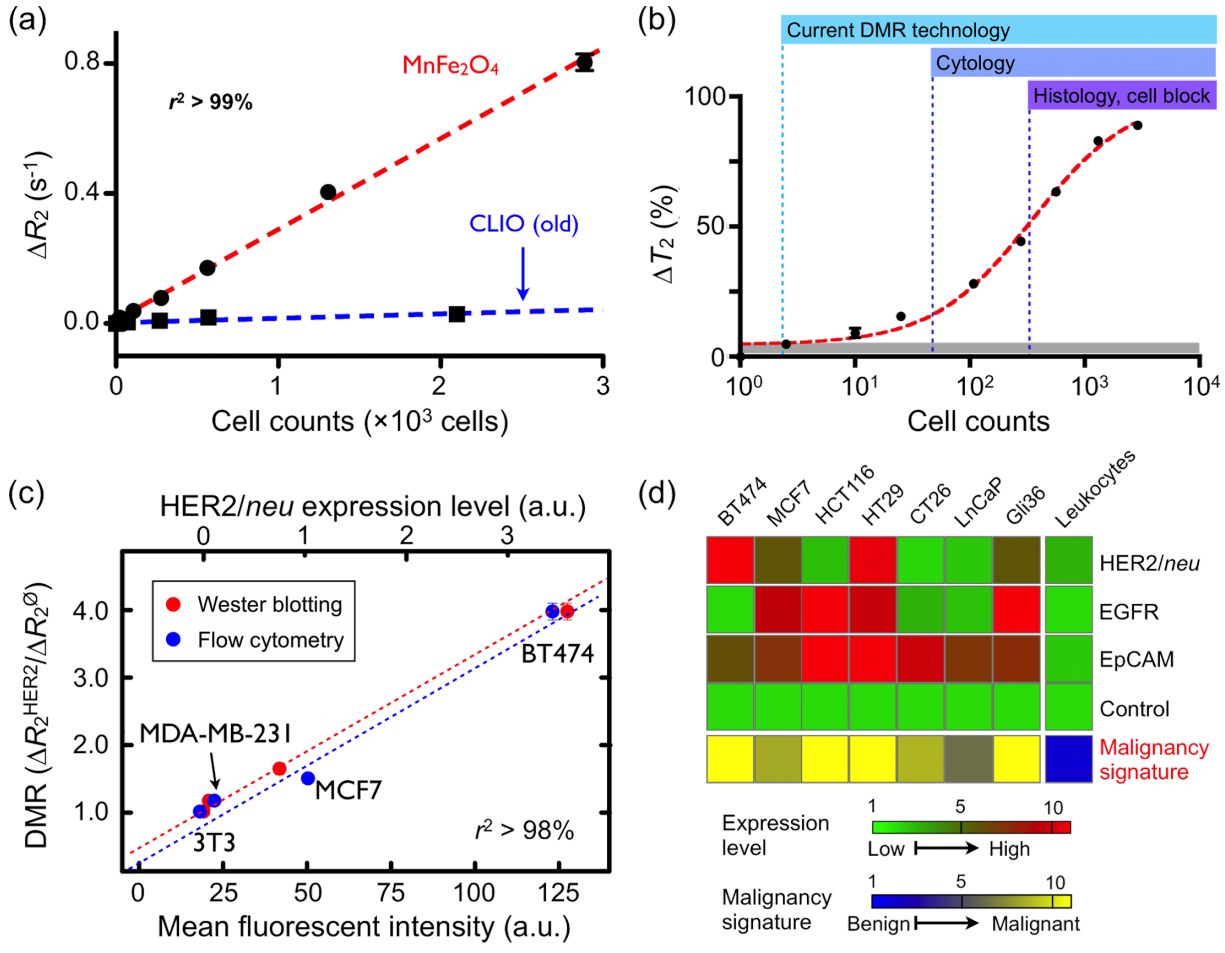


Figure 7: Tumor cell detection and profiling with the μNMR device. (a) Human breast cancer cells (BT474) were labeled with anti-Her2 CLIO and $MnFe_2O_4$ nanoparticles. The change in R_2 (R_2 =1/T_2) varied linearly with cell counts, and the detection sensitivity was 10× better using the more magnetic $MnFe_2O_4$ nanoparticles. (b) The detection sensitivity was approximately two cells (in 1 μL sample volume) with the improved μNMR device (Figure 4b) and the highly magnetic $MnFe_2O_4$ nanoparticles, making this detection platform superior to current clinical methods (cytology and histology). (c) DMR measurements correlated well with standard molecular analyses, such as flow cytometry and Western blot, but required substantially fewer cells. (d) Molecular profiling of fine-needle aspirates of mouse tumor xenografts. Three cancer markers (Her2/*neu*, EGFR, EpCAM) were profiled to increase the accuracy of diagnosis. Unmodified nanoparticles were used as a control to estimate cell concentration based on non-specific phagocytosis. (Reproduced with permission from Ref [15]. Copyright 2009 National Academy of Sciences, USA.)

and Western blot analysis (Figure 7c). Importantly, the DMR detection platform not only required far fewer cells than either of the alternative approaches, but also produced results in a fraction of the time (<15 minutes). The DMR platform has since been shown to be adaptable to rapid multi-target detection, where putative cancer cells can be profiled for multiple biomarkers; DMR is ideally suited to this use since it can perform measurements on a few cells in small sample volumes and in a multiplexed manner. Fine-needle aspirate biopsies from a panel of mouse xenograft tumors have already been successfully analyzed for Her2/*neu*, EGFR, and EpCAM expression. Furthermore, the multiple-marker targeting strategy has been shown to significantly improve the accuracy for correctly diagnosing cancer cells as malignant (Figure 7d). These, in addition to other advanced refinements to DMR sensing, are currently being applied to clinical trials of cancer cell profiling.

Conclusion

DMR represents a powerful combination of several cutting-edge technologies, namely nanomaterials, bioconjugation chemistry and microfabrication. As a novel technique, DMR offers a number of unique advantages, such as high detection sensitivity, rapid target measurement from minimal sample volumes, and the ability to profile a wide range of targets in a multiplexed manner. With new developments such as the advent of chip-based μNMR devices, optimized magnetic nanomaterials and advanced conjugation techniques, DMR shows potential as a robust and easy-to-use sensor system with significantly improved sensitivity and accuracy. Thus, it is likely that this technology will have broad applications in biomedicine, as well as clinical utility in point-of-care settings.

Acknowledgements

The authors thank N. Sergeyev for providing cross-linked dextran-coated iron oxide nanoparticles; Y. Fisher-Jeffes for reviewing the manuscript. This work was supported in part by NIH Grants (2RO1EB004626, U01-HL080731, U54-CA119349 and T32-CA79443). H. Shao acknowledges financial support from the B.S.-Ph.D. National Science Scholarship awarded by the Agency for Science, Technology and Research, Singapore.

References

1. Tamanaha, C. R.; Mulvaney, S. P.; Rife, J. C.; Whitman, L. J. *Biosens. Bioelectron.* **2008,** *24,* 1–13. doi:10.1016/j.bios.2008.02.009
2. Millen, R. L.; Nordling, J.; Bullen, H. A.; Porter, M. D.; Tondra, M.; Granger, M. C. *Anal. Chem.* **2008,** *80,* 7940–7946. doi:10.1021/ac800967t
3. Chemla, Y. R.; Grossman, H. L.; Poon, Y.; McDermott, R.; Stevens, R.; Alper, M. D.; Clarke, J. *Proc. Natl. Acad. Sci. U. S. A.* **2000,** *97,* 14268–14272. doi:10.1073/pnas.97.26.14268
4. Schaller, V.; Sanz-Velasco, A.; Kalabukhov, A.; Schneiderman, J. F.; Oisjoen, F.; Jesorka, A.; Astalan, A. P.; Krozer, A.; Rusu, C.; Enoksson, P.; Winkler, D. *Lab Chip* **2009,** *9,* 3433–3436. doi:10.1039/b912646e
5. Baselt, D. R.; Lee, G. U.; Natesan, M.; Metzger, S. W.; Sheehan, P. E.; Colton, R. J. *Biosens. Bioelectron.* **1998,** *13,* 731–739. doi:10.1016/S0956-5663(98)00037-2
6. Graham, D. L.; Ferreira, H. A.; Freitas, P. P.; Cabral, J. M. *Biosens. Bioelectron.* **2003,** *18,* 483–488. doi:10.1016/S0956-5663(02)00205-1
7. Li, G.; Sun, S.; Wilson, R. J.; White, R. L.; Pourmand, N.; Wang, S. X. *Sens. Actuators, A* **2006,** *126,* 98–106. doi:10.1016/j.sna.2005.10.001
8. Parkin, S. S.; Kaiser, C.; Panchula, A.; Rice, P. M.; Hughes, B.; Samant, M.; Yang, S. H. *Nat. Mater.* **2004,** *3,* 862–867. doi:10.1038/nmat1256
9. Brzeska, M.; Panhorst, M.; Kamp, P. B.; Schotter, J.; Reiss, G.; Puhler, A.; Becker, A.; Bruckl, H. *J. Biotechnol.* **2004,** *112,* 25–33. doi:10.1016/j.jbiotec.2004.04.018
10. Osterfeld, S. J.; Yu, H.; Gaster, R. S.; Caramuta, S.; Xu, L.; Han, S. J.; Hall, D. A.; Wilson, R. J.; Sun, S.; White, R. L.; Davis, R. W.; Pourmand, N.; Wang, S. X. *Proc. Natl. Acad. Sci. U. S. A.* **2008,** *105,* 20637–20640. doi:10.1073/pnas.0810822105
11. Millen, R. L.; Kawaguchi, T.; Granger, M. C.; Porter, M. D.; Tondra, M. *Anal. Chem.* **2005,** *77,* 6581–6587. doi:10.1021/ac0509049
12. Aytur, T.; Foley, J.; Anwar, M.; Boser, B.; Harris, E.; Beatty, P. R. *J. Immunol. Methods* **2006,** *314,* 21–29. doi:10.1016/j.jim.2006.05.006
13. Perez, J. M.; Josephson, L.; O'Loughlin, T.; Hogemann, D.; Weissleder, R. *Nat. Biotechnol.* **2002,** *20,* 816–820. doi:10.1038/nbt720
14. Lee, H.; Sun, E.; Ham, D.; Weissleder, R. *Nat. Med.* **2008,** *14,* 869–874. doi:10.1038/nm.1711
15. Lee, H.; Yoon, T. J.; Figueiredo, J. L.; Swirski, F. K.; Weissleder, R. *Proc. Natl. Acad. Sci. U. S. A.* **2009,** *106,* 12459–12464. doi:10.1073/pnas.0902365106
16. Lee, H.; Yoon, T. J.; Weissleder, R. *Angew. Chem., Int. Ed.* **2009,** *48,* 5657–5660. doi:10.1002/anie.200901791
17. Liu, Y.; Sun, N.; Lee, H.; Weissleder, R.; Ham, D. *Solid-State Circuits Conference Digest of Technical Papers (ISSCC), 2008 IEEE International* **2008,** 140–141. doi:10.1109/ISSCC.2008.4523096
18. Sun, N.; Liu, Y.; Lee, H.; Weissleder, R.; Ham, D. *IEEE J. Solid-State Circuits* **2009,** *44,* 1629–1643. doi:10.1109/JSSC.2009.2017007
19. Sun, N.; Yoon, T.-J.; Lee, H.; Andress, W.; Demas, V.; Prado, P.; Weissleder, R.; Ham, D. *Solid-State Circuits Conference Digest of Technical Papers (ISSCC), 2010 IEEE International* **2010,** 488–489. doi:10.1109/ISSCC.2010.5433836
20. Kittel, C. *Rev. Mod. Phys.* **1949,** *21,* 541–583. doi:10.1103/RevModPhys.21.541
21. Lu, A. H.; Salabas, E. L.; Schuth, F. *Angew. Chem., Int. Ed.* **2007,** *46,* 1222–1244. doi:10.1002/anie.200602866
22. Park, J.; Joo, J.; Kwon, S. G.; Jang, Y.; Hyeon, T. *Angew. Chem., Int. Ed.* **2007,** *46,* 4630–4660. doi:10.1002/anie.200603148
23. Jun, Y. W.; Lee, J. H.; Cheon, J. *Angew. Chem., Int. Ed.* **2008,** *47,* 5122–5135. doi:10.1002/anie.200701674
24. Frey, N. A.; Peng, S.; Cheng, K.; Sun, S. *Chem. Soc. Rev.* **2009,** *38,* 2532–2542. doi:10.1039/b815548h
25. Shen, T.; Weissleder, R.; Papisov, M.; Bogdanov, A. J.; Brady, T. J. *Magn. Reson. Med.* **1993,** *29,* 599. doi:10.1002/mrm.1910290504

26. Molday, R. S.; MacKenzie, D. *J. Immunol. Methods* **1982,** *52,* 353–367. doi:10.1016/0022-1759(82)90007-2
27. Lee, J. H.; Huh, Y. M.; Jun, Y. W.; Seo, J. W.; Jang, J. T.; Song, H. T.; Kim, S.; Cho, E. J.; Yoon, H. G.; Suh, J. S.; Cheon, J. *Nat. Med.* **2007,** *13,* 95–99. doi:10.1038/nm1467
28. Hyeon, T.; Lee, S. S.; Park, J.; Chung, Y.; Na, H. B. *J. Am. Chem. Soc.* **2001,** *123,* 12798–12801. doi:10.1021/ja016812s
29. Sun, S.; Zeng, H. *J. Am. Chem. Soc.* **2002,** *124,* 8204–8205. doi:10.1021/ja026501x
30. Liong, M.; Shao, H.; Haun, J. B.; Lee, H.; Weissleder, R. *Adv. Mater.*, in press. doi:10.1002/adma.201002219
31. Chen, Z.; Zhang, Y.; Zhang, S.; Xia, J.; Liu, J.; Xu, K.; Gu, N. *Colloids Surf., A* **2008,** *316,* 210–216. doi:10.1016/j.colsurfa.2007.09.017
32. Fauconnier, N.; Pons, J. N.; Roger, J.; Bee, A. *J. Colloid Interface Sci.* **1997,** *194,* 427–433. doi:10.1006/jcis.1997.5125
33. Jun, Y. W.; Huh, Y. M.; Choi, J. S.; Lee, J. H.; Song, H. T.; Kim, S.; Yoon, S.; Kim, K. S.; Shin, J. S.; Suh, J. S.; Cheon, J. *J. Am. Chem. Soc.* **2005,** *127,* 5732–5733. doi:10.1021/ja0422155
34. Josephson, L.; Perez, J. M.; Weissleder, R. *Angew. Chem., Int. Ed.* **2001,** *40,* 3204–3206. doi:10.1002/1521-3773(20010903)40:17<3204::AID-ANIE3204>3.0.CO;2-H
35. Gillis, P.; Koenig, S. H. *Magn. Reson. Med.* **1987,** *5,* 323–345. doi:10.1002/mrm.1910050404
36. Brooks, R. A. *Magn. Reson. Med.* **2002,** *47,* 388–391. doi:10.1002/mrm.10064
37. Perez, J. M.; Grimm, J.; Josephson, L.; Weissleder, R. *Neoplasia (Ann Arbor, MI, U. S.)* **2008,** *10,* 1066–1072.
38. Perez, J. M.; Josephson, L.; Weissleder, R. *ChemBioChem* **2004,** *5,* 261–264. doi:10.1002/cbic.200300730
39. Perez, J. M.; O'Loughin, T.; Simeone, F. J.; Weissleder, R.; Josephson, L. *J. Am. Chem. Soc.* **2002,** *124,* 2856–2857. doi:10.1021/ja017773n
40. Perez, J. M.; Simeone, F. J.; Saeki, Y.; Josephson, L.; Weissleder, R. *J. Am. Chem. Soc.* **2003,** *125,* 10192–10193. doi:10.1021/ja036409g
41. Perez, J. M.; Simeone, F. J.; Tsourkas, A.; Josephson, L.; Weissleder, R. *Nano Lett.* **2004,** *4,* 119–122. doi:10.1021/nl034983k
42. Josephson, L.; Kircher, M. F.; Mahmood, U.; Tang, Y.; Weissleder, R. *Bioconjugate Chem.* **2002,** *13,* 554–560. doi:10.1021/bc015555d
43. Sun, E. Y.; Josephson, L.; Kelly, K. A.; Weissleder, R. *Bioconjugate Chem.* **2006,** *17,* 109–113. doi:10.1021/bc050290e
44. Josephson, L.; Tung, C. H.; Moore, A.; Weissleder, R. *Bioconjugate Chem.* **1999,** *10,* 186–191. doi:10.1021/bc980125h
45. Sun, S.; Zeng, H.; Robinson, D. B.; Raoux, S.; Rice, P. M.; Wang, S. X.; Li, G. *J. Am. Chem. Soc.* **2004,** *126,* 273–279. doi:10.1021/ja0380852
46. Jang, J. T.; Nah, H.; Lee, J. H.; Moon, S. H.; Kim, M. G.; Cheon, J. *Angew. Chem., Int. Ed.* **2009,** *48,* 1234–1238. doi:10.1002/anie.200805149
47. Huh, Y. M.; Jun, Y. W.; Song, H. T.; Kim, S.; Choi, J. S.; Lee, J. H.; Yoon, S.; Kim, K. S.; Shin, J. S.; Suh, J. S.; Cheon, J. *J. Am. Chem. Soc.* **2005,** *127,* 12387–12391. doi:10.1021/ja052337c
48. Miguel, O. B.; Gossuin, Y.; Morales, M. P.; Gillis, P.; Muller, R. N.; Veintemillas-Verdaguer, S. *Magn. Reson. Imaging* **2007,** *25,* 1437–1441. doi:10.1016/j.mri.2007.04.006
49. Peng, S.; Wang, C.; Xie, J.; Sun, S. *J. Am. Chem. Soc.* **2006,** *128,* 10676–10677. doi:10.1021/ja063969h
50. Raghavan, A. S.; Hang, H. C. *Drug Discovery Today* **2009,** *14,* 178–184. doi:10.1016/j.drudis.2008.09.014
51. Devaraj, N. K.; Upadhyay, R.; Haun, J. B.; Hilderbrand, S. A.; Weissleder, R. *Angew. Chem., Int. Ed.* **2009,** *48,* 7013–7016. doi:10.1002/anie.200903233
52. Devaraj, N. K.; Hilderbrand, S.; Upadhyay, R.; Mazitschek, R.; Weissleder, R. *Angew. Chem., Int. Ed. Engl.* **2010,** *49,* 2869–2872. doi:10.1002/anie.200906120
53. Haun, J. B.; Devaraj, N. K.; Hilderbrand, S. A.; Lee, H.; Weissleder, R. *Nat. Nanotechnol.* **2010,** *5,* 660–665. doi:10.1038/nnano.2010.148
54. Grimm, J.; Perez, J. M.; Josephson, L.; Weissleder, R. *Cancer Res.* **2004,** *64,* 639–643. doi:10.1158/0008-5472.CAN-03-2798
55. Taktak, S.; Sosnovik, D.; Cima, M. J.; Weissleder, R.; Josephson, L. *Anal. Chem.* **2007,** *79,* 8863–8869. doi:10.1021/ac701976p
56. Kim, G. Y.; Josephson, L.; Langer, R.; Cima, M. J. *Bioconjugate Chem.* **2007,** *18,* 2024–2028. doi:10.1021/bc070110w
57. Zhao, M.; Josephson, L.; Tang, Y.; Weissleder, R. *Angew. Chem., Int. Ed.* **2003,** *42,* 1375–1378. doi:10.1002/anie.200390352
58. Tsourkas, A.; Hofstetter, O.; Hofstetter, H.; Weissleder, R.; Josephson, L. *Angew. Chem., Int. Ed.* **2004,** *43,* 2395–2399. doi:10.1002/anie.200352998
59. Sun, E. Y.; Weissleder, R.; Josephson, L. *Small* **2006,** *2,* 1144–1147. doi:10.1002/smll.200600204
60. Taktak, S.; Weissleder, R.; Josephson, L. *Langmuir* **2008,** *24,* 7596–7598. doi:10.1021/la8006298
61. Atanasijevic, T.; Shusteff, M.; Fam, P.; Jasanoff, A. *Proc. Natl. Acad. Sci. U. S. A.* **2006,** *103,* 14707–14712. doi:10.1073/pnas.0606749103
62. Koh, I.; Hong, R.; Weissleder, R.; Josephson, L. *Anal. Chem.* **2009,** *81,* 3618–3622. doi:10.1021/ac802717c
63. Koh, I.; Hong, R.; Weissleder, R.; Josephson, L. *Angew. Chem., Int. Ed.* **2008,** *47,* 4119–4121. doi:10.1002/anie.200800069
64. Schellenberger, E. J. R. *J. R. Soc. Interface* **2010,** *7,* S83–91. doi:10.1098/rsif.2009.0336.focus
65. Jaffer, F. A.; Weissleder, R. *Circ. Res.* **2004,** *94,* 433–445. doi:10.1161/01.RES.0000119321.18573.5A

License and Terms

This is an Open Access article under the terms of the Creative Commons Attribution License (http://creativecommons.org/licenses/by/2.0), which permits unrestricted use, distribution, and reproduction in any medium, provided the original work is properly cited.

The license is subject to the *Beilstein Journal of Nanotechnology* terms and conditions: (http://www.beilstein-journals.org/bjnano)

The definitive version of this article is the electronic one which can be found at: doi:10.3762/bjnano.1.17

Beilstein Journal of Nanotechnology

Magnetic interactions between nanoparticles

Steen Mørup*[1], Mikkel Fougt Hansen[2] and Cathrine Frandsen[1]

Review

Open Access

Address:
[1]Department of Physics, Building 307; Technical University of Denmark; DK-2800 Kongens Lyngby; Denmark and [2]Department of Micro- and Nanotechnology, DTU Nanotech, Building 345 East; Technical University of Denmark; DK-2800 Kongens Lyngby; Denmark

Email:
Steen Mørup* - morup@fysik.dtu.dk

* Corresponding author

Keywords:
dipole interactions; exchange interactions; spin structure; superferromagnetism; superparamagnetic relaxation

Beilstein J. Nanotechnol. **2010,** *1,* 182–190.
doi:10.3762/bjnano.1.22

Received: 10 September 2010
Accepted: 03 December 2010
Published: 28 December 2010

Guest Editors: U. Wiedwald and P. Ziemann

© 2010 Mørup et al; licensee Beilstein-Institut.
License and terms: see end of document.

Abstract

We present a short overview of the influence of inter-particle interactions on the properties of magnetic nanoparticles. Strong magnetic dipole interactions between ferromagnetic or ferrimagnetic particles, that would be superparamagnetic if isolated, can result in a collective state of nanoparticles. This collective state has many similarities to spin-glasses. In samples of aggregated magnetic nanoparticles, exchange interactions are often important and this can also lead to a strong suppression of superparamagnetic relaxation. The temperature dependence of the order parameter in samples of strongly interacting hematite nanoparticles or goethite grains is well described by a simple mean field model. Exchange interactions between nanoparticles with different orientations of the easy axes can also result in a rotation of the sub-lattice magnetization directions.

Review

Introduction

In nanostructured magnetic materials, interactions between, for example, nanoparticles or thin films in multilayer structures often play an important role. Long-range magnetic dipole interactions can have a strong influence on, e.g., the magnetic dynamics in samples containing ferromagnetic or ferrimagnetic nanoparticles. If nanoparticles or thin films are in close proximity, exchange interactions between surface atoms can be significant. An important example of magnetic proximity effects is exchange bias, which manifests itself as a shift of the hysteresis curves obtained after field cooling of a ferromagnetic or ferrimagnetic material in contact with an antiferromagnetic material [1-3]. This was first observed in nanoparticles consisting of a core of ferromagnetic cobalt covered by a shell of antiferromagnetic CoO [4]: This effect is nowadays utilized in read heads in computer hard disk drives. In a neutron study of Fe_3O_4/CoO multilayers, van der Zaag et al. [5] found that the Néel temperature of CoO was enhanced due to the exchange interaction with ferrimagnetic Fe_3O_4 layers with a Curie

temperature of about 850 K. Similarly, an increase of the Curie temperature of ferrimagnetic γ-Mn_2O_3 due to interaction with antiferromagnetic MnO has been found in MnO/γ-Mn_2O_3 core–shell particles [6].

The magnetic properties of non-interacting magnetic nanoparticles are often strongly influenced by superparamagnetic relaxation at finite temperatures. For a nanoparticle with uniaxial anisotropy and with the magnetic anisotropy energy given by the simple expression

$$E_a = KV \sin^2\theta \,, \tag{1}$$

there are energy minima at θ = 0° and θ = 180°, which are separated by an energy barrier KV. Here K is the magnetic anisotropy constant, V is the particle volume and θ is the angle between the magnetization vector and an easy direction of magnetization. At finite temperatures, the thermal energy may be sufficient to induce superparamagnetic relaxation, i.e., reversal of the magnetization between directions close to θ = 0° and θ = 180°. The superparamagnetic relaxation time is given by the Néel–Brown expression [7,8]

$$\tau = \tau_0 \exp\left(\frac{KV}{k_B T}\right) , \tag{2}$$

where k_B is Boltzmann's constant and T is the temperature. τ_0 is on the order of 10^{-13}–10^{-9} s and is weakly temperature dependent.

In experimental studies of magnetic nanoparticles, the timescale of the experimental technique is an important parameter. If the relaxation is fast compared to the timescale of the experimental technique one measures an average value of the magnetization, but if the relaxation time is long compared to the timescale of the experimental technique, one measures the instantaneous value of the magnetization. The superparamagnetic blocking temperature is defined as the temperature at which the superparamagnetic relaxation time equals the timescale of the experimental technique. In Mössbauer spectroscopy the timescale is on the order of a few nanoseconds, whereas it is on the order of picoseconds in inelastic neutron scattering studies. In DC magnetization measurements the timescale is in the range 1–100 seconds. In AC magnetization measurements the timescale can be varied by varying the frequency. Thus, the blocking temperature is not uniquely defined, but it depends on the timescale of the experimental technique.

If magnetic interactions between the particles are not negligible, they can have a significant influence on the superparamagnetic relaxation. Furthermore, the spin structure of nanoparticles can be affected by inter-particle interactions. In this short review, we first discuss how the superparamagnetic relaxation in nanoparticles can be influenced by magnetic dipole interactions and by exchange interactions between particles. Subsequently, we discuss how the spin structure of nanoparticles can be influenced by inter-particle exchange interactions.

Magnetic dipole interactions

Magnetic dipole interactions between atoms in crystals with magnetic moments of a few Bohr magnetons are too small to result in magnetic ordering above 1 K and are usually negligible compared to exchange interactions in magnetic materials. Therefore, magnetic dipole interactions have a negligible influence on the magnetic order in bulk materials at finite temperatures. However, nanoparticles of ferromagnetic and ferrimagnetic materials with dimensions around 10 nm can have magnetic moments larger than 10,000 Bohr magnetons, and therefore, dipole interactions between nanoparticles can have a significant influence on the magnetic properties.

In a sample of randomly distributed nanoparticles with average magnetic moment μ and average separation d, the dipole interaction energy of a particle is on the order of [9]

$$E_d \approx \frac{\mu_0}{4\pi}\frac{\mu^2}{d^3} \,, \tag{3}$$

where μ_0 is the permeability of free space. In samples with high concentrations of magnetic nanoparticles, which would be superparamagnetic if they were non-interacting, magnetic dipole interactions can result in ordering of the magnetic moments of the nanoparticles below a critical temperature T_0, where [9]

$$T_0 \approx \frac{E_d}{k_B} \,. \tag{4}$$

Systems of magnetic nanoparticles with only magnetic dipole interactions can be prepared by dispersing magnetic nanoparticles coated with surfactant molecules in a solvent. Often, nanoparticles have a broad size distribution that gives rise to a very broad distribution of superparamagnetic relaxation times of the isolated particles (Equation 2). To distinguish effects of single particle behavior from those of inter-particle interactions, a very narrow particle size distribution is required. Interparticle interactions can be varied by changing the concentration of the particles and can be studied in frozen samples. A wide variety of nanoparticle systems, including $Fe_{100-x}C_x$ [10], ε-Fe_3N [11], γ-Fe_2O_3 [12-14] and Fe_3O_4 [15] have been investigated. If the particles are randomly distributed and have a

random orientation of the easy axes, the magnetic properties can have similarities to those of spin glasses [10,11,14], and therefore these interacting nanoparticle systems are often called super-spin glasses.

Dipole interactions can have a significant influence on DC magnetization measurements. In zero field cooled (ZFC) magnetization studies one measures the temperature dependence of the magnetization in a small applied field after the sample has been cooled in zero field. Samples of non-interacting particles show a maximum in the ZFC curve at a temperature T_p related to the blocking temperature. Dipole interactions result in a shift of the maximum to a higher temperature. Field cooled (FC) magnetization curves are obtained in a similar way, but after cooling the sample in a small field. For samples of non-interacting particles, the FC magnetization curve increases with decreasing temperature below T_p, but interactions can result in an almost temperature independent magnetization below T_p. Such measurements have been used to investigate interaction effects in numerous studies, e.g., [11-13], and are useful for a qualitative characterization of samples of interacting nanoparticles. However, it is difficult to obtain quantitative information on the influence of interactions from DC magnetization measurements.

AC magnetization measurements can be used to obtain quantitative information on the relaxation time. Such measurements on samples of interacting nanoparticles have shown that the relaxation time diverges in the same manner as in a spin glass, when the sample is cooled towards the phase transition temperature T_0 [10,14,16-18], i.e., the relaxation time can be expressed by

$$\tau = \tau^* \left(\frac{T - T_0}{T_0} \right)^{-zv} , \qquad (5)$$

where τ* is the relaxation time of non-interacting particles and the critical exponent zv is on the order of 10. Another sign of spin-glass-like behavior is a divergence of the non-linear magnetic susceptibility when T_0 is approached from above [11,19]. Moreover, below T_0 the memory and rejuvenation phenomena that are characteristic for spin-glass behavior have been observed [20]. The studies of 'super spin-glass' behavior have recently been reviewed [21,22].

As an example, Figure 1 shows the relaxation time of suspensions of nearly monodisperse 4.7 nm $Fe_{100-x}C_x$ particles ($x \approx 22$) in decalin as a function of temperature. The data were obtained from AC susceptibility measurements. The open circles are data from a dilute sample, whereas the full circles are data for a concentrated sample. The temperature dependence of the relaxation time for the dilute sample is in accordance with Equation 2, whereas the temperature dependence of the relaxation time of the concentrated sample is in accordance with Equation 5, and the relaxation time diverges at $T_0 = 40$ K [10]. The insets show an electron micrograph of the particles and the particle size distribution.

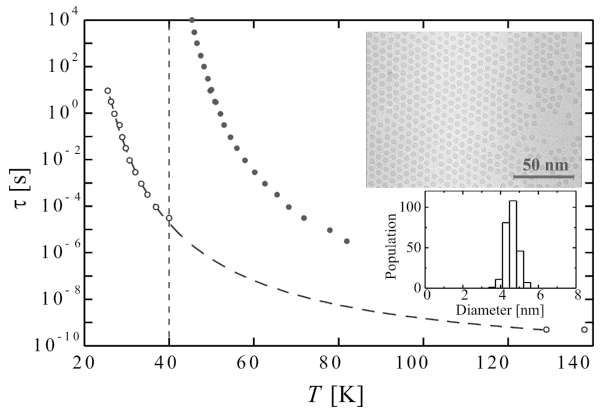


Figure 1: The relaxation time of 4.7 nm $Fe_{100-x}C_x$ nearly monodisperse particles suspended in decalin as a function of temperature. The data were obtained from AC susceptibility measurements. The open circles are data from a dilute sample, whereas the full circles are data for a concentrated sample. The insets show a transmission electron microscopy (TEM) image of the particles deposited on an amorphous carbon film and the corresponding particle size distribution obtained from the TEM images. Adapted from Djurberg, C.; Svedlindh, P.; Nordblad, P.; Hansen, M. F.; Bødker, F.; Mørup, S. Dynamics of an Interacting Particle System: Evidence of Critical Slowing Down, *Phys. Rev. Lett.* **1997,** *79,* 5154. Copyright (1997) by the American Physical Society.

Granular systems with a different content of metallic nanoparticles, e.g., Co [23] or $Co_{80}Fe_{20}$ [24] embedded in a non-magnetic matrix, have been prepared by sputtering of discontinuous metal–insulator multi-layers and subsequent annealing. These systems have shown both spin-glass-like ordering for moderately strong interactions and ferromagnetic ordering for very strong interactions [24]. The latter transition is attributed to a weak exchange coupling through magnetic impurities in the insulating matrix [24]. Similarly, in the Fe_xAg_{100-x} granular system of 2.5–3.0 nm Fe particles in an Ag matrix, a cross-over was observed from a spin-glass-like behavior of the particle moments for $x < 35$ to a ferromagnetic ordering of the particle moments for $35 < x < 50$ [25]. In this system, the magnetic particles also interact via the RKKY interaction because of the conducting Ag matrix.

Often, there is a tendency for magnetic nanoparticles to form chains, especially if they can move freely in an external magnetic field, for example, if they are suspended in a liquid. If the nanoparticles form chains, a ferromagnetic ordering of the

magnetic moments is favored in zero applied field with the magnetization along the chain direction [26,27]. Using a mean field model for an infinite chain of interacting nanoparticles with separation d, one finds that the ordering temperature is given by [27]

$$T_0 = 1.202 \frac{\mu_0}{\pi d^3} \frac{\mu^2}{3k_B} . \quad (6)$$

Thus, in general, strong dipole interactions result in suppression of the superparamagnetic relaxation. It is, however, remarkable that weak dipole interactions can result in faster superparamagnetic relaxation. This has been observed in Mössbauer studies of maghemite (γ-Fe_2O_3) nanoparticles [12,28], and the effect has been explained by a lowering of the energy barriers between the two minima of the magnetic energy [28-31].

Figure 2 shows a schematic illustration of interacting nanoparticles. Figure 2a illustrates isolated nanoparticles, dominated by superparamagnetic relaxation. Figure 2b shows interacting nanoparticles forming a "dipole glass". The nanoparticles in Figure 2c form a chain with aligned dipole moments.

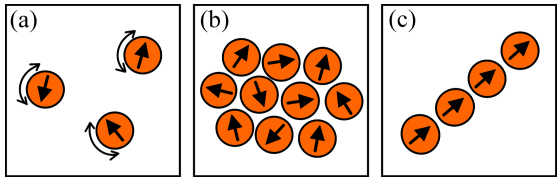


Figure 2: Schematic illustration of interacting magnetic nanoparticles. (a) Isolated nanoparticles dominated by superparamagnetic relaxation. (b) Interacting nanoparticles forming a dipole glass. (c) Nanoparticles forming a chain with aligned dipole moments.

By the use of off-axis electron holography, it is possible to obtain information about the magnetization direction of individual nanoparticles in ensembles of interacting ferro- or ferrimagnetic nanoparticles. This technique measures quantitatively and non-invasively the in-plane magnetic field component of a thin sample with a lateral resolution of a few nanometers [32,33]. From the obtained images, the influence of dipolar interactions between magnetic nanoparticles can be very apparent. For example, this technique has resolved an almost linear magnetic flux along the chain direction in a double chain of 24 ~70 nm magnetite (Fe_3O_4) particles in magnetotactic bacteria [33], and it has resolved magnetic flux closure in small rings of 5–7 Co particles with a diameter of about 25 nm [32].

Influence of exchange coupling between nanoparticles on magnetic relaxation

In a perfect antiferromagnetic material the net magnetization vanishes because the sublattice magnetizations have identical size but opposite directions. However, in nanoparticles, the finite number of magnetic ions results in a small net magnetic moment because of uncompensated spins in the surface and/or in the interior of the particles [34]. This magnetic moment is, however, usually so small that dipole interactions are almost negligible and the influence of dipole interactions on the superparamagnetic relaxation is therefore also expected to be negligible [35]. Nevertheless, several Mössbauer studies of, for example, hematite (α-Fe_2O_3) [35-38] and ferrihydrite [39] nanoparticles have shown that the superparamagnetic relaxation of antiferromagnetic nanoparticles can be significantly suppressed if the particles are in close proximity. This has been explained by exchange interaction between surface atoms of neighboring particles [35-38]. As an example, Figure 3 shows Mössbauer spectra of chemically prepared 8 nm hematite (α-Fe_2O_3) nanoparticles [36]. The spectra in Figure 3a were obtained from particles, which were coated with phosphate in order to minimize inter-particle interactions. The spectra in Figure 3b were obtained from a sample prepared by freeze-drying an aqueous suspension of uncoated particles from the same batch. At 18 K, the spectra of both coated and uncoated particles consist of a sextet with relatively narrow lines, indicating that relaxation effects are negligible. At 50 K the spectrum of the coated particles in Figure 3a show a superposition of a sextet and a doublet, which are due to particles below and

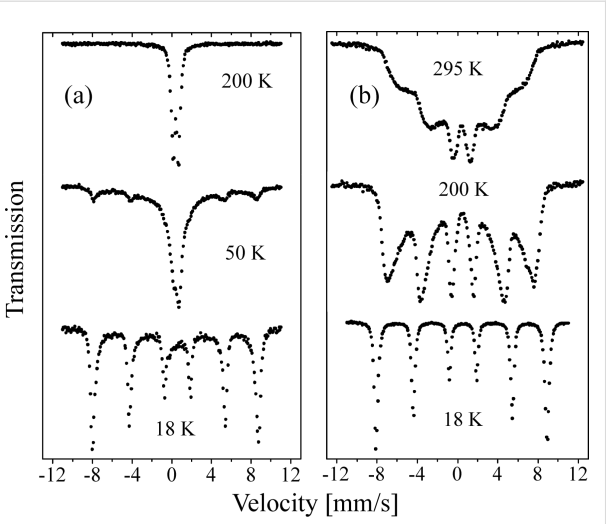


Figure 3: Mössbauer spectra of 8 nm hematite particles (a) coated (non-interacting) and (b) uncoated (strongly interacting) nanoparticles. The spectra were obtained at the indicated temperatures. Reprinted from Frandsen, C.; Mørup, S. Spin rotation in α-Fe_2O_3 nanoparticles by interparticle interactions, *Phys. Rev. Lett.* **2005,** *94,* 027202. Copyright (2005) by the American Physical Society.

above their blocking temperature, respectively. Both the sextet and the doublet have relatively narrow lines. The relative area of the doublet increases with increasing temperature at the expense of the sextet. At 200 K the sextet has disappeared and the spectra only show a quadrupole doublet, indicating that all particles show fast superparamagnetic relaxation ($\tau < 1$ ns). The presence of both a sextet and a doublet in the spectra in Figure 3a and the temperature dependence of the relative areas can be explained by the particle size distribution in combination with the exponential dependence of the relaxation time on the particle volume (Equation 2). In Mössbauer spectroscopy studies of magnetic nanoparticles the median blocking temperature of a sample is usually defined as the temperature where half of the spectral area is in the sextet and the remaining area is in the doublet.

The spectra of the dried, uncoated particles in Figure 3b show a quite different temperature dependence. As the temperature is increased, the lines gradually broaden and the average hyperfine field decreases, but even at 295 K there is no visible doublet in the spectrum. This shows that the superparamagnetic relaxation is strongly suppressed compared to the sample of coated particles. Thus, the different evolution of the spectra as a function of temperature clearly shows that the magnetic relaxation is qualitatively different in samples of non-interacting and interacting nanoparticles.

In several earlier publications it was assumed that the magnetic interactions between nanoparticles can be treated as an extra contribution to the magnetic anisotropy. If this were correct, the Mössbauer spectra of non-interacting and interacting particles should be qualitatively similar and the only difference should be a higher median superparamagnetic blocking temperature in samples of interacting nanoparticles. The different temperature dependence of the spectra in Figure 3a and Figure 3b shows that this assumption is incorrect. As discussed below, the influence of inter-particle interactions should rather be treated in terms of an interaction field [35,37,40].

Mössbauer data for strongly interacting antiferromagnetic particles have been analyzed using a "superferromagnetism" model [35,40], in which it is assumed that the magnetic energy of a particle, interacting with its neighbors, is given by

$$E = KV\sin^2\theta - \sum_{i,j} J_{ij}\,\vec{S}_i \cdot \vec{S}_j \ . \qquad (7)$$

Here, the first term represents the magnetic anisotropy energy. The second term is the interaction energy, where $\vec{S}_i$ and $\vec{S}_j$ are the surface spins belonging to the particle and the neighboring particles, respectively, and J_{ij} is the exchange coupling constant. The summation in Equation 7 may be replaced by a mean field, acting on the sublattice magnetization of the particle [35,37,40]

$$E = KV\sin^2\theta - J_{\text{eff}}\vec{M}(T)\cdot\left\langle\vec{M}(T)\right\rangle \ . \qquad (8)$$

$\vec{M}(T)$ represents the sub-lattice magnetization vector of a particle at temperature T, J_{eff} is an effective exchange coupling constant and $J_{\text{eff}}\left\langle\vec{M}(T)\right\rangle$ is an effective interaction mean field acting on $\vec{M}(T)$.

The magnetic energy (Equation 8) will depend on the angle between the easy axis, defined by the magnetic anisotropy and the interaction field. In recent studies it has been found that chemically prepared nanoparticles of antiferromagnetic hematite can in some cases be attached with a common orientation such that both the crystallographic and the magnetic order continue across the interface [38]. This is illustrated by the neutron diffraction data for 8 nm hematite nanoparticles prepared by freeze drying an aqueous suspension of uncoated particles, shown in Figure 4 [41]. The particles were prepared chemically by means of a method similar to the D-preparation described by Sugimoto et al. [42]. As in X-ray diffraction studies, the peaks in the neutron diffraction patterns of these nanoparticles are broadened, and the broadening is related to the crystallographic and the magnetic correlation lengths as described by the Scherrer formula [38]. The width of most of the neutron diffraction lines in Figure 4 is in accordance with

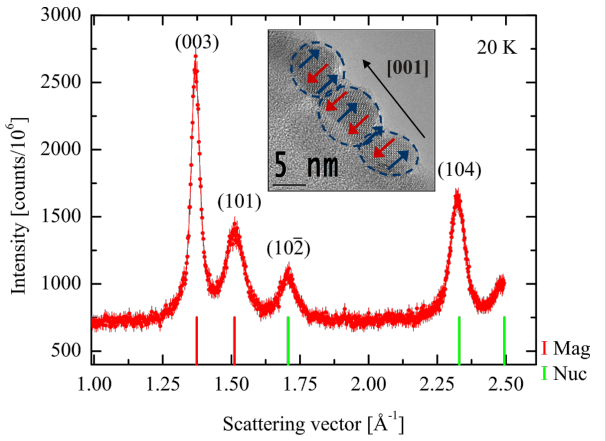


Figure 4: Neutron diffraction data for interacting 8 nm α-Fe_2O_3 particles obtained at 20 K. The inset shows a TEM image of three α-Fe_2O_3 particles attached along their common [001] axis. The antiferromagnetic order is indicated by the blue and red arrows superimposed on the TEM image. Adapted from Frandsen, C.; Bahl, C. R. H.; Lebech, B.; Lefmann, K.; Kuhn, L. T.; Keller, L.; Andersen, N. H.; von Zimmermann, M.; Johnson, E.; Klausen, S. N.; Mørup, S. Oriented attachment and exchange coupling of α-Fe_2O_3 nanoparticles, *Phys. Rev. B* **2005,** *72,* 214406. Copyright (2005) by the American Physical Society.

the particle size estimated from electron microscopy. However, the purely magnetic (003) peak is considerably narrower than the other peaks [38,41]. This shows that the magnetic correlation length in this direction is larger than the particle size, i.e., the magnetic (and the crystallographic) correlation extends over several particles. After gentle grinding, neutron diffraction studies showed that the width of the (003) peak becomes similar to those of the other peaks, indicating that the oriented attachment is destroyed [38]. In studies of nanoparticles of goethite (α-FeOOH) [40,43,44] it has also been found that there is a tendency for (imperfect) oriented attachment of grains.

When particles are attached with a common orientation, it may be a good first order approximation to assume that the interaction field and the anisotropy field are parallel [35,40] such that Equation 8 can be replaced by

$$E(\theta) \approx KV \sin^2\theta - J_{\text{eff}} M^2(T) b(T) \cos\theta \,, \qquad (9)$$

where $M(T)$ is the sub-lattice magnetization in the absence of magnetic fluctuations, and

$$b(T) = \left|\left\langle \vec{M}(T) \right\rangle\right| / M(T) \qquad (10)$$

is the order parameter.

The magnetic energy, $E(\theta)$ (Equation 9) is shown in Figure 5 for different values of the ratio between the interaction energy $J_{\text{eff}}M^2(T)b(T)$ and the anisotropy energy, KV. If the interaction energy is negligible compared to the anisotropy energy, the relaxation can be described in terms of transitions between the minima at 0° and 180°, but if the interaction energy is predominant, there is only one minimum, defined by the effective interaction field and the anisotropy. In the presence of a finite interaction field, there may be two minima with different energies. Then the average value of the sublattice magnetization is nonzero, and therefore a magnetic splitting appears in Mössbauer spectra even at high temperatures where the relaxation is fast. In thermal equilibrium, i.e., when all relaxation processes can be considered fast compared to the timescale of the Mössbauer spectroscopy, the temperature dependence of the order parameter can be calculated by use of Boltzmann statistics [35,40]

$$b(T) = \frac{\int_0^{\pi} \exp\left[-E(\theta)/k_{\text{B}}T\right] \sin\theta\cos\theta \,\mathrm{d}\theta}{\int_0^{\pi} \exp\left[-E(\theta)/k_{\text{B}}T\right] \sin\theta \,\mathrm{d}\theta} \,, \qquad (11)$$

where $E(\theta)$ is given by Equation 9. Equation 11 can be solved numerically to estimate the temperature dependence of the order parameter. If the relaxation is fast compared to the timescale of Mössbauer spectroscopy, the magnetic hyperfine splitting in the spectra will be proportional to $b(T)$. In samples where the magnetic anisotropy energy can be considered negligible compared to the interaction energy, the magnetic ordering of the particle moments will disappear at the ordering temperature given by

$$T_0 \approx \frac{J_{\text{eff}} M^2(T_0)}{3k_{\text{B}}} \,. \qquad (12)$$

The superferromagnetism model has been successfully used to fit data for interacting nanoparticles of hematite [35] and goethite grains [40].

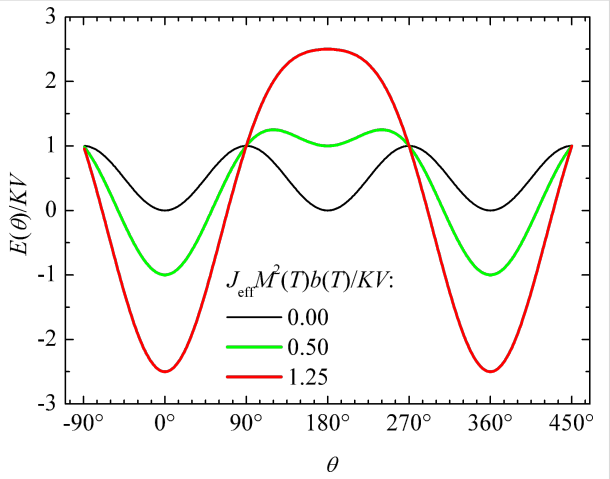


Figure 5: The normalized magnetic energy, $E(\theta)/KV$ (Equation 9) for different values of the ratio between the interaction energy $J_{\text{eff}}M^2(T)b(T)$ and the anisotropy energy, KV.

The variation in the local environments of the particles in a sample results in a distribution of the magnitudes of the order parameters. Consequently, the value of the order parameter at a given temperature is not the same for all parts of the sample, and this leads to a distribution of magnetic hyperfine fields, which explains the line broadening in the spectra. It is convenient to analyze the temperature dependence of chosen quantiles of the hyperfine field distribution when comparing with the theoretical superferromagnetism model (Equation 11) [35,40]. Figure 6 shows the temperature dependence of the order parameter, $b_{50}(T)$ of the 50% quantile of the hyperfine field distribution (the median hyperfine field) for interacting 20 nm hematite nanoparticles. The solid line is a fit to the superferromagnetism model (Equation 11). The order parameter vanishes at $T_0 \approx$ 390 K, where the particles become superparamagnetic. For comparison, the Néel temperature of bulk hematite is about 955 K.

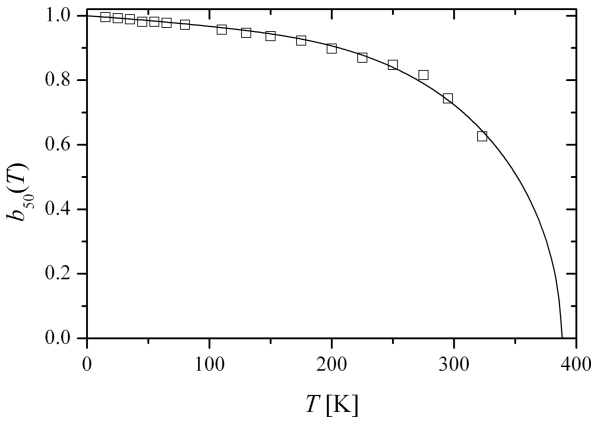


Figure 6: Temperature dependence of the median value of the order parameter, $b_{50}(T)$ for interacting 20 nm hematite nanoparticles. The open squares are the experimental data, and the solid line is a fit to the superferromagnetism model (Equation 11). Adapted from Hansen, M. F. ; Koch, C. B.; Mørup, S. Magnetic dynamics of weakly and strongly interacting hematite nanoparticles, *Phys. Rev. B* **2000,** *62,* 1124. Copyright (2000) by the American Physical Society.

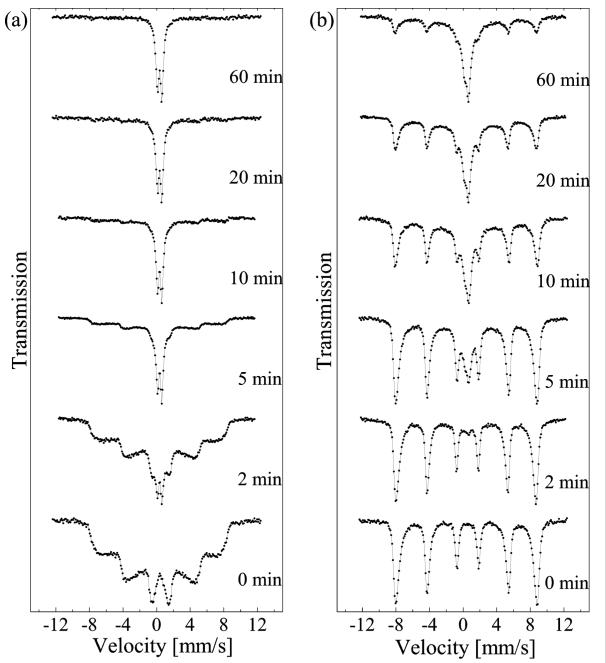


Figure 7: Mössbauer spectra of 8 nm hematite nanoparticles ground in a mortar with η-Al_2O_3 nanoparticles for the indicated periods of time. (a) Spectra obtained at room temperature. (b) Spectra obtained at 80 K. Reprinted with permission from Xu, M.; Bahl, C. R. H.; Frandsen, C.; Mørup, S. Inter-particle interactions in agglomerates of α-Fe_2O_3 nanoparticles: Influence of grinding, *J. Colloid Interface Science* **2004,** *279* 132–136. Copyright (2004) by Elsevier.

The strength of interactions between nanoparticles is very sensitive to the method of sample preparation. For example, gentle grinding of nanoparticles in a mortar can have a dramatic influence on the relaxation behavior. This is illustrated in Figure 7, which shows Mössbauer spectra of samples of 8 nm hematite nanoparticles, prepared by drying aqueous suspensions of chemically prepared particles and after grinding for different periods of time together with nanoparticles of η-Al_2O_3 [45]. At room temperature, the spectrum of the as-prepared sample shows a sextet with very broad lines, typical for samples in which the superparamagnetic relaxation is suppressed by inter-particle interactions. At 80 K the spectrum consists of a sextet with relatively narrow lines. On grinding for only a few minutes the appearance of an intense doublet in the room-temperature spectra is observed. This indicates that the inter-particle interactions are strongly reduced. The spectra obtained at 80 K after grinding show a superposition of sextets and doublets typical for non-interacting or weakly interacting nanoparticles. After 60 min grinding, all particles are superparamagnetic at room temperature, and most of them also at 80 K. Thus, gentle grinding appears to separate strongly interacting nanoparticles. In later studies it has been shown that after strongly interacting nanoparticles have been dispersed by intense ultrasonic treatment, the magnetic interactions can be re-established by drying suspensions of the dispersed particles [46].

Influence of inter-particle interactions on the spin structure in nanoparticles

The spin structure in nanoparticles may differ from that of the corresponding bulk materials, and magnetic inter-particle interactions can have a large influence on the spin orientation. In Mössbauer spectroscopy studies of magnetic materials, the spin orientation relative to the crystal axes may be studied by analyzing the quadrupole shift, ε of magnetically split spectra, which is given by the expression

$$\varepsilon = \varepsilon_0 \frac{3\cos^2\beta - 1}{2} \ . \qquad (13)$$

Here, β is the angle between the symmetry direction of the electric field gradient and the magnetic hyperfine field. In hematite, ε_0 = 0.200 mm/s, and the symmetry direction of the electric field gradient is parallel to the [001] axis of the hexagonal unit cell. In non-interacting hematite nanoparticles and in bulk hematite above the Morin transition temperature (~263 K), the magnetic hyperfine field is perpendicular to this direction (β = 90°), resulting in a quadrupole shift of −0.100 mm/s. In samples of interacting hematite nanoparticles the absolute value of the quadrupole shift at low temperatures is slightly smaller (ε ≈ −0.075 mm/s in interacting 8 nm particles [36]). This is illustrated in Figure 8a and indicates a rotation of the spin direction, corresponding to β ≈ 75°, i.e., an out-of-plane spin rotation of about 15°, induced by inter-particle interactions.

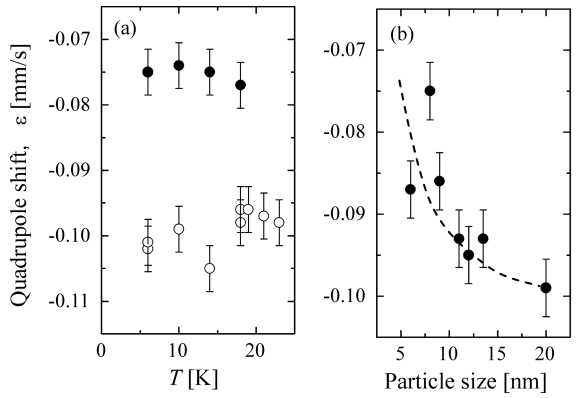


Figure 8: (a) The quadrupole shift of coated (open circles) and uncoated (solid circles) 8 nm hematite particles as a function of temperature. (b) The quadrupole shift of uncoated hematite nanoparticles at 20 K as a function of particle size. Reprinted from Frandsen, C.; Mørup, S. Spin rotation in α-Fe_2O_3 nanoparticles by interparticle interactions, *Phys. Rev. Lett.* **2005,** *94,* 027202. Copyright (2005) by the American Physical Society.

The spin rotation can be explained by interactions between hematite nanoparticles for which the easy axis forms the angle θ_0 with the interaction field. In this case Equation 9 should be replaced by

$$E(\theta) \approx KV \sin^2 \theta - J_{\text{eff}} M^2(T) b(T) \cos(\theta - \theta_0) \,. \qquad (14)$$

In the simple case when $\theta_0 = 90°$ one can find the analytical solution for the value of θ, which gives the lowest energy:

$$\sin\theta = \frac{J_{\text{eff}} M^2(T) b(T)}{2KV} \,. \qquad (15)$$

Figure 8b shows the quadrupole shift of uncoated hematite nanoparticles at 20 K as a function of particle size. There is an overall tendency that the deviation of ε from the bulk value decreases with increasing particle size, i.e., the rotation angle decreases with increasing particle size. This is at least qualitatively in agreement with the volume dependence of the rotation angle given by Equation 15.

In studies of interacting nanoparticles of hematite and NiO, a spin rotation much larger than 15° has been found. At low temperatures, the hematite particles showed quadrupole shifts up to around +0.16 mm/s, corresponding to $\beta \approx 21°$, i.e., an out-of-plane spin rotation of about 69° [41]. Furthermore, the quadrupole shifts were found to decrease with increasing temperature. This is also in accordance with Equation 15, because of the decrease of the order parameter, $b(T)$ with increasing temperature, as illustrated in Figure 6.

Conclusion

During the first decades after the discovery of superparamagnetism, almost all experimental data for the magnetic dynamics of nanoparticles were analyzed by use of the theoretical models for non-interacting particles by Néel [7] and Brown [8]. However, in many more recent studies it has been realized that magnetic interactions between nanoparticles often play a crucial role. Long-range magnetic dipole interactions are important in samples of ferromagnetic and ferrimagnetic nanoparticles unless the particles are well separated. In samples with a high particle concentration, the inter-particle dipole interactions can result in formation of a collective state. If the particles are randomly distributed, the collective state can have many similarities to a spin glass. In other cases, for example, if the particles form chains, their magnetic moments may be aligned. Studies of antiferromagnetic particles have shown that exchange interactions between particles in close proximity can also result in the formation of a collective state at temperatures where the particles would be superparamagnetic if isolated. The temperature dependence of the order parameter is in accordance with a simple mean field theory. Studies of hematite nanoparticles have shown that exchange interactions between magnetic nanoparticles with different orientations of the easy axes can result in a rotation of the spin structure. Thus, systems of interacting magnetic nanoparticles show a rich variety of phenomena that are interesting both for fundamental scientific studies and for applications of magnetic nanoparticles in, e.g., magnetic data storage media.

Acknowledgements

The work was supported by the Danish Council for Independent Research, Technology and Production Sciences (FTP) and Natural Sciences (FNU).

References

1. Berkowitz, A. E.; Takano, K. *J. Magn. Magn. Mater.* **1999,** *200,* 552–570. doi:10.1016/S0304-8853(99)00453-9
2. Nogués, J.; Schuller, I. K. *J. Magn. Magn. Mater.* **1999,** *192,* 203–232. doi:10.1016/S0304-8853(98)00266-2
3. Nogués, J.; Sort, J.; Langlais, V.; Skumryev, V.; Suriñach, S.; Muñoz, J. S.; Baró, M. D. *Phys. Rep.* **2005,** *442,* 65–117. doi:10.1016/j.physrep.2005.08.004
4. Meiklejohn, W. H.; Bean, C. P. *Phys. Rev.* **1956,** *102,* 1413–1414. doi:10.1103/PhysRev.102.1413
5. van der Zaag, P. J.; Ijiri, Y.; Borchers, J. A.; Feiner, L. F.; Wolf, R. M.; Gaines, J. M.; Erwin, R. W.; Verheijen, M. A. *Phys. Rev. Lett.* **2000,** *84,* 6102–6105. doi:10.1103/PhysRevLett.84.6102
6. Golosovsky, I. V.; Salazar-Alvarez, G.; López-Ortega, A.; González, M. A.; Sort, J.; Estrader, M.; Suriñach, S.; Baró, M. D.; Nogués, J. *Phys. Rev. Lett.* **2009,** *102,* 247201. doi:10.1103/PhysRevLett.102.247201
7. Néel, L. *Ann. Geophys. (C. N. R. S.)* **1949,** *5,* 99–136.

8. Brown, W. F., Jr. *Phys. Rev.* **1963,** *130,* 1677–1686. doi:10.1103/PhysRev.130.1677
9. Hansen, M. F.; Mørup, S. *J. Magn. Magn. Mater.* **1998,** *184,* 262–274. doi:10.1016/S0304-8853(97)01165-7
10. Djurberg, C.; Svedlindh, P.; Nordblad, P.; Hansen, M. F.; Bødker, F.; Mørup, S. *Phys. Rev. Lett.* **1997,** *79,* 5154–5157. doi:10.1103/PhysRevLett.79.5154
11. Mamiya, H.; Nakatani, I.; Furubayashi, T. *Phys. Rev. Lett.* **1998,** *80,* 177–180. doi:10.1103/PhysRevLett.80.177
12. Prené, P.; Tronc, E.; Jolivet, J. P.; Livage, J.; Cherkaoui, R.; Nogués, M.; Dormann, J. L.; Fiorani, D. *IEEE Trans. Magn.* **1993,** *29,* 2658–2660. doi:10.1109/20.280834
13. Tronc, E.; Prené, P.; Jolivet, J. P.; d'Orazio, F.; Lucari, F.; Fiorani, D.; Godinho, M.; Cherkaoui, R.; Nogues, M.; Dormann, J. L. *Hyperfine Interact.* **1995,** *95,* 129–148. doi:10.1007/BF02146310
14. Fiorani, D.; Dormann, J. L.; Cherkaoui, R.; Tronc, E.; Lucari, F.; D'Orazio, F.; Spinu, L.; Nogues, M.; Garcia, A.; Testa, A. M. *J. Magn. Magn. Mater.* **1999,** *196–197,* 143–147. doi:10.1016/S0304-8853(98)00694-5
15. Zhang, J.; Boyd, C.; Luo, W. *Phys. Rev. Lett.* **1996,** *77,* 390–393. doi:10.1103/PhysRevLett.77.390
16. Petracic, O.; Kleemann, W.; Binek, C. H.; Kakazei, G. N.; Pogorelov, Y. G.; Sousa, J. B.; Cardoso, S.; Freitas, P. P. *Phase Transitions* **2002,** *75,* 73–79. doi:10.1080/01411590290022969
17. López-Ruiz, R.; Luis, F.; Sesé, J.; Bartolomé, J.; Deranlot, C.; Petroff, F. *EPL* **2010,** *89,* 67011. doi:10.1209/0295-5075/89/67011
18. Parker, D.; Lisiecki, I.; Pelini, M. P. *J. Phys. Chem. Lett.* **2010,** *1,* 1139–1142. doi:10.1021/jz1001874
19. Jonsson, T.; Svedlindh, P.; Hansen, M. F. *Phys. Rev. Lett.* **1998,** *81,* 3976–3979. doi:10.1103/PhysRevLett.81.3976
20. Jönsson, P. E.; Hansen, M. F.; Nordblad, P. *Phys. Rev. B* **2000,** *61,* 1261–1266. doi:10.1103/PhysRevB.61.1261
21. Bedanta, S.; Klemann, W. *J. Phys. D: Appl. Phys.* **2009,** *42,* 013001. doi:10.1088/0022-3727/42/1/013001
22. Jönsson, P. E. *J. Nanosci. Nanotechnol.* **2010,** *10,* 6067–6071. doi:10.1166/jnn.2010.2591
23. Sankar, S.; Dender, D.; Borchers, J. A.; Smith, D. J.; Erwing, R. W.; Kline, S. R.; Berkowitz, A. E. *J. Magn. Magn. Mater.* **2000,** *221,* 1–9. doi:10.1016/S0304-8853(00)00391-7
24. Bedanta, S.; Eimüller, T.; Klemann, W.; Rhensius, J.; Stromberg, F.; Amaladass, E.; Cardoso, S.; Freitas, P. P. *Phys. Rev. Lett.* **2007,** *98,* 176601. doi:10.1103/PhysRevLett.98.176601
25. Alonso, J.; Fdez-Gubieda, M. L.; Barandiarán, J. M.; Svalov, A.; Fernández Barquín, L.; Alba Venero, D.; Orue, I. *Phys. Rev. B* **2010,** *82,* 054406. doi:10.1103/PhysRevB.82.054406
26. Sugawara, A.; Scheinfein, M. R. *Phys. Rev. B* **1997,** *56,* R8499–R8502. doi:10.1103/PhysRevB.56.R8499
27. Mørup, S. *IEEE Trans. Magn.* **1987,** *23,* 3518–3519. doi:10.1109/TMAG.1987.1065731
28. Mørup, S.; Tronc, E. *Phys. Rev. Lett.* **1994,** *72,* 3278–3281. doi:10.1103/PhysRevLett.72.3278
29. Berkov, D. V. *J. Magn. Magn. Mater.* **1998,** *186,* 199–213. doi:10.1016/S0304-8853(98)00078-X
30. Iglesias, O.; Labarta, A. *Phys. Rev. B* **2004,** *70,* 144401. doi:10.1103/PhysRevB.70.144401
31. Jönsson, P.; García-Palacios, J. L. *EPL* **2001,** *55,* 418–424. doi:10.1209/epl/i2001-00430-0
32. Dunin-Borkowski, R. E.; Kasama, T.; Wei, A.; Tripp, S. L.; Hÿtch, M. J.; Snoeck, E.; Harrison, R. J.; Putnis, A. *Microsc. Res. Tech.* **2004,** *64,* 390–402. doi:10.1002/jemt.20098
33. Thomas, J. M.; Simpson, E. T.; Kasama, T.; Dunin-Borkowski, R. E. *Acc. Chem. Res.* **2008,** 665–674. doi:10.1021/ar700225v
34. Néel, L. *C. R. Hebd. Seances Acad. Sci.* **1961,** *252,* 4075–4080.
35. Hansen, M. F.; Koch, C. B.; Mørup, S. *Phys. Rev. B* **2000,** *62,* 1124–1135. doi:10.1103/PhysRevB.62.1124
36. Frandsen, C.; Mørup, S. *Phys. Rev. Lett.* **2005,** *94,* 027202. doi:10.1103/PhysRevLett.94.027202
37. Kuhn, L. T.; Lefmann, K.; Bahl, C. R. H.; Ancona, S. N.; Lindgård, P.-A.; Frandsen, C.; Madsen, D. E.; Mørup, S. *Phys. Rev. B* **2006,** *74,* 184406. doi:10.1103/PhysRevB.74.184406
38. Frandsen, C.; Bahl, C. R. H.; Lebech, B.; Lefmann, K.; Kuhn, L. T.; Keller, L.; Andersen, N. H.; von Zimmermann, M.; Johnson, E.; Klausen, S. N.; Mørup, S. *Phys. Rev. B* **2005,** *72,* 214406. doi:10.1103/PhysRevB.72.214406
39. Berquó, T. S.; Erbs, J. J.; Lindquist, A.; Penn, R. L.; Banerjee, S. K. *J. Phys.: Condens. Matter* **2009,** *21,* 176005. doi:10.1088/0953-8984/21/17/176005
40. Madsen, D. E.; Cervera-Gontard, L.; Kasama, T.; Dunin-Borkowski, R. E.; Koch, C. B.; Hansen, M. F.; Frandsen, C.; Mørup, S. *J. Phys.: Condens. Matter* **2009,** *21,* 016007. doi:10.1088/0953-8984/21/1/016007
41. Frandsen, C.; Lefmann, K.; Lebech, B.; Bahl, C. R. H.; Ancoña, S. N.; Theil Kuhn, L.; Keller, L.; Mørup, S. (to be published).
42. Sugimoto, T.; Wang, Y.; Itoh, H.; Muramatsu, A. *Colloids Surf., A* **1998,** *134,* 265–279. doi:10.1016/S0927-7757(97)00103-9
43. Guydo, Y.; Mostrom, A.; Penn, R. L.; Banerjee, S. K. *Geophys. Res. Lett.* **2003,** *30,* 1512. doi:10.1029/2003GL017021
44. Nesterova, M.; Moreau, J.; Banfield, J. F. *Geochim. Cosmochim. Acta* **2003,** *67,* 1177–1187. doi:10.1016/S0016-7037(02)01180-8
45. Xu, M.; Bahl, C. R. H.; Frandsen, C.; Mørup, S. *J. Colloid Interface Sci.* **2004,** *279,* 132–136. doi:10.1016/j.jcis.2004.06.039
46. Frandsen, C.; Mørup, S. *J. Phys.: Condens. Matter* **2006,** *18,* 7079–7084. doi:10.1088/0953-8984/18/31/003

License and Terms

This is an Open Access article under the terms of the Creative Commons Attribution License (http://creativecommons.org/licenses/by/2.0), which permits unrestricted use, distribution, and reproduction in any medium, provided the original work is properly cited.

The license is subject to the *Beilstein Journal of Nanotechnology* terms and conditions: (http://www.beilstein-journals.org/bjnano)

The definitive version of this article is the electronic one which can be found at: doi:10.3762/bjnano.1.22

Beilstein Journal of Nanotechnology

Kinetic lattice Monte-Carlo simulations on the ordering kinetics of free and supported FePt $L1_0$-nanoparticles

Michael Müller and Karsten Albe*

Full Research Paper

Open Access

Address:
Institut für Materialwissenschaft, Technische Universität Darmstadt, Petersenstr. 32, D-64287 Darmstadt, Germany

Email:
Michael Müller - mueller@mm.tu-darmstadt.de; Karsten Albe* - albe@mm.tu-darmstadt.de

* Corresponding author

Keywords:
FePt; Monte-Carlo simulations; nanoparticles; ordering kinetics

Beilstein J. Nanotechnol. **2011,** *2,* 40–46.
doi:10.3762/bjnano.2.5

Received: 26 October 2010
Accepted: 22 December 2010
Published: 17 January 2011

Guest Editors: U. Wiedwald and P. Ziemann

© 2011 Müller and Albe; licensee Beilstein-Institut.
License and terms: see end of document.

Abstract

The ordering kinetics in free and supported $L1_0$ nanoparticles was studied by means of lattice-based kinetic Monte-Carlo simulations. Starting from a fully disordered particle of Wulff shape, the simulations show that the nucleation of ordered domains is starting quickly on various (100) facets but is retarded in the particle volume due to the lack of vacancies compared with a thin film geometry. If a substrate is present, we do not find significant differences in the ordering behavior. This holds true, even if we impose a massively increased thermodynamic driving force for interface segregation, because the nucleation of ordered domains on free facets is significantly faster than the bulk diffusion of the segregating species to the interface. In cases where wetting of the substrate or surface facetting occurs, we find that diffusional atomic motion on the surface goes along with an enhanced long-range order.

Introduction

Nanoparticles in ordered $L1_0$ structures like FePt and CoPt are considered as candidate materials for magnetic storage media [1] and biomedical applications [2] because the superparamagnetic limit – where a thermally stable magnetization direction can be expected – is in the range of a 5–10 nm. It has been shown experimentally that ordered arrays of particles with monodisperse size distribution can be prepared by various synthesis routes ([3] and references therein). The as-prepared particles, however, are in most cases partially disordered and can also contain twin planes [4]. In the past, major attention has been paid to the problem of installing internal order without affecting the particle arrangement and size by annealing procedures. As the phase stability of finite phases can be massively affected by the presence of surfaces or interfaces, it was initially

even unclear if the single-crystalline ordered configuration represented the thermodynamic equilibrium. At this point, computer simulation studies revealed that nanoparticles larger than 5–6 nm in diameter are single-crystalline and ordered at ambient conditions [5-9], while partially ordered or twinned configurations can be considered as metastable. If the particle composition is properly adjusted (taking into account the surface segregation effects), the ordering temperature is only a weak function of particle size [10]. The question to what extent the ordering kinetics is affected by the small particle size and how the ordering kinetics can be enhanced, has gained much less attention in the past. Rellinghaus et al. [11] concluded from an analysis of particles prepared and annealed in the gas phase, that the ordering kinetics controlled by volume diffusion is relatively slow while Wiedwald et al. [12] showed that the annealing temperature of FePt nanoparticles can be reduced after He-irradiation which points to the fact that athermal vacancies assist in the particle ordering. In principle, ordering requires the rearrangement of atoms on the available lattice sites. Since the $L1_0$ structure is close-packed, we can safely ignore that other mechanisms like interstitial diffusion play a role for atomic rearrangements. It is rather the vacancy-mediated site exchange that is responsible for the ordering. Therefore, the ordering kinetics depends on the concentration and mobility of vacancies in the nanoparticle. In a recent paper, we have shown that the thermal vacancy concentration in the inner part of a metallic nanoparticle is significantly reduced [13]. This can be attributed to the excess energy of surface formation that leads to an $1/r$-dependence of the vacancy formation energy. Considering this, one can anticipate that the ordering kinetics is slower than in the bulk counterpart because of the reduced vacancy concentration. On the other hand, the formation of $L1_0$ domains is a nucleation process and therefore the presence of surface sites can facilitate the formation of ordered domains. In addition, the interface to the substrate could also affect the ordering. If we imagine that a (100)-oriented substrate is ideally commensurate with the FePt lattice and one constituent would preferentially segregate to the interface, the $L1_0$ domain formation could be promoted in this scenario by thermodynamic driving forces imposing the correct stacking sequence.

In this paper, we present lattice-based kinetic Monte-Carlo simulations of FePt nanoparticles that reveal the influence of free surfaces, bulk vacancies and interaction with a substrate on the disorder–order transition. After describing the methodology, the case of a free particle is studied and compared to a thin film geometry. Then, we investigate the role of a commensurate substrate by varying the thermodynamic driving force for interface segregation. Finally, we conclude with a summary of our results.

Results and Discussion

Simulation method and modified Ising-type Hamiltonian

The ordering kinetics in FePt nanoparticles is investigated by an n-fold way kinetic Monte-Carlo algorithm [14,15]. The simulations are initialized with a random distribution of Fe and Pt atoms on a fcc lattice. In each step of the simulation, all possible jumps of atoms to neighboring empty lattice sites are identified. To allow a dynamical interpretation of the simulations, the transition rate ν_j is calculated for each jump j by

$$\nu_j = \nu_0 \times \begin{cases} \exp\left(-\dfrac{E^{\mathrm{mig}}}{k_B T}\right) & \text{for } \Delta E_j \le 0, \\ \exp\left(-\dfrac{\Delta E_j + E^{\mathrm{mig}}}{k_B T}\right) & \text{for } \Delta E_j > 0. \end{cases} \quad (1)$$

Here, ΔE_j is the change of energy in the system associated with transition j which is calculated using a modification of the Ising-type Hamiltonian with second nearest neighbor interactions as described in [10]. For simplicity, the attempt frequency ν_0 and the migration barrier E^{mig} are assumed independent of the type of the jumping atom or its chemical surrounding. One of the transitions is accepted in each step and a time variable is incremented by $\Delta t = -\ln r / (\sum_j \nu_j)$, where r is a random number between 0 and 1.

This kinetic Monte-Carlo algorithm allows to study ordering processes in FePt bulk materials as well as nanoparticles. If a single vacancy is introduced in a lattice with periodic boundary conditions, a rearrangement of atoms by the vacancy diffusion mechanism in bulk materials is simulated. Instead, by initializing the simulation with a particle in the center of an otherwise empty lattice, surface diffusion occurs naturally. As described in [6], the random generation and annihilation of vacancies at the surface then gives rise to a thermal concentration of vacancies in the volume of the particle. In consequence, the absolute values of the interaction energies in the Ising-type Hamiltonian have to be adjusted in order to reproduce reasonable values for the vacancy formation energy. In doing so, important properties like the phase diagram and the segregation behavior of the model described in [10] remain unchanged. The set of modified parameters and the resulting vacancy formation energies E_v^f in various chemical surroundings are listed in Table 1. Using these values, the vacancy formation energies in the pure fcc Fe and fcc Pt phases agree well with the experimental values of 1.71 eV for Fe [16] and 1.35 eV for Pt [17], respectively.

Due to a lack of reference values for the FePt alloy system, experimental data on Pt self-diffusion are used to determine the

Table 1: Modified parameters of the Ising-type Hamiltonian of [9] and the resulting vacancy formation energies E_v^f for various configurations.

Parameter	Value [eV]	Vacancy configuration	E_v^f [eV]
ε_1^{FeFe}	−0.269	vacancy in fcc Fe	1.61
ε_1^{PtPt}	−0.219	vacancy in fcc Pt	1.31
ε_1^{FePt}	−0.337	Fe site in $L1_0$ FePt	1.89
ε_2^{FeFe}	0	Pt site in $L1_0$ FePt	1.79
ε_2^{PtPt}	0	Fe site in A1 FePt	1.85
ε_2^{FePt}	0.00186	Pt site in A1 FePt	1.70

parameters ν_0 and E^{mig}. Ehrhart [17] reports an attempt frequency of $\nu_0 = 4 \times 10^{13}$ s^{-1} and an activation energy of $Q = E_v^f + E^{mig} = 2.8$ eV for Pt self-diffusion. As predicted by our Ising-type Hamiltonian, the average formation energy of a vacancy in FePt alloys is 1.8 eV. Therefore, an attempt frequency $\nu_0 = 4 \times 10^{13}$ s^{-1} and a migration energy $E^{mig} = 1$ eV should provide realistic estimates for the present simulations.

Kinetics of ordering in bulk FePt alloys

In order to validate the choice of our model parameters, the ordering kinetics of a FePt bulk crystal predicted by the simulations have been compared to annealing experiments on sputtered FePt thin films at a temperature of 973 K [18]. The bulk crystal has been modeled by periodic boundary conditions applied to a lattice of 70 × 70 × 70 fcc unit cells which corresponds to $N = 1{,}372{,}000$ lattice sites. By randomly distributing Fe and Pt atoms and introducing a single vacancy, the lattice has been initialized and the *n*-fold way algorithm described above was used for simulating the dynamics of ordering. In the simulation of a bulk material, the vacancy concentration is fixed at $C_v^{sim} = 1/N$ while in a real system, a temperature dependent vacancy concentration of $C_v^{real}(T) \approx \exp(-1.8\ \text{eV}/k_B T)$ would be observed. In the latter case, the average vacancy formation energy in FePt alloys predicted by the Ising-type Hamiltonian is assumed. In order to re-late the time variable of the *n*-fold way algorithm to a real-time, it has to be scaled by the factor $C_v^{sim}/C_v^{real}(T)$.

At each step of the simulation, the amount of order has been analyzed by calculating the long range order (LRO) parameter as defined in [10] and by counting the fraction of atoms that possess a completely ordered nearest neighborhood. The time evolution of both order parameters is plotted in Figure 1 in comparison to experiments on sputtered FePt films of 10 nm thickness [18]. Because of the large number of atoms, the simulations did not result in a single-domain ordered crystal. Instead, ordered domains with different *c*-axis orientation have been observed. To provide a reasonable measurement of the amount of order, the LRO parameter plotted in Figure 1 has been calculated by summing up the individual domains. A value close to 1, i.e., complete ordering, is obtained after approximately one hour of real-time. Compared to that, the parameter describing the fraction of $L1_0$-ordered atoms initially rises on a much shorter time scale, only reflecting the presence of local order. At the end of the simulation the value is well below 1.0 which indicates the fraction of atoms that residing in antiphase boundaries.

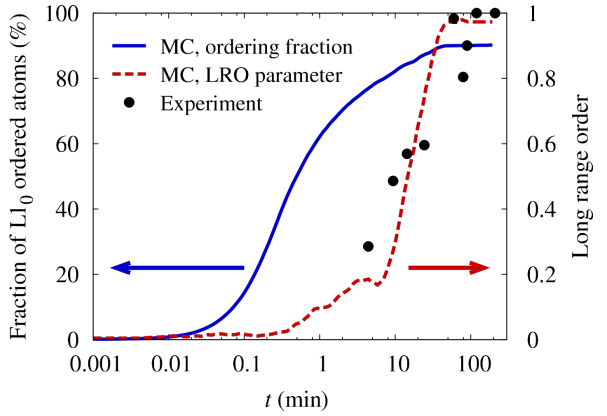


Figure 1: Comparison of simulated ordering kinetics in bulk FePt alloys with results from annealing experiments on sputtered thin films [18]. The temperature in both, experiment and simulation, is 973 K.

In experiments, the presence of different domains has also been observed by dark-field (DF) transmission electron microscopy [18]. In consequence, the total ordered volume fraction has been determined by combining DF images from three independent directions. Therefore, the degree of order reported in [18] corresponds to the additive LRO parameter plotted in Figure 1 and an excellent agreement between the simulations and the experiments can be observed. Given the simplicity of the model and the uncertainties in the parameters ν_0, E^{mig} as well as the vacancy formation energy, such an exact agreement can be considered coincidental to some extent. However, it shows that the chosen values for ν_0 and E^{mig} at least represent a reasonable estimate for diffusion parameters in FePt bulk alloys.

Free FePt nanoparticles

By using the model parameters described before, the evolution of ordering was studied for an initially disordered 5 nm particle with closed shells. In this case, nucleation, migration and annihilation of vacancies is fully described by the computer model and no additional assumptions are imposed. In Figure 2, the evolution of the ordering fraction at 1000 K is plotted in comparison to a bulk sample. Since it is expected that surface diffu-

sion can increase the transformation rate in near-surface layers, the particle has been divided into a spherical core of diameter of 3.2 nm, followed by three layers of thickness of 0.3 nm each. By separately analyzing the ordering fraction in all layers, the transition rate can be separated into surface and volume contributions. The effect of surface diffusion is clearly visible in Figure 2. A given amount of ordering is reached within a shorter time scale the closer a layer is positioned to the surface. Compared to the simulations of the bulk crystal, it becomes clear that the ordering in near-surface layers proceeds at a higher rate than in bulk material. In contrast to that, the core of the particle possesses the lowest transformation rate from the disordered to the ordered phase which is due to the lack of vacancies.

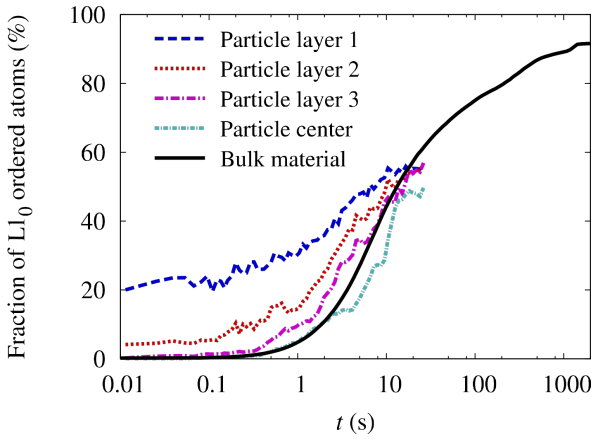


Figure 2: Evolution of ordering fraction in a free FePt nanoparticle of D = 5 nm compared to the case of bulk material. For analyzing the contribution of surface and volume effects, the particle has been divided into a spherical core of diameter of 3.2 nm, followed by three layers of thickness of 0.3 nm, with layer 1 denoting the surface. The temperature is 1000 K. Initially, the fraction of ordering was zero in all layers.

The kinetic Monte-Carlo simulations of the free FePt nanoparticles were terminated after approximately 30 s of real annealing time which corresponds to one month of computing time. This low efficiency of the algorithm originates from the sampling of the thermal vacancy concentration in the particle. Within the simulated time scale, the ordering fraction plotted in Figure 2 indicates that only 50% of the particle has been transformed. On the other hand, the structure of the particle at the end of the simulation run, which is analyzed in Figure 3, suggests that a rather high degree of order has been achieved. Because of the statistical nucleation of the $L1_0$ phase, however, the whole particle is divided into several ordered domains with different c-axis orientation. Approximately 50% of the atoms reside in antiphase boundaries, explaining the low value of the ordering fraction.

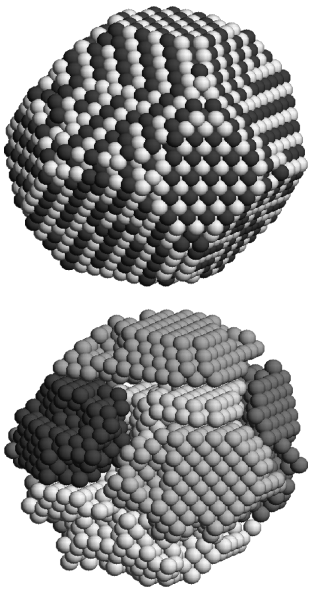


Figure 3: Structure of a free 5 nm particle after 30 s of annealing time at 1000 K. Top: Pt atoms are displayed light gray, Fe atoms dark gray. Bottom: Atoms in antiphase boundaries have been removed and the gray scale visualizes atoms that belong to the same ordered domain.

Due to the existence of multiple domains, the ordering fraction in the bulk material has also reached a value of only 60% after 30 s of annealing time. As can be observed in Figure 2, the annealing process has to be continued for up to 30 min in real-time to eliminate most of the antiphase boundaries. Reaching these time scales in the particle simulations, however, would require computing times of up to 5 years which is not feasible. Even if the ordering process in free FePt nanoparticles could not be followed up to the final stage, options for increasing the transformation rate can be extracted. The effectiveness of these options will be tested in the following. On the one hand, the important contribution of surface diffusion to atomic mobility has been demonstrated. As a consequence, it should be possible to enhance the transformation by increasing the amount of surface diffusion. Furthermore, a random nucleation of $L1_0$-ordered domains with different c-axis orientation occurs in free particles and long annealing times are needed for obtaining a single domain structure. In order to reduce the random nucleation, a preferential c-axis orientation can be induced. By controlling the interface energetics between the particle and a substrate, the possibility for realizing enhanced surface diffusion and a preferential ordering direction in supported FePt nanoparticles is investigated in the following.

Supported FePt nanoparticles

In order to model the energetics of supported FePt nanoparticles, the lattice Hamiltonian was extended by nearest neighbor bond energies of Fe and Pt atoms to a substrate, denoted by

$\varepsilon^{\mathrm{FeSub}}$ and $\varepsilon^{\mathrm{PtSub}}$, respectively. The relative strength of the atom interactions with the substrate was measured by the ratios $\varphi^{\mathrm{Fe}} = \varepsilon^{\mathrm{FeSub}} / \varepsilon_1^{\mathrm{FeFe}}$ and $\varphi^{\mathrm{Pt}} = \varepsilon^{\mathrm{PtSub}} / \varepsilon_1^{\mathrm{PtPt}}$. The lattice Hamiltonian restricts the investigations to an epitaxial relation between the substrate and the nanoparticles. Furthermore, only the (100) surface of the substrate was considered.

By varying the strength of the interactions with the substrate, the interface energetics of the supported particles can be modified. Two general cases are considered: First, the relative strength of the interactions of the substrate is assumed to be identical for both elements. In this case, the parameters $\varphi^{\mathrm{Fe}} = \varphi^{\mathrm{Pt}}$ determine the wetting angle of the particle in equilibrium with the substrate. Second, it is assumed that only Pt has a significant binding energy to the substrate, with $\varphi^{\mathrm{Fe}} = 0$ and $\varphi^{\mathrm{Pt}} > 0$. In addition to wetting, the parameters then provide a driving force for segregation of Pt at the interface to the substrate which prefers a *c*-axis orientation of the $L1_0$ structure perpendicular to the substrate.

For generating the initial configuration for kinetic Monte-Carlo simulations of supported particles, a particle of 5 nm in diameter has been equilibrated at 2×10^4 K. Since melting is excluded in the lattice model, a completely disordered particle of Wulff shape is produced, which is positioned on top of the substrate, as illustrated in Figure 4A.

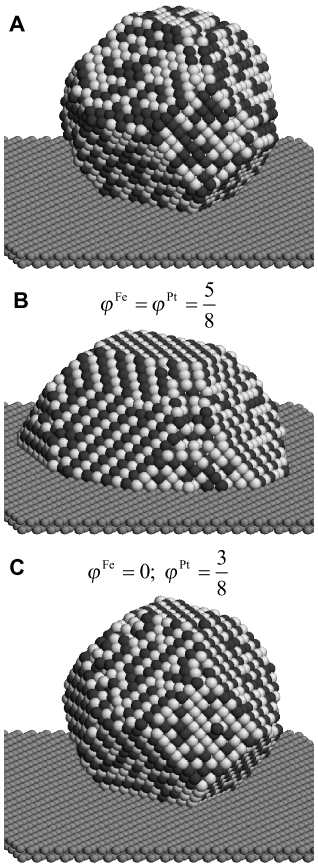


Figure 4: Snapshots of supported FePt nanoparticles illustrating the different interface energetics investigated by the Monte-Carlo simulations. A) A disordered particle of Wulff shape with *D* = 5 nm used at input structure in all simulations. B) Outcome of a simulation with identical Fe-substrate and Pt-substrate interactions leading to strong wetting. C) Outcome of a simulation with only Pt-substrate interactions. The temperature is 1000 K.

Identical Fe–substrate and Pt–substrate interactions

If strong wetting of the particle with the substrate occurs, the wetting process after deposition of the particle is accompanied by a considerable amount of surface diffusion. To test if this effect can be used for improving the ordering kinetics in FePt nanoparticles, a strong interaction of Fe and Pt atoms with the substrate ($\varphi^{\mathrm{Fe}} = \varphi^{\mathrm{Pt}} = 5/8$) is assumed. Starting with five different initial configurations for both supported and unsupported particles, annealing simulations were run for 20 s at 1000 K. A typical outcome of a simulation is depicted in Figure 4B, where the strong wetting and the presence of ordered domains is clearly visible. In Figure 5, the evolution of the LRO parameter is analyzed quantitatively and the ordering kinetics is compared to the free particles. The degree of order varies strongly within both classes of particles. This is explained by the presence of multiple ordered domains because a preferred ordering direction is not present. In the supported particles, however, the LRO parameter tends to show a rapid increase up to a value of 0.2 within a short annealing time of less than 0.1 s. During this time, all free particles remain completely disordered. By monitoring the height of the center of mass of the supported particles over the substrate (top panel in Figure 5), this initial increase in ordering can clearly be related to the wetting process. In addition to wetting facetting also contributes to an enhanced ordering if an initially spherical particle is deposited. This can be seen by comparing the time evolution of the long-range order of the spherical with an initially facetted particle.

The mass transport from the particle surface towards the substrate is therefore accompanied by a simultaneous adjustment of order. However, after the wetting process has been completed, the LRO parameter does not increase up to an annealing time of 1 s, from where on the ordering process in the free particles also sets in. Interestingly, the initial increase of ordering in the supported particles does not lead to a higher degree of ordering compared to the free particles at the end of the simulations. The highest LRO parameter is even found in an unsupported particle. The wetting process only takes place during the initial stages of ordering and the enhancement of diffusion in the supported particles does not persist during the coarsening stage at which the number of ordered domains is reduced. Moreover,

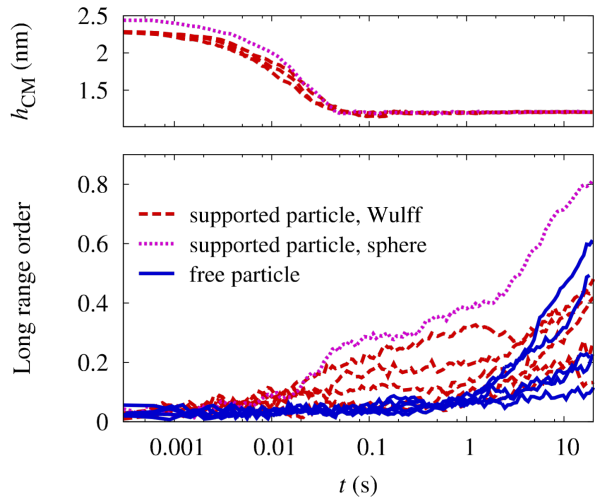


Figure 5: Bottom panel: Evolution of LRO parameter with annealing time at 1000 K in free and supported FePt nanoparticles of D = 5 nm and identical Fe–substrate and Pt–substrate interactions. Top panel: Position of the center of mass of supported FePt nanoparticles, measured in height over the substrate h_{CM}.

surface diffusion does not assist in driving out the antiphase boundaries in the particle volume. As the simulations show, strong wetting does not noticeably increase the ordering kinetics.

Pt–substrate interactions only

To induce an energetically preferred ordering direction in the particles, only Pt–substrate interactions with $\varphi^{Pt} = 3/8$ and $\varphi^{Fe} = 0$ are assumed. As described before, it is not possible to simulate the complete ordering process in FePt nanoparticles within reasonable computing times. Therefore, to compare the ordering in supported particles with a segregation tendency to free particles, the kinetics of the process have been enhanced by artificially increasing the vacancy generation rate. In the simulations of free FePt particles, an average thermal vacancy generation rate of 640 vacancies per second has been measured. By introducing an additional vacancy generation event – which consists of removing a random atom from the interior of the particle with a frequency of 6400 s^{-1} and inserting it on the surface – a tenfold increase of the vacancy generation rate has been achieved in the simulations of this section.

In Figure 4C, the outcome of simulations with an increased vacancy generation rate after an annealing time of 20 s at 1000 K is depicted for a particle with only Pt–substrate interactions. The particle has a truncated octahedral shape and Pt clearly segregates from the interface to the substrate. This segregation imposes a preferential ordering direction with the c-axis perpendicular to the substrate, since ordering in other directions generates an antiphase boundary with the segregated layer. However, by comparing the evolution of the LRO parameter in supported and free particles in Figure 6, a positive effect of the segregation on the ordering kinetics cannot be identified. An inspection of the process shows that the segregation of Pt from the interface occurs at a slower time scale than the initial nucleation of ordered domains. Therefore, the energetic preference of the perpendicular direction is not effective during the nucleation stage and the whole ordering process is again limited by the elimination of the antiphase boundaries. Furthermore, the segregation layer only penalizes the wrong ordering directions by the antiphase boundary and has no effect on the volume of the particle. This only leads to small energy differences between perpendicular and horizontal ordering. In result, the prevailing ordering direction at the end of the ordering process is dictated more by statistics than by the global energy minimum.

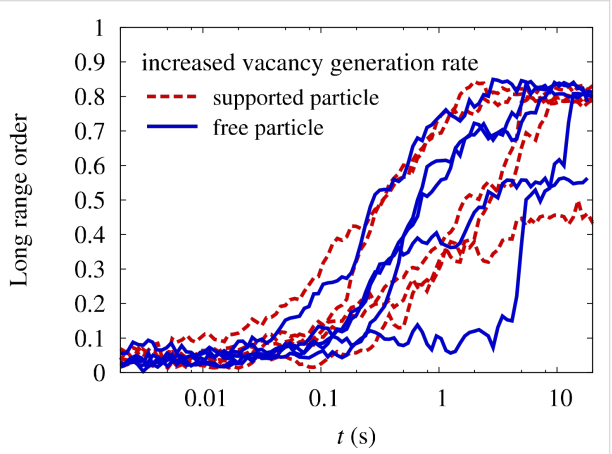


Figure 6: Evolution of LRO parameter with annealing time at 1000 K in free and supported FePt nanoparticles with only Pt-substrate interactions. In order to speed up the simulations, the vacancy generation rate has been increased by a factor ten compared to the thermal vacancy generation rate.

Conclusion

The ordering kinetics of FePt nanoparticles has been investigated by kinetic Monte-Carlo simulations based on a modification of the Ising-type lattice Hamiltonian used before [10]. In order to validate the choice of attempt frequencies and migration barriers for atomic diffusion, the variation of ordering with annealing time in a FePt bulk alloy was compared to annealing experiments on sputtered thin films.

From our simulations of free nanoparticles the important influence of surface diffusion on the ordering transition can be seen. In near-surface layers, the A1–$L1_0$ transformation proceeds at a higher rate than in the particle core. Because of the statistical nucleation of the ordered phase, however, no single domain particles are obtained and an elimination of the antiphase

boundaries could not be observed within the time scales accessible by the simulations. Simulations including a crystalline support show that, even if strong interface segregation is assumed, no influence on the disorder–order transition can be expected. The fact that free, non-supported facets have easier access to free volume for generating vacancies, leads to a higher nucleation rate for ordered domains on free facets compared to the migration rate of segregating species. In conclusion, our study reveals the physical reasons for the slow installment of order in $L1_0$ nanoparticles: Firstly, the relative lack of bulk vacancies and secondly, the occurrence of antiphase boundaries which are due to the nucleation of ordered domains on various (100) facets. Our results suggest that generating athermal vacancies by simultaneous irradiation with ions during the annealing procedure could be a means for improving internal order in $L1_0$ nanoparticles.

Acknowledgements

Generous grants of computing time by the Center for Scientific Computing at the Johann Wolfgang Goethe-University, Frankfurt, Germany and the HHLR at the TU Darmstadt are gratefully acknowledged.

References

1. Sun, S.; Murray, C. B.; Weller, D.; Folks, L.; Moser, A. *Science* **2000,** *287,* 1989. doi:10.1126/science.287.5460.1989
2. Kim, D. K.; Kan, D.; Veres, T.; Normadin, F.; Liao, J. K.; Kim, H. H.; Lee, S. H.; Zahn, M.; Muhammed, M. *J. Appl. Phys.* **2005,** *97,* 10Q918. doi:10.1063/1.1860851
3. Sun, S. H. *Adv. Mater.* **2006,** *18,* 393. doi:10.1002/adma.200501464
4. Stappert, S.; Rellinghaus, B.; Acet, M.; Wassermann, E. F. *Eur. Phys. J. D* **2003,** *24,* 351. doi:10.1140/epjd/e2003-00132-7
5. Müller, M.; Erhart, P.; Albe, K. *Phys. Rev. B* **2007,** *76,* 155412. doi:10.1103/PhysRevB.76.155412
6. Müller, M.; Albe, K. *Acta Mater.* **2007,** *55,* 6617. doi:10.1016/j.actamat.2007.08.030
7. Gruner, M. E.; Rollmann, G.; Entel, P.; Farle, M. *Phys. Rev. Lett.* **2008,** *100,* 087203. doi:10.1103/PhysRevLett.100.087203
8. Chepulskii, R. V.; Butler, W. H.; van de Walle, A.; Curtarolo, S. *Scr. Mater.* **2010,** *62,* 179. doi:10.1016/j.scriptamat.2009.10.019
9. Alam, A.; Kraczek, B.; Johnson, D. D. *Phys. Rev. B* **2010,** *82,* 024435. doi:10.1103/PhysRevB.82.024435
10. Müller, M.; Albe, K. *Phys. Rev. B* **2005,** *72,* 094203. doi:10.1103/PhysRevB.72.094203
11. Rellinghaus, B.; Mohn, E.; Schultz, L.; Gemming, T.; Acet, M.; Kowalik, A.; Kock, B. F. *IEEE Trans. Magn.* **2006,** *42,* 3048. doi:10.1109/TMAG.2006.880087
12. Wiedwald, U.; Klimmer, A.; Kern, B.; Han, L.; Boyen, H. G.; Ziemann, P.; Fauth, K. *Appl. Phys. Lett.* **2007,** *90,* 062508. doi:10.1063/1.2472177
13. Müller, M.; Albe, K. *Acta Mater.* **2007,** *55,* 3237. doi:10.1016/j.actamat.2007.01.022
14. Bortz, A. B.; Kalos, M. H.; Lebowitz, J. L. J. *Comput. Phys.* **1975,** *17,* 10. doi:10.1016/0021-9991(75)90060-1
15. Fichthorn, K. A.; Weinberg, W. H. *J. Chem. Phys.* **1991,** *95,* 1090. doi:10.1063/1.461138
16. Kim, S. M.; Buyers, W. J. L. *J. Phys. F: Met. Phys.* **1978,** *8,* L103. doi:10.1088/0305-4608/8/5/001
17. Ehrhart, P. Atomic defects in Metals. In *Landolt-Börnstein: Numerical data and functional relationships in science and technology;* Ullmaier, H.; Madelung, O.; Hellwege, K.-H., Eds.; Group III, Condensed Matter, Vol. 25; Springer: Heidelberg, Germany, 1991.
18. Ristau, R. A.; Barmak, K.; Lewis, L. H.; Coffey, K. R.; Howard, J. K. *J. Appl. Phys.* **1999,** *86,* 4527. doi:10.1063/1.371397

License and Terms

This is an Open Access article under the terms of the Creative Commons Attribution License (http://creativecommons.org/licenses/by/2.0), which permits unrestricted use, distribution, and reproduction in any medium, provided the original work is properly cited.

The license is subject to the *Beilstein Journal of Nanotechnology* terms and conditions: (http://www.beilstein-journals.org/bjnano)

The definitive version of this article is the electronic one which can be found at: doi:10.3762/bjnano.2.5

Beilstein Journal of Nanotechnology

Structure, morphology, and magnetic properties of Fe nanoparticles deposited onto single-crystalline surfaces

Armin Kleibert[1], Wolfgang Rosellen[2], Mathias Getzlaff[2] and Joachim Bansmann[*3]

Full Research Paper

Open Access

Address:
[1]Swiss Light Source, Paul Scherrer Institut, 5232 Villigen, Switzerland, [2]Institut für Angewandte Physik, Universität Düsseldorf, 40225 Düsseldorf, Germany and [3]Institut für Oberflächenchemie und Katalyse, Universität Ulm, 89081 Ulm, Germany

Email:
Armin Kleibert - armin.kleibert@psi.ch;
Wolfgang Rosellen - wolfgang.rosellen@gmx.de;
Mathias Getzlaff - getzlaff@uni-duesseldorf.de;
Joachim Bansmann* - joachim.bansmann@uni-ulm.de

* Corresponding author

Keywords:
epitaxy; iron; magnetic nanoparticles; Ni(111); RHEED; spontaneous self-alignment; STM; W(110); XMCD

Beilstein J. Nanotechnol. **2011,** *2,* 47–56.
doi:10.3762/bjnano.2.6

Received: 19 November 2010
Accepted: 10 January 2011
Published: 21 January 2011

Guest Editors: U. Wiedwald and P. Ziemann

© 2011 Kleibert et al; licensee Beilstein-Institut.
License and terms: see end of document.

Abstract

Background: Magnetic nanostructures and nanoparticles often show novel magnetic phenomena not known from the respective bulk materials. In the past, several methods to prepare such structures have been developed – ranging from wet chemistry-based to physical-based methods such as self-organization or cluster growth. The preparation method has a significant influence on the resulting properties of the generated nanostructures. Taking chemical approaches, this influence may arise from the chemical environment, reaction kinetics and the preparation route. Taking physical approaches, the thermodynamics and the kinetics of the growth mode or – when depositing preformed clusters/nanoparticles on a surface – the landing kinetics and subsequent relaxation processes have a strong impact and thus need to be considered when attempting to control magnetic and structural properties of supported clusters or nanoparticles.

Results: In this contribution we focus on mass-filtered Fe nanoparticles in a size range from 4 nm to 10 nm that are generated in a cluster source and subsequently deposited onto two single crystalline substrates: fcc Ni(111)/W(110) and bcc W(110). We use a combined approach of X-ray magnetic circular dichroism (XMCD), reflection high energy electron diffraction (RHEED) and scanning tunneling microscopy (STM) to shed light on the complex and size-dependent relation between magnetic properties, crystallographic structure, orientation and morphology. In particular XMCD reveals that Fe particles on Ni(111)/W(110) have a significantly lower (higher) magnetic spin (orbital) moment compared to bulk iron. The reduced spin moments are attributed to the

random particle orientation being confirmed by RHEED together with a competition of magnetic exchange energy at the interface and magnetic anisotropy energy in the particles. The RHEED data also show that the Fe particles on W(110) – despite of the large lattice mismatch between iron and tungsten – are not strained. Thus, strain is most likely not the origin of the enhanced orbital moments as supposed before. Moreover, RHEED uncovers the existence of a spontaneous process for epitaxial alignment of particles below a critical size of about 4 nm. STM basically confirms the shape conservation of the larger particles but shows first indications for an unexpected reshaping occurring at the onset of self-alignment.

Conclusion: The magnetic and structural properties of nanoparticles are strongly affected by the deposition kinetics even when soft landing conditions are provided. The orientation of the deposited particles and thus their interface with the substrate strongly depend on the particle size with consequences regarding particularly the magnetic behavior. Spontaneous and epitaxial self-alignment can occur below a certain critical size. This may enable the obtainment of samples with controlled, uniform interfaces and crystallographic orientations even in a random deposition process. However, such a reorientation process might be accompanied by a complex reshaping of the particles.

Introduction

Ferromagnetic clusters and nanoparticles have gained huge interest due to their interesting fundamental properties as well as their possible applications in data storage media, chemistry, biotechnology and medicine [1-4]. First, Stern–Gerlach measurements proved that ferromagnetic particles may exhibit enhanced and strongly size-dependent magnetic moments [5]; and even non-magnetic materials can show ferromagnetism at the nanoscale [6]. In these systems, the enhanced magnetism in clusters is basically ascribed to the high surface-to-volume ratio. Similarly to magnetic thin films or surfaces, the reduced coordination at the cluster surface leads to significantly higher magnetic spin moments compared to the respective bulk materials. In *3d* transition metals, the magnetic spin moment is large compared to the orbital moment. The orbital moment is usually strongly quenched in bulk materials in comparison to single atoms, and thus, the spin moment is mainly responsible for the total magnetization of the material. However, the orbital moment is an important microscopic quantity in magnetism since it is strongly related to the magneto-crystalline anisotropy energy which, in turn, determines many macroscopic properties of magnetic samples [7,8]. Moreover, the orbital moments are much higher at surfaces or in clusters than in the bulk [9-12]. As a consequence, the orbital contribution to the total magnetization – although small in magnitude – is of fundamental interest, especially in low dimensional systems (for an overview see, e.g., [1,13-15]). For any application the particles have to be supported by or be embedded into a suitable medium. Many studies showed that the cluster–substrate interaction has an tremendous impact on the resulting magnetic properties. The physical origin of such a behavior may be caused, e.g., by strain effects resulting from the interface or a (often anisotropic) compression of the lattice (such as phase transitions from bcc to bct), a phenomenon well-known from ultrathin films on single crystalline surfaces [16]. In special cases, the magnetic anisotropy energy in the nanoparticle may be orders of magnitudes larger than in bulk-like materials. An example for such a case is given by FeCo alloy nanoparticles, where extremely high magnetic anisotropy energies have first been predicted [17] and later on found experimentally in thin films and nanoparticles [18-20].

For technical applications of nanoparticles, homogeneous size distribution is of great importance to guarantee comparable physical properties in an ensemble of particles. Chemistry-based routines [21-23], reaching both a homogeneous particle size and a well-ordered arrangement, are appropriate methods for large-area applications. However, besides homogeneous size-distribution, uniformity in the particle orientation might also be desired. This is particularly important in magnetic devices where well-defined magnetization axes and switching fields are required to store or to process information. Since it is known that even mono-dispersed particles can show significant variations in their magnetic anisotropy energies and in the orientation of their magnetization axes [24], strategies to achieve uniformity in these properties are highly demanding. Physically based nanoparticle preparation techniques are less favorable for large-area applications, but they often provide better control over interfaces and purity and are thus more appropriate for fundamental research and characterization of the magnetic properties. Particularly, they avoid the additional complexity given by the presence of solvents and ligands used in wet-chemical techniques. Thus, to unveil the processes that happen when pure nanoparticles come in contact with a well-defined substrate, we have investigated mass-filtered Fe nanoparticles being deposited from the gas phase onto single-crystalline surfaces under soft-landing conditions. In particular, we combine in situ (i) XMCD to determine their magnetic spin and orbital moments, (ii) RHEED to get access to their crystallographic structure and orientation and (iii) STM to observe their real space morphology on the substrate. The goal of the

manuscript is to correlate the structure and the morphology of deposited iron nanoparticles with their magnetic properties.

Experimental

Experiments on exposed mass-filtered Fe nanoparticles on (ferromagnetic) supports require in situ cluster deposition as well as surface sensitive analysis techniques performed under ultrahigh vacuum conditions. To motivate the need of our combined approach, we first introduce the arc cluster ion source (ACIS) and its deposition characteristics before presenting the magnetic and structural data obtained by XMCD, RHEED and STM.

Cluster generation and deposition by means of ACIS

Fe nanoparticles are generated in the gas phase using a continuously working ACIS for nanoparticle deposition experiments (Figure 1). The design of this source is based on the experience with the pulsed arc cluster ion source (PACIS) in the group of Meiwes-Broer (University of Rostock, Germany) [25]. There, the PACIS is mainly used to produce small size-selected clusters for gas phase experiments in combination with pulsed lasers or other pulsed light sources [26]. For the present experiments the PACIS design has been modified to allow a high and continuous flux of mass-filtered nanoparticles (size regime: 4 nm to 25 nm) with a moderate size distribution in surface science experiments [27,28]. The resulting ACIS is ultrahigh vacuum compatible, small in size to allow easy transportation and can be flexibly attached to different experimental stations, e.g., laboratory-based STM experiments, different end stations at synchrotron light sources such as BESSY (Berlin, Germany) and more recently, the Elmitech PEEM at the SIM beamline of the Swiss Light Source of the Paul Scherrer Institute (Villigen, Switzerland) [29].

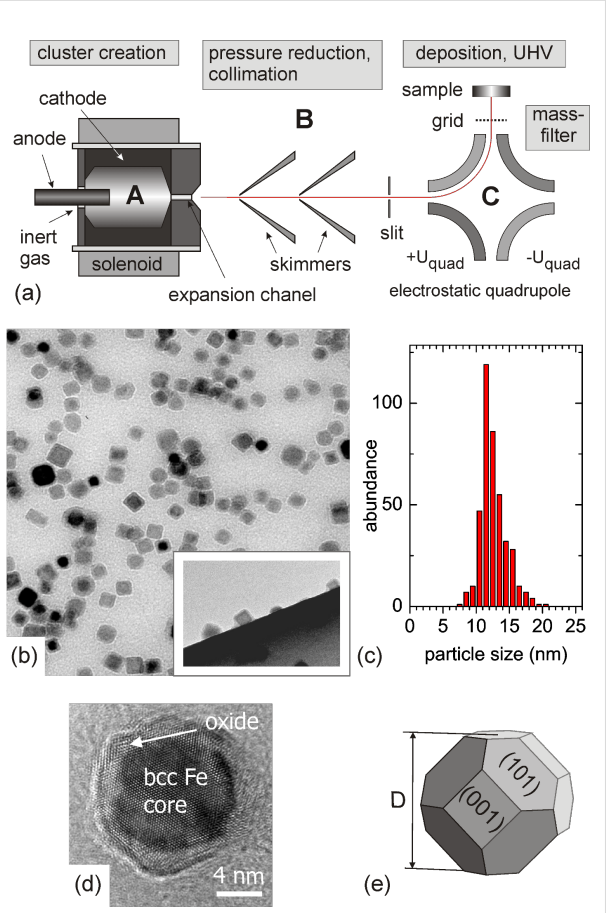


Figure 1: (a) Schematic drawing of the ACIS. (b) TEM image of a typical nanoparticle deposit on a carbon coated copper grid. The side view in the inset reveals compact three-dimensional shapes. (c) Size distribution of Fe particle sizes from (b) including the oxide shell. (d) High resolution TEM image of a single particle showing a 2 nm thick oxide shell surrounding the crystalline Fe core. (e) Schematics of the equilibrium shape of pure crystalline Fe particles as expected from a Wulff construction in the present particle size range [32].

The ACIS consists of three different stages as shown in Figure 1a: (A) the cluster aggregation part based on a hollow cathode made from the target material (here: Fe with a purity of higher than 99%), (B) a dual pumping stage with an oil-free roots pump (250 $m^3 \cdot h^{-1}$) and a turbo molecular pump (250 $l \cdot s^{-1}$) to reduce the huge amount of noble gas (Ar and He) required for the erosion process and (C) a mass-filtering unit based on an electrostatic quadrupole. The cluster material is eroded from the hollow cathode in the presence of the noble gas (at a pressure around 20–40 mbar) using an arc discharge. Small aggregates of this material are kinetically accelerated by collisions in the nozzle and in a weak supersonic expansion to almost the velocity of the seeding gas. The composition of the carrier gas (Ar and He) is controlled by two individual mass flow controllers. After pumping off most of the noble gas, the Fe nanoparticles enter the electrostatic quadrupole deflector which acts as a mass-filtering unit. Different from other gas aggregation sources [30], about 50% of the particles are positively and negatively charged (mostly single charged) and are thus deflected in the electric field of the electrostatic quadrupole. Due to their nearly constant velocity after the expansion process in the hollow cathode, the kinetic energy of the particles is directly related to their mass allowing a separation by using an electrostatic energy dispersive element. The particle deposition finally takes place in a UHV preparation chamber at a residual (noble gas) pressure of about 1×10^{-6} mbar during operation of the source. More recently, a set of aerodynamic lenses has been added to increase the available particle size range and to improve the cluster flux [31].

The size distribution and structure of the Fe particles in the mass-selected cluster beam is deduced from ex situ transmis-

sion electron microscopy (TEM). A typical (air exposed) nanoparticle deposit on a carbon coated copper grid is given in Figure 1b. The side view in the inset shows compact particles with mostly cubic shapes due to the partial oxidation. Electron diffraction reveals the presence of metallic bcc Fe and Fe oxides as, e.g., Fe_3O_4 [27]. A size distribution of the oxidized Fe particles displayed in Figure 1b is given in Figure 1c and yields D_{oxi} = (12.0 ± 1.4) nm. To obtain the actual mean size of the pure Fe nanoparticles, the distribution in Figure 1c needs to be corrected for the effect of partial oxidation. High resolution TEM of the exposed particles reveals metallic cores surrounded by an oxidic shell with a thickness of about 2 nm as shown in Figure 1d. The respective size correction then leads to D = (9.6 ± 1.5) nm for the pure particles before air exposure. High resolution TEM images also reveal that the metallic cores are single crystalline with bcc structure in most of the particles. Similar observations are reported for Fe particle sizes down to 4 nm [33,34]. We may note that at smaller sizes transitions to other structures may occur and thus experimental characterization is always important [35-37].

Energy considerations show that single crystalline bcc Fe nanoparticles in the size range from 4 to 10 nm have an equilibrium shape given by six (001) and twelve (110) surface facets according to a Wulff construction [32,33]. A schematic drawing of such a particle with a diameter D is shown in Figure 1e. This shape has also been found experimentally in pure Fe particles generated by the ACIS source [38]. The low kinetic energy per atom (usually less than 0.1 eV per atom) of the nanoparticles allows soft-landing deposition experiments well below the fragmentation threshold [39]. Accordingly, recent STM studies revealed that the shape of larger particles (D > 4 nm) is only weakly affected when being deposited onto single crystalline substrates, i.e., the height of supported particles as measured with STM corresponds well with the size being determined by TEM [28,40,41]. This is a particular strength of soft-landing techniques. Therefore, they also allow to obtain particle deposits far away from thermal equilibrium which otherwise are hardly accessible.

These advantages make particle deposition techniques very attractive for fundamental research on size-dependent phenomena. However, even under soft-landing conditions, the deposition process cannot be neglected in experiments. Indeed, as we will show, the deposition kinetics may have a crucial impact on the resulting particle properties: First, the random nature of the deposition technique is expected to lead to a large variety of orientations of the particles. For instance, the Fe nanoparticles studied here may finally rest with their (110) or their (001) facets on the substrate with arbitrary azimuthal orientation (Figure 1e). The different contact interfaces may have a strong impact on the particle properties, e.g., due to hybridization effects, interface-induced strain or magnetic anisotropy contributions. The influence of the interface is size-dependent and increases with decreasing particle size and may even dominate over intrinsically size-dependent properties. Second, kinetic energy and interface energy are released upon landing on the surface. The resulting heat may rapidly anneal the particles before the thermal energy is dissipated into the substrate. Depending on the available total energy and the size of the particles, the latter may realign or even reshape on the surface with respective consequences for their resulting properties.

Results and Discussion

In previous works it was found that magnetic nanoparticles show surprisingly strong variations in their properties – such as the magnetic anisotropy energies or microscopic spin and orbital contributions to the total magnetization – when being in contact with different substrates or embedded into different matrices [20,38,42-44]. Here, we focus on Fe nanoparticles being deposited onto different magnetic and non-magnetic single crystalline surfaces. Single crystalline substrates were chosen to provide well-defined and atomically flat substrates. Magnetic substrates are used to magnetize the particles along a well-defined direction by employing the strong exchange interaction at the interface to suppress possible superparamagnetic fluctuations of the particle magnetization [8]. Previous measurements on Fe nanoparticles deposited onto hcp Co(0001)/W(110) revealed bulk-like magnetic spin moments, but surprisingly large orbital moments being twice as large when compared to the respective bulk value [38]. To study the influence of the substrate on these properties, Fe nanoparticles (NPs) have now been investigated on fcc Ni(111)/W(110).

The W(110) substrates were obtained by cycles of heating in oxygen atmosphere as described in the literature [45]. The Ni films with a thickness of about 15 ML were grown by thermal evaporation at a rate of 0.1 atomic monolayers per minute. To obtain a flat and relaxed surface, the films were thermally annealed at 320 K. The clean W(110) surface and the structural quality of the films were checked by means of low energy electron diffraction (LEED). Details regarding the growth and magnetic properties of Ni films on W(110) can be found in the literature [46-48]. Subsequently to film preparation, mass-filtered Fe nanoparticles were deposited from the ACIS cluster source. Figure 2a and Figure 2b show X-ray absorption spectra in the vicinity of the L_2 and L_3 edges of both, the Ni(111) substrate and Fe nanoparticles with D = (7.6 ± 1.5) nm, respectively. The data were recorded with circularly polarized synchrotron radiation provided by the helical undulator beamline UE46-PGM1 at the electron storage ring BESSY (Berlin).

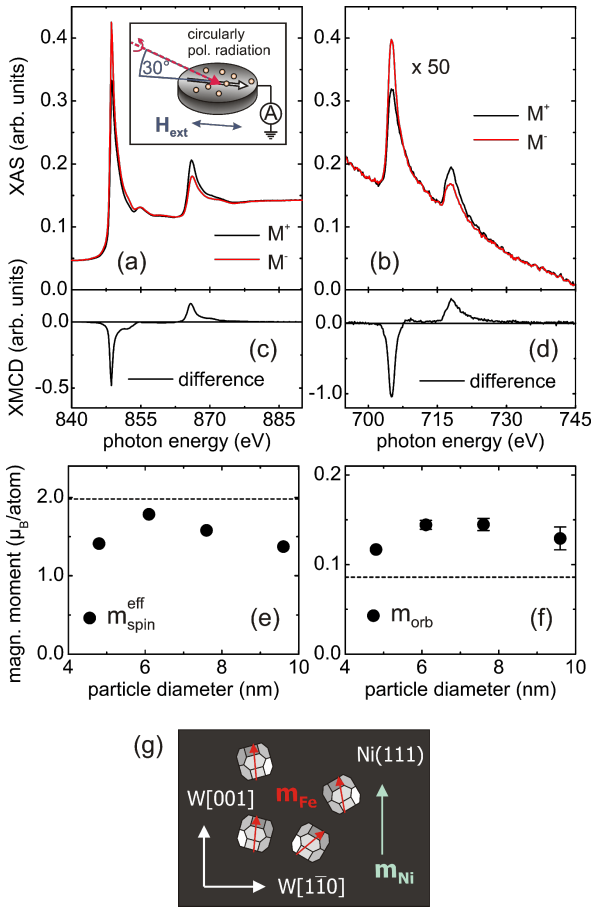


Figure 2: (a) X-ray absorption spectra of the Ni(111) substrate. Inset: Schematics of the experiment. (b) XAS spectra of the Fe NPs with a diameter of (7.6 ± 1.5) nm. (c),(d): Ni- and Fe-related XMCD spectra. Lower part: Size-dependent magnetic spin moments (e) and magnetic orbital moments (f) of the Fe NPs. (g) Sketch of the magnetization directions (m_{Ni}, m_{Fe}) of the sample as discussed further below.

The experimental setup is shown in the inset of Figure 2a, the X-rays impinge at an angle of 30° at the sample. The substrate is oriented with its easy magnetic axis, i.e., the W[001]-direction, parallel to the plane of incidence. The data were obtained by recording the total electron yield at each photon energy and by switching the Ni film magnetization with a short external magnetic field pulse at each data point (a current of ≈100 A through two coils, 180 windings, magnetic field ≈1700 G). The photon helicity was kept fixed. Note that the nanoparticle data in Figure 2b are scaled by a factor of 50. The low magnitude of the Fe signal relative to that of the Ni spectra reflects a well diluted deposit with about 200 particles per μm^2 on the surface [38]. At this density, interactions between the particles can be neglected.

Figure 2c and Figure 2d show magnetic dichroism spectra (given by the difference of the XA spectra with opposite magnetization directions, M^+ and M^-, respectively) for both components, the Ni films as well as the Fe NPs. The identical sign in both XMCD spectra reveals a ferromagnetic (parallel) coupling of the particles to the substrate magnetization. This behavior is expected due to the strong exchange coupling of the interface. Applying the XMCD sum rules as shown in [49,50] reveals the magnetic moments of the substrate and the nanoparticles, respectively. For the Ni films bulk-like moments are found, thus indicating fully saturated magnetization [51]. In the case of the Fe particles self-saturation effects – which lead to a significant underestimation of the magnetic spin and more importantly of the magnetic orbital moments – have to be corrected. These effects are well-known for thin films [52] and their description has recently been extended to supported nanoparticles [53]. After further corrections regarding the incomplete degree of circular polarization, the angle of 30° between the photon propagation vector and the sample magnetization, the effective magnetic spin and orbital moments were obtained as displayed in Figure 2e and Figure 2f (details of the data analysis are described in [38]). The spin moments in Figure 2e vary slightly with the particle size but are always well below the corresponding Fe bulk value of m_{spin}^{eff} = 1.98 μ_B [49] (dashed line). In contrast, the magnetic orbital moments presented in Figure 2f are, in all cases, well above the corresponding bulk value of m_{orb} = 0.085 μ_B [49] (dashed line).

The magnitude of the orbital moments is similar to our previous findings on Fe nanoparticles in contact with Co(0001)/W(110) [38]. A detailed analysis showed that the observed moments are not explained by the well-known enhancement of the orbital magnetic moments at bulk surfaces or, respectively, nanoparticle surfaces (e.g., [10] and references therein). Instead, the data suggest that the orbital moments are also altered in the particle volume. From the literature it is known that the magnetic moments in iron are highly sensitive to the actual lattice symmetry [54,55]. In [38], we therefore assumed that surface and interface related strain in the nanoparticles as, e.g., observed in [56] could be the origin of such enhanced orbital moments. Similarly, the reduced magnetic spin moments in Figure 2e could be due to, e.g., tetragonal lattice distortions. Thus, to shed more light on these findings, it is essential to directly study the structure of the particles upon deposition onto a single crystalline substrate.

To assess the crystallographic structure and orientation of supported particles in situ, RHEED [57] was used. A schematics of the experimental setup is shown in Figure 3a, details can be found in [58]. The experiments were performed on Fe nanoparticles upon deposition onto the bare W(110) surface. The data in Figure 3a, Figure 3b and Figure 3c are part of a recent study published in [59]. The system Fe/W(110) is

particularly interesting for studying substrate-induced strain effects in deposited nanoparticles due to the large lattice misfit of 9.5% and the well-known strain relaxation in thin Fe films grown on W(110). The latter gives rise to a complex interplay between structure and magnetic properties [60,61]. The grazing incidence and the high cross section of electrons with matter make RHEED ideally suited for nanoparticle experiments, even for highly diluted samples. Moreover, this method probes both, the Fe nanoparticles and the W(110) substrate, simultaneously. Thus, one can study the relative orientation of the particles with respect to the lattice of the substrates. In addition, the substrate serves as a well-defined reference for studying quantitatively possible strains in the particles.

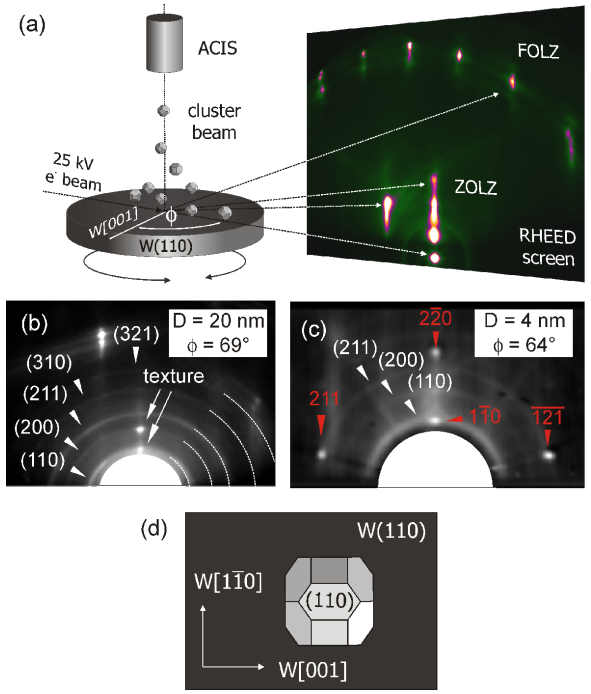


Figure 3: (a) Schematics of the in situ RHEED setup [58] (b) and (c): RHEED diffraction patterns from (b) larger (20 nm) and small (c) particles (4 nm). (d) Schematic drawing of uniformly oriented Fe particles on W(110).

To illustrate the method Figure 3a shows a large diffraction pattern of the bare W(110) substrate. The characteristic streaks aligned on two half circles around the central beam correspond to the zeroth and first order Laue zone (ZOLZ and FOLZ). Here, these W(110) streaks serve as a reference for the orientation of the sample and for the analysis of the diffraction pattern of the Fe nanoparticles. Deposition of mass-filtered Fe particles with a size of D = 20 nm results in the appearance of diffraction rings as shown in Figure 3b. This pattern – being similar to common powder diffraction data – is independent of the azimuthal sample orientation Φ and thus indicates a random orientation of the nanoparticles on the substrate. It is found for particles with sizes ranging from 25 nm down to about 4 nm. Comparing the Fe induced rings with the well-defined positions of the W(110) streaks reveals a bulk-like Fe lattice constant in the nanoparticles. Thus, despite of the large lattice mismatch with the substrate, the particles possess a bulk-like Fe lattice. A texture in the (200) and (110) rings (marked by arrows in Figure 3b) also shows that the particles preferentially rest on their (001) and (110) surface facets, however, without any preferential azimuthal orientation.

These data allow a major conclusion for the interpretation of the magnetic moments presented in Figure 2e and Figure 2f: Strain in the particles can largely be excluded as a possible origin of altered magnetic spin and orbital moments. More precisely, we may note that our size-dependent RHEED data indicate that strain might still be present in the first few layers from the interface [59], analogously to the findings in closed Fe films on W(110), where strain relaxation takes place within the first four layers [62]. However, a 6 nm particle (as shown in Figure 1e) consists of about several tens of atomic (001) or (110) layers, respectively. Thus, the major particle volume can be considered as relaxed; strain does not contribute to the altered magnetic spin and orbital moments. Before we discuss other alternative explanations for the observed magnetic moments, we may focus on another related interesting and important phenomenon that may occur when depositing nanoparticles onto single crystalline substrates.

At a particle size of 4 nm, additional angular dependent spot patterns (indicated by arrows) occur in RHEED as shown in Figure 3c [59]. Analyzing this pattern reveals the onset of a spontaneous epitaxial alignment. In particular, we observe a parallel alignment of the (110) planes and the [001] directions of Fe and W, which is well-known from Fe films grown thermally on W(110). The remaining ring pattern in Figure 3c shows that there are still some randomly oriented particles. However, below 4 nm full alignment of the Fe particles is found. Together with the above discussed Wulff shape of the particles, these findings suggest that an ensemble of particles with uniform shape and orientation on the substrate has formed (as shown in Figure 3d). However, landing and relaxation kinetics during (and after) the impact of the particles on the surface may potentially lead to significant deviations from this simple picture and thus require additional attention.

To shed more light on the deposition kinetics we have performed first STM investigations on the morphology of Fe NPs on W(110). The overview image in Figure 4a shows randomly distributed nanoparticles with a diameter of about 7 nm as deposited from the ACIS source. Analogously to earlier

findings, the height measured in STM corresponds well to the respective diameter measured by TEM. The apparent lateral particle dimensions of about 50 nm in Figure 4a are due to tip convolution effects in the STM which become important when the particle size is comparable or larger than the tip diameter [63]. The tip convolution in general also superimposes details of the particle shape as, e.g., surface facets. Numerical deconvolution of the STM images has been shown to provide a tool to reconstruct features of the nanoparticle morphology [64]. Figure 4b and Figure 4c show such reconstructed images of two particles. The images indeed show indications for particle shapes according to the Wulff construction (see the schematics in the figures). Moreover, the particles in Figure 4b and Figure 4c may rest on their (001) and (110) facets with arbitrary azimuthal orientations as expected from the RHEED data for particles of this size.

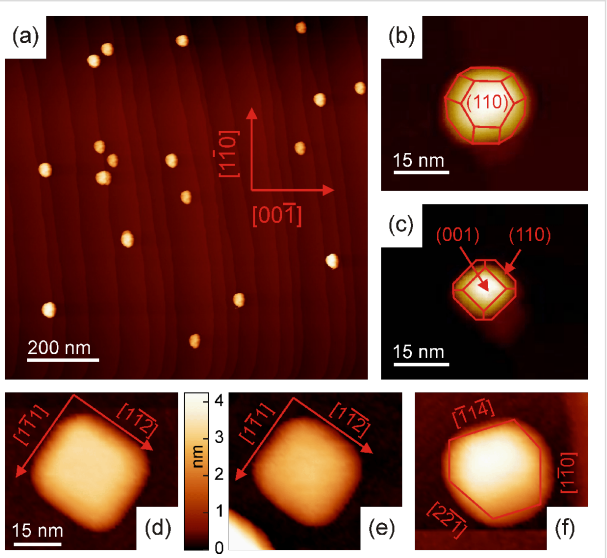


Figure 4: (a) STM image of mass-filtered Fe nanoparticles (mean diameter of 7 nm) deposited onto W(110). Tunneling parameters: U = 1.0 V, I = 0.5 nA. (b) and (c): Tip deconvolution of the STM images reveals surface facets consistent with the random orientation as found by means of RHEED. (d)–(f): At smaller sizes (D < 4 nm) some particles show edges along different crystallographic directions of the substrate. These directions do not correspond to the simple model discussed earlier (Figure 3d).

When depositing smaller particles with D = 4 nm, we observe structural features at about 20% of the particles even without the need for numerical deconvolution as shown in Figure 4d, Figure 4e and Figure 4f. The remaining particles appear rounder or show stronger irregular tip features. The particles in Figure 4d, Figure 4e and Figure 4f show edges along certain crystallographic directions of the W(110) substrate as denoted in the figures. Thus, we attribute these more regularly shaped particles to the onset of spontaneous alignment being observed by RHEED. However, the facets seen in Figure 4d, Figure 4e and Figure 4f do not correspond to the simple model derived from the RHEED data (Figure 3d). In fact the Wullf shape model with only (001) and (110) surface facets suggests sharp edges along the {111}, {001}, and {110} directions of the substrate. Thus, the data in Figure 4d, Figure 4e and Figure 4f hint at the presence of higher index surface facets which are energetically less favorable. We therefore assume that the observed shape reflects a state far from thermal equilibrium forming due to the complex landing kinetics of the smaller particles which are connected with the spontaneous reorientation process.

Recent molecular-dynamics (MD) simulations give microscopic insight into the processes in nanoparticle deposition experiments [65]. In particular, it turns out that upon impact the particles are temporarily disordered. The subsequent recrystallization happens on a ps time scale and may result in partial or full epitaxy of the particles. Thereby, the alignment with the substrate is achieved by a thermally activated ejection of dislocations which form upon deposition. The final state of the supported particles depends on their size and the available kinetic and interface energy. Once the energy is dissipated the particles remain trapped in their respective state until further relaxation processes are activated at the present sample temperature. Our room temperature experiments show stable particle properties over periods of several hours. Thus, we conclude that the kinetic barriers for further relaxation are relatively high, and dislocations are effectively trapped in those particles which are not aligned with the substrate. Note that dislocations locally reduce the symmetry in the crystal lattice and, thus, the MD simulations together with the random orientation found for larger particles (D > 4 nm) may provide an alternative explanation for the strongly enlarged orbital moments presented in Figure 2f. Namely, trapped dislocations might induce enhanced magnetic orbital moments in deposited nanoparticles.

The reduced spin moments in Figure 2e might also be related to the random orientation of the particles. Most likely, the deposition process also leads to statistically distributed magnetic anisotropy axes. The competition between the anisotropy energy and the exchange interaction with the substrate can then lead to non-collinear spin structures in the particles [66]. As a result, the magnetic spin moments of the particles are no longer parallel to the magnetization of the substrate but are canted by a certain angle towards the direction of the individual anisotropy axis as sketched in Figure 2g. Thus, in the present XMCD experiments we would only probe the averaged projection of the magnetization in the particle ensemble which leads to an apparently reduced magnetic moment in the sum rule analysis. The fact that we observed bulk-like spin moments in similar Fe nanoparticles on hcp Co(0001)/W(110) [38] may reflect that the

exchange interaction clearly dominated over the magnetic anisotropy energies in the latter system while on fcc Ni(111)/W(110) the anisotropy energy strongly determines the magnetization direction of the particles [66]. Alternatively, a substrate-induced fcc/bcc competition in the nanoparticles could lead to reduced spin moments in Figure 2e as, e.g., observed for Fe nanostructures grown on fcc Cu(111) in [67].

Conclusion

We have presented a combined XMCD, RHEED, and STM study on the magnetic, structural and morphological properties of Fe nanoparticles deposited from the gas phase onto single crystalline substrates under soft landing conditions. In the XMCD experiments strongly enhanced magnetic orbital, but reduced magnetic spin moments (compared to respective bulk values) in Fe nanoparticles on fcc Ni(111)/W(110) were found. In situ RHEED revealed a random orientation and bulk-like lattice constants in the Fe nanoparticles, and thus excludes strain effects as the main origin of the altered magnetic moments. Instead, we propose the presence of deposition-induced dislocations in the Fe nanoparticles as the main contribution for the enhanced magnetic orbital moments. The reduced spin moments could be due to the competition between randomly oriented anisotropy axes and the exchange interaction with the substrate. Furthermore, we have shown that below a critical size – being 4 nm in the case of Fe on W(110) – the particles are able to spontaneously align on a single crystalline substrate. STM experiments, however, hint at a complex reshaping of the particles which may happen simultaneously.

The experimental results demonstrate the impact of the deposition kinetics on the physical properties of supported nanoparticles, even under soft landing conditions. Combining RHEED and STM with other methods provides a lot of information on the nanoparticles. The complex relation of structure, orientation and morphology also underlines the need for experiments with single particle sensitivity [68]. Such data are not only relevant for magnetism, but also for charge transport phenomena and catalytic activities of supported nanoparticles in heterogeneous catalysis. Our findings are also relevant for chemically produced particles which are subsequently dispersed on a surface. In such a case, the dispersion process will also result in a random orientation of the particles with the respective consequences for their properties. Rapid annealing by short laser pulses may provide a tool to obtain uniformly orientated particles in this situation, but the shapes can be affected in an undesired manner. Thus, to gain full control over shape and orientation – even in mono-dispersed nanoparticle deposits that are potentially of interest for applications as well as for fundamental research – remains challenging.

Acknowledgements

We acknowledge the Helmholtz-Zentrum Berlin - Electron storage ring BESSY II for provision of synchrotron radiation at beamline UE46 PGM and we would like to thank Dr. D. Schmitz and Dr. E. Holub-Krappe for their assistance. Furthermore we would like to thank Prof. Dr. K.-H. Meiwes-Broer (University of Rostock, Germany) for his continuous support before and after the experiments. Andris Voitkans is acknowleged for his contribution to the RHEED experiments. We gratefully acknowledge financial support by the Deutsche Forschungsgemeinschaft (DFG) via the priority program SPP 1153 (Clusters at Surfaces: Electron Structure and Magnetism) via the grants BA 1612/3-3, DFG KL 2188/1-3, and DFG GE 1026/4-3.

References

1. Bansmann, J.; Baker, S. H.; Binns, C.; Blackman, J. A.; Bucher, J.-P.; Dorantes-Dávila, J.; Dupuis, V.; Favre, L.; Kechrakos, D.; Kleibert, A.; Meiwes-Broer, K.-H.; Pastor, G. M.; Perez, A.; Toulemonde, O.; Trohidou, K. N.; Tuaillon, J.; Xie, Y. *Surf. Sci. Rep.* **2005,** *56,* 189. doi:10.1016/j.surfrep.2004.10.001
2. Huber, D. L. *Small* **2005,** *1,* 482. doi:10.1002/smll.200500006
3. Meiwes-Broer, K.-H. *Clusters on surfaces;* Springer-Verlag: Berlin, 2000.
4. Hütten, A.; Sudfeld, D.; Ennen, I.; Reiss, G.; Wojczykowski, K.; Jutzi, P. *J. Magn. Magn. Mater.* **2005,** *293,* 93. doi:10.1016/j.jmmm.2005.01.048
5. Billas, I. M. L.; Châtelain, A.; de Heer, W. A. *Science* **1994,** *265,* 1682. doi:10.1126/science.265.5179.1682
6. Cox, A. J.; Louderback, J. G.; Bloomfield, L. A. *Phys. Rev. Lett.* **1993,** *71,* 923. doi:10.1103/PhysRevLett.71.923
7. Bruno, P. *Phys. Rev. B* **1989,** *39,* 865. doi:10.1103/PhysRevB.39.865
8. Aharoni, A. *Introduction to the Theory of Ferromagnetism;* Oxford University Press: Oxford, 2000.
9. Tischer, M.; Hjortstam, O.; Arvanitis, D.; Dunn, J. H.; May, F.; Baberschke, K.; Trygg, J.; Wills, J. M.; Johansson, B.; Eriksson, O. *Phys. Rev. Lett.* **1995,** *75,* 1602. doi:10.1103/PhysRevLett.75.1602
10. Šipr, O.; Košuth, M.; Ebert, H. *Phys. Rev. B* **2004,** *70,* 174423. doi:10.1103/PhysRevB.70.174423
11. Edmonds, K. W.; Binns, C.; Baker, S. H.; Thornton, S. C.; Norris, C.; Goedkoop, J. B.; Finazzi, M.; Brookes, N. B. *Phys. Rev. B* **1999,** *60,* 472. doi:10.1103/PhysRevB.60.472
12. Lau, J. T.; Föhlisch, A.; Nietubyc, R.; Reif, M.; Wurth, W. *Phys. Rev. Lett.* **2002,** *89,* 057201. doi:10.1103/PhysRevLett.89.057201
13. Kortright, J. B.; Awschalon, D. D.; Stöhr, J.; Bader, S. D.; Idzerda, Y. U.; Parkin, S. S. P.; Schuller, I. K.; Siegmann, H.-C. *J. Magn. Magn. Mater.* **1999,** *207,* 7. doi:10.1016/S0304-8853(99)00485-0
14. Dürr, H. A.; Eimüller, T.; Elmers, H.-J.; Eisebitt, S.; Farle, M.; Kuch, W.; Matthes, F.; Martins, M.; Mertins, H.-C.; Oppeneer, P. M.; Plucinski, L.; Schneider, C. M.; Wende, H.; Wurth, W.; Zabel, H. *IEEE Trans. Magn.* **2009,** *45,* 15. doi:10.1109/TMAG.2008.2006667
15. Kodama, R. H. *J. Magn. Magn. Mater.* **1999,** *200,* 359. doi:10.1016/S0304-8853(99)00347-9
16. Boeglin, C.; Bulou, H.; Hommet, J.; Le Cann, X.; Magnan, H.; Le Fèvre, P.; Chandesris, D. *Phys. Rev. B* **1999,** *60,* 4220. doi:10.1103/PhysRevB.60.4220

17. Burkert, T.; Nordström, L.; Eriksson, O.; Heinonen, O. *Phys. Rev. Lett.* **2004,** *93,* 027203. doi:10.1103/PhysRevLett.93.027203
18. Andersson, G.; Burkert, T.; Warnicke, P.; Björck, M.; Sanyal, B.; Chacon, C.; Zlotea, C.; Nordström, L.; Nordblad, P.; Eriksson, O. *Phys. Rev. Lett.* **2006,** *96,* 037205. doi:10.1103/PhysRevLett.96.037205
19. Winkelmann, A.; Przybylski, M.; Luo, F.; Shi, Y.; Barthel, J. *Phys. Rev. Lett.* **2006,** *96,* 257205. doi:10.1103/PhysRevLett.96.257205
20. Bansmann, J.; Kleibert, A.; Getzlaff, M.; Fraile Rodríguez, A.; Nolting, F.; Boeglin, C.; Meiwes-Broer, K.-H. *Phys. Status Solidi B* **2010,** *247,* 1152. doi:10.1002/pssb.200945516
21. Sun, S.; Murray, C. B.; Weller, D.; Folks, L.; Moser, A. *Science* **2000,** *287,* 1989. doi:10.1126/science.287.5460.1989
22. Chaubey, G. S.; Barcena, C.; Poudyal, N.; Rong, C.; Gao, J.; Sun, S.; Liu, J. P. *J. Am. Chem. Soc.* **2007,** *129,* 7214. doi:10.1021/ja0708969
23. Ethirajan, A.; Wiedwald, U.; Boyen, H.-G.; Kern, B.; Han, L.; Klimmer, A.; Weigl, F.; Kästle, G.; Ziemann, P.; Fauth, K.; Cai, J.; Behm, R. J.; Oelhafen, P.; Walther, P.; Biskupek, J.; Kaiser, U. *Adv. Mater.* **2007,** *19,* 406. doi:10.1002/adma.200601759
24. Rohart, S.; Repain, V.; Tejeda, A.; Ohresser, P.; Scheurer, F.; Bencok, P.; Ferré, J.; Rousset, S. *Phys. Rev. B* **2006,** *73,* 165412. doi:10.1103/PhysRevB.73.165412
25. Siekmann, H. R.; Lüder, C.; Faehrmann, J.; Lutz, H. O.; Meiwes-Broer, K.-H. *Z. Phys. D: At., Mol. Clusters* **1991,** *20,* 417. doi:10.1007/BF01544026
26. Fennel, T.; Meiwes-Broer, K.-H.; Tiggesbäumker, J.; Reinhard, P.-G.; Dinh, P. M.; Suraud, E. *Rev. Mod. Phys.* **2010,** *82,* 1793. doi:10.1103/RevModPhys.82.1793
27. Methling, R.-P.; Senz, V.; Klinkenberg, E.-D.; Diederich, T.; Tiggesbäumker, J.; Holzhüter, G.; Bansmann, J.; Meiwes-Broer, K.-H. *Eur. Phys. J. D* **2001,** *16,* 173. doi:10.1007/s100530170085
28. Kleibert, A.; Passig, J.; Meiwes-Broer, K.-H.; Getzlaff, M.; Bansmann, J. *J. Appl. Phys.* **2007,** *101,* 114318. doi:10.1063/1.2745330
29. Fraile Rodríguez, A.; Kleibert, A.; Bansmann, J.; Nolting, F. *J. Phys. D: Appl. Phys.* **2010,** *43,* 474006. doi:10.1088/0022-3727/43/47/474006
30. Binns, C. *Surf. Sci. Rep.* **2001,** *44,* 1. doi:10.1016/S0167-5729(01)00015-2
31. Passig, J.; Meiwes-Broer, K.-H.; Tiggesbäumker, J. *Rev. Sci. Instrum.* **2006,** *77,* 093304. doi:10.1063/1.2349619
32. Wulff, G. *Z. Kristallogr.* **1901,** *34,* 449.
33. Vystavel, T.; Palasantzas, G.; Koch, S. A.; De Hosson, J. T. M. *Appl. Phys. Lett.* **2003,** *82,* 197. doi:10.1063/1.1536716
34. Jamet, M.; Wernsdorfer, W.; Thirion, C.; Dupuis, V.; Mélinon, P.; Pérez, A.; Mailly, D. *Phys. Rev. B* **2004,** *69,* 024401. doi:10.1103/PhysRevB.69.024401
35. Baker, S. H.; Roy, M.; Gurman, S. J.; Louch, S.; Bleloch, A.; Binns, C. *J. Phys.: Condens. Matter* **2004,** *16,* 7813. doi:10.1088/0953-8984/16/43/020
36. Baletto, F.; Ferrando, R. *Rev. Mod. Phys.* **2005,** *77,* 371. doi:10.1103/RevModPhys.77.371
37. Lümmen, N.; Kraska, T. *Nanotechnology* **2004,** *15,* 525. doi:10.1088/0957-4484/15/5/021
38. Kleibert, A.; Meiwes-Broer, K.-H.; Bansmann, J. *Phys. Rev. B* **2009,** *79,* 125423. doi:10.1103/PhysRevB.79.125423
39. Haberland, H.; Insepov, Z.; Moseler, M. *Phys. Rev. B* **1995,** *51,* 11061. doi:10.1103/PhysRevB.51.11061
40. Kleibert, A.; Bulut, F.; Gebhardt, R. K.; Rosellen, W.; Sudfeld, D.; Passig, J.; Bansmann, J.; Meiwes-Broer, K.-H.; Getzlaff, M. *J. Phys.: Condens. Matter* **2008,** *20,* 445005. doi:10.1088/0953-8984/20/44/445005
41. Rosellen, W.; Kleinhans, C.; Hückelkamp, V.; Bulut, F.; Kleibert, A.; Bansmann, J.; Getzlaff, M. *Phys. Status Solidi B* **2010,** *247,* 1032. doi:10.1002/pssb.200945569
42. Luis, F.; Bartolomé, F.; Petroff, F.; Bartolomé, J.; García, L. M.; Deranlot, C.; Jaffrès, H.; Martínez, M. J.; Bencok, P.; Wilhelm, F.; Rogalev, A.; Brookes, N. B. *Europhys. Lett.* **2006,** *76,* 142. doi:10.1209/epl/i2006-10242-2
43. Pierce, J. P.; Torija, M. A.; Gai, Z.; Shi, J.; Schulthess, T. C.; Farnan, G. A.; Wendelken, J. F.; Plummer, E. W.; Shen, J. *Phys. Rev. Lett.* **2004,** *92,* 237201. doi:10.1103/PhysRevLett.92.237201
44. Fauth, K.; Ballentine, G. E.; Praetorius, C.; Kleibert, A.; Wilken, N.; Voitkans, A.; Meiwes-Broer, K.-H. *Phys. Status Solidi B* **2010,** *247,* 1170. doi:10.1002/pssb.200945607
45. Bode, M.; Pascal, R.; Wiesendanger, R. *Surf. Sci.* **1995,** *344,* 185. doi:10.1016/0039-6028(95)00873-X
46. Farle, M.; Berghaus, A.; Li, Y.; Baberschke, K. *Phys. Rev. B* **1990,** *42,* 4873. doi:10.1103/PhysRevB.42.4873
47. Sander, D.; Schmidthals, C.; Enders, A.; Kirschner, J. *Phys. Rev. B* **1998,** *57,* 1406. doi:10.1103/PhysRevB.57.1406
48. Schmidthals, C.; Sander, D.; Enders, A.; Kirschner, J. *Surf. Sci.* **1998,** *417,* 361. doi:10.1016/S0039-6028(98)00689-X
49. Chen, C. T.; Idzerda, Y. U.; Lin, H.-J.; Smith, N. V.; Meigs, G.; Chaban, E.; Ho, G. H.; Pellegrin, E.; Sette, F. *Phys. Rev. Lett.* **1995,** *75,* 152. doi:10.1103/PhysRevLett.75.152
50. Stöhr, J.; König, H. *Phys. Rev. Lett.* **1995,** *75,* 3748. doi:10.1103/PhysRevLett.75.3748
51. Bansmann, J.; Getzlaff, M.; Kleibert, A.; Bulut, F.; Gebhardt, R. K.; Meiwes-Broer, K.-H. *Appl. Phys. A: Mater. Sci. Process.* **2006,** *82,* 73. doi:10.1007/s00339-005-3342-x
52. Nakajima, R.; Stöhr, J.; Idzerda, Y. U. *Phys. Rev. B* **1999,** *59,* 6421. doi:10.1103/PhysRevB.59.6421
53. Fauth, K. *Appl. Phys. Lett.* **2004,** *85,* 3271. doi:10.1063/1.1804600
54. Moruzzi, V. L.; Marcus, P. M.; Schwarz, K.; Mohn, P. *Phys. Rev. B* **1986,** *34,* 1784. doi:10.1103/PhysRevB.34.1784
55. Marcus, P. M.; Moruzzi, V. L.; Qiu, S.-L. *Phys. Rev. B* **1999,** *60,* 369. doi:10.1103/PhysRevB.60.369
56. Pfeifer, M. A.; Williams, G. J.; Vartanyants, I. A.; Harder, R.; Robinson, I. K. *Nature (London)* **2006,** *442,* 63. doi:10.1038/nature04867
57. Braun, W. *Applied RHEED;* Springer: Berlin, 1999.
58. Kleibert, A.; Voitkans, A.; Meiwes-Broer, K.-H. *Phys. Status Solidi B* **2010,** *247,* 1048. doi:10.1002/pssb.200945496
59. Kleibert, A.; Voitkans, A.; Meiwes-Broer, K.-H. *Phys. Rev. B* **2010,** *81,* 073412. doi:10.1103/PhysRevB.81.073412
60. Fruchart, O.; Jubert, P. O.; Eleoui, M.; Cheynis, F.; Borca, B.; David, P.; Santonacci, V.; Liénard, A.; Hasegawa, M.; Meyer, C. *J. Phys.: Condens. Matter* **2007,** *19,* 053001. doi:10.1088/0953-8984/19/5/053001
61. Ślęzak, T.; Ślęzak, M.; Zajac, M.; Freindl, K.; Kozioł-Rachwał, A.; Matlak, K.; Spiridis, N.; Wilgocka-Ślęzak, D.; Partyka-Jankowska, E.; Rennhofer, M.; Chumakov, A. I.; Stankov, S.; Rüffer, R.; Korecki, J. *Phys. Rev. Lett.* **2010,** *105,* 027206. doi:10.1103/PhysRevLett.105.027206
62. Bethge, H.; Heuer, D.; Jensen, C.; Reshöft, K.; Köhler, U. *Surf. Sci.* **1995,** *331-333,* 878. doi:10.1016/0039-6028(95)00166-2

63. Hövel, H.; Barke, I. *Prog. Surf. Sci.* **2006,** *81,* 53. doi:10.1016/j.progsurf.2006.01.002
64. Sell, K.; Kleibert, A.; von Oeynhausen, V.; Meiwes-Broer, K.-H. *Eur. Phys. J. D* **2007,** *45,* 433. doi:10.1140/epjd/e2007-00213-7
65. Järvi, T. T.; Kuronen, A.; Meinander, K.; Nordlund, K.; Albe, K. *Phys. Rev. B* **2007,** *75,* 115422. doi:10.1103/PhysRevB.75.115422
66. Fraile Rodríguez, A.; Kleibert, A.; Bansmann, J.; Voitkans, A.; Heyderman, L.; Nolting, F. *Phys. Rev. Lett.* **2010,** *104,* 127201. doi:10.1103/PhysRevLett.104.127201
67. Ohresser, P.; Ghiringhelli, G.; Tjernberg, O.; Brookes, N. B.; Finazzi, M. *Phys. Rev. B* **2000,** *62,* 5803. doi:10.1103/PhysRevB.62.5803
68. Fraile Rodríguez, A.; Nolting, F.; Bansmann, J.; Kleibert, A.; Heyderman, L. J. *J. Magn. Magn. Mater.* **2007,** *316,* 426. doi:10.1016/j.jmmm.2007.03.093

License and Terms

This is an Open Access article under the terms of the Creative Commons Attribution License (http://creativecommons.org/licenses/by/2.0), which permits unrestricted use, distribution, and reproduction in any medium, provided the original work is properly cited.

The license is subject to the *Beilstein Journal of Nanotechnology* terms and conditions: (http://www.beilstein-journals.org/bjnano)

The definitive version of this article is the electronic one which can be found at: doi:10.3762/bjnano.2.6

Beilstein Journal of Nanotechnology

Structural and magnetic properties of ternary $Fe_{1-x}Mn_xPt$ nanoalloys from first principles

Markus E. Gruner* and Peter Entel

Full Research Paper

Open Access

Address:
Faculty of Physics and Center for Nanointegration, CeNIDE, University of Duisburg-Essen, D-47048 Duisburg, Germany

Email:
Markus E. Gruner* - Markus.Gruner@uni-due.de

* Corresponding author

Keywords:
density functional theory; Fe–Pt; magnetic data recording; magnetostructural transition; Mn–Pt

Beilstein J. Nanotechnol. **2011,** *2,* 162–172.
doi:10.3762/bjnano.2.20

Received: 11 November 2010
Accepted: 09 February 2011
Published: 16 March 2011

Guest Editors: U. Wiedwald and P. Ziemann

© 2011 Gruner and Entel; licensee Beilstein-Institut.
License and terms: see end of document.

Abstract

Background: Structural and magnetic properties of binary Mn–Pt and ternary $Fe_{1-x}Mn_xPt$ nanoparticles in the size range of up to 2.5 nm (561 atoms) have been explored systematically by means of large scale first principles calculations in the framework of density functional theory. For each composition several magnetic and structural configurations have been compared.

Results: The concentration dependence of magnetization and structural properties of the ternary systems are in good agreement with previous bulk and thin film measurements. At an intermediate Mn-content around $x = 0.25$ a crossover between several phases with magnetic and structural properties is encountered, which may be interesting for exploitation in functional devices.

Conclusion: Addition of Mn effectively increases the stability of single crystalline $L1_0$ particles over multiply twinned morphologies. This, however, compromises the stability of the ferromagnetic phase due to an increased number of antiferromagnetic interactions. The consequence is that only small additions of Mn can be tolerated for data recording applications.

Introduction

Magnetic transition metal alloy nanoparticles provide a large variety of possibilities in several technological fields, such as biomedical diagnostics or therapy, catalysis or even mechanical actuation [1-9] and have become the focus of much research. Another application, widely discussed in recent years, is in the field of ultra-high density magnetic recording. Here, an exponential increase in storage density has been encountered over a long period of time keeping apace with the analogous development in semiconductor technology known as Moore's law. A further continuation of this trend by increasing miniaturization, however, is threatened by hard to surmount physical limitations. Probably the most severe is the so-called superparamagnetic

limit. This derives from the fact that the Néel relaxation law, which relates the relaxation time τ of the magnetization to the exponential of the product of anisotropy constant K_u times the grain volume V divided by temperature:

$$\tau = \tau_0 \exp\left(\frac{K_u V}{k_B T}\right) . \quad (1)$$

This imposes a lower boundary on the possible size of a grain made of a specific material, as this is supposed to keep its magnetization direction at ambient conditions unaffected by thermal relaxation for a sufficient amount of time, which is essentially given by τ.

Therefore, it is deemed necessary to switch to new types of recording media in future. Two concepts have been extensively discussed in this context: The first is to abandon contemporary polycrystalline media consisting of several tens or hundreds of loosely coupled grains per bit, each of them being subject to Néels relaxation law (Equation 1) and switch to a patterned medium where one bit is essentially represented by one single crystalline dot or nanoparticle [10-12]. Another promising strategy to obtain a substantial increase in integration density is to improve the materials constant K_u, which together with the particle volume is part of the exponential and thus allows a very effective way of decreasing V [13,14]. The most promising materials in this respect are probably $L1_0$ ordered FePt and CoPt [7,13,15-18]. For these materials, hypothetical lower limits for the particle diameters can be derived from Equation (1) being as small as 3 nm if the bulk values of the anisotropy constant are assumed. Both materials owe their large magnetocrystalline anisotropy to the strong hybridization of the electronic states of the 3d and 5d elements [19]. In addition, the $L1_0$ order, which is defined by a layer-wise alternating stacking of the elements along the [001] direction, reduces the cubic symmetry to tetragonal and thus allows for large uniaxial contributions: The lattice sites are characterized by a tetragonally distorted face centered cubic coordination with a slightly shortened c axis. However, the corresponding phase with cubic symmetry is described by the CsCl structure (B2), possessing a bcc-type rather than a fcc-type coordination. Thus the effective tetragonal distortion can be deemed to be quite large.

In reality, the ad hoc extrapolation from Equation (1) transpires to be of limited applicability as it has been discovered that $L1_0$ particles with a sufficient magnetocrystalline anisotropy are difficult to obtain in the corresponding size range [16,20-23]. It is certainly a straight-forward idea to seek the problem in the lower dimensionality of the particles. These naturally contain a significant percentage of surface atoms with diameters of a few nanometers. Several authors have therefore argued that at small particle sizes ordering is suppressed due to surface-induced disorder and segregation [21,24]. Both effects can be related to a change in the effective pair interactions between the different elements due to the decreased number of surface bonds which reduces the driving force of order or may induce other atomic arrangements which are not possible in the bulk. Consequently, it is natural to question, whether a completely ordered $L1_0$ arrangement will be the stable ground state structure in the desired size regime [25-27]. Corroborating evidence comes from high resolution transmission electron microscopy (HRTEM) which shows that multiply twinned morphologies such as icosahedra and decahedra occur already at particle sizes around 6 nm in gas phase experiments [28,29]. These morphologies consist of several strained twins – twenty in the case of Mackay icosahedra and five in the case of decahedra. Although the twins may be perfectly $L1_0$ ordered, they will not exhibit a significant uniaxial magnetocrystalline anisotropy because of the different crystallographic orientations of the individual twins in the particle.

The evolution of multiply twinned morphologies has been traced back to a competition between surface and volume energy contributions, which vary with particle size. This can be understood by means of a phenomenological third order polynomial law which expresses the binding energy as a function of the lateral system dimension, i. e., the third root of the system size N (for a discussion, see, e. g., [30]):

$$E(N) = aN + bN^{2/3} + cN^{1/3} + d . \quad (2)$$

The coefficients a, b, c, and d describe the contributions to the binding energy arising from the particle volume, the facets, the edges and the vertices, respectively. They account for the shape of the particle, internal strains and interfaces and, of course, the materials bulk properties themselves. With decreasing system size, the coefficients b, c and d become one after the other important and it is straightforward to conceive that a morphology which can come up with a larger fraction of higher coordinated surfaces (and thus lower surface energy) due to twinning may become competitive with single-crystalline structures, which lack (energetically unfavorable) internal interfaces and strain in the volume part. This has been studied in depth for empirical models [30-34]. However, due to the complexity of the electronic interactions especially in magnetic materials, only parameter free first principles methods within the framework of density functional theory [35], which take into account materials properties on the electronic level, can be expected to

provide useful theoretical predictions for a novel material combination with systematically improved properties. For real materials, such as the ones under consideration, the critical magnitude of the surface to volume ratio leading to crossover effects between different geometries can be expected to be in the range from a few hundred to several thousands of atoms. One suitable way to control the shape at a given size is by designing the ratio of the surface energy of different faces. Experimentally this may be achieved by tailoring the preparation conditions, e.g, by choosing suitable ligands in wet-chemical approaches [36,37]. Other authors suggest tackling the kinetics of the ordering processes and structure formation, e.g., by irradiation [38-41]. Both approaches are difficult to model on the basis of first principles calculations. Alternatively, one can try to increase the energy related to internal lattice defects, such as twin boundaries, by deliberate design of the alloy composition. This could effectively disfavor multiply twinned morphologies, while the resulting trends can be monitored on the electronic level in the framework of large scale density functional theory calculations. At this point, it should be kept in mind that segregated and multiply twinned morphologies may open up other fields of application. Core–shell structures are specially of interest, since enriching the catalytically active material (e. g., Pt or Pd) at the surface may reduce cost while the magnetic core provides another possibility for further manipulation [42]. In addition, the formation of an Pt-enriched shell may protect the Fe from oxidation [43].

A first step in the prediction of new materials for a specific purpose is to establish systematic trends between different alloys, which allow the energetic preference of a given morphology by a given material to be understood. By selecting components from suitable binary systems, systematic variation of the composition under addition of a ternary component can be attempted. The theoretical determination of ternary phase diagrams is an extremely demanding task for bulk systems and it becomes even harder if the size dependence must be accounted for as an additional variable. An important first step in this direction is thus to characterize changes in the energetic order of paradigmatic morphologies in binary alloys, which take place if one of the components is completely replaced by another element. A survey of such an effort covering 3d–5d alloys with elements in the vicinity of Fe–Pt in the periodic table has recently been undertaken by one of the authors [44]. The purpose of the current work is the extension to a ternary alloy in one specific case by means of large scale ab initio total energy calculations in the framework of density functional theory. For representative system sizes in the range of a few nanometers, where the surface-to-volume ratio is balanced and competitive effects should be expected such calculations are nowadays feasible on state-of-the-art supercomputer hardware such as the IBM Blue Gene/P at Forschungszentrum Jülich. The calculations presented here mainly concentrate on one size, 561 atoms, which corresponds to a diameter of about 2.5 nm. Clusters of this size possess a fraction of 45% surface atoms characterized by a reduced coordination in the first neighbor shell and are thus predetermined to monitor the competition between surface and bulk contributions with changing valence electron number.

Computational

The calculations were carried out using the Vienna Ab-initio Simulation Package (VASP) [45], which expands the wavefunctions of the valence electrons into a plane wave basis set. The interaction with the nuclei and the core electrons is described within the projector augmented wave (PAW) approach [46] which yields an excellent compromise between speed and accuracy. For the accurate description of structural properties of ferrous alloys, the use of the generalized gradient approximation (GGA) for the representation of the exchange–correlation functional is mandatory. In the present work, the formulation of Perdew and Wang [47,48] in connection with the spin interpolation formula of Vosko, Wilk and Nusair [49] was used. Since the objects under consideration are zero-dimensional and thus non-periodic, the *k*-space sampling was restricted to the Γ-point in combination with Gaussian Fermi surface broadening. Its width was initially chosen as 50 meV and subsequently reduced to 10 meV. The description of the electronic properties with a plane wave basis requires a periodic setup. Thus all clusters were placed into a supercell, which requires a sufficient amount of vacuum separating the periodic images. The size of the cell was chosen such that a separation of of around 9 Å could be maintained. In order to restrict the numerical demands, a medium cutoff for the plane wave energy of E_{cut} = 270 V was used. For the same reason, only the electrons in the partially filled 3d and 4s shells were treated explicitly as valence electrons for the 3d elements, and the corresponding restriction was also made for the 4d and 5d elements. This has proven to be a reasonable compromise in a recent ab initio study of the lattice dynamics of ordered Fe rich alloys with Pt group elements [50]. For a few selected isomers, single-point calculations with an increased value E_{cut} = 335 eV were carried out for comparison. The energy differences between the isomers turned out to change by less than 0.1 meV/atom, which is far better than the overall accuracy in the order of several meV/atom that can usually be expected for calculations of this type.

A scalar relativistic formulation of the Hamiltonian was employed throughout. Thus within this work, only spin moments are reported omitting the orbital contributions, which might become sizeable in small particles and at the surfaces. The geometrical optimizations were carried out on the Born–Oppenheimer surface using the conjugate gradient

method. The structural relaxations were stopped when the energy difference between two consecutive relaxations was less than 0.1 meV, leading to a convergence of forces down to the order of 10 meV/Å. The symmetrization of wavefunctions and forces was consistently switched off in all calculations.

The systematic search for the most stable structures of a given cluster size and composition involves the systematic scan of the potential energy surface, which is practically unfeasible from first principles for the system sizes under consideration. Therefore, the comparison is restricted to a pragmatic choice of selected morphologies, the so-called magic-number clusters. These have proven to be a good starting point as they appear to be particularly stable for the late 3d elements [51], especially Ni and Co. Their size N is can be expressed by the number n of closed geometric shells:

$$N = 1/3\left(10n^3 + 15n^2 + 11n + 3\right) = 13, 55, 147, 309, 561, 923, 1415, \ldots \quad (3)$$

Magic-size clusters allow a comparison of several paradigmatic geometries to be made: Cuboctahedra with a face centered cubic (fcc) or tetragonal structure, Mackay icosahedra [52] and Ino decahedra [53]. In the present study, only icosahedra and cuboctahedra are considered. The latter only with perfect $L1_0$ order (but with different magnetic configurations), while for the icosahedra both ordered and disordered arrangements are taken into account. The composition of a perfectly ordered binary cluster motif generally varies with system size, atomic arrangement and termination of the surfaces. In our studies it was kept fixed to allow for the construction of single crystalline structures with a perfect $L1_0$ arrangement of 3d and 5d layers, and Pt covered [001] surfaces. In the present case, a cluster of $N = 561$ atoms contains 265 3d and 296 5d atoms. In order to describe ternary compositions, Fe atoms were replaced by Mn on randomly chosen 3d sites. This is a reasonable starting point for the investigation of ternary 3d–5d alloys, since both limiting binary cases exhibit $L1_0$ order and the ordering tendencies in terms of 3d and 5d elements can be considered to be much stronger due to the large difference in size and electronic properties than for the 3d elements Fe and Mn, which are neighbors in the periodic table. Again, the configurations were kept fixed for all calculations with the same morphology type and composition. This leaves aside possible effects due to segregation of one elemental species to the surface or internal interfaces as twin boundaries.

Results and Discussion

The size dependent evolution of morphologies of near stoichiometric Fe–Pt, Co–Pt and also partially Mn–Pt particles has been subject of recent publications by the authors [26,27,54-56]. A brief summary of the main results will therefore be given below.

In the case of magic number Fe–Pt clusters with up to seven close geometric shells, the most favorable morphology found so far has been identified as an icosahedron with onion-ring-like alternating Fe and Pt shells and Pt covered (111) facets. The arrangement of the atomic species within the cluster can also be understood as an individual $L1_1$ ordering of the twins. The bulk $L1_1$ order is characterized by an alternation of close packed 3d and 5d layers along the space diagonal (in contrast to the layering along the c axis in $L1_0$). This is found in bulk only for CuPt [57].

The onion-ring structure is, for diameters around 2.5 nm ($N = 561$), lower by 30 meV/atom than the $L1_0$ ordered single crystalline structure, which we would rather prefer for data storage applications due to its allegedly large magnetocrystalline anisotropy energy. The stability of the multiply twinned structures is even greater in CoPt, the second candidate discussed in the introduction. Here, segregated core–shell structures are the dominating lowest energy morphologies for $N = 561$ being up to 120 meV/atom lower than the $L1_0$ ordered isomers. Also the aforementioned onion-ring structure turns out to be much more favorable than in the Fe–Pt case. This trend can be understood by considering bulk and surface contribution to Equation 2. Ab initio calculations predict a nearly linear increase of the energy difference between $L1_0$ and $L1_1$ structure of equiatomic alloys between Pt and 3d transition metals with decreasing valence electron concentration e/a [58]. While the $L1_1$ phase is energetically lowest in CuPt, the $L1_0$ phase is clearly favored for CoPt and even more so for FePt and MnPt. On the other hand, recent surface energy calculations [55] have shown that $L1_1$ FePt and CoPt alloys possess extremely low surface energies for purely Pt covered (111) surfaces. The corresponding values are significantly lower than the contribution for all other low index surfaces that have been obtained for the $L1_0$ arrangement. Modeling the competition of the surface and bulk energy contributions by varying with cluster size, in keeping with Equation 2, yields appropriate trends in the crossover sizes [55] which are furthermore in good agreement with the ab initio cluster calculations. We thus conclude that for FePt and CoPt the energy gain from the surface contribution is large enough to stabilize the $L1_1$ order in the particle core at sufficiently small particle sizes and also compensates the energy which is required for the formation of twin boundaries. In larger particles, however, some kind of hybrid arrangement should be expected, which will allow for $L1_0$ order in the particle core and a change to an onion-ring arrangement in the surface layers. Onion-ring and hybrid morphologies have been considered for

other alloys [59-61] as well as for Fe–Pt in the context of surface induced disorder [24,62-64]. This has been verified very recently in a combined ab initio and Monte Carlo approach [65], while representations of hybrid arrangements have also been found to be competitive with the layer-wise and shell-wise ordered morphologies in a recent large scale first principles approach [56].

It is known from several first principles investigations [66-69] that FePt in its $L1_0$ phase is at the brink of magnetic instability and exhibits a latent tendency to form a layer-wise antiferromagnetic (AF) spin order. This is accompanied by a slight increase of the tetragonal distortion with respect to the fcc lattice constant. Such a phase has not been observed in experiment so far, but may become apparent if potentially antiferromagnetic components such as Mn are added. According to the suggestion of Brown and coworkers [67], the suppression of the magnetic instability in pure FePt can be ascribed to the incomplete order of the experimental samples which introduces Fe atoms into the Pt layers. This modifies the effective interlayer coupling and mediates an indirect ferromagnetic (FM) interaction between the adjacent 3d layers, which overrides the smaller direct antiferromagnetic coupling across the Pt layer. The validity of this model has been verified in large scale first principles calculation of a partially disordered $L1_0$ cluster [68]. Furthermore, it has been argued that spin–orbit interaction provides further stabilization of the FM phase [66,70].

The element resolved electronic structure provides another way to obtain a qualitative understanding of the chemical trends on the energetic order of morphologies [26,27,54]. A comparison of the densities of states of the Fe–Pt, Co–Pt and Mn–Pt $L1_0$ cuboctahedra and onion-ring icosahedra, which was carried out by the authors in [27], reveals that for both morphologies the change of the electron number induces a nearly perfectly rigid shift of the 3d minority spin states, while the 5d and the majority states remain nearly unaffected. This makes the distribution of the minority spin 3d states in the vicinity of the Fermi level a decisive factor for the evolution of the stability of the structures with composition. When replacing Fe by Co, the additional d electrons of Co necessarily fill up the minority channel, because the majority spin states are occupied. This shifts the contributions of Co to lower energies. The corresponding shift, however, is larger for the onion-ring icosahedron, since the density of the $L1_0$ minority 3d states encounter a steep increase above E_F (which is less pronounced for the multiply twinned structures) while the electron densities at the Fermi level E_F are nearly the same for the isomers. This results in a different contribution to the band energy with respect to the $L1_0$ reference. Following this simple picture, the opposite might be expected to happen in Mn–Pt, as 3d electrons here are removed. This seems indeed to be the case, if Fe is completely replaced by Mn. Figure 1 demonstrates that the alternating icosahedron is located approximately 65 meV/atom above the 561-atom $L1_0$ cuboctahedron (as compared to ≈ 30 meV/atom below for FePt). The ferromagnetic, ordered icosahedron, which is nearly degenerate for $Fe_{265}Pt_{296}$, has become unstable in the Mn–Pt system for sizes above 147 atoms. During the geometric optimization procedure it transforms downhill to a perfect $L1_0$ cuboctahedron. This proves that the Mackay path is a also realistic transformation path for binary magic-number transition metal systems but, in addition, assures that a simple energy minimization effectively helps to discriminate the most important classes of structures. It should be noted at this point that the simple rigid band picture does not hold quite as nicely here as for the replacement of Fe by Co. As shown in [27], for the onion-ring structure a completely ferromagnetic configuration could not be obtained leading to antiferromagnetic alignment of parts of the Mn spins with respective contributions in the majority spin channel above the Fermi level and in the minority channel below, which alter the overall shape of the total DOS.

This points out the major drawback in using Mn as stabilizing agent for $L1_0$ particles for magnetic recording purposes: Its preference for antiferromagnetic ordering, which is well known for the bulk system and also present in nanoparticles. The lowest energy isomer shown in Figure 1 is an $L1_0$ cuboctahedron with staggered antiferromagnetic arrangement of the spins within the Mn layers. Thus, the restriction to binary systems by systematic exchange of one element does not yield substantial improvements with respect to their applicability for data recording purposes. In fact, the only component identified so far in our studies that raises hope to suppress substantially multiply twinned structures by co-alloying is Mn. However, as Mn might elicit the latent antiferromagnetic tendencies which are present in pure Fe–Pt as discussed above, an unfavorable change of the magnetic structure with increasing Mn content might be the consequence. On the other hand, it has been shown from fully relativistic electronic structure calculations of the bulk alloy that in the ferromagnetic phase small admixture of Mn will increase the magnetocrystalline anisotropy energy [71], while Lai and Ho found for chemically prepared particles with diameters around 4 nm that adding Mn is beneficial for the coercivity, which the authors ascribe in the first instance to an improved $L1_0$ order of their particles [72].

It is therefore of increased interest to take a look at this system in more detail. In the present study this was realized by exchanging a given fraction of Fe sites randomly by Mn, leaving the Pt sites untouched: The configurations of the Fe–Pt system served as a pre-optimized template. Afterwards, the clusters underwent an optimization of the ionic positions as in

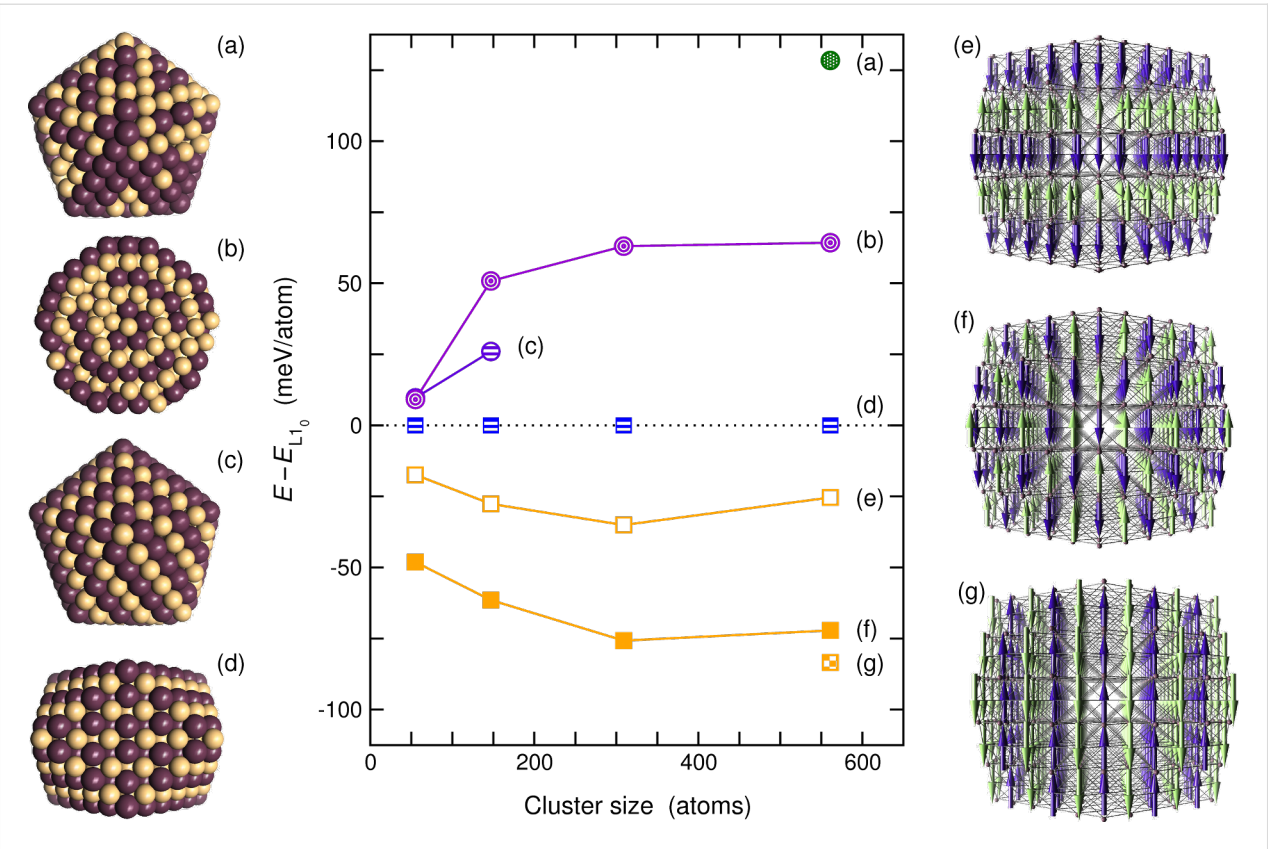


Figure 1: Energies of Mn–Pt clusters of various morphologies and sizes. The energy reference is marked by the $L1_0$ cuboctahedron. The letters in parentheses refer to the corresponding structures which are depicted at both sides of the diagram (only the structures with $N = 561$ atoms are shown). These are: (a) the disordered icosahedron, (b) the onion-ring icosahedron in cross section, (c) an ordered icosahedron, (d) the ferromagnetic $L1_0$ cuboctahedron, (e) an antiferromagnetic cuboctahedron with layered spin arrangement perpendicular to the *c* axis, (f) a staggered antiferromagnetic cuboctahedron and (g) an antiferromagnetic cuboctahedron with spin arrangement layered parallel to the *c* axis. Orange spheres (or, respectively, blue and green arrows) refer to Mn atoms, purple spheres to Pt. Colors and symbols: Shaded green circles denote disordered icosahedra (a). Triply nested circles refer to icosahedra with shell-wise ordering tendencies (b), hatched blue to violet symbols the ordered structures (c) and (d). Orange symbols denote $L1_0$ cuboctahedra with antiferromagnetic ordering of the 3d moments (e)–(g). The lines are only guides for the eye.

the other cases. Comparison is restricted here to $L1_0$ cuboctahedra and onion-ring icosahedra with 561 atoms (265 3d metal and 296 Pt atoms). For the ordered $L1_0$ clusters, different magnetic configurations were taken into account: The perfect ferromagnet, the staggered and layered antiferromagnet as well as a ferromagnetic configuration where the Mn spins are reversed with respect to the Fe spins. The icosahedra were always initialized with a ferromagnetic configuration, but again at the Mn-rich side several spins could not be prevented from flipping spontaneously.

The phase diagram of ternary $Fe_{1-x}Mn_xPt$ was examined experimentally in detail by Menshikov et al. [73] by means of X-ray and neutron diffraction measurements on a powder sample. The authors found that the alloy assumes a nearly, but not perfectly $L1_0$ ordered tetragonal structure for all compositions. The degree of tetragonality strongly increases at low Mn content up to an equiatomic mixture of both elements and reaches finally values of $c/a \approx 0.92$ for nearly pure MnPt. The authors describe the magnetic structure to evolve from a ferromagnet with an easy axis perpendicular to the Fe and Pt planes at $x = 0$ to a staggered antiferromagnetic structure with easy plane anisotropy in the range $0.25 \leq x \leq 0.5$. On the Mn rich side, the orientation of the moments switches back to perpendicular to the antiferromagnetically ordering 3d planes. In between, the authors report for the low temperature range ferro- and antiferromagnetic regions with canted moments. Later, Meyer and Thiele [74] investigated the same system as epitaxial films grown on MgO. Their XRD (X-ray diffraction) data essentially confirmed the structural properties reported in [73] despite possible mechanical strains due to the thin film setup. Using a vibrating sample magnetometer for saturation magnetization and hysteresis loop and X-ray magnetic circular dichroism (XMCD) to obtain the element resolved orientation of the moments, the authors observed a linear decrease of the average magnetization with increasing Mn-content, which finally vanishes completely around $x = 0.5$. From their XMCD data, the authors conclude that Mn and Fe predominately align in an

antiparallel fashion over the whole composition range and thus rule out a composition-dependent sign change in the Fe–Mn magnetic exchange constant which was postulated by Menshikov [73,75].

The left side of Figure 2 depicts the energetic order of the clusters as a function of the Mn concentration. Random replacement of up to 20% of the Fe sites by Mn decreases the stability of the multiply twinned structure significantly, such that a crossover with the ferromagnetic $L1_0$ cuboctahedron already occurs around 25 atom % Mn. On the other hand, the possibility of different antiferromagnetic structures at either end of the composition range as well as the possible presence of competing ferro- and antiferromagnetic exchange interactions must be taken into account in the ternary system. Therefore, also the layered and staggered antiferromagnetic configurations were included in the comparison. In addition, in the Fe-rich part, a ferrimagnetic setup was considered with Mn spins entirely aligned antiparallel to the ferromagnetically ordered Fe-spins. In fact, up to $x \lesssim 30$, this configuration represents the most favorable of the cuboctahedral isomers and has the lowest energy of all structures under consideration for $x \gtrsim 17$.

Because of the latent antiferromagnetic tendencies in FePt, a small fraction of Mn atoms will make the layer-wise antiferromagnetic cuboctahedron more favorable than the ferromagnetic reference, which consequently turns out very close in energy to the ferrimagnetic isomer. Since in the layered antiferromagnet, the Mn atoms were initially parallel to the Fe atoms, one might expect an analogous lowering of the energy, which could make this configuration the most favorable $L1_0$-type structure in this concentration range. However, as discussed above, for binary Fe–Pt such a configuration will effectively be suppressed by a small amount of disorder in the system, due to Fe or Mn occupying a Pt site and mediating an effective ferromagnetic interlayer coupling. On the other hand the staggered antiferromagnet, which is the most favorable isomer for compositions with more than 40% of Mn atoms, is not affected by this kind of disorder. The energetic order of the $L1_0$ coincides very well with the experimental saturation magnetization obtained by Meyer and Thiele [74], which is shown by the black stars in the right panel of Figure 2. It obeys essentially the same concentration dependence as the ferrimagnetic isomer for $x \lesssim 40$ and vanishes when the staggered antiferromagnet becomes the ground state. The layered spin configuration exhibits, in spite of its AF nature, a finite spin moment throughout. This results from the uneven number of 3d layers in the 561-atom cluster with five complete geometric shells. The consequence is that due to symmetry reasons the moments within the outermost 3d layers are aligned in the same direction and therefore do not compensate each other. The staggered AF on the other hand has a nearly vanishing total spin moment apart from a residual value

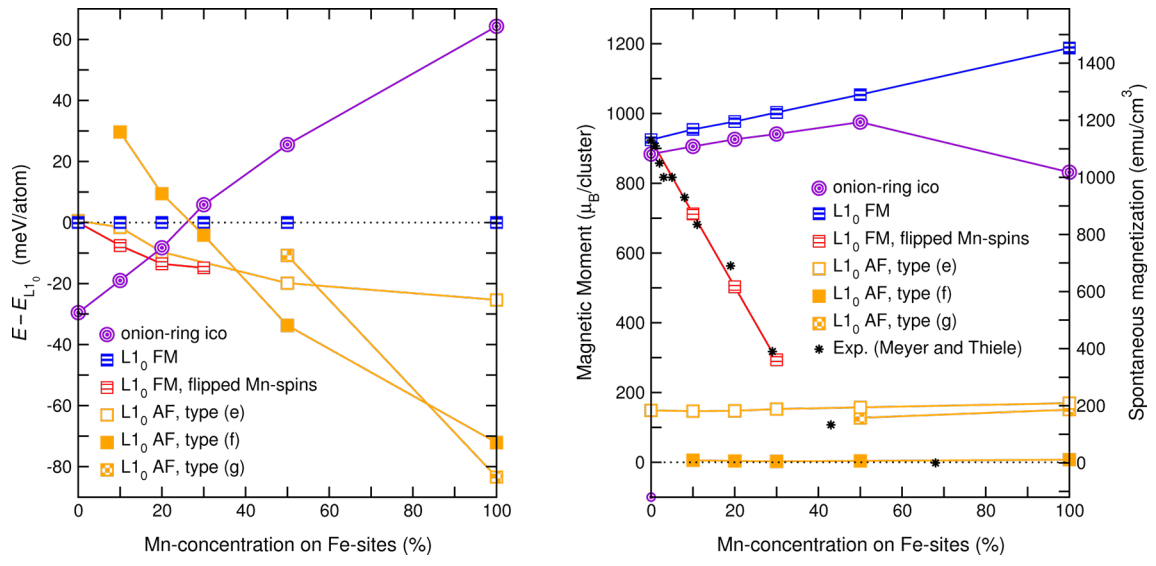


Figure 2: Energetic order (left panel) and magnetization (right panel, left scale) of ternary 561 atom Fe–Mn–Pt clusters with different morphologies and magnetic structures as a function of composition (Fe sites randomly replaced by Mn). Blue squares denote the ferromagnetic (FM) and perfectly ordered $L1_0$ isomer (d), which again is chosen as reference for each composition, violet nested circles the alternating icosahedron (b). Orange square refer to antiferromagnetic (AF) clusters: Filled symbols to a staggered antiferromagnetic configuration (f), open symbols to a layerwise alternating arrangement of ferromagnetic 3d layers parallel to the *c* axis (e), half-filled symbols to an antiferromagnetic arrangement layered perpendicular to *c* (g). Red symbols denote a ferromagnetic configuration (d), where Fe and Mn moments point in opposite directions. The black stars refer to the experimental saturation magnetization (right scale) obtained by Meyer and Thiele [74].

of a few Bohr magnetons, which results from a small number of uncompensated spins in the edge and corner parts. Indeed, low temperature ferromagnetism in combination with exchange bias effects originating from uncompensated surface spins has been observed experimentally in annealed binary MnPt nanoparticles with diameters between 2.3 nm and 4.1 nm [76]. The kink of the otherwise linear evolution of the spin magnetic moment of the icosahedral cluster at large Mn content is due to the barely stable FM configuration in Mn rich particles, which is reflected in spontaneous spin-flips decreasing the magnetization.

A very interesting aspect of this system is that there is a crossover between various magnetic and structural phases between 15 and 50% Mn on Fe sites. While the crossover point between icosahedra and cuboctahedra is determined by the competition between surface and volume contributions to the total energy and thus strongly size dependent, this is far less the case for the $L1_0$ isomers with different magnetic structures, as here the surfaces are of identical composition and thus play a much less dominant role.

In order to allow a direct comparison of structural cluster properties with bulk and thin film experiment, the distances between the layers and interlayer distances have been calculated from the averaged projections of the position vectors in the direction of the face normal. These yield the corresponding interlayer distances, which are finally averaged to obtain the effective lattice parameters a and c of the $L1_0$ type clusters. A comparison of the lattice constant a between calculation and the experimental values of Meyer and Thiele [74] and Menshikov et al. [73] is provided in Figure 3 (left panel). In contrast to the other magnetic isomers, which are characterized by a considerable change of a with x, the lattice constant of the staggered AF remains nearly constant over the whole concentration range. This trend agrees well with the experimental observation in the Mn rich part ($x \gtrsim 50$), while for $x \lesssim 30$ the measured values coincide nicely with the steeper slope of the ferro- and ferrimagnetic isomers, which indicates at least one change of the magnetic structure in between. A similar picture is obtained for the composition dependence of the tetragonality, as given by the ratio c/a (Figure 3, right panel). Here again, the c/a ratio of the staggered AF undergoes only a slight variation, while for the FM isomer a strong decrease is observed finally reaching a value as low as $c/a = 0.81$ for MnPt. At the Fe rich end this is also the case for the ferromagnetic configuration with inverted Mn spins, which, however, shows with increasing Mn content a less strong variation compared to the pure FM case.

Conclusion

The results demonstrate, that the addition of Mn to the Fe–Pt system by trend stabilizes antiferromagnetic order. Nevertheless, at small Mn concentrations, magnetically inhomogeneous states with antiparallel Mn moments are competitive which are

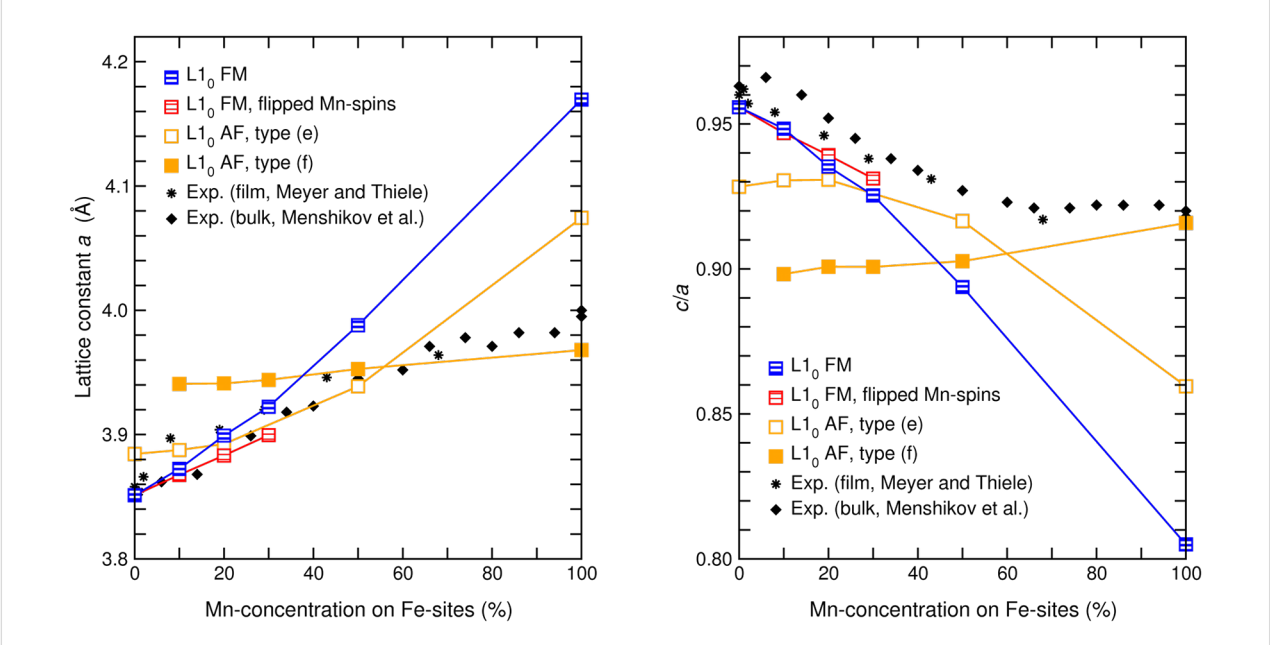


Figure 3: Lattice constant (left panel) and c/a ratio (right panel) of ternary 561-atom Fe–Mn–Pt clusters with different morphologies and magnetic structures as a function of the composition. Symbols as in Figure 2. The lattice parameters were obtained by averaging the interlayer distances in the respective directions. The values are compared with the experimental XRD data obtained at room temperature by Meyer and Thiele [74] for thin films (black stars) and Menshikov et al. [73] for bulk powder samples (black diamonds).

still ferromagnetic at large. Although the antiferromagnetic admixture to a ferromagnetic $L1_0$ configuration must be expected to decrease the performance of $Fe_{1-x}Mn_xPt$ nanoclusters in data recording applications, such a configuration might provide a suitable compromise as it improves the structural properties. To answer this question finally, further investigations are necessary taking into account the impact of increased magnetic disorder on finite temperature properties and spin–orbit interaction in the framework of fully relativistic first principles calculations. It might also be necessary to investigate how far increased segregation of one species to surface and interfaces could affect the energetic order of the paradigmatic morphologies.

Finding various phases with different structural and magnetic properties in a close interval of composition and energy gives rise to the hope that this material may allow the selection of specific magnetic or structural modifications with a fairly small energetic effort, which could be provided by an external magnetic field. In this respect, it looks promising that the latent tendencies of FePt for a layered AF structure is in fact stabilized by the addition of a few percent of Mn. FM and AF configurations show a considerable difference in their c/a ratio while the energy differences are small. However, one must keep in mind that an effective device would require extremely high degrees of order of the active material, which might be particularly difficult to realize on the nanoscale, as outlined in the introduction. However, interesting crossover effects can also be expected in the region $0.3 \leq x \leq 0.6$, where the experimental c/a and the lattice parameter a change their slope and different magnetic structures become competitive in energy. If composition and degree of order are carefully tuned, it might be possible to select the ferro or ferrimagnetic phase by an external magnetic field, while the ground state is still AF. In fact, Menshikov et al. [73] demonstrated in their experiments, that an external magnetic field can induce a magnetization at finite temperatures in the vicinity of the Néel temperature, which decays again towards high as well as towards low temperatures. The authors explain this fact with the presence of FM clusters with possible diameter of 5–10 nm in an otherwise AF matrix. From the present results a spin glass like ground state must also be considered. This question might be resolved in a later stage by additional simulations with statistical models making use of ab initio exchange parameters, which can be easily determined in bulk calculations. This, however, is beyond the scope of the present work. Nevertheless, the fact that a magnetic field can induce a magnetized state, which, however, does not necessarily relate to a higher degree of magnetic order, i. e., a lower magnetic entropy, raises the hope that a suitably designed material might exhibit a significant inverse magnetocaloric effect and thus be of potential interest for magnetic cooling purposes. In combination with the corresponding changes in lattice parameters and atomic volumes (the latter is substantially larger for the FM case), which can be inferred from Figure 3, the entropy change associated with the magnetic transition might become sizeable. As the changes in lattice parameter and c/a can be in the order of a few percent, it might also be worthwhile to explore in more detail, whether corresponding magnetic field induced structural changes can be used for magnetomechanical devices on the nanoscale, which could, e.g., consist of $Fe_{1-x}Mn_xPt$ nanoparticles embedded in an organic matrix.

Acknowledgements

The authors would like to thank Ulf Wiedwald, Paul Ziemann, Mehmet Acet and Michael Farle for stimulating discussions. Large parts of the calculations were carried out on the IBM Blue Gene/P supercomputer of the John von Neumann Institute for Computing at Forschungszentrum Jülich, Germany. The substantial support of the staff of Jülich Supercomputing Centre (JSC) and IBM is gratefully acknowledged. Financial support by the Deutsche Forschungsgemeinschaft through SPP 1239 and SFB 445 is also greatly acknowledged.

References

1. Toshima, N.; Yonezawa, T. *New J. Chem.* **1998,** *22,* 1179. doi:10.1039/a805753b
2. Šafařík, I.; Šafaříková, M. *Monatsh. Chem.* **2002,** *133,* 737. doi:10.1007/s007060200047
3. Pankhurst, Q. A.; Conolly, J.; Jones, S. K.; Dobson, J. *J. Phys. D: Appl. Phys.* **2003,** *36,* R167. doi:10.1088/0022-3727/36/13/201
4. Tartaj, P.; del Puerto Morales, M.; Veintemillas-Verdaguer, S.; Gonzáles-Carreño, T.; Serna, C. J. *J. Phys. D: Appl. Phys.* **2003,** *36,* R182. doi:10.1088/0022-3727/36/13/202
5. Ferrando, R.; Fortunelli, A.; Johnston, R. L. *Phys. Chem. Chem. Phys.* **2008,** *10,* 640. doi:10.1039/b709000e
6. Zayak, A. T.; Beckman, S. P.; Tiago, M. L.; Entel, P.; Chelikowsky, J. R. *J. Appl. Phys.* **2008,** *104,* 074307. doi:10.1063/1.2988189
7. Alloyeau, D.; Ricolleau, C.; Mottet, C.; Oikawa, T.; Langlois, C.; Bouar, Y. L.; Braidy, N.; Loiseau, A. *Nat. Mater.* **2009,** *8,* 940. doi:10.1038/nmat2574
8. Kita, E.; Oda, T.; Kayano, T.; Sato, S.; Minagawa, M.; Yanagihara, H.; Kishimoto, M.; Mitsumata, C.; Hashimoto, S.; Yamada, K.; Ohkohchi, N. *J. Phys. D: Appl. Phys.* **2010,** *43,* 474011. doi:10.1088/0022-3727/43/47/474011
9. Shao, H.; Yoon, T.-Y.; Liong, M.; Weissleder, R.; Lee, H. *Beilstein J. Nanotechnol.* **2010,** *1,* 142. doi:10.3762/bjnano.1.17
10. Sun, S.; Murray, C. B.; Weller, D.; Folks, L.; Moser, A. *Science* **2000,** *287,* 1989. doi:10.1126/science.287.5460.1989
11. Kodama, H.; Momose, S.; Ihara, N.; Uzumaki, T.; Tanaka, A. *Appl. Phys. Lett.* **2003,** *83,* 5253. doi:10.1063/1.1635980
12. Sun, S. *Adv. Mater.* **2006,** *18,* 393. doi:10.1002/adma.200501464
13. Weller, D.; Moser, A. *IEEE Trans. Magn.* **1999,** *35,* 4423. doi:10.1109/20.809134
14. Plumer, M. L.; van Ek, J.; Weller, D., Eds. *The Physics of Ultra-High-Density Magnetic Recording;* Springer: Berlin, 2001.

15. Yang, X.; Liu, C.; Ahner, J.; Yu, J.; Klemmer, T.; Johns, E.; Weller, D. *J. Vac. Sci. Technol., B: Microelectron. Nanometer Struct.–Process., M eas., Phenom.* **2004,** *22,* 31. doi:10.1116/1.1633283
16. Held, G. A.; Zeng, H.; Sun, S. *J. Appl. Phys.* **2004,** *95,* 1481. doi:10.1063/1.1635669
17. Perez, A.; Dupuis, V.; Tuaillon-Combes, J.; Bardotti, L.; Prével, B.; Bernstein, E.; Mélinon, P.; Favre, L.; Hannour, A.; Jamet, M. *Adv. Eng. Mater.* **2005,** *7,* 475. doi:10.1002/adem.200400220
18. Tournus, F.; Tamion, A.; Blanc, N.; Hannour, A.; Bardotti, L.; Prével, B.; Ohresser, P.; Bonet, E.; Epicier, T.; Dupuis, V. *Phys. Rev. B* **2008,** *77,* 144411. doi:10.1103/PhysRevB.77.144411
19. Solovyev, I. V.; Dederichs, P. H.; Mertig, I. *Phys. Rev. B* **1995,** *52,* 13419. doi:10.1103/PhysRevB.52.13419
20. Stahl, B.; Ellrich, J.; Theissmann, R.; Ghafari, M.; Bhattacharya, S.; Hahn, H.; Gajbhiye, N. S.; Kramer, D.; Viswanath, R. N.; Weissmüller, J.; Gleiter, H. *Phys. Rev. B* **2003,** *67,* 014422. doi:10.1103/PhysRevB.67.014422
21. Miyazaki, T.; Kitakami, O.; Okamoto, S.; Shimada, Y.; Akase, Z.; Murakami, Y.; Shindo, D.; Takahashi, Y. K.; Hono, K. *Phys. Rev. B* **2005,** *72,* 144419. doi:10.1103/PhysRevB.72.144419
22. Dmitrieva, O.; Rellinghaus, B.; Kästner, J.; Liedke, M. O.; Fassbender, J. *J. Appl. Phys.* **2005,** *97,* No. 10N112. doi:10.1063/1.1853211
23. Wiedwald, U.; Han, L.; Biskupek, J.; Kaiser, U.; Ziemann, P. *Beilstein J. Nanotechnol.* **2010,** *1,* 24. doi:10.3762/bjnano.1.5
24. Yang, B.; Asta, M.; Mryasov, O. N.; Klemmer, T. J.; Chantrell, R. W. *Scr. Mater.* **2005,** *53,* 417. doi:10.1016/j.scriptamat.2005.04.038
25. Müller, M.; Albe, K. *Acta Mater.* **2007,** *55,* 6617. doi:10.1016/j.actamat.2007.08.030
26. Gruner, M. E.; Rollmann, G.; Entel, P.; Farle, M. *Phys. Rev. Lett.* **2008,** *100,* 087203. doi:10.1103/PhysRevLett.100.087203
27. Gruner, M. E.; Entel, P. *J. Phys.: Condens. Matter* **2009,** *21,* 293201. doi:10.1088/0953-8984/21/29/293201
28. Dai, Z. R.; Sun, S.; Wang, Z. L. *Surf. Sci.* **2002,** *505,* 325. doi:10.1016/S0039-6028(02)01384-5
29. Wang, R.; Dmitrieva, O.; Farle, M.; Dumpich, G.; Ye, H. Q.; Poppa, H.; Kilaas, R.; Kisielowski, C. *Phys. Rev. Lett.* **2008,** *100,* 017205. doi:10.1103/PhysRevLett.100.017205
30. Baletto, F.; Ferrando, R. *Rev. Mod. Phys.* **2005,** *77,* 371. doi:10.1103/RevModPhys.77.371
31. van de Waal, B. W. *J. Chem. Phys.* **1989,** *90,* 3407. doi:10.1063/1.455848
32. Raoult, B.; Farges, J.; de Feraudy, M.-F.; Torchet, G. *Philos. Mag. B* **1989,** *60,* 881. doi:10.1080/13642818908209749
33. Doye, J. P. K.; Calvo, F. *Phys. Rev. Lett.* **2001,** *86,* 3570. doi:10.1103/PhysRevLett.86.3570
34. Cleveland, C. L.; Landmann, U. *J. Chem. Phys.* **1991,** *94,* 7376. doi:10.1063/1.460169
35. Hohenberg, P.; Kohn, W. *Phys. Rev.* **1964,** *136,* B864. doi:10.1103/PhysRev.136.B864
36. Ung, D.; Tung, L. D.; Caruntu, G.; Delaportas, D.; Alexandrou, I.; Prior, I. A.; Thanh, N. T. K. *CrystEngComm* **2009,** *11,* 1309. doi:10.1039/b823290n
37. Paz-Borbon, L.; Johnston, R.; Barcaro, G.; Fortunelli, A. *Eur. Phys. J. D* **2009,** *52,* 131. doi:10.1140/epjd/e2009-00041-9
38. Wiedwald, U.; Klimmer, A.; Kern, B.; Han, L.; Boyen, H.-G.; Ziemann, P.; Fauth, K. *Appl. Phys. Lett.* **2007,** *90,* 062508. doi:10.1063/1.2472177
39. Penuelas, J.; Andreazza, P.; Andreazza-Vignolle, C.; Tolentino, H. C.; De Santis, M.; Mottet, C. *Phys. Rev. Lett.* **2008,** *100,* 115502. doi:10.1103/PhysRevLett.100.115502
40. Järvi, T. T.; Pohl, D.; Albe, K.; Rellinghaus, B.; Schultz, L.; Fassbender, J.; Kuronen, A.; Nordlund, K. *EPL* **2009,** *85,* 26001. doi:10.1209/0295-5075/85/26001
41. Müller, M.; Albe, K. *Beilstein J. Nanotechnol.* **2011,** *2,* 40. doi:10.3762/bjnano.2.5
42. Wang, R.; Dmitrieva, O.; Farle, M.; Dumpich, G.; Acet, M.; Mejia-Rosales, S.; Perez-Tijerina, E.; Yacaman, M. J.; Kisielowski, C. *J. Phys. Chem. C* **2009,** *113,* 4395. doi:10.1021/jp811280k
43. Han, L.; Wiedwald, U.; Kuerbanjiang, B.; Ziemann, P. *Nanotechnology* **2009,** *20,* 285706. doi:10.1088/0957-4484/20/28/285706
44. Gruner, M. E. *J. Phys. D: Appl. Phys.* **2010,** *43,* 474008. doi:10.1088/0022-3727/43/47/474008
45. Kresse, G.; Furthmüller, J. *Phys. Rev. B* **1996,** *54,* 11169. doi:10.1103/PhysRevB.54.11169
46. Kresse, G.; Joubert, D. *Phys. Rev. B* **1999,** *59,* 1758. doi:10.1103/PhysRevB.59.1758
47. Perdew, J. P. In *Electronic Structure of Solids '91;* Ziesche, P.; Eschrig, H., Eds.; Akademie Verlag: Berlin, 1991.
48. Perdew, J. P.; Wang, Y. *Phys. Rev. B* **1992,** *45,* 13244. doi:10.1103/PhysRevB.45.13244
49. Vosko, S. H.; Wilk, L.; Nusair, M. *Can. J. Phys.* **1980,** *58,* 1200. doi:10.1139/p80-159
50. Gruner, M. E.; Adeagbo, W. A.; Zayak, A. T.; Hucht, A.; Entel, P. *Phys. Rev. B* **2010,** *81,* 064109. doi:10.1103/PhysRevB.81.064109
51. Pellarin, M.; Baguenard, B.; Vialle, J. L.; Lerme, J.; Broyer, M.; Miller, J.; Perez, A. *Chem. Phys. Lett.* **1994,** *217,* 349. doi:10.1016/0009-2614(93)E1474-U
52. Mackay, A. L. *Acta Crystallogr.* **1962,** *15,* 916. doi:10.1107/S0365110X6200239X
53. Ino, S. *J. Phys. Soc. Jpn.* **1969,** *27,* 941. doi:10.1143/JPSJ.27.941
54. Entel, P.; Gruner, M. E. *J. Phys.: Condens. Matter* **2009,** *21,* 064228. doi:10.1088/0953-8984/21/6/064228
55. Dannenberg, A.; Gruner, M. E.; Hucht, A.; Entel, P. *Phys. Rev. B* **2009,** *80,* 245438. doi:10.1103/PhysRevB.80.245438
56. Gruner, M. E. *J. Phys.: Conf. Ser.* **2010,** *200,* 072039. doi:10.1088/1742-6596/200/7/072039
57. Clark, J. F.; Pinski, F. J.; Johnson, D. D.; Sterne, P. A.; Staunton, J. B.; Ginatempo, B. *Phys. Rev. Lett.* **1995,** *74,* 3225. doi:10.1103/PhysRevLett.74.3225
58. Dannenberg, A.; Gruner, M. E.; Entel, P. *J. Phys.: Conf. Ser.* **2010,** *200,* 072021. doi:10.1088/1742-6596/200/7/072021
59. Cheng, D.; Wang, W.; Huang, S. *J. Phys. Chem. B* **2006,** *110,* 16193. doi:10.1021/jp063721e
60. Calvo, F. *Faraday Discuss.* **2008,** *138,* 75. doi:10.1039/b702732j
61. Cheng, D.; Cao, D. *Chem. Phys. Lett.* **2008,** *461,* 71. doi:10.1016/j.cplett.2008.06.062
62. Müller, M.; Albe, K. *Phys. Rev. B* **2005,** *72,* 094203. doi:10.1103/PhysRevB.72.094203
63. Yang, B.; Asta, M.; Mryasov, O. N.; Klemmer, T. J.; Chantrell, R. W. *Acta Mater.* **2006,** *54,* 4201. doi:10.1016/j.actamat.2006.05.013
64. Müller, M.; Erhart, P.; Albe, K. *Phys. Rev. B* **2007,** *76,* 155412. doi:10.1103/PhysRevB.76.155412
65. Chepulskii, R. V.; Butler, W. H.; van de Walle, A.; Curtarolo, S. *Scr. Mater.* **2010,** *62,* 179. doi:10.1016/j.scriptamat.2009.10.019
66. Zeng, H.; Sabirianov, R.; Mryasov, O.; Yan, M. L.; Cho, K.; Sellmyer, D. J. *Phys. Rev. B* **2002,** *66,* 184425. doi:10.1103/PhysRevB.66.184425

67. Brown, G.; Kraczek, B.; Janotti, A.; Schulthess, T. C.; Stocks, G. M.; Johnson, D. D. *Phys. Rev. B* **2003,** *68,* 052405. doi:10.1103/PhysRevB.68.052405
68. Gruner, M. E. *J. Phys. D: Appl. Phys.* **2008,** *41,* 134015. doi:10.1088/0022-3727/41/13/134015
69. Lu, Z.; Chepulskii, R. V.; Butler, W. H. *Phys. Rev. B* **2010,** *81,* 094437. doi:10.1103/PhysRevB.81.094437
70. Mryasov, O. N.; Nowak, U.; Guslienko, K. Y.; Chantrell, R. W. *EPL* **2005,** *69,* 805. doi:10.1209/epl/i2004-10404-2
71. Burkert, T.; Eriksson, O.; Simak, S. I.; Ruban, A. V.; Sanyal, B.; Nordström, L.; Wills, J. M. *Phys. Rev. B* **2005,** *71,* 134411. doi:10.1103/PhysRevB.71.134411
72. Lai, C.-H.; Ho, C.-H. *J. Appl. Phys.* **2005,** *97,* No. 10J314. doi:10.1063/1.1853278
73. Menshikov, A. Z.; Antropov, V. P.; Gasnikova, G. P.; Dorofeyev, Y. A.; Kazantzev, V. A. *J. Magn. Magn. Mater.* **1987,** *65,* 159. doi:10.1016/0304-8853(87)90321-0
74. Meyer, G.; Thiele, J.-U. *Phys. Rev. B* **2006,** *73,* 214438. doi:10.1103/PhysRevB.73.214438
75. Menshikov, A. Z. *Physica B* **1988,** *149,* 249. doi:10.1016/0378-4363(88)90250-1
76. Ho, C.-H.; Lai, C.-H. *IEEE Trans. Magn.* **2006,** *42,* 3069. doi:10.1109/TMAG.2006.880110

License and Terms

This is an Open Access article under the terms of the Creative Commons Attribution License (http://creativecommons.org/licenses/by/2.0), which permits unrestricted use, distribution, and reproduction in any medium, provided the original work is properly cited.

The license is subject to the *Beilstein Journal of Nanotechnology* terms and conditions: (http://www.beilstein-journals.org/bjnano)

The definitive version of this article is the electronic one which can be found at: doi:10.3762/bjnano.2.20

Beilstein Journal of Nanotechnology

Extended X-ray absorption fine structure of bimetallic nanoparticles

Carolin Antoniak

Review

Open Access

Address:
Fakultät für Physik and Center for Nanointegration Duisburg–Essen (CeNIDE), Universität Duisburg–Essen, Lotharstr. 1, 47048 Duisburg, Germany

Email:
Carolin Antoniak - carolin.antoniak@uni-due.de

Keywords:
bimetallic alloys; EXAFS; FePt; nanoparticles; wavelets; XAS

Beilstein J. Nanotechnol. **2011,** *2,* 237–251.
doi:10.3762/bjnano.2.28

Received: 18 October 2010
Accepted: 08 April 2011
Published: 11 May 2011

Guest Editors: U. Wiedwald and P. Ziemann

© 2011 Antoniak; licensee Beilstein-Institut.
License and terms: see end of document.

Abstract

Electronic and magnetic properties strongly depend on the structure of the material, especially on the crystal symmetry and chemical environment. In nanoparticles, the break of symmetry at the surface may yield different physical properties with respect to the corresponding bulk material. A useful tool to investigate the electronic structure, magnetic behaviour and local crystallographic structure is X-ray absorption spectroscopy. In this review, recent developments in the field of extended X-ray absorption fine structure measurements and in the analysis methods for structural investigations of bimetallic nanoparticles are highlighted. The standard analysis based on Fourier transforms is compared to the relatively new field of wavelet transforms that have the potential to outperform traditional analysis, especially in bimetallic alloys. As an example, the lattice expansion and inhomogeneous alloying found in FePt nanoparticles is presented, and this is discussed below in terms of the influence of employed density functional theory calculations on the magnetic properties.

Introduction

Since the discovery of X-rays in 1895 by Röntgen, the field of spectroscopy methods using this regime of the electromagnetic spectrum has reached a very important status nowadays, e.g., in material sciences, physics, chemistry, and biology. The advent of synchrotron radiation sources in the 1960s set a milestone in the improvement of the brilliance of X-ray radiation, i.e., of the number of emitted photons per second per unit solid angle in a narrow energy bandpass (usually 0.1%). The increase in average brilliance of X-rays available from artificial sources, from the first X-ray tubes to synchrotron radiation sources of the third generation, is a remarkable factor of about 10^{13}. For next generation free electron lasers an additional increase in the peak brilliance by ten orders of magnitude is aimed for [1].

A detailed description of synchrotron radiation sources and optical devices can be found, e.g., in [2-6]. The interested reader may also be referred to [7], in which the electrodynamics behind synchrotron radiation are explained. Here we

focus on state-of-the-art X-ray absorption spectroscopy (XAS) on 3rd generation synchrotron sources such as the ESRF and BESSY II.

In general, XAS deals with the excitation of core-level electrons, with their element-specific binding energies, by incident X-rays. After absorption of an X-ray photon, a core-hole remains at the former state of the photoelectron and there exist two relaxation channels for de-excitation of the atom: After the transition of another electron from an energetically higher level into the core-hole state, the resulting energy gain either drives the emission of a fluorescence photon or an Auger electron. The X-ray absorption can be measured by detection of the emitted fluorescence photons (fluorescence yield, FY) or by detection of the Auger and secondary electrons (electron yield, EY). For thin samples, the absorption can also be measured in transmission geometry by comparing the intensity of incident X-rays to the intensity of X-rays passed through the sample.

At low photoelectron energies, ranging from the absorption edge up to about 100 eV above, XAS is sensitive to the electronic structure around the absorbing atom and gives rise to the X-ray absorption near-edge structure (XANES). In the energy range above the XANES region – typically from 100 eV to 1000 eV above the absorption edge – the extended X-ray absorption fine structure (EXAFS) contains information about the type and distance of atoms in the local environment of the absorbing atom.

In the literature several examples can be found for EXAFS analysis on nanoparticle systems, e.g., Co [8], CdS [9], CdSe [10], SnO_2 [11] and Au [12] nanoparticles, as well as Ag nanoparticles embedded in glass [13,14]. To discuss the advantages and possible drawbacks of EXAFS analysis in nanoparticulate systems, this paper is organised as follows: In the next few subsections, the basics of XANES and EXAFS are shortly summarised. The second section focuses on the EXAFS analysis either on the basis of standard Fourier transform (FT) methods or by using a wavelet transform (WT). As an example, recent results on FePt nanoparticles are presented after a short summary of different preparation methods. The EXAFS results are also discussed regarding the influence of local structure and composition on the magnetic properties in an alloy, before conclusions are given in the last section.

Review

X-ray absorption near-edge structure (XANES)

The XANES includes information about the density of states (DOS) of the absorbing atoms. More precisely, the XANES is connected to the unoccupied electronic DOS of the excited atom in the presence of a core-hole. In this section, the description of the XANES by the standard one-electron (quasiparticle) picture is briefly summarised. More sophisticated approaches based on the Bethe–Salpeter equation for a two-particle system in quantum field theory have also been developed [15,16]. However, since the quasiparticle approximation leads to a good agreement between theory and experiment in common cases, it is specifically presented below. A discussion as to why this simple approach works fairly well can be found in the work of J. J. Rehr [17].

As known from visible light, the intensity of X-rays after passing through matter of a certain thickness, x, obeys the Lambert–Beer law:

$$I(E,x) = I_0(E)\exp\left[-\mu(E)x\right] \ , \tag{1}$$

where I_0 is the (energy dependent) intensity of incident X-rays and μ is the absorption coefficient. Since for photon energies below 20 keV the photoeffect dominates over Raleigh and Compton scattering, μ can be approximated by the photoabsorption coefficient, which is proportional to the absorption cross-section. The latter is given by the transition probability per unit time, P_{fi}, from the initial state i to the final state f, normalised to the photon flux. P_{fi} can be described using Fermi's Golden Rule in the one-electron approximation:

$$P_{\mathrm{fi}} \propto \sum_{\mathrm{f,i}} M_{\mathrm{fi}}^2 \cdot \left[1-\mathrm{n}(E_{\mathrm{F}})\right] \cdot \delta\left[\hbar\omega-(E_{\mathrm{f}}-E_{\mathrm{i}})\right] \ , \tag{2}$$

where $1-\mathrm{n}(E_{\mathrm{F}})$ is the density of unoccupied final states and the δ-function reflects the conservation of energy in the absorption process. The transition matrix element can be written within the electric dipole approximation (E1) as

$$M_{\mathrm{fi}}^2 = \left|\left\langle \mathrm{f}\left|\mathrm{PA}\right|\mathrm{i}\right\rangle\right|^2 \ , \tag{3}$$

where P is the electron's momentum operator and A is the electric field vector containing the polarisation of the X-rays. For this case, transitions are allowed according to the dipole selection rules

$$\Delta m_{\mathrm{s}} = 0, \ \Delta m_{\mathrm{l}} = \pm 1 \ . \tag{4}$$

The spin rule $\Delta m_{\mathrm{s}} = 0$ reflects the fact that the electron transitions exclude a spin flip, and $\Delta m_{\mathrm{l}} = \pm 1$ is the Laporte rule [18]. Essentially, the Laporte rule states that transitions are forbidden between states that have the same symmetry with respect to the inversion operation, and it originates from a quantum mechan-

ical selection rule which states that parity should be inverted during an electronic transition.

In the E1 approximation, electron transitions, e.g., from the 1s state (K absorption edge) to p states and from 2p states ($L_{3,2}$ absorption edges) to d states, are described. In the electric quadrupole (E2) approximation, additional Laporte-forbidden electron transitions according to $\Delta m_l = \pm 2$ are included, e.g., from s to d states. They are connected to a loss of symmetry that can occur for various reasons, e.g., by Jahn–Teller distortion or vibrational asymmetries in complexes. A short general description of the "appearance of 'forbidden lines' in spectra" can be found in [19] together with the discussion of higher order terms, i.e., the octopole. A more elaborate presentation on this topic can be found, e.g., in [20].

Writing the transition matrix elements in the E1 approximation (Equation 3) already suggests that some kinds of dichroism may exist, i.e., polarisation dependent absorption. In fact there are several types of X-ray dichroism such as X-ray natural linear dichroism (XNLD) [21,22] and natural circular dichroism (XNCD) [23], X-ray magnetic linear dichroism (XMLD) [24,25], X-ray magnetic circular dichroism (XMCD) [26,27], and the more exotic X-ray non-reciprocal linear dichroism [28] and magnetochiral dichroism (XMχD) [29]. In a microscopic picture, this dependence of the absorption on the polarisation of incident X-rays is caused by an anisotropy of the charge (or spin) distribution, either by bonding that yields natural dichroism or by magnetic ordering that yields magnetic dichroism. A general formulation of linear and circular dichroism was given by Carra and Altarelli [30] and an overview of the different types of dichroism can be found, e.g., in [31].

Extended X-ray absorption fine structure (EXAFS)

In a simplistic picture, the outgoing photoelectron of the atom excited by X-rays can interfere with the backscattered waves from neighbouring atoms. That leads to the oscillatory structure in X-ray absorption spectra far above the absorption edge and was named EXAFS by Prins and Lytle [32].

Beside this microscopic picture, the EXAFS can be related, in terms of electrodynamics, to the influence of atoms close to the absorbing atom on the transition matrix elements [33]. Investigations of these influences, i.e., the scattering of the photoelectron, give the possibility to extract information about the distance and type of atoms in the vicinity of the absorbing atoms. By means of this short-range effect, EXAFS oscillations can also be obtained from non-crystalline materials in contrast to classical diffraction methods such as X-ray diffraction or electron diffraction. Regarding the case of nanoparticles, the accuracy in structural and chemical characterisation by EXAFS analysis is not lowered by line broadening, as it is in the case of diffraction methods.

The EXAFS $\chi(k)$ is extracted from the absorption spectrum after subtraction of a background related to the absorption of a free atom embedded in the electronic structure of the solid. Thus,

$$\chi(k) = \frac{\mu(k) - \mu_{\text{atom}}(k)}{\mu_{\text{atom}}(k=0)} \quad , \tag{5}$$

where k is the photoelectron wave number according to

$$k = \sqrt{\frac{2m_{\text{e}}}{\hbar^2}\left(E - E_0\right)} \quad . \tag{6}$$

with the threshold energy E_0. A theoretical framework for the EXAFS description was established in the 1970s by several groups [34-37]. Within multiple scattering theory, the EXAFS can be described as the sum of the imaginary part of contributions from different scattering paths [38,39]:

$$\chi(k) = \sum_{\text{j}} \text{Im}\left[\tilde{\chi}_{\text{j}}(k)\right] \quad , \tag{7}$$

$$\begin{aligned}\tilde{\chi}_{\text{j}}(k) = &\frac{S_0^2 N_{\text{j}}^{\text{eff}} F_{\text{j}}(k)}{kR_{\text{j}}^2} \exp\left[2ikR_{\text{j}} + i\delta_{\text{j}}(k)\right] \\ &\times \exp\left[-\frac{2R_{\text{j}}}{\lambda(k)} - 2k^2\sigma_j^2\right] \quad .\end{aligned} \tag{8}$$

In this equation, S_0^2 denotes an amplitude reduction factor due to many-body effects, $N_{\text{j}}^{\text{eff}}$ is the effective coordination number, $F_{\text{j}}(k)$ is the effective scattering amplitude, R_{j} is half the total of the scattering path, $\lambda(k)$ is the mean free path length of the photoelectron wavenumber, δ_{j} is an effective total phase shift including contributions from the absorber atoms and all scattering atoms, and $\exp(-2k^2\sigma_{\text{j}}^2)$ is the EXAFS Debye–Waller factor.

Over the last few decades, special cases of EXAFS such as its magnetic counterpart MEXAFS [40-43], as well as surface EXAFS [44,45], have also drawn much attention. In the latter case, the surface sensitivity is ensured by detecting the Auger electron emission of a particular element as a function of photon energy [36], partial FY [46,47] or total FY [48]. Also atomic EXAFS has been discussed assuming interstitial charges as scattering centres [49-51].

EXAFS analysis

Nowadays, EXAFS analysis is usually carried out by the comparison of experimental data with calculated spectra. Its theory is implemented, e.g., in FEFF [38,39], WIEN2k [52], GNXAS [53], the Munich SPR-KKR algorithm [54] and others [55]. For a detailed analysis, quantifying lattice parameters and local chemical composition, the comparison to calculated EXAFS is indispensable. Fitting programs such as FEFFIT [56], based on the FEFF algorithm, try to find the best agreement between the calculated EXAFS and experimental data either in *k*-space or after Fourier transformation in real space. FEFFIT uses the cumulant expansion method [57,58] with the first four cumulants (ΔR, σ^2, C_3, C_4) of the pair distribution function (PDF) of atoms around the absorber atom. To account for thermal or configurational disorder, the complex wavenumber p is introduced and should be used instead of k. The imaginary part of p represents losses of photoelectron coherence, which includes the mean free path and core-hole lifetime. The resulting modified EXAFS equation (Equation 8) can be written as [59]:

$$\begin{aligned}\tilde{\chi}_{\mathrm{j}}(k) = &\frac{S_0^2 N_{\mathrm{j}}^{\mathrm{eff}} F_{\mathrm{j}}(k)}{k(\Delta R_{\mathrm{j}} + R_{\mathrm{j}})^2} \exp\left[2ikR_{\mathrm{j}} + i\delta_{\mathrm{j}}(k)\right] \\ &\times \exp\left[2i(p\Delta R_{\mathrm{j}} - 2p\sigma_{\mathrm{j}}^2 / R_{\mathrm{j}} - 2p^3 C_{3,\mathrm{j}} / 3)\right] \\ &\times \exp\left[-2R_{\mathrm{j}} / \lambda(k) - 2p^2\sigma_{\mathrm{j}}^2 - 2p^4 C_{4,\mathrm{j}} / 3)\right] \quad .\end{aligned} \tag{9}$$

However, for each system it is essential to check whether or not it is necessary to include the fourth-order and third-order cumulants in the fitting procedure.

In contrast to the Fourier based method, a wavelet transform offers the possibility to obtain information directly about changes in the local environment of the absorbing atoms compared to a known reference sample without calculation of the EXAFS data by numerical approaches. In the following, the analysis of EXAFS on the basis of a standard Fourier transform method is described in more detail as well as wavelet transforms as a useful tool, which is rarely used for this application. Both methods first require a background subtraction from the experimental data, as already mentioned above (Equation 5). This is usually performed by using the AUTOBK algorithm [60] that approximates $\mu_{\mathrm{atom}}(k)$ by a spline and minimises, in a fitting procedure, the non-structural oscillations in $\chi(k)$. These oscillations correspond to distances in real space that are too short to be related to neighbouring atoms.

EXAFS analysis based on Fourier transform

The discussion of the Fourier transform (FT) of experimental EXAFS data, as carried out after the pioneering work of Sayers, Lytle, and Stern in 1970 [61], is commonly employed for a structural analysis. It can be used for a quantification of the coordination number of absorbing atoms and the distance of backscattering atoms from the absorber, which is essential for any numerical EXAFS analysis on the basis of Equation 9. In addition, the elemental species of backscattering atoms have to be known for subsequent fitting of the numerical simulation to the experimental data.

For a proper FT of experimental data, $\chi(k)$ is usually weighted by k^{n} with n = 1, 2, 3 to compensate for the reduction of the EXAFS amplitude with increasing k. The value of n can give a rough estimation of the type of backscattering atom since the k dependence of the backscattering amplitude, and consequently, the amplitude of $\chi(k)$, depends on the atomic number. The lighter the element, the lower is the amplitude at high values of k. Examples of the k dependence of light and heavier atoms can be seen in Figure 1. The effective backscattering amplitude has been calculated for oxygen (Z = 8), Fe (Z = 26), and Pt (Z = 78); the former as one example for very light elements; Fe and Pt since experimental results on Fe_xPt_{1-x} alloys will be discussed later. It can clearly be seen that the k dependence of the effective backscattering amplitude is unique for each element. Light elements mainly exhibit one main peak only as a function of k, while for heavy elements, such as Pt, the spectral shape of the backscattering amplitude may be more complicated. In the case of elements with $78 \leq Z \leq 90$, a strong reduction in the backscattering amplitude over a small range connected to a more rapidly changing phase – e.g., at k = 60 nm^{-1} in the case of Pt –, is known in literature as the generalised Ramsauer–Townsend effect [62,63]. In a simple picture, the wavelength of the outgoing photoelectron (about 0.1 nm for k = 60 nm^{-1}) is well-matched to the size of the scatterer. In this case, the photoelectron may tunnel through the scattering potential and the scattering cross-section vanishes leading to a dip in the backscattering amplitude at a fairly distinct wave number. By standard FT based analysis employing the FEFF code [38,39], the wave number dependent amplitude of simulated EXAFS oscillations can be fitted to experimental data by changing the local composition around the absorber atom. With this method the elemental species can be identified with a typical error of ±2 in the atomic number. Especially in chemically disordered systems of more than one element, the identification of the backscattering atoms and their distance to the absorber by this trial and error method is not efficient, and the elements have to be preselected.

The real space distance of the backscattering atoms to the absorber can be estimated by an FT of the experimental $\chi(k)$ since it will give a pseudo-radial distribution function (RDF) of the distances of backscattering atoms. Note that this is not the

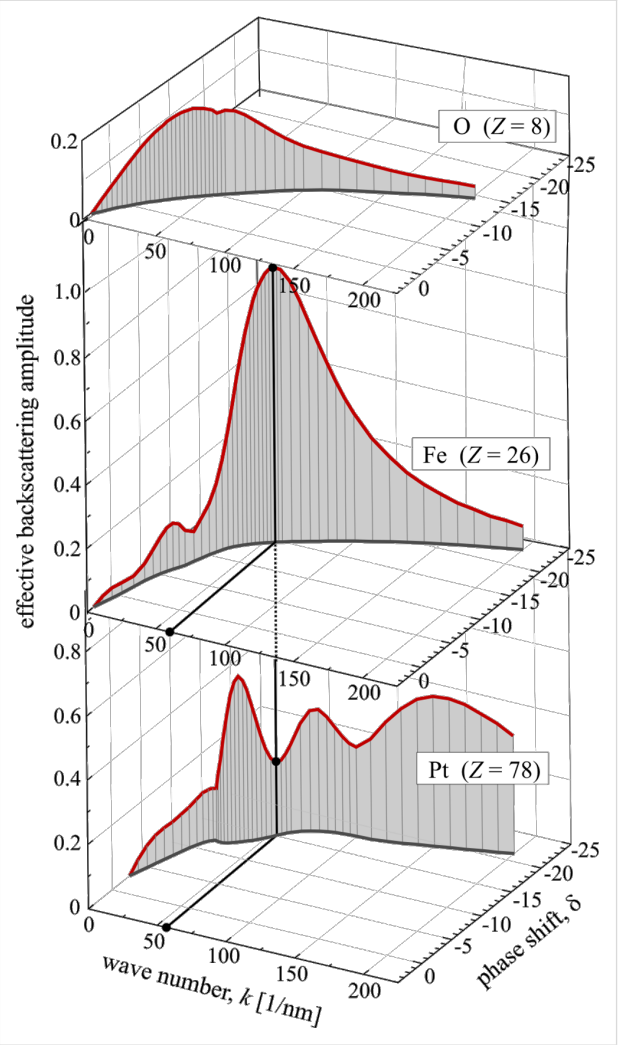


Figure 1: Effective backscattering amplitude of O, Fe, and Pt as a function of wave number and phase shift. At k = 60 nm^{-1} Fe has it maximum backscattering amplitude, while it exhibits a local minimum in the case of Pt due to the Ramsauer–Townsend effect.

geometric radial distance obtained after an FT, since the EXAFS phase shift is included in the experimental data, which yields a shift of the RDF to smaller values of the distance r. An example of experimental EXAFS data in k-space and real space is shown in Figure 2. In this case, the data have to be multiplied by a window function W since for low values of k (XANES regime) the resonant absorption dominates the scattering effects, and for high values of k the signal-to-noise ratio becomes too small. The data are shown only in the region of non-vanishing values of the window function. The forward FT (FFT) can be written as

$$\hat{\chi}(r) = \int_{-\infty}^{\infty} W k^{n} \chi(k) \exp\left[-2ikr\right] \mathrm{d}k \quad . \qquad (10)$$

Very commonly used window functions W are, e.g., the Hann window (sometimes called Hanning window in the literature) and the Kaiser–Bessel window. The window should be chosen in such a way that the data interval starts and ends at a k value of zero-crossing of $\chi(k)$. The backward FT (BFT) of the pseudo-RDF should match the original data in the region where the window function leads to non-vanishing results, as shown in Figure 2 where in the lower panel the original data (grey line) are plotted together with the BFT of the FFT data (red dotted line). In this specific case a Kaiser–Bessel window has been used with a sharp truncation (dk = 1 nm^{-1}) starting at $k \approx 21$ nm^{-1} and ending at $k \approx 147$ nm^{-1} for FFT, and (dr = 0.01 nm) starting at $r \approx 0.14$ nm and ending at $r \approx 0.46$ nm for BFT.

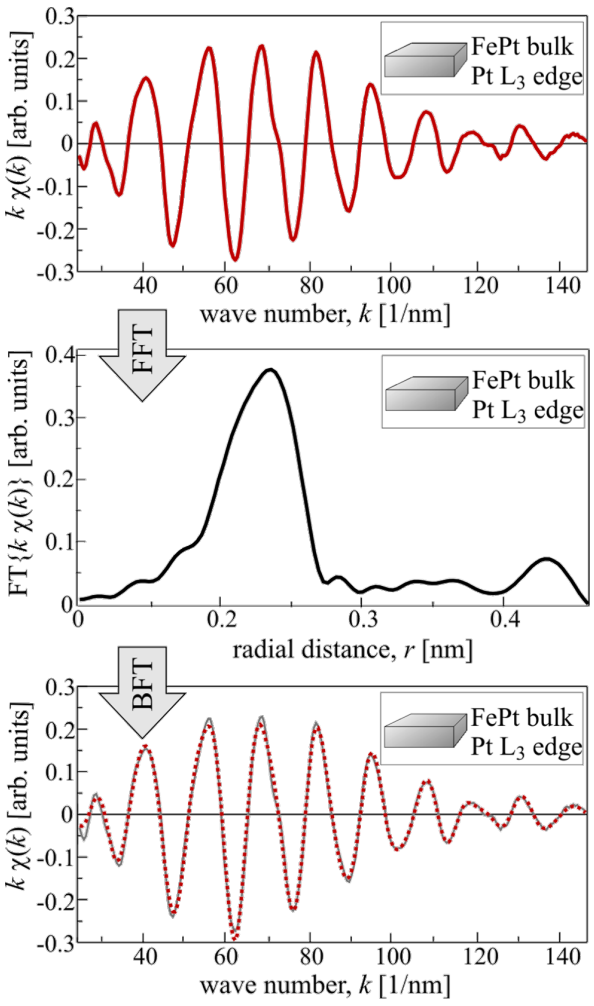


Figure 2: Experimental EXAFS data measured at the Pt L_3 absorption edge of FePt bulk material at room temperature (upper panel). The forward FT (FFT) yields a pseudo-RDF (centre) that recovers (red dotted line, lower panel) the original data (grey line, lower panel) after application of a backward FT (BFT). Details on the window functions used here can be found in the text.

Wavelet transforms

An obvious disadvantage of FT is that it only has a resolution in Fourier space and not in the space of original data. In EXAFS analysis, the FT magnitude of experimental data provides resolution in the radial distance of neighbouring scatterers, however, the information is lost at the wave number k at which the scatterer contributes. Since the position in k-space is related to the atomic species of the backscattering atom, important information is lost in the magnitude of the transformed signal.

It is possible to lessen this problem through the use of a short-term Fourier transform (STFT), which determines the Fourier coefficients of the original data multiplied by a window function, i.e., the k dependent EXAFS data are transformed in several intervals of k. However, this leads to a high resolution in k only, at the expense of good resolution in r, and vice versa, since cutting the signal corresponds to a convolution between the original data and the cutting window. Convolution in k is identical to multiplication in r, and since the FT of a sharp cut contains all possible values of r, the FT of the EXAFS data will be smeared out.

This shows that cutting the signal into several parts is the right way to obtain resolution in k, but the cutting has to be performed carefully so as not to lose good resolution in Fourier space. The most recent solution up to now is the wavelet transform (WT).

WTs gained much attention in the 1990s after the discovery of a family of orthogonal continuous wavelets by Daubechies [64]. Wavelets are square-integrable functions and the integral over the wavelet is zero:

$$\int_{-\infty}^{\infty} \Psi(k)\mathrm{d}k = 0 \qquad (11)$$

Today wavelets are widely used to extract information from audio signals and images, and for compression/decompression algorithms. However, in EXAFS analysis they are only used occasionally [65-69].

The main idea behind the wavelet transform (WT) is to replace the infinitely expanded periodic oscillations in an FT by using located wavelets as a kernel for the integral transformation: A scalable mother wavelet or analysing wavelet, $\Psi(k)$, is used as a window function for the transform. The basis of the transformed signal is the so-called baby wavelets generated not only by translation but also by scaling of the mother wavelet. As an example, Figure 3 shows the real part of a Gabor wavelet that is used for EXAFS analysis, as discussed below. Starting from a mother wavelet (red curve), the first set of baby wavelets (blue curves) can easily be generated. The obtained family of wavelets can be written as

$$\left\{\Psi_{ab} = \frac{1}{\sqrt{a}}\Psi\left(\frac{k-b}{a}\right) : (a,b) \in \mathbb{R}_+ \times \mathbb{R}\right\} \quad . \qquad (12)$$

The scaling factor, a, is the most important parameter to solve the signal-cutting problem mentioned above. The wavelet as a window for the transform is shifted along the signal, and for every position the WT is calculated. This process is repeated in many cycles using scaled wavelets, i.e., wavelets with a stronger or weaker localisation in k, which results in a collection of WT of different parts of the original signal, with different resolutions. Merging all the information, WT yields a high resolution in both r- and k-space. Of course, similar to FT the WT is a complete transformation, i.e., the backward transformation recovers the original signal without loss of information, which is the sine qua non in data analysis. For the EXAFS analysis presented here, the Gabor wavelets have been used which have a structure similar to a typical EXAFS signal, since it consists of a slowly varying amplitude term, while the phase term is oscillating rapidly. Another similar family of wavelets that can be used for the purpose of EXAFS analysis is built from Morlet wavelets. In the work of Funke et al. [67], Morlet wavelets have been used to analyse the short-range structure of a Zn–Al layered double hydroxide. Figure 3 shows the real part of some Gabor wavelets. The WT of the EXAFS signal can be written as

$$\begin{aligned}\hat{\chi}_{WT}(r,k) &= \left\langle \Psi_{ab}, \chi(k)\right\rangle \\ &= (2r)^{-1/2}\int_{-\infty}^{\infty} k'^{n}\,\chi(k')\Psi^*\left[2r(k'-k)\right]\mathrm{d}k' \quad ,\end{aligned} \qquad (13)$$

where Ψ^* is the complex conjugate of the wavelet, shifting of the wavelet corresponds to b = k and the scaling to a = $(2r)^{-1}$.

The advantage of a WT with respect to an FT is visualised in Figure 4, where two different sample signals are plotted and analysed. The two wave packets contributing to the sample signal on the left hand side and on the right hand side of Figure 4 are the same except for their position in k. While in the first signal (Figure 4, left) the two packets are well-separated, they have the same position in k in the other signal (Figure 4, right). In the time–frequency domain it would mean that they occur at the same time for the latter case. In the reciprocal k-space (the real-space domain of EXAFS) it can be interpreted as a signal from two different elements with either a distinct difference in the position of maximum backscattering amplitude

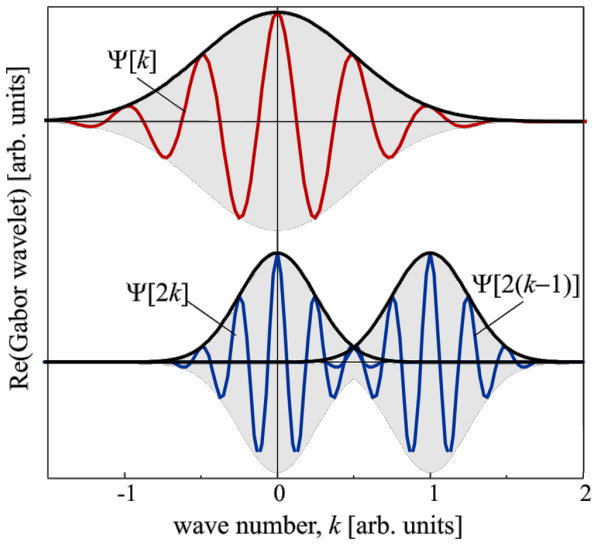


Figure 3: Real part of a Gabor mother wavelet (red curve) and baby wavelets generated by scaling and shifting (blue curves).

(first sample signal), or with the same position of maximum backscattering amplitude. Since the position of maximum backscattering amplitude is related to the atomic number of an element, as discussed before, one may state that the first sample signal describes EXAFS arising from two backscattering elements with a clear difference in their atomic number Z, whereas the second sample signal can be assigned to EXAFS caused by the same element (or two elements with slightly different atomic numbers).

The FT shown in Figure 4 is in both cases the same RDF, i.e., the information on the k position of the different wave packets is lost. In the WT the two different sample signals can still be distinguished, and both the position in k and the corresponding radial distance r can be extracted. The WT of the sample signal with well-separated wave packets shows two maxima: one located at the point ($k \approx 46$ nm^{-1}, $r \approx 0.16$ nm) and the other at ($k \approx 120$ nm^{-1}, $r \approx 0.05$ nm). The WT of the sample signal with coinciding wave packets also shows two maxima, but at ($k \approx 46$ nm^{-1}, $r \approx 0.16$ nm) and ($k \approx 46$ nm^{-1}, $r \approx 0.05$ nm).

In all cases, the values of k and r where the maxima are located are the same as those used for the generation of the sample signal. Compared to the FT of the signals, the r values are also the same. Since one usually does not know where the maximum in k-space is located for different contributions, a WT is

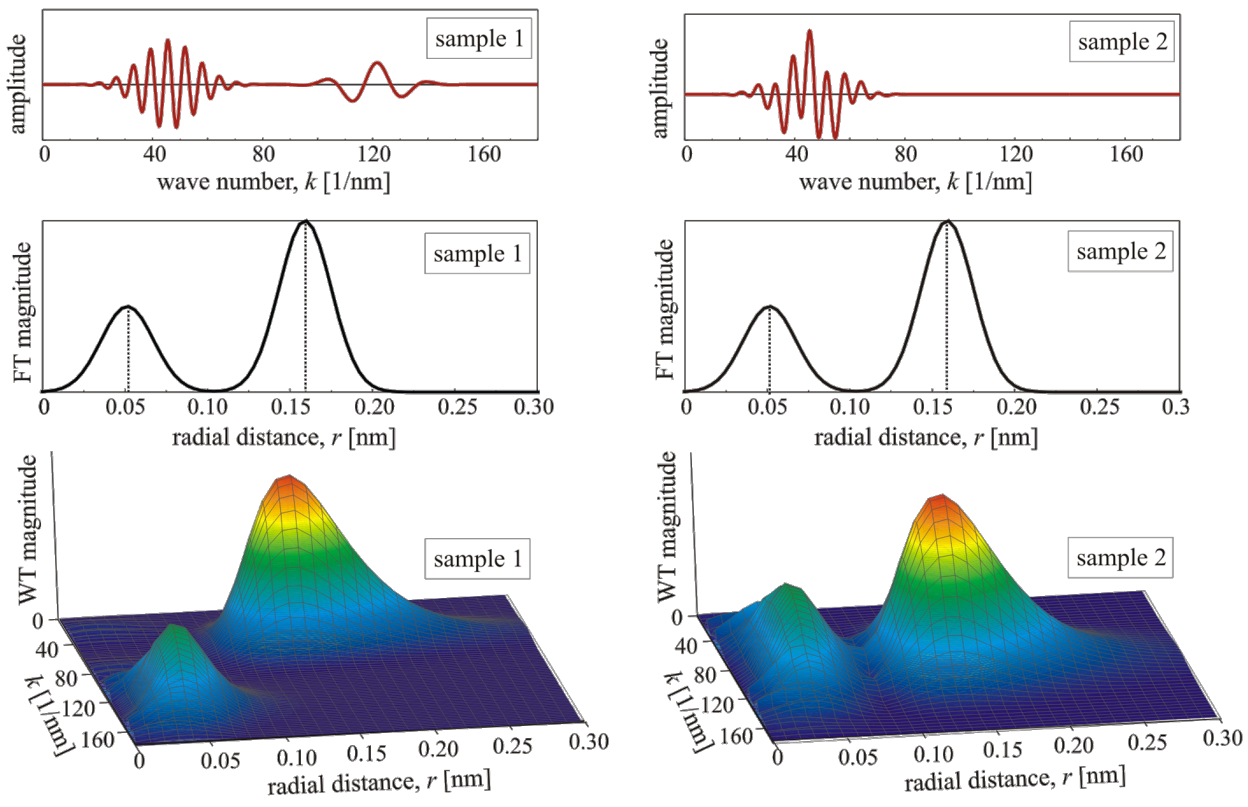


Figure 4: Two different sample signals (upper panel) that show the same radial distance function after FT (centre), but clearly different WT signals (lower panel).

currently the only method to receive information of the signal both in k-space and in real space. This is especially useful in EXAFS analysis of alloys in which different types of backscatterers are distributed on a regular lattice. A detailed discussion on the influence of rapid phase changes in EXAFS signals on the WT, and the limitations of WTs, can be found in the work of Funke et al. [67].

The application of WT and FT to experimental data is presented in the next section through the discussion of recent results on FePt nanoparticles [68,69]. In order to facilitate the interpretation of spectral features in the EXAFS data and their WT, Figure 5 shows the WT of Fe and Pt bulk material and, for clarity, the projection of the WT on the (k,r)-plane is added. For the case of Fe, one main peak is located around k = 60–70 nm^{-1}, as expected from the k dependence of the backscattering amplitude of Fe presented in Figure 1. For small k values the maximum is located around $r \approx 0.20$ nm, and for large values it is located around $r \approx 0.23$ nm. For intermediate k values, around the global maximum, the position in r of the local maxima (black dotted line in Figure 5) changes with k indicating a non-linear k dependence of the EXAFS phase shift

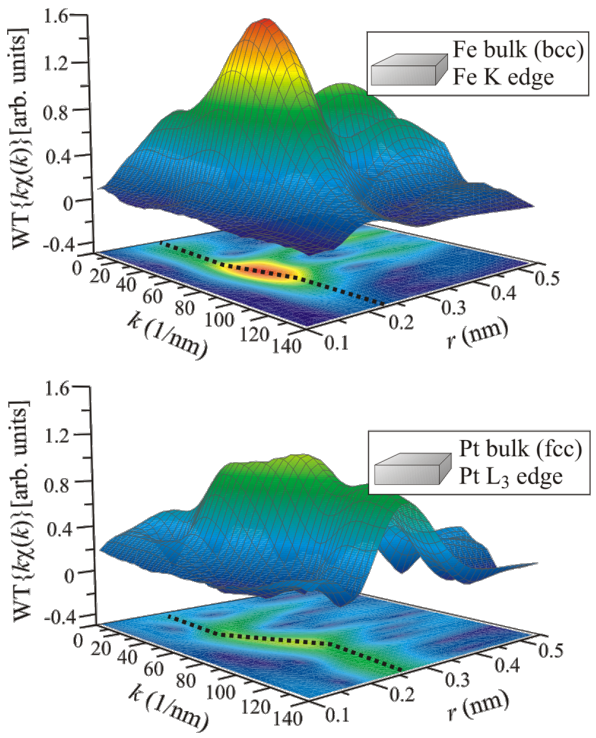


Figure 5: WT of room temperature EXAFS data for Fe (upper graphic) and Pt (lower graphic) reference samples measured at the Fe K and Pt L_3 absorption edge, respectively.

[70]. Actually, one may consider the phase shift shown in Figure 1 for the case of Fe to change linearly for $k < 40$ nm^{-1} and $k > 100$ nm^{-1} while a distinct curvature is visible in the region in between. This is even more pronounced for the case of Pt with its rapidly changing phase in the same region of k. The position in r for the local maxima is around $r \approx 0.20$ nm for low values of k, and for large values located around $r \approx 0.26$ nm. In agreement with the k dependence of the backscattering amplitude shown in Figure 1, the maximum WT amplitude is reduced with respect to Fe, exhibits several peaks and has a larger magnitude at high k values.

FePt nanoparticles

From the technological perspective, FePt has become one of the most interesting nanostructured materials (see, e.g., [71-74]), since its large magnetic anisotropy of 6×10^6 J·m^{-3} [75-78] in the chemically ordered state with $L1_0$ crystal symmetry makes it the prime candidate for new ultrahigh density storage media. The formation of the $L1_0$ ordered phase is driven by volume diffusion and can be induced by post-deposition annealing of the nanoparticles or in-flight annealing of FePt nanoparticles synthesised by condensation from the gas phase before landing onto a substrate as described below.

Gas phase synthesis

FePt nanoparticles can be prepared by an inert gas condensation method based on a DC magnetron sputtering process from alloy targets in a continuous gas flow of helium and argon [79,80]. In general, the experimental setup for preparing nanoparticles from the gas phase is composed of three parts: A nucleation chamber, a sintering oven and a deposition chamber. After nucleation and particle growth in the nucleation chamber with liquid nitrogen cooled walls, the particles pass the sintering oven and can be in-flight annealed before deposition onto a substrate. Due to the short flight time through the sintering oven (about 1 s or less depending on the gas flow rate), annealing has to take place at very high temperatures around 1000–1300 K in order to obtain the chemically ordered $L1_0$ phase in the nanoparticles. It has been shown that it is possible to prepare chemically disordered Fe_xPt_{1-x} particles with diameters in the range of 3 nm < d < 20 nm that are single crystalline or multiple twinned with an icosahedral shape. Size and morphology can be tuned by changing the inert gas pressure and the sintering temperature [79]. It was found that the icosahedral particles are thermally stable and cannot easily be transformed into the $L1_0$ phase. This indicates inadequate volume diffusion in the icosahedral particles probably due to a lack of a sufficient number of vacancies.

A method to destabilise the icosahedral shape, and to promote the formation of single-crystalline fcc FePt nanoparticles, is the

introduction of oxygen during particle preparation [81]. However, the formation of the $L1_0$ phase was not observed indicating that the volume diffusion is still inadequate in this method. For gas phase synthesised nanoparticles, a possible surface segregation of Pt has recently been discussed [82] as it is also known for thin FePt films [83]. In addition, an indication of a stronger lattice expansion towards the surface layer was found by analysis of transmission electron microscope (TEM) images [82]. However, since the particles were exposed to air before being transferred into the TEM, oxidation may also be responsible for the lattice expansion at the surface layers. In order to exclude the influences of oxidation and other contaminations on the investigated structure, EXAFS of in situ cleaned and oxide-free FePt nanoparticles seems to be a suitable tool to study the intrinsic structural properties of pure metallic nanoparticles.

Wet-chemical synthesis

A possible organometallic route to synthesise FePt nanoparticles follows the approach by S. Sun et al. [84] by the reduction of platinum diacetylacetonate, $Pt(acac)_2$ and thermal decomposition of iron pentacarbonyl, $Fe(CO)_5$, in hexadecane-1,2-diol at about 300 °C. The chemical reactions were initiated in the presence of the surfactants oleic acid and oleyl amine, thus providing a route to synthesise nanoparticles of a chemically disordered Fe_xPt_{1-x} alloy surrounded by the surfactants. After cooling to room temperature, the particles were precipitated by adding ethanol and separated by centrifugation. After this procedure, the particles were dispersed in *n*-hexane with surfactants, precipitated out and centrifuged once again. This can be repeated several times, until a stable dispersion of nanoparticles in *n*-hexane is obtained. The nanoparticles can be brought onto a naturally oxidised Si substrate using the spin coating technique, dip coating or just by putting a small droplet of nanoparticle dispersion onto the substrate. The shell of organic ligands prevents the agglomeration of the nanoparticles and drives the formation of hexagonally self-assembled superlattices.

The quality of the hexagonal arrangement can be improved by an excess of surfactants in the dispersion. Subsequent annealing of the nanoparticles has been tried as a route to obtain nanoparticles in the $L1_0$ state. Due to the thermal decomposition of the ligand shell during the annealing process and the enhanced mobility of the nanoparticles at elevated temperatures, this procedure leads to sintering of the nanoparticles especially for small diameters below 6 nm. Much effort has been taken to prevent sintering using different methods, e.g., linking of the nanoparticles to the substrate by special molecules [85-88]. Another method that has been successfully applied is the coverage of the nanoparticle monolayer, e.g., by carbon [77] or embedding in a NaCl matrix [89].

EXAFS results and discussion

In order to gain more insight into thermally activated diffusion processes in FePt nanoparticles, it is useful to analyse the crystal structure and the homogeneity of the chemically disordered alloy. The results presented here in detail were obtained on nanoparticles prepared by the wet-chemical route described above. The magnetic properties are also compared to the properties of FePt nanoparticles synthesised by condensation from the gas phase. By EXAFS analysis it was found that there exists (i) a lattice expansion with respect to the corresponding bulk material in wet-chemically synthesised FePt nanoparticles [90] and (ii) a compositional inhomogeneity in chemically disordered nanoparticles, i.e., Fe atoms are in an Fe-rich environment and Pt atoms are in a Pt-rich environment [68,69].

Figure 6 shows the experimental EXAFS data at the Pt L_3 absorption edge for FePt in the bulk and nanoparticulate system, respectively, and their FT and WT. While the lattice expansion can clearly be resolved [90], it is difficult to obtain small compositional changes by an FT. However, one may notice a drop of the envelope of $\chi(k)$ data measured at the Pt L_3 edge of nanoparticles compared to the data obtained from bulk material and a shoulder in the FT correlated to this drop. This can be interpreted as a Pt enrichment around Pt absorbers in nanoparticles, since the backscattering amplitude of Pt exhibits a local minimum at $k = 60$ nm^{-1} reducing the amplitude of χ(k), while Fe has its maximum backscattering amplitude around this value of k, as can be seen in Figure 1. The differences can be seen more clearly in the WT of EXAFS data shown in the lower panel of Figure 6.

The WT exhibits a global maximum around $k \approx 60$ nm^{-1} and $r \approx 0.22$ nm for the bulk material and $k \approx 60$ nm^{-1}, $r \approx 0.24$ nm for the nanoparticles indicating the lattice expansion in the particles. The maximum amplitude of the WT is strongly reduced for the nanoparticles and the shape differs significantly from the WT of bulk data especially in the region of low k values. In addition, the centroid of the plotted area is slightly shifted towards higher k values that may already indicate a Pt enrichment with respect to the bulk material. By comparison to the reference data shown in Figure 5, this interpretation becomes obvious: While for the FePt bulk material the WT is dominated by the sharp maximum related to Fe backscattering atoms, in the case of nanoparticles the WT is similar to the smoother WT of Pt backscattering atoms. That means that in the nanoparticles, the Pt absorber atoms are surrounded by more Pt backscattering atoms than in the bulk material, although the average composition determined by energy-dispersive X-ray spectroscopy (EDS) is the same for the two samples. This difference is not a conflict between EXAFS and EDS results, but simply reflects the fact that an averaging technique such as

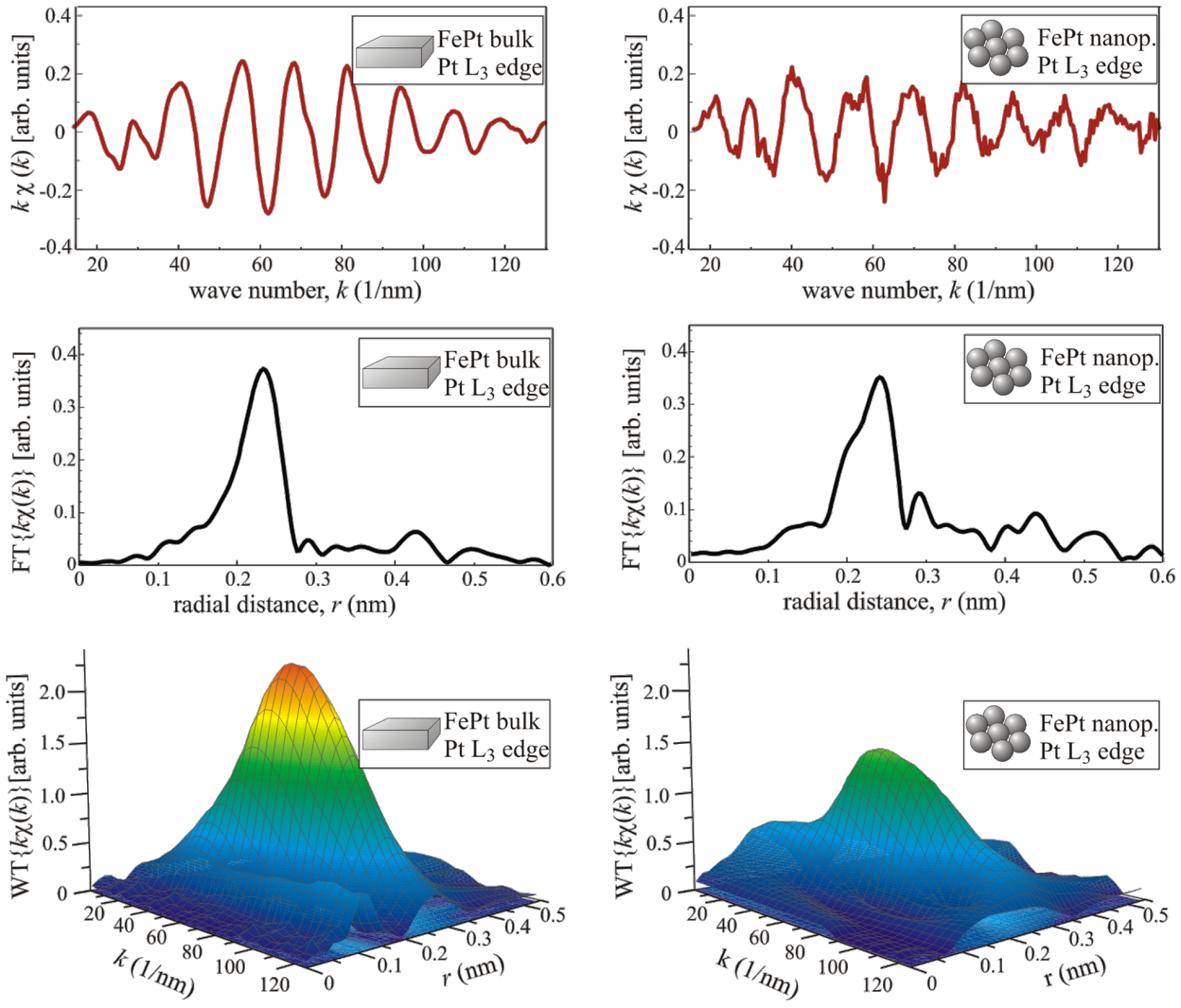


Figure 6: Room temperature EXAFS data of FePt bulk material (left panel) and nanoparticles (right panel) measured at the Pt L_3 absorption edge, their Fourier transform, and wavelet transform.

EDS does not allow for the detection of an inhomogeneous composition of the investigated sample, whereas the EXAFS technique does. The reason is that EXAFS stems from scattering of the photoelectron by the local surroundings of the probed atoms. Thus, it can be concluded that the Pt absorbing atoms are in a Pt-rich environment and thus, Fe atoms are in an Fe-rich environment. The latter has also been proven by similar analysis of EXAFS measured at the Fe K absorption edge as can be seen in Figure 7: After subtraction of the WT of bulk data, the difference in the number of Fe and Pt backscattering atoms becomes even more evident. (For original $\chi(k)$ data see [68,69].) At the Pt L_3 edge the difference has a minimum at the position of maximum backscattering amplitude of Fe ($k \approx 60$ nm^{-1}, $r \approx 0.2$ nm) and a maximum around the corresponding Pt position ($k \geq 120$ nm^{-1}, $r \approx 0.2$ nm). At the Fe K edge it is the opposite way round. For clarity, in Figure 7 black dotted lines denote the position of local maxima and minima of the projected WT magnitude. Although the data clearly show the compositional inhomogeneity within the nanoparticles, a quantification of the nearest neighbour atoms of either Fe or Pt is not possible directly. However, it is useful to know for further calculations of EXAFS, e.g., by FEFF, since the structure and chemical composition have to be modelled as exactly as possible in order to get reasonable results.

The best agreement between calculated EXAFS and experimental data of nanoparticles were found assuming (40 ± 8) atom % Fe around the Pt atoms and (70 ± 12) atom % Fe around the Fe atoms and a lattice constant of (0.387 ± 0.004) nm [68,69]. For the case of the FePt bulk ma-

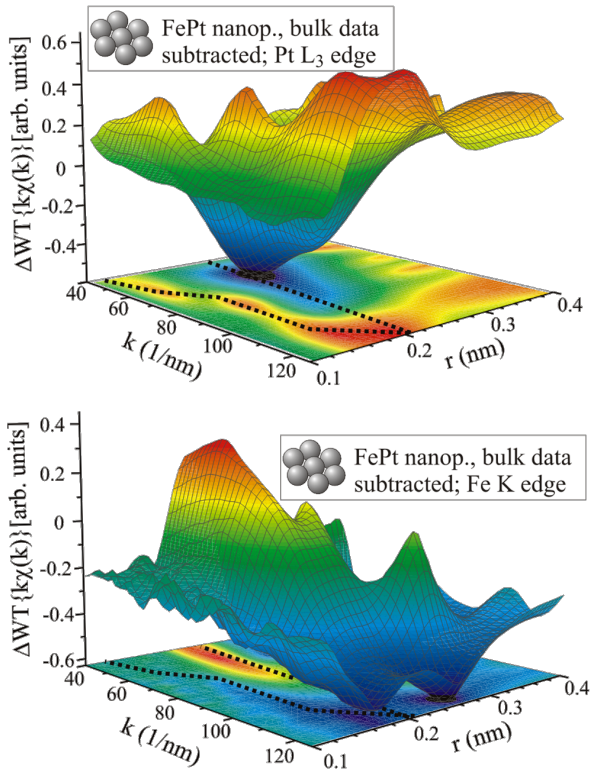


Figure 7: WT of room temperature EXAFS data of FePt nanoparticles measured at the Pt L_3 (upper graphic) and Fe K absorption edge (lower graphic) after subtraction of the WT of the corresponding bulk data [68].

terial, the same composition around Fe and Pt atoms within experimental errors was obtained in agreement with the averaged composition measured by EDS, (56 ± 3) atom %, and a lattice constant of (0.383 ± 0.003) nm [68,69,90].

The differences in structure and local chemical environment may also strongly affect the magnetic properties of the nanoparticles compared to the corresponding bulk material as will be discussed below.

Discussion: Influence on magnetic properties

The magnetic properties strongly depend on the lattice spacing and the chemical environment around an atom. Thus, both lattice expansion and inhomogeneous composition are expected to change the magnetism of FePt nanoparticles with respect to the bulk material. The influence of the chemical environment on the magnetic moments of the Fe atoms in Fe_xPt_{1-x} bulk materials have been investigated by XMCD analysis and spin polarised relativistic Korringa–Kohn–Rostoker (SPR-KKR) calculations [54,91]: The higher the Fe content in the alloy, the smaller the spin magnetic moment at the Fe sites. Changes of the orbital magnetic moment and the Pt moments are negligible with respect to the strong decrease of the Fe spin magnetic moment. The results from SPR-KKR calculations are shown in Figure 8. For the lattice constants, the experimentally determined values were used [68] as input for the calculations. It can clearly be seen that the spin magnetic moments at the Pt sites remained largely unchanged around $\mu_S(Pt) \approx 0.22\ \mu_B$ for different compositions between $x = 32$ atom % and $x = 68$ atom %, the orbital magnetic moment increased slightly with increasing Fe content from $\mu_l(Pt) \approx 0.042\ \mu_B$ to $0.048\ \mu_B$. The orbital magnetic moment at the Fe sites showed a similar behaviour and increased from $\mu_l(Fe) \approx 0.06\ \mu_B$ to $0.078\ \mu_B$ in the composition range investigated in this work. The Fe spin magnetic moment decreased with increasing Fe content from about $3.0\ \mu_B$ at $x = 32$ atom % to $2.75\ \mu_B$ at $x = 68$ atom %.

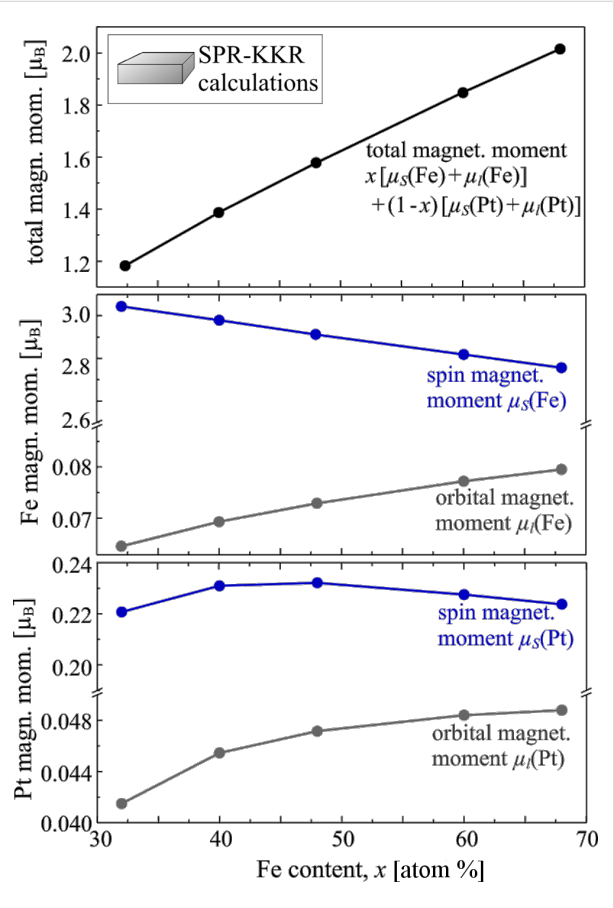


Figure 8: Composition dependence of spin and orbital magnetic moments at the Fe and Pt sites in chemically disordered Fe_xPt_{1-x} alloys and the total magnetic moment calculated using the SPR-KKR method.

However, the total magnetic moment averaged over the different lattice sites increased almost linearly with increasing Fe content as is also known from experimental data using conventional magnetometry such as SQUID or VSM magnetometry [92].

Compared to experimental data on Fe_xPt_{1-x} bulk-like alloys [54], it seems to be a general trend that the calculations lead to increased spin magnetic moments at the Fe sites, whereas the orbital magnetic moments are slightly underestimated. At the Pt sites the calculated values are decreased by a factor of about two, but this is in agreement with other calculated values reported in the literature [93].

The reason for this disagreement between theory and experiment is as yet unclear. However, the qualitative composition dependence is in good agreement with the experimentally obtained one.

Regarding the effect of a lattice expansion in FePt nanoparticles, calculations offer the unique possibility to study this influence without changing any other parameter. In Figure 9, the SPR-KKR results are shown for an FePt alloy with a lattice constant of 0.381 nm as reported in the literature [94], 0.387 nm in the case of the nanoparticles, and an extremely large value of 0.4 nm corresponding to a lattice expansion of 5% with respect to the bulk value in literature. At the Fe sites, both spin and orbital magnetic moment increased with increasing lattice constant as expected in a simple picture assuming that larger lattice spacing results in a more localised electronic structure yielding more atomic-like values of magnetic moments. At the Pt sites, the orbital magnetic moment increased as well, whereas the spin magnetic moment exhibited only a slight decrease with increasing lattice constant. The total magnetic moment is larger for larger lattice parameters, but all the changes are rather small. Similar trends are reported for other ferromagnetic or antiferromagnetic materials, e.g. for bcc and fcc Fe [95]. Experimentally, the magnetic moments of FePt nanoparticles were found to be reduced with respect to the correspondent bulk material by about 20–30% [68,69].

Since the lattice expansion leads to larger magnetic moments in the order of a few percent this cannot be an appropriate explanation. However, the inhomogeneous composition can easily yield such a significant reduction of magnetic moments when the magnetic moments of nanoparticles are compared to those of bulk or bulk-like materials with the same *averaged* composition. It turns out that the magnetic moments should be assigned to the local composition around the Fe atoms since the Fe atoms, with their large magnetic moments and sensitivity to local changes, dominate the total magnetic moment.

Interestingly, reduced magnetic moments are also reported for fcc FePt nanoparticles prepared by condensation from the gas phase [96]. From this finding one may conclude that the inhomogeneity can be found in Fe_xPt_{1-x} particles independent of the preparation method. The preferential formation of Fe-rich and Pt-rich regions within the nanoparticles could also influence the formation of the $L1_0$ state and lower the degree of chemical order. Beside the Fe_xPt_{1-x} system, a local deviation of the composition with respect to the averaged value may also occur in nanoparticles of various binary alloys.

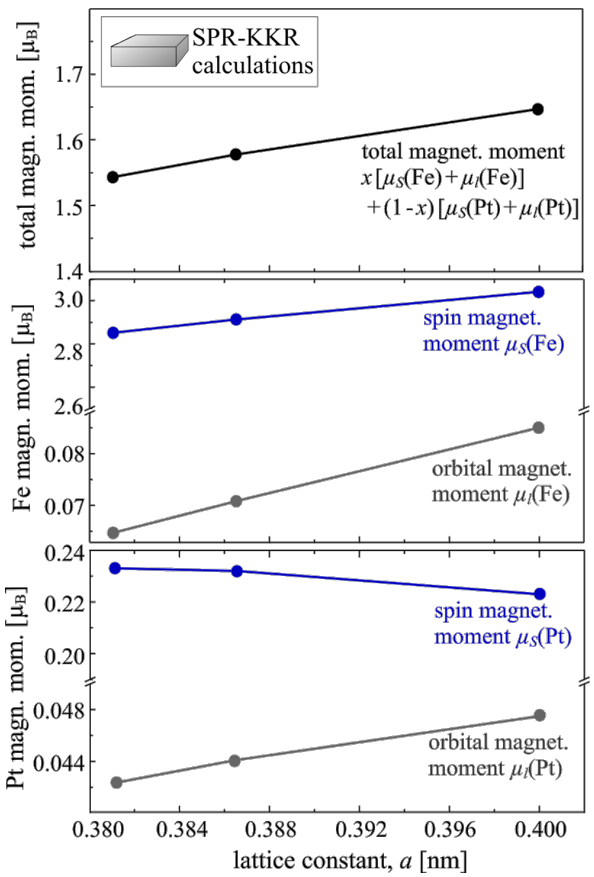


Figure 9: Dependence of spin and orbital magnetic moments at the Fe and Pt sites in chemically disordered FePt alloys for different lattice constants calculated using the SPR-KKR method (x = 0.5).

Conclusion

Wavelet transforms are introduced as an analysis method for EXAFS data with the potential to outperform standard Fourier based approaches especially in bimetallic alloys. The main idea behind the wavelet transform is to replace the infinitely expanded periodic oscillations in a Fourier transform by located wavelets as a kernel for the integral transformation, yielding high resolution in both real space and in *k*-space. Since the maximum backscattering amplitude exhibits different dependences on *k* for different elements, the wavelet transform visualises not only the radial distance distribution but gives also an indication of the type of backscattering atoms surrounding the absorbing atom. Thus, deviations in the local chemical environment in alloys can directly be visualised by comparison to a reference sample as it was shown for the case of FePt nano-

particles. The importance of such a detailed study of the (local) structure for data interpretation in terms of magnetic or electronic characterisation was discussed on the basis of magnetic moments of Fe_xPt_{1-x} alloys measured by XMCD [68] and calculated using the SPR-KKR method. In summary, the different aspects of X-ray absorption spectroscopy, from the XANES region and its dichroism effects, to EXAFS analysis give the possibility to characterise fully nanoparticle systems regarding crystallographic and electronic structure as well as magnetic properties.

Acknowledgements

For useful discussions H. Wende is gratefully acknowledged. This work was carried out in close collaboration with M. Spasova, A. Trunova, and M. Farle (U. Duisburg–Essen), A. Rogalev and F. Wilhelm (ESRF), and K. Fauth (U. Würzburg). For their valuable support during beamtimes, we would like to thank P. Voisin and S. Feite (ESRF) as well as the HZB-BESSY II staff, in particular T. Kachel and H. Pfau. For help with the SPR-KKR calculations, J. Minár, M. Košuth, and H. Ebert (LMU Munich) are acknowledged and S. Sun (Brown U.) for the synthesis of nanoparticles. Financially supported by DFG (SFB 445), ESRF, EU (MRTN-CT-2004-0055667, SyntOrbMag), and BMBF (05 ES3XBA/5).

References

1. Altarelli, M. From Third- to Fourth-generation Light Sources: Free-Electron Lasers in the UV and X-ray Range. In *Magnetism and Synchrotron radiation – New trends;* Beaurepaire, E.; Bulou, H.; Scheurer, F.; Kappler, J. P., Eds.; Springer Proceedings in Physics, Vol. 133; Springer: Berlin, Heidelberg, 2010; pp 407–419.
2. Wiedemann, H. *Synchrotron Radiation;* Springer: Heidelberg, Germany, 2002.
3. Attwood, D. *Soft X-rays and extreme ultraviolet radiation;* Cambridge University Press: Cambridge, U.K., 1999.
4. Peatman, W. B. *Gratings, Mirrors, and Slits;* Gordon and Breach Science Publishers: New York, 1997.
5. Erko, A.; Idir, M.; Krist, T.; Michette, A. G., Eds. *Modern Developments in X-ray and Neutron Optics;* Springer Series in Optical Science, Vol. 137; Springer: Berlin, Germany, 2008.
6. Wille, K. *Physik der Teilchenbeschleuniger und Synchrotronstrahlungsquellen,* 2nd ed.; Teubner: Stuttgart, Germany, 1996.
7. Jackson, J. D. *Classical Electrodynamics,* 3rd ed.; John Wiley & Sons: New York, 1998.
8. Cheng, G.; Carter, J. D.; Guo, T. *Chem. Phys. Lett.* **2004,** *400,* 122–127. doi:10.1016/j.cplett.2004.10.095
9. Rockenberger, J.; Tröger, L.; Kornowski, A.; Vossmeyer, T.; Eychmüller, A.; Feldhaus, J.; Weller, H. *J. Phys. Chem. B* **1997,** *101,* 2691–2701. doi:10.1021/jp963266u
10. Marcus, M. A.; Brus, L. E.; Murray, C.; Bawendi, M. G.; Prasad, A.; Alivisatos, A. P. *Nanostruct. Mater.* **1992,** *1,* 323–335. doi:10.1016/0965-9773(92)90039-Z
11. Davis, S. R.; Chadwick, A. V.; Wright, J. D. *J. Phys. Chem. B* **1997,** *101,* 9901–9908. doi:10.1021/jp971756w
12. Zanchet, D.; Tolentino, H.; Martins Alves, M. C.; Alves, O. L.; Ugarte, D. *Chem. Phys. Lett.* **2000,** *323,* 167–172. doi:10.1016/S0009-2614(00)00424-3
13. Dubiel, M.; Brunsch, S.; Tröger, L. *J. Phys.: Condens. Matter* **2000,** *12,* 4775–4789. doi:10.1088/0953-8984/12/22/310
14. Dubiel, M.; Haug, J.; Kruth, H.; Hofmeister, H.; Seifert, W. *J. Phys.: Conf. Ser.* **2009,** *190,* 012123. doi:10.1088/1742-6596/190/1/012123
15. Rohlfing, M.; Louie, S. G. *Phys. Rev. B* **2000,** *62,* 4927–4944. doi:10.1103/PhysRevB.62.4927
16. Soininen, J. A.; Shirley, E. L. *Phys. Rev. B* **2001,** *64,* 165112. doi:10.1103/PhysRevB.64.165112
17. Rehr, J. J. *Found. Phys.* **2003,** *33,* 1735–1742. doi:10.1023/A:1026277520940
18. Laporte, O.; Meggers, W. F. *J. Opt. Soc. Am. Rev. Sci. Instrum.* **1925,** *11,* 459–460. doi:10.1364/JOSA.11.000459
19. Huff, L. D.; Houston, W. V. *Phys. Rev.* **1930,** *36,* 842–846. doi:10.1103/PhysRev.36.842
20. Van. Vleck, J. H. *J. Phys. Chem.* **1937,** *41,* 67–80. doi:10.1021/j150379a006
21. Stöhr, J.; Baberschke, K.; Jaeger, R.; Treichler, R.; Brennan, S. *Phys. Rev. Lett.* **1981,** *47,* 381–384. doi:10.1103/PhysRevLett.47.381
22. Chen, C. T.; Tjeng, L. H.; Kwo, J.; Kao, H. L.; Rudolf, P.; Sette, F.; Fleming, R. M. *Phys. Rev. Lett.* **1992,** *68,* 2543–2546. doi:10.1103/PhysRevLett.68.2543
23. Goulon, J.; Goulon-Ginet, C.; Rogalev, A.; Gotte, V.; Malgrange, C.; Brouder, C.; Natoli, C. R. *J. Chem. Phys.* **1998,** *108,* 6394–6403. doi:10.1063/1.476046
24. van der Laan, G.; Thole, B. T.; Sawatzky, G. A.; Goedkoop, J. B.; Fuggle, J. C.; Esteva, J.-M.; Karnatak, R.; Remeika, J. P.; Dabkowska, H. A. *Phys. Rev. B* **1986,** *34,* 6529–6531. doi:10.1103/PhysRevB.34.6529
25. Thole, B. T.; van der Laan, G.; Sawatzky, G. A. *Phys. Rev. Lett.* **1985,** *55,* 2086–2088. doi:10.1103/PhysRevLett.55.2086
26. Erskine, J. L.; Stern, E. A. *Phys. Rev. B* **1975,** *12,* 5016–5024. doi:10.1103/PhysRevB.12.5016
27. Schütz, G.; Wagner, W.; Wilhelm, W.; Kienle, P.; Zeller, R.; Frahm, R.; Materlik, G. *Phys. Rev. Lett.* **1987,** *58,* 737–740. doi:10.1103/PhysRevLett.58.737
28. Goulon, J.; Rogalev, A.; Goulon-Ginet, C.; Benayoun, G.; Paolasini, L.; Brouder, C.; Malgrange, C.; Metcalf, P. A. *Phys. Rev. Lett.* **2000,** *85,* 4385–4388. doi:10.1103/PhysRevLett.85.4385
29. Goulon, J.; Rogalev, A.; Wilhelm, F.; Goulon-Ginet, C.; Carra, P.; Cabaret, D.; Brouder, C. *Phys. Rev. Lett.* **2002,** *88,* 237401. doi:10.1103/PhysRevLett.88.237401
30. Carra, P.; Altarelli, M. *Phys. Rev. Lett.* **1990,** *64,* 1286–1288. doi:10.1103/PhysRevLett.64.1286
31. Stöhr, J.; Siegmann, H. C. *Magnetism – From Fundamentals to Nanoscale Dynamics;* Springer: Berlin, Heidelberg, 2006.
32. Lytle, F. In *Physics of Non-Crystalline Solids;* Prins, J. A., Ed.; North-Holland Pub.: Amsterdam, 1965; pp 12–30.
33. de L. Kronig, R. *Z. Phys.* **1932,** *75,* 468–475. doi:10.1007/BF01342238
34. Sayers, D. E.; Stern, E. A.; Lytle, F. W. *Phys. Rev. Lett.* **1971,** *27,* 1204–1207. doi:10.1103/PhysRevLett.27.1204
35. Lee, P. A.; Pendry, J. B. *Phys. Rev. B* **1975,** *11,* 2795–2811. doi:10.1103/PhysRevB.11.2795
36. Lee, P. A. *Phys. Rev. B* **1976,** *13,* 5261–5270. doi:10.1103/PhysRevB.13.5261
37. Ashley, C. A.; Doniach, S. *Phys. Rev. B* **1975,** *11,* 1279–1288. doi:10.1103/PhysRevB.11.1279

38. Ankudinov, A. L.; Ravel, B.; Rehr, J. J.; Conradson, S. D. *Phys. Rev. B* **1998,** *58,* 7565–7576. doi:10.1103/PhysRevB.58.7565
39. Zabinsky, S. I.; Rehr, J. J.; Ankudinov, A.; Albers, R. C.; Eller, M. J. *Phys. Rev. B* **1995,** *52,* 2995–3009. doi:10.1103/PhysRevB.52.2995
40. Brouder, C.; Alouani, M.; Giorgetti, C.; Dartyge, E.; Baudelet, F. *Spin-Orbit Influenced Spectroscopies of Magnetic Solids*, Ebert, H.; Schütz, G., Eds.; Lecture Notes in Physics, Vol. 466; Springer: Berlin, Germany; 1996.
41. Wende, H.; Wilhelm, F.; Poulopoulos, P.; Rogalev, A.; Goulon, J.; Schlagel, D. L.; Lograsso, T. A.; Baberschke, K. *Nucl. Instrum. Methods Phys. Res., Sect. A* **2001,** *467–468,* 1426–1429. doi:10.1016/S0168-9002(01)00675-1
42. Nakamura, T.; Mizumaki, M.; Watanabe, Y.; Nanao, S. *J. Phys. Soc. Jpn.* **1998,** *67,* 3964–3968. doi:10.1143/JPSJ.67.3964
43. Wende, H. *Rep. Prog. Phys.* **2004,** *67,* 2105–2181. doi:10.1088/0034-4885/67/12/R01
44. Citrin, P. H.; Eisenberger, P.; Hewitt, R. C. *J. Vac. Sci. Technol. (N. Y., NY, U. S.)* **1977,** *15,* 449. doi:10.1116/1.569591
45. Citrin, P. H.; Eisenberger, P.; Hewitt, R. C. *Phys. Rev. Lett.* **1978,** *41,* 309–312. doi:10.1103/PhysRevLett.41.309
46. Gudat, W.; Kunz, C. *Phys. Rev. Lett.* **1972,** *29,* 169–172. doi:10.1103/PhysRevLett.29.169
47. Stöhr, J.; Denley, D.; Perfetti, P. *Phys. Rev. B* **1978,** *18,* 4132–4135. doi:10.1103/PhysRevB.18.4132
48. Martens, G.; Rabe, P.; Schwenter, N.; Werner, A. *J. Phys. C* **1978,** *11,* 3125. doi:10.1088/0022-3719/11/14/032
49. Wende, H.; Srivastava, P.; Chauvistré, R.; May, F.; Baberschke, K.; Arvanitis, D.; Rehr, J. J. *J. Phys.: Condens. Matter* **1997,** *9,* L427–L433. doi:10.1088/0953-8984/9/31/002
50. Wende, H.; Baberschke, K. *J. Electron Spectrosc. Relat. Phenom.* **1999,** *101–103,* 821–826. doi:10.1016/S0368-2048(98)00431-9
51. Tromp, M.; van Bokhoven, J. A.; Slagt, M. Q.; Klein Gebbink, R. J. M.; van Koten, G.; Ramaker, D. E.; Koningsberger, D. C. *J. Am. Chem. Soc.* **2004,** *126,* 4090–4091. doi:10.1021/ja031885s
52. Blaha, P.; Schwarz, K.; Madsen, G. K. H.; Kvasnicka, D.; Luitz, J. *WIEN2k, An Augmented Plane Wave Local Orbitals Program for Calculating Crystal Properties;* Schwarz, K., Ed.; TU Wien: Wien, Austria, 2001.
53. Filipponi, A.; Di Cicco, A.; Natoli, C. R. *Phys. Rev. B* **1995,** *52,* 15122–15134. doi:10.1103/PhysRevB.52.15122
54. Ebert, H. In *Electronic Structure and Physical Properties of Solids;* Dreyssé, H., Ed.; Lecture Notes in Physics, Vol. 535; Springer: Berlin, Germany, 2000; pp 191–246.
55. Müller, J. E.; Jepsen, O.; Wilkins, J. W. *Solid State Commun.* **1982,** *42,* 365–368. doi:10.1016/0038-1098(82)90154-5
56. Newville, M. *J. Synchrotron Radiat.* **2001,** *8,* 322–324. doi:10.1107/S0909049500016964
57. Bunker, G. *Nucl. Instrum. Methods* **1983,** *207,* 437–444. doi:10.1016/0167-5087(83)90655-5
58. Kendall, M. G. *The Advanced Theory of Statistics;* Hodder Arnorld: London, 1958; Vol. 1.
59. Newville, M. *J. Synchrotron Radiat.* **2001,** *8,* 96–100. doi:10.1107/S0909049500016290
60. Newville, M.; Līviņš, P.; Yacoby, Y.; Rehr, J. J.; Stern, E. A. *Phys. Rev. B* **1993,** *47,* 14126–14131. doi:10.1103/PhysRevB.47.14126
61. Sayers, D.; Lytle, F.; Stern, E. A. *Adv. X-Ray Anal.* **1970,** *13,* 248–271.
62. McKale, A. G.; Veal, B. W.; Paulikas, A. P.; Chan, S.-K.; Knapp, G. S. *Phys. Rev. B* **1988,** *38,* 10919–10921. doi:10.1103/PhysRevB.38.10919
63. Faxén, H.; Holtsmark, J. *Z. Phys.* **1927,** *45,* 307–324. doi:10.1007/BF01343053
64. Daubechies, I. *Ten lectures on wavelets;* Society for Industrial and Applied Mathematics: Philadelphia, 1992.
65. Shao, X.; Shao, L.; Zhao, G. *Anal. Commun.* **1998,** *35,* 135–137. doi:10.1039/a800360b
66. Yamaguchi, K.; Ito, Y.; Mukoyama, T.; Takahashi, M.; Emura, S. *J. Phys. B: At., Mol. Opt. Phys.* **1999,** *32,* 1393–1408. doi:10.1088/0953-4075/32/5/028
67. Funke, H.; Scheinost, A. C.; Chukalina, M. *Phys. Rev. B* **2005,** *71,* No. 094110. doi:10.1103/PhysRevB.71.094110
68. Antoniak, C.; Spasova, M.; Trunova, A.; Fauth, K.; Wilhelm, F.; Rogalev, A.; Minár, J.; Ebert, H.; Farle, M.; Wende, H. *J. Phys.: Condens. Matter* **2009,** *21,* No. 336002. doi:10.1088/0953-8984/21/33/336002
69. Antoniak, C.; Spasova, M.; Trunova, A.; Fauth, K.; Farle, M.; Wende, H. *J. Phys.: Conf. Ser.* **2009,** *190,* No. 012118. doi:10.1088/1742-6596/190/1/012118
70. Remark: The relation between a non-linear phase shift and the occurrence of an inclined WT magnitude is well-known from the time-frequency domain where such signals are called “chirp” functions.
71. Sun, S.; Murray, C. B. *J. Appl. Phys.* **1999,** *85,* 4325–4330. doi:10.1063/1.370357
72. Dorman, J. L.; Fiorani, D.; Tronc, E. In *Magnetic Relaxation in Fine-Particle Systems;* Prigogine, I.; Rice, S. A., Eds.; Advances in Chemical Physics, Vol. 98; John Wiley & Sons, Inc.: Hoboken, NJ, 2007; pp 283–494. doi:10.1002/9780470141571.ch4
73. Chantrell, R. W.; Weller, D.; Klemmer, T. J.; Sun, S.; Fullerton, E. E. *J. Appl. Phys.* **2002,** *91,* 6866–6868. doi:10.1063/1.1447175
74. Chen, M.-P.; Nishio, H.; Kitamoto, Y.; Yamamoto, H. *J. Appl. Phys.* **2005,** *97,* No. 10J321. doi:10.1063/1.1861274
75. Ivanov, O. A.; Solina, L. V.; Demshina, V. A.; Magat, L. M. *Phys. Met. Metallogr. (Transl. of Fiz. Met. Metalloved.)* **1973,** *35,* 81.
76. Visokay, M. R.; Sinclair, R. *Appl. Phys. Lett.* **1995,** *66,* 1692–1694. doi:10.1063/1.113895
77. Thiele, J.-U.; Folks, L.; Toney, M. F.; Weller, D. K. *J. Appl. Phys.* **1998,** *84,* 5686–5692. doi:10.1063/1.368831
78. Shima, T.; Takanashi, K.; Takahashi, Y. K.; Hono, K. *Appl. Phys. Lett.* **2004,** *85,* 2571–2573. doi:10.1063/1.1794863
79. Stappert, S.; Rellinghaus, B.; Acet, M.; Wassermann, E. F. *J. Cryst. Growth* **2003,** *252,* 440–450. doi:10.1016/S0022-0248(03)00935-7
80. Qiu, J.-M.; Judy, J. H.; Weller, D.; Wang, J.-P. *J. Appl. Phys.* **2005,** *97,* No. 10J319. doi:10.1063/1.1855211
81. Stappert, S.; Rellinghaus, B.; Acet, M.; Wassermann, E. F. *Eur. Phys. J. D* **2003,** *24,* 351–354. doi:10.1140/epjd/e2003-00132-7
82. Wang, R. M.; Dmitrieva, O.; Farle, M.; Dumpich, G.; Ye, H. Q.; Poppa, H.; Kilaas, R.; Kisielowski, C. *Phys. Rev. Lett.* **2008,** *100,* No. 017205. doi:10.1103/PhysRevLett.100.017205
83. Creemers, C.; Deurinck, P. *Surf. Interface Anal.* **1997,** *25,* 177–190. doi:10.1002/(SICI)1096-9918(199703)25:3<177::AID-SIA219>3.0.CO;2-T
84. Sun, S.; Murray, C. B.; Weller, D.; Folks, L.; Moser, A. *Science* **2000,** *287,* 1989–1992. doi:10.1126/science.287.5460.1989
85. Yu, A. C. C.; Mizuno, M.; Sasaki, Y.; Inoue, M.; Kondo, H.; Ohta, I.; Djayaprawira, D.; Takahashi, M. *Appl. Phys. Lett.* **2003,** *82,* 4352–4354. doi:10.1063/1.1584791

86. Colvin, V. L.; Goldstein, A. N.; Alivisatos, A. P. *J. Am. Chem. Soc.* **1992,** *114,* 5221–5230. doi:10.1021/ja00039a038
87. Sun, S.; Anders, S.; Hamann, H. F.; Thiele, J.-U.; Baglin, J. E. E.; Thomson, T.; Fullerton, E. E.; Murray, C. B.; Terris, B. D. *J. Am. Chem. Soc.* **2002,** *124,* 2884–2885. doi:10.1021/ja0176503
88. Mizuno, M.; Sasaki, Y.; Yu, A. C. C.; Inoue, M. *Langmuir* **2004,** *20,* 11305–11307. doi:10.1021/la0481694
89. Li, D.; Poudyal, N.; Nandwana, V.; Jin, Z.; Elkins, K.; Liu, J. P. *J. Appl. Phys.* **2006,** *99,* No. 08E911. doi:10.1063/1.2166597
90. Antoniak, C.; Trunova, A.; Spasova, M.; Farle, M.; Wende, H.; Wilhelm, F.; Rogalev, A. *Phys. Rev. B* **2008,** *78,* No. 041406R. doi:10.1103/PhysRevB.78.041406
91. *The Munich SPRKKR Package,* Version 3.6; Ebert, H. Ludwig-Maximilian University: Munich, 2006.
92. Landolt, H.; Börnstein, R. *Numerical data and Functional Relationships in Science and Technology, New Series III/19a;* Springer: Berlin, Germany, 1986.
And references therein.
93. Perlov, Ya.; Ebert, H.; Yaresko, A. N.; Antonov, V. N.; Weller, D. *Solid State Commun.* **1998,** *105,* 273–278. doi:10.1016/S0038-1098(97)10037-0
94. Landolt, H.; Börnstein, R. *Numerical data and Functional Relationships in Science and Technology, New Series IV/5e;* Springer: Berlin, Germany, 1995.
And references therein.
95. Herper, H. C.; Hoffmann, E.; Entel, P. *Phys. Rev. B* **1999,** *60,* 3839–3848. doi:10.1103/PhysRevB.60.3839
96. Dmitrieva, O.; Spasova, M.; Antoniak, C.; Acet, M.; Dumpich, G.; Kästner, J.; Farle, M.; Fauth, K.; Wiedwald, U.; Boyen, H.-G.; Ziemann, P. *Phys. Rev. B* **2007,** *76,* No. 064414. doi:10.1103/PhysRevB.76.064414

License and Terms

This is an Open Access article under the terms of the Creative Commons Attribution License (http://creativecommons.org/licenses/by/2.0), which permits unrestricted use, distribution, and reproduction in any medium, provided the original work is properly cited.

The license is subject to the *Beilstein Journal of Nanotechnology* terms and conditions: (http://www.beilstein-journals.org/bjnano)

The definitive version of this article is the electronic one which can be found at:
doi:10.3762/bjnano.2.28

Beilstein Journal of Nanotechnology

Effect of large mechanical stress on the magnetic properties of embedded Fe nanoparticles

Srinivasa Saranu[1], Sören Selve[2], Ute Kaiser[2], Luyang Han[3], Ulf Wiedwald[3], Paul Ziemann[3] and Ulrich Herr[*1]

Full Research Paper

Open Access

Address:
[1]Institute for Micro- and Nanomaterials, Ulm University, Germany, [2]Institute for Electron Microscopy,Ulm University, Germany, and [3]Institute of Solid State Physics, Ulm University, Germany

Email:
Ulrich Herr* - ulrich.herr@uni-ulm.de

* Corresponding author

Keywords:
hydrogen in metals; magnetic anisotropy; magnetic data storage; magneto-elastic interactions; nanoparticles; superparamagnetism; thin films

Beilstein J. Nanotechnol. **2011,** *2,* 268–275.
doi:10.3762/bjnano.2.31

Received: 22 February 2011
Accepted: 17 May 2011
Published: 01 June 2011

This article is part of the Thematic Series "Properties and applications of magnetic nanoparticles".

Associate Editor: P. Leiderer

© 2011 Saranu et al; licensee Beilstein-Institut.
License and terms: see end of document.

Abstract

Magnetic nanoparticles are promising candidates for next generation high density magnetic data storage devices. Data storage requires precise control of the magnetic properties of materials, in which the magnetic anisotropy plays a dominant role. Since the total magneto-crystalline anisotropy energy scales with the particle volume, the storage density in media composed of individual nanoparticles is limited by the onset of superparamagnetism. One solution to overcome this limitation is the use of materials with extremely large magneto-crystalline anisotropy. In this article, we follow an alternative approach by using magneto-elastic interactions to tailor the total effective magnetic anisotropy of the nanoparticles. By applying large biaxial stress to nanoparticles embedded in a non-magnetic film, it is demonstrated that a significant modification of the magnetic properties can be achieved. The stress is applied to the nanoparticles through expansion of the substrate during hydrogen loading. Experimental evidence for stress induced magnetic effects is presented based on temperature-dependent magnetization curves of superparamagnetic Fe particles. The results show the potential of the approach for adjusting the magnetic properties of nanoparticles, which is essential for application in future data storage media.

Introduction

Magnetic data storage has been an integral part of computer system technology for many decades and this will most probably remain so in the near future. Over the years, the basic technology of the hard disc, which allows access to magnetic information stored as individual data bits in a magnetic thin film, has been improved without changing the basic concept of moving a read/write head over a rotating disk surface. The impressive advancement in storage density (usually measured in bits per square inch of disc surface) has been achieved by successive reductions of the bit size leading to higher total

capacities. This development is associated with the introduction of new technologies, such as the magneto-resistive read heads first based on the anisotropic magneto-resistance (AMR) and later on the giant magneto-resistance (GMR) and tunnel magneto-resistance (TMR) effect. In conventional magnetic thin films, each bit comprises a large number of magnetic grains, which are coupled by dipolar interactions and, to some extent, by inter granular exchange coupling. The necessity for incorporation of many grains in each bit arises from the requirement for a sufficiently large signal-to-noise ratio. A further increase of the storage density would require a reduction of the size of individual grains.

The magnetization behavior of small particles has been a topic of interest for many years [1,2]. For particle diameters less than a critical size, a single domain state is expected. In such a case, the magnetization of the particle can be represented by one single magnetic moment which adjusts its direction under the influence of local anisotropies, such as the magneto-crystalline anisotropy field, and external fields. In addition, thermal fluctuations may lead to instability of the magnetization over time, as described by Néel [2] and Brown [3]. If the total anisotropy energy $K_{\mathrm{eff}} \cdot V$ per grain approaches a lower limit of $K_{\mathrm{eff}} \cdot V \approx 50–60\ k_{\mathrm{B}}T$, the magnetization will switch in an uncontrolled way within a period of 10 years which is generally considered as not acceptable for data storage applications; here, K_{eff} is the effective anisotropy energy density, V is the volume of the particle and $k_{\mathrm{B}}T$ the thermal energy. The loss of stability can, in principle, be avoided by the use of materials with high coercivity [4], such as chemically ordered FePt or CoPt alloys. However, the use of such materials is limited by the achievable magnetic field of the write head. Patterned media have been discussed as another possible solution, where the data bits are stored in single grains arranged in a regular manner. This would reduce the noise contribution from the irregular domain (bit) boundaries. Spontaneous self-organization of magnetic nanoparticles, as demonstrated first by Sun and co-workers [5] and subsequently by applying micellar preparation techniques [6], has opened up new possibilities for generating this type of media. Another approach for stabilization of the magnetization in small particles is the coupling to an antiferromagnet [7,8]. This leads to an increase in the coercivity and additionally, to an exchange bias field, which may shift the magnetization curves along the field axis. This approach is similar to the method used for the pinning of the magnetization of the reference layer in spin valve sensors. In this context, it should be noted that magnetic nanoparticles also have applications in other fields, such as medical treatment, diagnostics and imaging [9].

A precise control of the magnetic anisotropy energy is most important for the design of future magnetic data storage media. The total effective magnetic anisotropy K_{eff} is a superposition of contributions from magneto-crystalline (K_{mc}), shape (K_{shape}), interface (K_{int}) and magneto-elastic (K_{me}) energies:

$$K_{\mathrm{eff}} = K_{\mathrm{mc}} + K_{\mathrm{shape}} + K_{\mathrm{int}} + K_{\mathrm{me}} \quad (1)$$

The values of K_{mc} range from typically 10^4 to several times 10^5 J/m^3 for Fe, Ni and Co, and up to $6 \cdot 10^6$ J/m^3 for FePt at ambient temperature [4]. The maximum of K_{shape} is given by $1/2 \cdot \mu_0 \cdot M_{\mathrm{s}}^2$, which can also reach values around 10^6 J/m^3 for typical saturation magnetization M_{s} values of about 10^6 A/m. Since the contribution from K_{int} depends on the density of interfaces, it reaches comparable values only when the layer thickness or multilayer periodicities are set in the range of 1 nm. The contribution of K_{me} may be estimated for isotropic materials by $K_{\mathrm{me}} = 3/2 \cdot \lambda \cdot \sigma$, where λ is the magnetostriction constant and σ is the mechanical stress. The value of λ varies from typical values of 10^{-4}–10^{-5} for most materials up to 10^{-3} for some rare earth alloys. To be comparable with the other contributions to the effective anisotropy, stresses in the GPa (10^9 Pa) range would be required. However, in thin films and other nanostructured materials plastic deformation by dislocation glide is constrained by the presence of surfaces and interfaces. Therefore, large elastic stresses may be present in these materials. In such systems, K_{me} may contribute significantly to K_{eff}. It has recently been demonstrated that thin CoFe and Ni films subjected to large biaxial stresses show variations of K_{eff} of up to 50% [10]. Even larger modifications up to 100% have been achieved in Co/Pd multilayers with perpendicular anisotropy [11]. In these materials, which are interesting as potential perpendicular recording media, the interface anisotropy energy may exceed the shape anisotropy for short multilayer periodicities and cause the magnetization to align perpendicular to the plane of the film in the absence of an external field. The modification of the magnetic anisotropy by large lattice distortions and the generation of additional perpendicular anisotropies has also been demonstrated in the case of CoFe alloys, which show large increases in magnetic anisotropy when subjected to tetragonal distortions by incorporation of the material into CoFe/Pt superlattices [12] or growth on Pd(001) surfaces [13].

In the present contribution, we extend the investigations of the stress effect on the magnetic anisotropy to the study of Fe nanoparticles embedded in a nonmagnetic film. If the particles are spherical and do not experience a strong dipolar interaction, the value of K_{shape} should be very low. Bulk Fe has a K_{mc} of only about $5 \cdot 10^4$ J/m^3 , so that contributions from K_{me} should modify the magnetic behaviour of the nanoparticles even at moderate stress values. We first introduce the experimental method for applying stress and provide evidence for the pres-

ence of large biaxial stresses. Then we present results from SQUID magnetometry of Fe nanoparticles in the stressed and stress-free state for the same sample over a range of temperatures.

Results and Discussion

Deposition and structure of the Fe nanoparticles

The Fe nanoparticles used in this study were prepared by plasma-assisted gas phase condensation [14]. This method allows deposition of both, elemental [15] and alloy clusters with rather narrow size distributions. By combination with a film deposition technique, in situ embedding of the clusters is possible. This can not only be used to protect the clusters from oxidation, but also to yield new functionalities such as those exhibited in granular giant magneto-resistance (GMR) systems [16,17] or the introduction of exchange bias effects in nanoparticle systems [18]. Although the arrangement of the deposited clusters on the substrate surface is generally random, it has been recently demonstrated that a self-assembly of the clusters is possible by deposition on a polymer film which subsequently coats and separates the particles [19]. The particle size distribution generated under these conditions was examined by scanning electron microscopy (SEM) and atomic force microscopy (AFM). Figure 1 shows a representative sample of Fe nanoparticles deposited on a silicon wafer. The particle diameters follow a log-normal distribution, typical for the gas condensation technique [20], with a mean size of 13.3 nm and distribution width σ = 2.6 nm. For structural investigations by transmission electron microscopy (TEM), the particles were covered in situ with a thin SiO_x layer to avoid oxidation during the transfer to the TEM. Figure 2 shows a representative TEM image of Fe particles. Different sets of lattice planes can be observed in the particle, proving that the particles themselves consist of subparticles with different lattice orientations. This indicates that the particles are most likely formed by agglomeration of small primary clusters during transport in the inert carrier gas. Figure 3 shows the electron diffraction pattern obtained from a number of such particles. The superposition of the diffraction spots leads to Debye–Scherrer rings which can all be attributed to Bragg reflections from bcc Fe, proving that the Fe nanoparticles crystallize in the bcc phase.

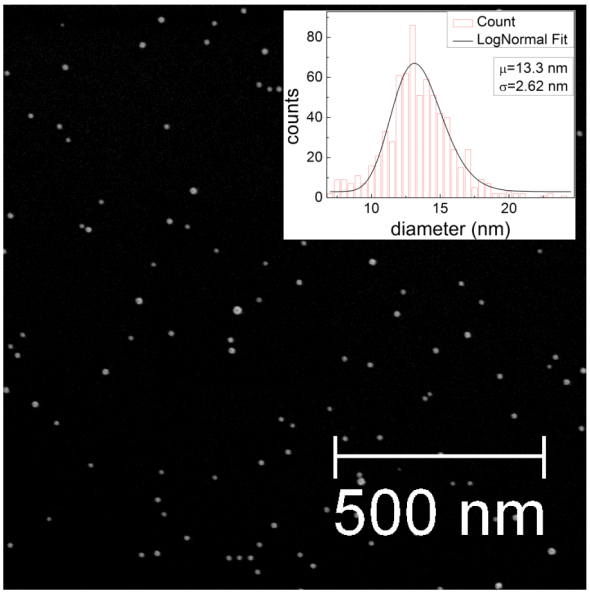


Figure 1: Scanning electron micrograph of Fe nanoparticles deposited on Si. The average particle size observed is 13.3 nm.

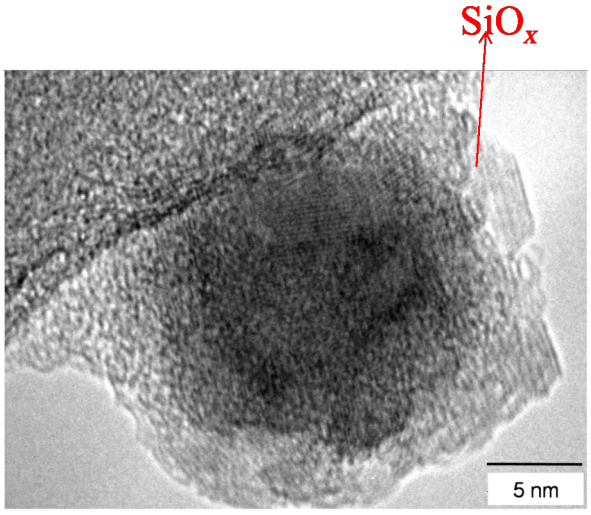


Figure 2: Transmission electron microscope image of Fe nanoparticles (dark contrast) coated with a thin SiO_x layer (brighter contrast).

Embedding and stress application procedure

In this work, stress was applied to the nanoparticles by increasing the volume of the substrate on which they have been deposited through loading it with hydrogen after the deposition process. This method has previously been successfully applied in the case of thin films of Ni, FeCo and Co/Pd [10,11,21]. Ta foils (thickness 200 μm) were used as substrates, which can be loaded with hydrogen up to concentrations of several 10% at quite low temperatures if a Pd coating is applied to the surface of the Ta [22]. This leads to changes of the linear dimensions of up to 3%. The actual stress generated in the films depends on the transfer of the elastic strain in the substrate to the particle embedding film. This transfer depends crucially on the interface properties and is also limited by the onset of plastic deformation. Previous computer simulations of Co nanoparticles

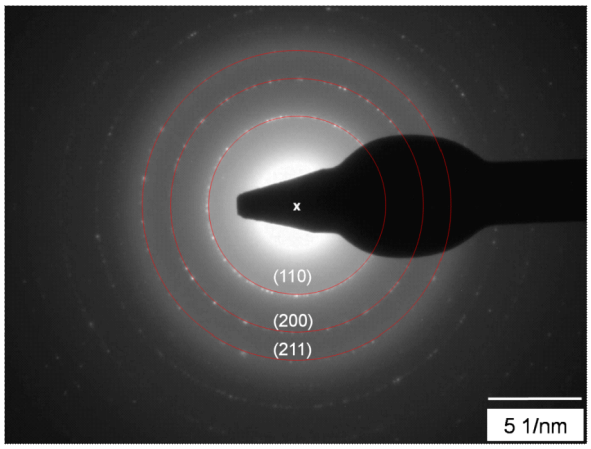


Figure 3: Electron diffraction pattern of the Fe nanoparticles. The Miller indices of the respective lattice planes belong to the bcc structure of Fe.

deposited on a Cu substrate [23] showed that strain transfer from substrate to particles depends on the structure of the interface, and that the strain is also limited to the part of the nanoparticle adjacent to the interface. To achieve large and uniform elastic deformation of the nanoparticles, it is more appropriate to embed them into a continuous film. In addition, an adhesion layer of Ta has previously been used to improve the strain transfer [24]. In this study, the Fe nanoparticles were embedded in Cu films. The procedure consisted of an initial deposition of a 10 nm thick Cu base layer on the Ta substrate, followed by deposition of the nanoparticles in a second step. Finally, the particles were capped with a 20 nm thick Cu layer. This procedure was repeated twice, in order to achieve a higher magnetic signal, resulting in a total Cu film thickness of 50 nm (see Experimental section). The Cu films may also protect the Fe particles from oxidation if exposed to atmospheric conditions. The solubility of H in Cu at equilibrium is very low [25], so we did not expect any effects from H dissolution in the Cu films during the loading procedure. Another advantage of using a Cu film is that the strain in the film can be directly measured by X-ray diffraction, which would be difficult for the Fe nanoparticles alone due to the low scattering intensity. The stress in the Cu film was determined in standard Bragg–Brentano geometry, where the in-plane stress can be calculated from the measured variation of the interplanar distance of the lattice planes parallel to the film plane. For calculation of the stress, an average elastic constant of the Cu film and the embedded Fe nanoparticles should be used. However, since the volume fraction of the Fe nanoparticles was only 0.04%, the average elastic modulus of the film with the nanoparticles was practically identical to the modulus of Cu, E_{Cu} = 110 GPa.

The samples were loaded under a hydrogen pressure of 2 bar at a temperature of 100 °C for durations of up to several hours. After each loading cycle, the lattice parameters of the Ta and the Cu were determined by X-ray diffraction. The volume expansion of the Ta foils led to a shift of the Ta Bragg reflections to lower diffraction angles, while at the same time the Poisson contraction of the Cu film in the direction perpendicular to the film plane resulted in a shift of the Cu(111) fcc peak to higher angles. Both effects can be observed in Figure 4, in which X-ray diffraction patterns of the samples in the as-prepared state and after 24 h exposure to hydrogen gas are shown. The presence of a strong Cu(111) reflection indicates textured growth of the Cu layer with the close packed planes parallel to the substrate surface. The Ta(110) peak shifts from $2\Theta = 38.51°$ to 38.20°. This corresponds to an expansion by 0.78% in the direction perpendicular to the surface. Since the Ta foil is much thicker than the Cu film, the expansion of the Ta foil occurs in the same way in the plane of the foil. The Cu film has to follow this expansion, which reflects itself in a contraction perpendicular to the film surface [21]. The observed shift of the Cu(111) peak from $2\Theta = 43.383°$ to 43.421° corresponds to a contraction of $\varepsilon_z = -0.083\%$. Applying Hooke's law for elastically isotropic media, this leads to an in-plane strain of $\varepsilon_x = 0.09\%$ in the Cu film. The biaxial stress can then be calculated using $\sigma = \varepsilon_x E_{Cu}/(1-\nu)$, (where ν is Poisson's ratio), resulting in a tensile stress value $\sigma = +0.15$ GPa for the Cu film with the embedded Fe nanoparticles. Another result is that the in-plane strain in the Cu film is lower than the strain in the Ta substrate. This can be a result of plastic deformation inside the Cu film, or of some sliding processes at the Ta/Cu interface leading to incomplete transfer of strain from the Ta to the Cu film.

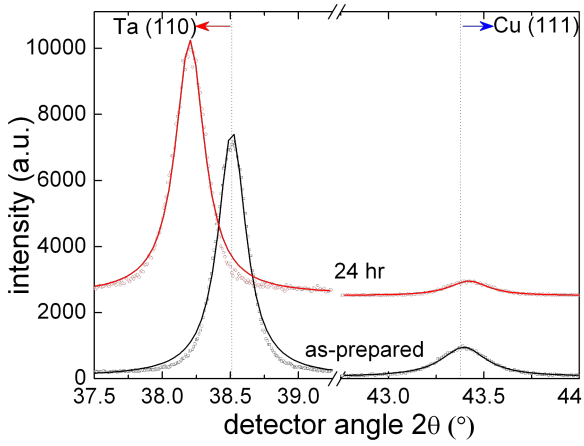


Figure 4: X-ray diffraction patterns (Cu Kα radiation) of Fe nanoparticles embedded in a Cu film on a Ta substrate in the as-prepared state and after 24 h of loading with hydrogen. The solid lines represent fits to the measured data using Lorentz functions.

Magnetic properties

Since the H remains in the Ta substrates after loading for a long time [9], it is possible to study the effect of stress on the properties of the nanoparticle by standard ex-situ techniques after the loading process. To investigate the effect of the applied stress on the magnetic properties of the Fe nanoparticles, measurements in a SQUID magnetometer were performed over a range of temperatures. Figure 5 shows the magnetization curves of the 13 nm embedded Fe nanoparticles at a temperature T = 10 K; the magnetic field was applied parallel to the plane of the film (in-plane). The paramagnetic signal of the Ta substrate was fitted with a straight line and has been subtracted from the data. Note that the total ferromagnetic moment of Fe nanoparticles ($8.3\cdot10^{-6}$ emu) in saturation is only about 2% of the paramagnetic signal of the Ta substrate at 5000 Oe. At this temperature, the particles show a ferromagnetic behaviour. It should be noted that in the as-prepared state the Fe nanoparticles show a superparamagnetic behaviour in our SQUID measurements at 300 K. A direct comparison of the identical sample before and after hydrogen loading showed an almost identical coercivity, but a significant increase of the M_r/M_s ratio (M_r is the remanence) from M_r/M_s = 0.11 in the as-prepared state to M_r/M_s = 0.22 in the loaded state. In addition, the saturation field H_s decreased from a value of about 4 to 5 kOe in the as-prepared state to about 2.5 to 3 kOe in the loaded state (the determination of more precise values for H_s is hindered by the scatter in the measured magnetization data). Both observations indicate a modification of the total effective magnetic anisotropy K_{eff} by the H loading procedure.

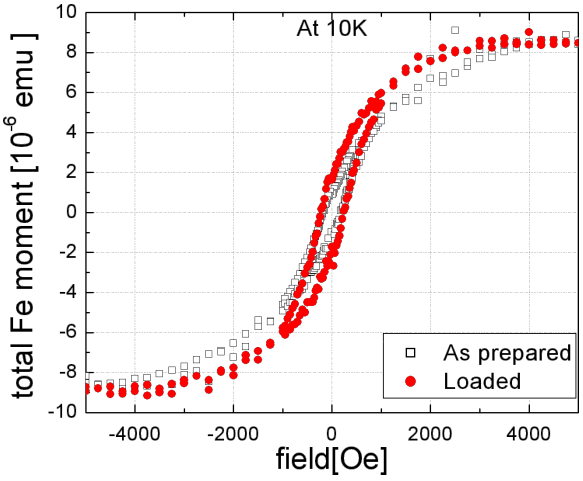


Figure 5: In-plane hysteresis curves of the embedded Fe nanoparticles measured at 10 K in as-prepared state (open squares) and after loading of the Ta substrate with H (red circles).

Considering the orientation of the applied field, it appears that the anisotropy has an additional in-plane component after H loading, which leads to a stronger tendency of the magnetization to align in the plane of the film. This can explain both the larger M_r/M_s ratio (since the component of M parallel to the film plane is measured here) and the reduction of H_s. It should be noted that the observation of these changes does not contradict the fact that the coercivity does not change. The coercivity depends on the magnetization reversal process which may, in principle, occur by rotation mechanisms restricted to the plane of the film, since the external field is applied parallel to it. In this case one would not expect to see much effect of the additional anisotropy component on the magnetization reversal process, since under the state of biaxial stress there will be no preferential orientation of the magnetization inside each particle towards any specific direction in the plane of the film. However, the fact that H_s changes is a clear indication of a modified magnetic anisotropy, since it directly measures the energy necessary for alignment of the magnetization with the applied magnetic field. From the difference between the hysteresis loops before and after the loading, the contribution of K_{me} can be estimated to $K_{me} = 4\cdot10^4$ J/m^3, which is of similar magnitude as the effects of stress previously observed in Ni films [10]. For the calculation of K_{me}, we have assumed here that Fe nanoparticles have the bulk saturation magnetization. We point out that the change of the shape anisotropy due to the elastic deformation of the nanoparticles does not lead to a contribution of comparable size [26].

We have also studied magnetic properties of the embedded Fe nanoparticles at different temperatures. Figure 6 shows the magnetization curves for the loaded sample measured at 10 K and 300 K. Although a large reduction of the coercivity is observed at 300 K compared to 10 K, there is a small remnant magnetization indicating that at least some of the particles show ferromagnetic behaviour at 300 K. This may be attributed to the presence of a small fraction of larger Fe nanoparticles (as indicated by the size distribution given in Figure 1). We note here that there may be a small error induced by the subtraction of the large paramagnetic signal of the Ta substrate; therefore, the small difference between the magnetization curves at 300 K and 10 K for high applied fields (where the paramagnetic Ta contribution is large) is within the error of the measurement.

One characteristic feature of superparamagnetic behaviour is the existence of a blocking temperature T_B, below which the magnetic fluctuations are “frozen in” on the time scale of the respective measurement. A standard technique to characterize superparamagnetic particles is the comparison of the magnetization versus temperature curves, recorded during heating from low temperature (below T_B) to room temperature. The measurements are performed after previously cooling with applied field (field cooled, FC) or without an external applied magnetic field

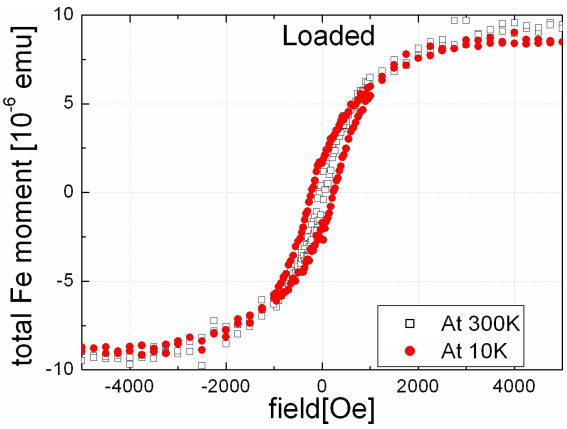


Figure 6: In-plane hysteresis curves of the embedded Fe nanoparticles after loading of the Ta substrate with H, measured at 10 K (filled red circles) or 300 K (open squares).

(zero field cooled, ZFC). The thermo-magnetic curves are typically measured in a small applied field. In this study, we applied a field of 100 Oe during the measurements.

Figure 7 shows a comparison of the FC and ZFC curves of the same sample before and after H loading of the Ta substrate. The ZFC curves show a very similar behaviour before and after loading, whereas the FC curves differ for both samples. As a result, the temperature above which the FC and the ZFC curves fall together (called convergence temperature T_{con} here) shifts from about T_{con}= 170 K in the as-prepared state to about T_{con} = 220 K after H loading. In fact, we do not necessarily expect to see a shift of the blocking temperature T_B (determined by the maxima of the ZFC curves) as a result of an additional magneto-elastic anisotropy contribution. As in the static magnetization measurements, we measure only the magnetization component in the direction of the applied field, which is in the plane of the film here. The fact that T_B does not change indicates that we do not "trap" the magnetization in local minima separated by a barrier. Under the applied biaxial stress, the magneto-elastic anisotropy contribution will add to the other anisotropies present, and we will only see an effect on T_B if the result would be such a "trap state". However, since there is no preferred easy axis direction generated by the biaxial stress in the case of materials with positive magnetostriction, it is not at all evident that we should get such a state. The fact that T_B does not change indicates that the magnetization may fluctuate in the plane of the film in the same way as before the H loading. In terms of the "energy landscape" picture often used to describe the onset of superparamagnetism, this would translate to a shift of the whole landscape to a lower value without modification of the peak-to-valley differences (as far as only in-plane rotations of the magnetization are concerned). It does not, however, contradict the observed changes of H_s and the M_r/M_s ratio which result from a preferred orientation of the magnetization in the plane of the film without any special easy axis direction.

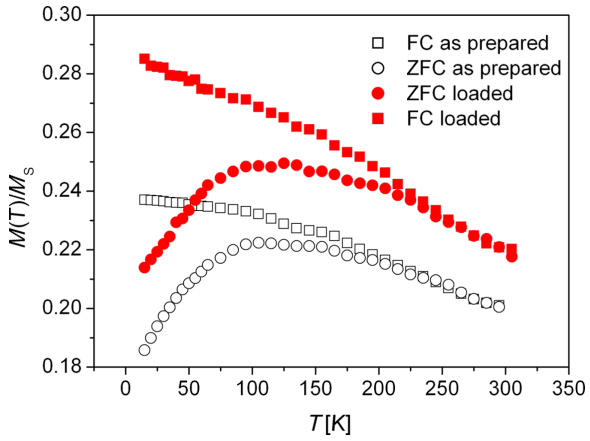


Figure 7: ZFC (circles) and FC (squares) magnetization curves of the Fe nanoparticles embedded in Cu film in the as-prepared state (open symbols) and after loading of the Ta substrate with H (filled red symbols) at H = 100 Oe. The magnetization values have been normalized to the saturation magnetization M_s at 10 K.

If we apply the standard criterion 25 $k_BT_B = K_{eff}V$ also as a rough estimate for the effect on T_{con}, then a shift of 50 K in T_{con} would correspond to an increase of the effective anisotropy energy density K_{eff} by approximately $1.5\cdot10^4$ J/m^3 for 13 nm diameter particles. This is similar to the contribution from K_{me} estimated from the hysteresis curves above. One may use a simple estimation of the magneto-elastic energy in the form $K_{me} = 3/2\cdot\sigma\cdot\lambda$, where λ is the magnetostriction constant of the material. Using $\lambda = 8\cdot10^{-6}$ as an estimate for Fe [27], the observed change of K_{eff} would correspond to a stress of about 1 GPa, which is larger than the average stress in the Cu film as estimated from the X-ray diffraction experiments. It is unclear at the moment whether this is due to a deviation of the local stress value in the Fe nanoparticles from the average stress in the Cu film, or due to a deviation of λ from the value for bulk Fe.

It is interesting to compare these results with earlier research on Fe nanoparticles. A recent report on the structure, morphology and magnetic properties of Fe nanoparticles deposited on single crystal surfaces can be found in [28]. In earlier studies, Methling et al. [29] observed the onset of superparamagnetism in size-selected Fe clusters at room temperature for sizes below 11 nm. However, the particles studied here, of nominally 13 nm diameter, behave superparamagnetically in the as-prepared state at room temperature. The difference may result from a slight over estimation of the average size in this study due to the method used (evaluation of SEM images). Such an over estimation could also arise from a non-spherical shape of the nanopar-

ticles, as has been observed in [30] where a height-to-width ratio of 0.85 was found for Fe nanoparticles produced under similar conditions.

Another interesting point is the low value of the M_r/M_s ratio observed for our Fe nanoparticles. According to the Stoner–Wohlfarth model, a value of $M_r/M_s = 0.5$ would be expected for a random distribution of the easy axis for particles with uniaxial anisotropy. For the Fe nanoparticles investigated here, a cubic anisotropy is expected which would further increase the ratio of M_r/M_s. The low value found here could result from dipolar interactions between particles stacked vertically above each other (which might occur during the deposition of the second layer of Fe nanoparticles). Dipolar interaction can also influence the dynamic behavior of the magnetization [31]. In addition, the Fe nanoparticles may also experience Ruderman–Kittel–Kasuya–Yosida (RKKY) like coupling through the Cu matrix, which depends on the details of the arrangement of the particles. On the other hand it is well-known that the particle surfaces may lead to additional anisotropies in nanoparticles. For example, in Co nanoparticles this leads to size dependent effective anisotropies [32]. As a result, the spin structure can assume a non-collinear state as a minimum energy configuration, which would also lead to a reduction of the M_r/M_s ratio. A recent study of the properties of individual Fe nanoparticles by photoemission spectroscopy [33] indicates that, depending on the size of the nanoparticles, different spin structures may result. It should be mentioned here that the presence of sub-particles with different lattice orientation in our samples may lead to a reduction of the crystalline anisotropy according to the random anisotropy model, which is commonly applied to explain the properties of nanocrystalline soft magnets [34]. This effect could further increase the influence of local surface anisotropies on the local spin structure.

Finally, it is noted that the contribution of K_{me} to the anisotropy in magnetic nanoparticles may be combined with any of the other contributions as given in Equation 1. It may therefore be useful for the optimization of the magnetic properties of future magnetic data storage media.

Conclusion

In conclusion, it has been demonstrated that large biaxial stress, as a result of hydrogen loading of the substrate of embedded Fe nanoparticles in the size regime of 13 nm, leads to a modification of their magnetic properties. Results of static magnetization measurements have been presented showing large increases of the M_r/M_s ratio and a reduction of the saturation field of the nanoparticles. The temperature dependent magnetization curves obtained after field cooling are also influenced by the applied stress. The results may be explained by an additional magnetoelastic anisotropy which leads to an "easy plane" rather than an "easy axis". The results may be useful for the optimization of the magnetic properties of future magnetic data storage media.

Experimental

Iron (Fe) nanoparticles were generated using a custom-built plasma gas condensation (PGC) chamber. Iron metal "vapour" was generated using a 2" magnetron sputter source (MAK II) which was loaded with a 99.95% pure Fe target. A continuous argon (Ar) gas stream, adjusted using a mass flow controller, was used as the sputtering gas source and also acts as a condensation gas. A constant Ar pressure of 0.85 mbar was maintained in the PGC chamber for generating Fe nanoparticles. At this Ar pressure iron metal vapour, generated at a sputtering power of 30 W, condenses in to small nuclei, which grow further by adding Fe atoms or cluster–cluster aggregation. The distance between the first aperture in the PGC chamber and the sputter source (called the aggregation length) influences the particle size. In this study, an aggregation length of 170 mm was used. Nanoparticles formed in the PGC chamber were transported to the deposition chamber by maintaining a lower pressure in the deposition chamber compared to PGC chamber. The base pressure of the deposition chamber was lower than $1 \cdot 10^{-7}$ mbar. Using another 4" sputter source and a thermal evaporator, both located inside the deposition chamber, thin films could be deposited on the substrate simultaneously with the Fe particles. In this way, embedding of the Fe nanoparticles on the chosen substrate into a protective film could be achieved. For structural analysis in the TEM, Fe nanoparticles were deposited on copper TEM grids covered with holey carbon films, and subsequently covered by deposition of a 5 nm thick SiO_x film on top using thermal evaporation. Ta foil of 200 µm thickness was used as a substrate for the stress application. One side of the Ta foil was polished to an RMS roughness of less than 5 nm using chemo-mechanical polishing. The other side of the Ta foil was coated with 100 nm of palladium, which acts as a catalyst for the hydrogen loading. Afterwards a 10 nm thick Ta adhesion layer was deposited on the polished side by DC sputtering. On top of the Ta layer, a 10 nm Cu layer was thermally evaporated. Fe nanoparticles generated in the PGC chamber were then deposited on the Cu layer for 300 s. After deposition, the Fe nanoparticles were covered with a 20 nm thick Cu layer. To get a reasonably large magnetic signal for the magnetic measurements, another set of Fe nanoparticles was deposited using the same parameters as before. Finally, a 20 nm thick Cu layer was deposited as a protective cover.

Acknowledgements

Financial support by the Baden-Württemberg Stiftung in the framework of the "Functional Nanostructures" program is gratefully acknowledged.

References

1. Stoner, E. C.; Wohlfarth, P. *Philos. Trans. R. Soc. London A* **1948,** *240,* 599–642. doi:10.1098/rsta.1948.0007
2. Néel, L. *Ann. Geophys. (C. N. R. S.)* **1949,** *5,* 99–136.
3. Brown, W. F., Jr. *Phys. Rev.* **1963,** *130,* 1677–1686. doi:10.1103/PhysRev.130.1677
4. Weller, D.; Moser, A.; Folks, L.; Best, M. E.; Lee, W.; Toney, M. F.; Schwickert, M.; Thiele, J.-U.; Doerner, M. F. *IEEE Trans. Magn.* **2000,** *36,* 10–15. doi:10.1109/20.824418
5. Sun, S.; Murray, C. B.; Weller, D.; Folks, L.; Moser, A. *Science* **2000,** *287,* 1989–1992. doi:10.1126/science.287.5460.1989
6. Ethirajan, A.; Wiedwald, U.; Boyen, H.-G.; Kern, B.; Han, L.; Klimmer, A.; Weigl, F.; Kästle, G.; Ziemann, P.; Fauth, K.; Schütz, G.; Jun, C.; Behm, R. J.; Büttner, M.; Romanyuk, A.; Oelhafen, P.; Walther, P.; Biskupek, J.; Kaiser, U. *Adv. Mater.* **2007,** *19,* 406–410. doi:10.1002/adma.200601759
7. Skumryev, V.; Stoyanov, S.; Zhang, Y.; Hadjipanayis, G.; Givord, D.; Nogues, J. *Nature* **2003,** *423,* 850–853. doi:10.1038/nature01687
8. Nogues, J.; Sort, J.; Langlais, V.; Doppiu, S.; Dieny, B.; Munoz, J. S.; Surinach, S.; Baro, B. D.; Stoyanov, S.; Zhang, Y. *Int. J. Nanotechnol.* **2005,** *2,* 23–42.
9. Reiss, G.; Huetten, A. *Nat. Mater.* **2005,** *4,* 725–726. doi:10.1038/nmat1494
10. Hamann, J. E.; Mohanan, S.; Herr, U. *J. Appl. Phys.* **2007,** *102,* 113910. doi:10.1063/1.2821309
11. Mohanan, S.; Herr, U. *J. Appl. Phys.* **2007,** *102,* No. 093903. doi:10.1063/1.2802993
12. Andersson, G.; Burkert, T.; Warnicke, P.; Björck, M.; Sanyal, B.; Chacon, C.; Zlotea, C.; Nordström, L.; Nordblad, P.; Erikson, O. *Phys. Rev. Lett.* **2006,** *96,* 037205. doi:10.1103/PhysRevLett.96.037205
13. Winkelmann, A.; Przybylski, M.; Luo, F.; Shi, Y.; Barthel, J. *Phys. Rev. Lett.* **2006,** *96,* 257205. doi:10.1103/PhysRevLett.96.257205
14. Wegner, K.; Piseri, P.; Tafreshi, H. V.; Milani, P. *J. Phys. D: Appl. Phys.* **2006,** *39,* R439–R459. doi:10.1088/0022-3727/39/22/R02
15. Hihara, T.; Sumiyama, K. *J. Appl. Phys.* **1998,** *84,* 5270–5276. doi:10.1063/1.368776
16. Rubin, S.; Holdenried, M.; Micklitz, H. *Eur. Phys. J. B* **1998,** *5,* 23–28. doi:10.1007/s100510050414
17. Serrano-Guisan, S.; Di Domenicantonio, G.; Abid, M.; Abid, J.; Hillenkamp, M.; Gravier, L.; Ansermet, J.; Felix, C. *Nat. Mater.* **2006,** *5,* 730–734. doi:10.1038/nmat1713
18. Rui, X.; Sun, Z. G.; Xu, Y.; Sellmyer, D. J.; Shield, J. E. *J. Appl. Phys.* **2005,** *97,* No. 10K310. doi:10.1063/1.1853271
19. Terheiden, A.; Rellinghaus, B.; Stappert, S.; Acet, M.; Mayer, C. *J. Chem. Phys.* **2004,** *121,* 510–516. doi:10.1063/1.1760077
20. Granqvist, C. G.; Buhrman, R. A. *J. Appl. Phys.* **1976,** *47,* 2200–2219. doi:10.1063/1.322870
21. Mohanan, S.; Smetanin, M.; Weissmüller, J.; Herr, U. *Scr. Mater.* **2009,** *60,* 756–759. doi:10.1016/j.scriptamat.2009.01.005
22. Pick, M. A.; Davenport, J. W.; Strongin, M.; Dienes, G. J. *Phys. Rev. Lett.* **1979,** *43,* 286–289. doi:10.1103/PhysRevLett.43.286
23. Zhou, J.; Saranu, S.; Herr, U. *J. Phys.: Conf. Ser.* **2009,** *144,* 012010. doi:10.1088/1742-6596/144/1/012010
24. Remhof, A.; Song, G.; Sutter, C.; Schreyer, A.; Siebrecht, R.; Zabel, H.; Güthoff, F.; Windgasse, J. *Phys. Rev. B* **1999,** *59,* 6689–6699. doi:10.1103/PhysRevB.59.6689
25. Massalski, T. B., Ed. *Binary alloy phase diagrams;* ASM International: Materials Park, Ohio, 1990.
26. Osborn, J. A. *Phys. Rev.* **1945,** *67,* 351–357. doi:10.1103/PhysRev.67.351
27. Chen, C.-W. *Magnetism and Metallurgy of Soft Magnetic Materials;* Dover Publications: New York, 1986.
28. Kleibert, A.; Rosellen, W.; Getzlaff, M.; Bansmann, J. *Beilstein J. Nanotechnol.* **2011,** *2,* 47–56. doi:10.3762/bjnano.2.6
29. Methling, R.-P.; Senz, V.; Klinkenberg, E.-D.; Diederich, T.; Tiggesbäumker, J.; Holzhüter, G.; Bansmann, J.; Meiwes-Broer, K. H. *Eur. Phys. J. D* **2001,** *16,* 173–176. doi:10.1007/s100530170085
30. Kleibert, A.; Bulut, F.; Gebhardt, R. K.; Rosellen, W.; Sudfeld, D.; Passig, J.; Bansmann, J.; Meiwes-Broer, K. H.; Getzlaff, M. *J. Phys.: Condens. Matter* **2008,** *20,* 445005. doi:10.1088/0953-8984/20/44/445005
31. Majetich, S. A.; Sachan, M. *J. Phys. D: Appl. Phys.* **2006,** *39,* R407–R422. doi:10.1088/0022-3727/39/21/R02
32. Respau, M.; Broto, J. M.; Rakoto, H.; Fert, A. R.; Thomas, L.; Barbara, B.; Verelst, M.; Snoeck, E.; Lecante, P.; Mosset, A.; Osuna, J.; Ould Ely, T.; Amiens, C.; Chaudret, B. *Phys. Rev. B* **1998,** *57,* 2925–2935. doi:10.1103/PhysRevB.57.2925
33. Fraile Rodriguez, A.; Kleibert, A.; Bansmann, J.; Voitkans, A.; Heyderman, L.; Nolting, F. *Phys. Rev. Lett.* **2010,** *104,* 127201. doi:10.1103/PhysRevLett.104.127201
34. Herzer, G. *IEEE Trans. Magn.* **1990,** *26,* 1397–1402. doi:10.1109/20.104389

License and Terms

This is an Open Access article under the terms of the Creative Commons Attribution License (http://creativecommons.org/licenses/by/2.0), which permits unrestricted use, distribution, and reproduction in any medium, provided the original work is properly cited.

The license is subject to the *Beilstein Journal of Nanotechnology* terms and conditions: (http://www.beilstein-journals.org/bjnano)

The definitive version of this article is the electronic one which can be found at: doi:10.3762/bjnano.2.31